HAL
open science

Metallic nano-structures for light-trapping in ultra-thin GaAs and CIGS solar cells

Clément Colin

To cite this version:

Clément Colin. Metallic nano-structures for light-trapping in ultra-thin GaAs and CIGS solar cells. Other [cond-mat.other]. Université Paris Sud - Paris XI, 2013. English. NNT : 2013PA112305 . tel-00998396

HAL Id: tel-00998396

https://theses.hal.science/tel-00998396v1

Submitted on 6 Jun 2014

HAL is a multi-disciplinary open access archive for the deposit and dissemination of scientific research documents, whether they are published or not. The documents may come from teaching and research institutions in France or abroad, or from public or private research centers.

L'archive ouverte pluridisciplinaire **HAL**, est destinée au dépôt et à la diffusion de documents scientifiques de niveau recherche, publiés ou non, émanant des établissements d'enseignement et de recherche français ou étrangers, des laboratoires publics ou privés.

THÈSE DE DOCTORAT
Spécialité Physique

ÉCOLE DOCTORALE 422:
Sciences et technologies de l'information des télécommunications et des sytèmes

Présentée par

Clément COLIN

pour l'obtention du

Diplôme de Docteur de l'Université Paris Sud

Sujet de la thèse:

Metallic nanostructures for light-trapping in ultra-thin GaAs and CIGS solar cells

soutenue le 18 Décembre 2013

Composition du jury :

M. PELOUARD Jean-Luc	LPN	Directeur de thèse
M. GUILLEMOLES Jean-François	IRDEP	Co-Directeur de thèse
M. COLLIN Stéphane	LPN	Encadrant
M. ESCOUBAS Ludovic	IM2NP	Rapporteur
M. LERONDEL Gilles	LNIO	Rapporteur
M. TIWARI Ayodhya	EMPA	Examinateur
M. VIVIEN Laurent	IEF	Examinateur

Thèse réalisée au Laboratoire de Photonique et de Nanostructures
LPN - CNRS, Route de Nozay, 91460
Tél : +33 01 69 63 60 00
Web : http://www.lpn.cnrs.fr

et à Institut de Recherche et Développement sur l'Energie Photovoltaique
IRDEP - CNRS/EDF/Chimie ParisTech
6 quai Watier, 78400 Chatou
Tél : +33 01 30 87 84 38
Web : http://www.irdep.cnrs-bellevue.fr

Sous la direction de Jean-Luc Pelouard jean-luc.pelouard@lpn.cnrs.fr
Co-direction Jean-François Guillemoles jf-guillemoles@chimie-paristech.fr

Encadrement Stéphane Collin stéphane.collin@lpn.cnrs.fr

Financement Allocation Doctorant Ingénieur Centre National de la Recherche Scientifique, cofinancée EDF

Acknowledgments

Ce travail de thèse a été réalisé dans deux laboratoires de la région parisienne : le Laboratoire de Photonique et de Nanostructures (LPN) du CNRS, à Marcoussis et l'Institut de Recherche et Développement sur l'Energie Photovoltaïque (IRDEP), unité mixte entre le CNRS, EDF et Chimie ParisTech à Châtou. Je remercie Messieurs Jean-Yves Marzin et Dominique Mailly, directeurs du LPN, de m'avoir accueilli dans leur laboratoire. Je regrette simplement la disparition de ma pince fétiche de salle blanche au moment où je l'ai laissée seule dans la même salle que Dominique. Je remercie également toute l'équipe administrative et le service informatique du LPN pour leur aide au quotidien. De même, je remercie Monsieur Daniel Lincot de m'avoir accueilli à l'IRDEP. Je salue également Daniel pour sa capacité inégalée à enflammer les foules et à remonter le moral lorsqu'il défend le photovoltaïque en toutes occasions. Je me rappelle bien du jour où j'ai passé mon entretient au LPN pour ce qui allait être mon stage de fin de master. C'était la première fois que je naviguais en transports en commun en région parisienne et ce fût bien être la dernière (« comment ça le bus prend l'autoroute ? »). Cependant je remercie Jean-Luc Pelouard et Stéphane Collin de m'avoir motivé à venir et à poursuivre en thèse sur un sujet et dans environnement exceptionnels. Merci à Jean-Luc pour avoir assuré la direction de ma thèse, pour le règlement de tous les détails administratifs et financiers, pour sa vision scientifique lors des réunions et pour l'animation de la communauté photovoltaïque française auquel il participe fortement. Merci à Stéphane pour son encadrement de tous les jours et son humeur, elle aussi, toujours égale. Je pense avoir grandement appris auprès de son inflexible rigueur qui me fait tant défaut. Merci pour les discussions, les relectures sans relâche, les corrections nombreuses, les idées, la disponibilité, la patience, bref pour à peu près tout. Son aide a été précieuse pour ce travail et il ne serait pas tel qu'il est sans lui : ma formation par la recherche, je la lui dois ! Lorsque j'ai commencé ma thèse et que je me suis associé avec l'IRDEP sur le papier, j'ai également appris à connaître Jean-François Guillemoles, mon directeur de thèse à l'IRDEP, que je tiens à remercier chaleureusement. Son enthousiasme et son nombre d'idées à la minute font quasiment partie de l'Histoire, en tout cas de la mienne. Merci de m'avoir poussé à proposer des choses et à partir en conférence

(San Francisco !). Merci à lui d'avoir co-dirigé cette thèse avec toute la culture et les connaissances scientifiques et photovoltaïques dont il dispose.

Je remercie Monsieur Laurent Vivien d'avoir accepté de présider mon jury.

Je tiens à exprimer toute ma gratitude à Messieurs Ludovic Escoubas et Gilles Lerondel pour avoir accepté la charge de rapporteur et pour l'intérêt qu'ils ont porté à l'égard de mon travail. Je les remercie pour leurs lectures et leurs intéressantes suggestions. Je remercie également Pr. Ayodhya Tiwari de m'avoir fait l'honneur d'être membre du jury malgré un planning très serré. Je remercie chaque membre du jury pour l'excellente discussion qui a animé ma soutenance, cette dernière restera pour moi un très bon moment.

Je remercie chaleureusement le CNRS et EDF (cette dernière représenté dans mon cas par Messieurs Matthieu Versavel et Yves Shlumberger à l'IRDEP) pour avoir financé mon projet et ma vie de recherche ainsi que pour m'avoir donné accès à deux environnements de recherche de grande qualitié. Je remercie également l'école doctorale STITS pour la gestion de ma thèse ainsi que l'Université Paris XI de m'avoir offert un poste de moniteur à l'IUT de Cachan. Cette expérience aura été très riche et marquante pour moi et je remercie tous mes collègues (notamment Patrick Ruiz, Romain Corcolles, Christophe Vermaelen et Fabien Parrain) qui m'ont aidé et formé pendant ces trois ans.

J'aimerais également remercier tous mes collègues du LPN, le laboratoire qui m'aura accueilli la plupart du temps, et spécialement le groupe Phydis. Merci à Christophe et Nathalie d'abord, les deux gardiens du savoir technologique du groupe. J'ai tellement appris dans la bonne humeur à leurs côtés qu'il est difficile d'exprimer tout les remerciements qui s'imposent mais c'est certainement grâce à eux que j'ai passé autant de bon temps en salle blanche. Merci à Christophe, homme de sport, de cinéma, de musique et de Bretagne pour toutes les discussions, les prêts, les dégustations, les blagues, les coups de mains salvateurs et les observations MEB interminables qui ont précédés ma formation. Merci à Nathalie pour les insols, la scie, les pommes de sa maman, nos sorties piscines et sa gentillesse. Merci à Andrea pour son dynamisme, sa culture techno et sa contribution à mon projet. Il aura également été incontournable dans ma formation et je le remercie pour sa bonne humeur constante et pour ce qu'il m'a appris ainsi que pour les bières partagées avec lui, en conférence ou ailleurs. Merci à Fabrice pour ses discussions toujours originales, et c'est le moins que l'on puisse dire, et pour son soutient inépuisable en informatique. Merci à Nicolas Péré-Laperne, post-doc canonisé, Saint-Patron de la techno lui aussi. Il aura vraiment été un « papa » pour moi lorsque j'ai commencé ma thèse et je lui dois énormément, que ce soit pour son travail et sa formation en salle blanche que pour le soutienà mon projet. Merci à Petru pour les même raisons, pour les lifts difficiles made in ICFO et les

mesures FTIR, pour son incroyable gentillesse et sa patience d'acier. Merci à Gulnar et Ngoc pour leur aide en techno (et les séances interminables d'AFM) ainsi que pour leur bienveillance à notre égard.

Je voudrais ensuite un remerciement spécial pour tous les membres du service technologie du LPN. Beaucoup de mes amis d'école n'ont jamais apprécié les salles blanches. Cependant, je pense que celle du LPN pourrait leur faire changer d'avis. Je remercie profondément la direction et tous les acteurs de la centrale pour permettre à nous, étudiants, de bénéficier de cet environnement d'exception et d'une formation unique sans nous faire ressentir les pressions du financement. J'ai pu être formé à quasiment tous les équipements que j'ai croisés et tenter de nouveaux développements techno et ce dans la bonne humeur et sans aucune contrainte de temps. Amazing ! Merci à Xavier pour les discussions musique, les dépôts diélectriques et les sessions ellipso/reflecto au LPN ou chez Horiba. Merci à David, Laurent et Rémi pour leur disponibilité, leur gentillesse et les innombrables dépôts réalisés. Merci à Laurence pour les gravures ainsi qu'à Stéphane pour les mêmes raisons, les bonnes discussions scientifiques autant que personnelles et les séances de kung-fu à l'heure du déjeuner: malgré son dynamisme certain, je préfère rester debout quand je fais des arts martiaux ! Merci à Christian pour les secours MEB, Jean-Claude pour les blouses (!) et sa rigueur, et à Christophe R. pour son soutient en litho et sur le bonder, à Kamel pour le back-end et enfin à Luc et Edmond pour leur aide sur la partie litho élec.

Finalement, un grand petit mot pour les autres, ceux qui ont partagés mon quotidien, pas toujours côté travail mais dont l'aide est tout aussi précieuse. D'abord bien sûr, ceux qui ont partagé mon bureau et notre petite équipe photovoltaïque. Merci à Inès qui aura été ma co-bureau mais surtout mon compagnon de thèse pendant trois ans. Même thématique, mêmes écoles, mêmes abstracts, mêmes confs : que de bons moments partagés que ce soit sur un kayak avec le vent en pleine face que dans un resto étrange de Hambourg ou encore en trinquant au Jägermeister. Merci pour ses relectures, ses conseils et toute son aide du côté administratif (haha) : elle aussi a beaucoup de crédit dans cette thèse! Je dois aussi la féliciter pour sa propre thèse qui aura été éclatante malgré quelques aléas de sujet et qu'elle aura réussi à boucler bien avant moi pour partir en retraite dans le grand Nord. Bon vent à elle et j'espère que nos chemins se recroiseront. Merci à Nicolas, qu'Inès et moi avons élu meilleur successeur de thématique de l'Histoire, tant sa gentillesse et son dévouement sont hors du commun. Merci pour tous les coups de main et pour les bons moments, je le félicite par avance pour sa thèse plus qu'excellente et lui souhaite bon courage et le meilleur pour la suite. Merci à Florian pour les discussions séries, livres, jeu-vidéo et science (quand même) ainsi que plein de bon moments, en conf, à l'IRDEP ou au LPN. Bon courage à lui ! Merci ensuite à Benoît, le plus fraîchement arrivé dans l'équipe PV, pour les dis-

cussions que l'on a pu avoir lui et moi. Je lui souhaite une bonne thèse et surtout une bonne expérience au Japon, en espérant que tout se passe comme il le souhaite (enfin sur le IBSC, il va falloir se lever tôt). Merci à Grégory, qui aura partagé notre bureau pendant plus d'un an, pour ses blagues et les bons moments. Merci à Emilie Sakat, partie sous le soleil d'Italie, pour ses pots libanais incroyables, sa bonne humeur, ses bons conseils et le voyage à SF. Merci à Christelle pour les moments de rigolades, la soirée moules sans frites et les intenses discussions ! Merci à Benjamin, collègue thésard presque synchro de soutenance avec qui j'ai pu partager les derniers sentiments de thèse, de recherche de job et d'organisation de soirée de thèse ! Merci à Patrick pour ses conseils, à Clément pour ses jeux du midi, à Erwan collègue stagiaire du début, à Ha pour ses spécialités culinaires vietnamienne (Moon cake et œufs couvés !), merci à Simon, Juan, Charlie, Mickaël, Emilie Stevler, Alejandra, Alexandre, Paul, Quentin, Thomas, Anne-Claire, Hugo, Valerian, Xuan, Elsa et tous autres thésards/post-docs présents ou passés qui ont rythmé ma vie au LPN, en conférence, lors d'un pot ou d'une soirée. Merci enfin à mon ami Armand, autre âme perdue de Grenoble revenu se réfugier au LPN, pour nos échanges de livres et de films et nos discussions autour de lectures que nos transports en commun nous laissaient tout le loisir de pratiquer.

Passons du côté IRDEP maintenant : merci à tous mes collègues, permanents ou non, qui m'ont aidé lors de cette thèse. Merci à Negar pour la coordination du projet ULTRACIS, pour sa gentillesse et pour m'avoir aidé à mettre en place des tas de choses pour mon projet. Merci à Laurent pour son aide précieuse en caractérisation et les bons moments en conférence. Merci à Marie, Frédéric et Nathanaëlle pour leur aide en dépôt à l'IRDEP et pour les soirées en Allemagne (finalement, je n'aurais pas organisé mon karaoké...). Merci à Myriam pour ses aides multiples à tous niveaux et nos discussions au LPN, à l'IRDEP dans le RER ou en conférence. Merci à Zacharie qui m'aura bien fait rire ainsi que pour son aide et celle de Benoît sur les techniques de transfert de couches fines de CIGS. Merci également à Anne-Laure, Pierre T-V, Nicolas, Valérie, Gilles, Grégory et Sana pour leur aide. Merci enfin aux doctorants qui m'ont aidé et avec qui j'ai passé de bons moments, notamment au JNPV et en conférence: Florian (encore), Thibaud (ancien stagiaire du LPN, merci pour tes travaux sur la gravure du CIGS !), Amaury (pour la manip PLE, San Francisco), Arthur (calculs porteurs chauds et San Francisco !), Torben (incroyable tour guide à Francfort), Jean (une séance mémorable de microsoudure), Pierre (pour la sphère intégrante), Jorge, Hugo, Eric et Tarik.

Je souhaite remercier également les laboratoires partenaires de mon projet sans qui ces résultats n'auraient pas été possibles. Merci à Philippe Lalanne et Cristophe Sauvan de l'Institut d'Optique pour les discussions intéressantes, pour nous avoir mis à disposition leur code de calcul et pour avoir assuré le service après-vente avec

efficacité et rapidité ! Merci aux personnes de l'ILV d'avoir accueilli un profane dans leurs salles de chimie : merci à Arnaud pour ses conseils, un grand merci à Isabelle pour sa gentillesse et le temps incroyable qu'elle a passé avec moi sur l'amincissement de CIGS (et la SAA !), merci à Dimitri pour les même raisons et enfin merci à Muriel pour les longues et expertes caractérisations sur CIGS (avec un rapport de 30 pages pour une journée de travail s'il vous plaît !).

Merci à tous ceux que j'ai rencontré, lors de collaborationz ou conférences : Romain, Guillaume, Bertrand, etc...

Finalement, il me faut adresser mes derniers remerciements à toutes les personnes qui m'ont soutenu (heureusement) en dehors des laboratoires : mes amis et ma famille à qui je dédie cette thèse. Pour commencer, j'aimerais citer et surtout féliciter mes amis de Grenoble qui se sont lancés et ont mené à bien comme moi une thèse sur Paris ou ailleurs : Pierre et ses damnées supernovæ, son code super bien huilé et annoté, nos discussions sur tout et rien, sur la et sa musique, les bonnes bières et le pastis qu'il ne m'aura pas encore faire avaler ; Kevin et ses transitions obscures d'un atome inconnu de tous, héraut énorme de la Recherche d'abord puis d'autres choses ensuite (j'espère qu'il trouvera sa voie !), ses discours sans concession sur la politique et le reste, son envie de débattre et son intégrité ! (Merci d'ailleurs à ces deux larons de m'avoir poussé vers la guitare : le premier comme une improbable muse et l'autre pour m'avoir tanné à juste titre pendant une bonne année) ; Armand et nano lasers et sa cohérence sur 100 000 kms, sa façon de voir la vie pas comme les autres, nos discussions ahurissantes sur les femmes et les livres, donc ; Barbara et ses mystérieuses cellules, son sourire et pour les « fêtages de weekend » que l'on continue de faire même quand elle était en Angleterre ; Romain, le mec le plus calé en électronique que je connaisse : bonne chance au Japon.

Merci à mes nouveaux amis de Paris pour leur soutien et les soirées : Hélène, Camille, Honza et Florent.

Merci aux autres personnes de Grenoble : Geoffroy pour les soirées incroyables et dantesques dans lesquelles il arrive à m'emmener, sa gentillesse, nos discussions et le Champagne ; Aurélie qui n'aura finalement pas réussi à se séparer des montagnes ; Delphine (et maintenant Guillaume) pour nos bons moments, maintenant sur Paris aussi. Enorme pensée pour tous mes amis de Bretagne, qui le sont restés depuis toutes ses années et sur qui je peux toujours compter pour des moments exceptionnels en la Sainte Terre du beurre salé ou ailleurs, pour les aventures multiples et diverses qui rythment nos vies depuis pas loin de 10 ans : Matthieu bien sûr, même s'il est partie dans la voie obscure de l'énergie, et Antoine pour tout leur soutien depuis 14 ans ! Lucile (belle-couz de chox), (Elodie (et les conseils buccodentaire), Priscille (et les conseils de Droit !), Loïc et Caro et Hamiltonton,

Simon, Mathieu, Elise et Gwendal, Gaël et Fanny (et Margaux !), Rozenn et William et Marc.

Merci à Claude et Marie-Ange pour leur soutien précieux.

Merci enfin à ma famille : mes parents qui m'ont donné la chance d'arriver jusqu'ici (merci à mon père d'avoir relu une partie de ma thèse), ma sœur Anne-Gwenn, Sylvain et mes nièces adorées, ma sœur Fanny (pour avoir relu et corrigé l'anglais de ma thèse, un immense merci !), mes tantes Annick et Claudette pour leur soutien, ma Mémé et ma Grand-Mère pour toujours avoir une pensée pour moi, mon Pépé et mon Grand-Père, Elise et Marc et Michel, mes oncles et tantes.

Merci à Cécile qui partage ma vie depuis plus de 6 ans maintenant (et ça va continuer !) et sans qui vraisemblablement je ne serais pas arrivé au bout de cette thèse. Merci pour son soutien sans retenue dans cette aventure et pour m'avoir supporté lors des moments les plus difficiles. Elle mérite haut la main les derniers crédits de cette thèse !

Contents

Acknowledgments **i**

Contents **vii**

General introduction **1**

1 Photovoltaics status and trends : toward ultra-thin solar cells **5**
1.1 Overview of the photovoltaic situation 6
1.2 Inorganic photovoltaic conversion 7
1.2.1 Solar spectrum and Standard Test Conditions 7
1.2.2 Photo-generation of carriers 8
1.2.3 Carrier separation 9
1.2.4 Carrier collection and recombination processes 11
1.2.5 Device operation and J-V characteristic 11
1.3 Selective solar cell technologies overview 14
1.3.1 Crystalline silicon solar cells 15
1.3.2 GaAs and III-V solar cells 16
1.3.3 Thin film technology 17
1.4 Toward ultra-thin solar cells : opportunities and challenges 22
1.4.1 A cost-driven research 22
1.4.2 Electronic transport 24
1.4.3 Light absorption in ultra-thin solar cells 25
1.4.4 Case study : current status in thinning CIGS solar cells . . 26
1.5 Conclusion 30

2 Light management in solar cells : state-of-the-art **33**
2.1 Introduction 33
2.2 Decreasing the reflection losses 34
2.3 Interface texture 35
2.3.1 Ergodic limit 36
2.3.2 The case of thin-films 36

2.4 Periodic nanophotonic structures for PV 37
2.5 Plasmonics for photovoltaic 39
2.5.1 Introduction to plasmonics 39
2.5.2 Plasmonic scattering 42
2.5.3 Local absorption enhancement 43
2.5.4 Coupling to waveguide mode 43
2.6 Review of novel light management in the case of GaAs and CIGS solar cells 45
2.7 Conclusion and discussion 48

3 Nano-photonic and plasmonic: tools and concepts 51
3.1 Introduction 51
3.2 Metal/Insulator/Metal (MIM) nano-cavity array structure 52
3.2.1 Presentation of the structure 52
3.2.2 Optical response of MIM nano-cavity array 53
3.2.3 Resonance mechanism 53
3.2.4 Critical coupling condition and achievement of perfect optical absorption 54
3.2.5 State-of-the-art: 2D - Metal/insulator/metal (MIM) structure and omnidirectional total absorption 56
3.3 Plasmonic in the visible for gallium arsenide and silver 57
3.4 RETICOLO code: exact Maxwell equation solver 58
3.4.1 Principle 59
3.4.2 Input parameters 60
3.4.3 Application to this manuscript 60
3.5 Conclusion 61

4 Metal/Semi-conductor/Metal (MSM) nano-cavity arrays for broadband multi-resonant absorption in ultra-thin GaAs layer 63
4.1 Introduction 64
4.2 Optical indices and approximations 64
4.3 Reference GaAs solar cell 65
4.4 One-dimensional (1D) nano-cavity array structure 68
4.4.1 Description of the structure 68
4.4.2 Absorption spectrum for the one-dimensional array 68
4.5 Resonant absorption mechanisms analysis 70
4.5.1 The Fabry-Perot model 70
4.5.2 Resonance C: horizontal Fabry-Pérot MSM cavity 72
4.5.3 Resonance A et B: vertical Fabry-Perot cavities. 75
4.5.4 Influence of the wire width 76
4.5.5 Influence of the GaAs thickness 76

4.5.6 Summary . . . 77
4.6 Fundamental properties of the structure . . . 78
4.6.1 Critical coupling condition . . . 78
4.6.2 Absorption in metal . . . 82
4.6.3 Flexibility and optimization . . . 85
4.6.4 Study of the angular dependence . . . 87
4.7 From 1D to 2D structures: polarization independence . . . 90
4.8 Performances and comparison to literature . . . 92
4.9 Conclusion . . . 93

5 Experimental evidence of broadband multi-resonant absorption in ultra-thin GaAs layers 97
5.1 Introduction . . . 98
5.2 Fabrication of GaAs demonstrators . . . 98
5.2.1 Constraints of fabrication . . . 98
5.2.2 Process overview . . . 99
5.2.3 Details of the fabrication process . . . 100
5.3 Optical characterization setups . . . 108
5.4 Optical characterization of Ag/GaAs/Au nano-cavity array demonstrators . . . 110
5.4.1 Optical response of planar GaAs/Au samples . . . 110
5.5 Study of the influence of an aluminum-doped zinc oxyde (ZnO:Al) encapsulation layer on the absorption spectrum . . . 113
5.5.1 Role of the extra ZnO:Al layer . . . 113
5.5.2 Optical response of planar ZnO:Al/GaAs/Au samples . . . 114
5.5.3 Multi-resonant and broadband total absorption measurement on the encapsulated nano-cavity array demonstrators . . . 115
5.5.4 Influence of the width of the particle on the total absorption spectrum and discussion about fabrication tolerance . . . 116
5.5.5 Influence of the incident light angle on the total absorption spectrum . . . 117
5.5.6 Comparison to literature . . . 119
5.6 Conclusion . . . 120

6 Light-trapping in ultra-thin crystalline solar cells: application to GaSb and CIGS 123
6.1 Introduction . . . 124
6.2 Application to GaSb and hot carrier solar cells . . . 126
6.2.1 Motivation: opportunities and challenges in hot carrier solar cells . . . 126
6.2.2 Efficient light confinement in a 25 nm-thick GaSb structure 127

6.2.3 Performances as a hot carrier solar cell and conclusion . . . 132
6.3 Application to CIGS and low-cost, efficient thin-film solar cells . . . 134
6.3.1 Introduction . . . 134
6.3.2 Generalities about numerical calculations on CIGS . . . 134
6.3.3 Reference planar CIGS solar cell . . . 135
6.3.4 Nearly perfect absorption in a 45 nm-thick CIGS layer with a nano-cavity array design . . . 137
6.3.5 Geometrical parametric study . . . 141
6.4 Toward a complete CIGS solar cell: 100 nm-thick CIGS nano-cavity array solar cell . . . 145
6.4.1 Presentation and discussion about the ultra-thin CIGS solar cell . . . 146
6.4.2 Broadband absorption enhancement in the 100 nm-thick CIGS structure . . . 147
6.4.3 Study of the angular dependence . . . 149
6.4.4 Replacing the buffer layer: from CdS to ZnS . . . 149
6.4.5 Conclusion . . . 150
6.5 Back nano-structured CIGS solar cells . . . 151
6.5.1 Introduction . . . 151
6.5.2 150 nm-thick Back nano-structured CIGS solar cell . . . 152
6.5.3 Optimization of the short circuit current for different thickness of CIGS . . . 157
6.6 Conclusion and perspectives . . . 159

7 Fabrication process of ultra-thin nano-structured CIGS solar cells 161
7.1 Previous results of the ULTRACIS project and context of this work 162
7.2 Fabrication of flat ultra-thin CIGS layer on alternative substrate . 163
7.2.1 Goal and context . . . 163
7.2.2 Substrate transfer process . . . 164
7.2.3 Etching and polishing . . . 165
7.3 Patterning CIGS layers . . . 167
7.3.1 Goal and problematic . . . 167
7.3.2 Degassed-assisted patterning soft-UV nano-imprint lithography (DAP NIL) . . . 168
7.3.3 Lift-off process on a flat CIGS surface . . . 173
7.3.4 Back nano-structured mirror . . . 174
7.3.5 Conclusion . . . 176
7.4 Optical characterization of back nano-structured CIGS solar cells . 177
7.5 Conclusion and perspectives on optoelectronic characterization of ultra-thin nano-structured CIGS solar cells . . . 178

Conclusion and perspectives 181

Appendix 187

A Optical constants used in the numerical calculations 189
A.1 Optical constants of CIGS 189
A.2 Optical constants of CdS 192
A.3 Optical constants of Mo 193
A.4 Optical constants of GaAs 194
A.5 Optical constants of GaSb 194
A.6 Optical constants of silver 194
A.7 Optical constants of gold 195
A.8 Optical constants of i-ZnO 195
A.9 Optical constants of ZnO:Al 196
A.10 Optical constants of MgF_2 196
A.11 Optical constants of ZnS 196

B Electromagnetic field intensity maps 199
B.1 25 nm-thick GaAs nano-cavity array structure of Chapter 4 199
B.2 25 nm-thick GaSb nano-cavity array structure of Chapter 6 201
B.3 45 nm-thick CIGS nano-cavity array structure of Chapter 6 202
B.4 100 nm-thick CIGS nano-cavity array solar cell of Chapter 6 204
B.5 Back nano-structured 150 nm-thick CIGS solar cell of Chapter 6 . . 206

C Résumé 209

D List of publications 229

Bibliography 231

General introduction

Context and objectives

There is a strong demand for new solutions concerning light management for solar cells. These last years, the photovoltaic research field has really become aware of the importance this problematic. Among other axis of research, the strong reduction (by a factor of 10) of the thickness of solar cells has be identified as a promising solution to solve issues in terms of manufacturing, cost reductions and terra-watt (TW) development of the solar cell technology. The challenge is to provide the appropriate light management that is be able to keep up with this ambitious objective. The efficient control of light is one of the current limiting factors toward more efficient and cheaper solar cells and is a key to new concepts in PV.

In response, the nano-photonic and plasmonic communities have offered solutions to control light at the sub-wavelength scale. The task is vast due to the variety of technologies, materials and devices already existing in the PV community. Most of the propositions in the literature are dedicated to hydrogenated amorphous silicon (a-Si:H) because this material has a high density of defects and the device needs to be very thin to have an efficient collection of carriers. Some designs have already shown their ability to confine light in very thin layers (thickness = 100-200 nm) with photonic crystals [1] or a patterned metallic back contact [2–4]. In both cases, the active layer is structured and is therefore reserved to non-crystalline material. The strong reduction of thickness of the absorber has been less studied in the case of crystalline materials and there is still a lot of work to do (and therefore opportunities) to achieve ultra-thin crystalline solar cells.

The Laboratory for Photonics and Nanostructures (LPN) has been developing for years expertise in nanophotonics and clean-room technologies for photodetector devices in the near-infrared and middle-infrared region. In 2006, the Institut de Recherche et Dévelopement sur l'Energie Photovoltaïque (IRDEP), specialist in PV and chalcopyrite technologies, has approached LPN in the frame of the french project ANR THRIPV (Très Hauts Rendements et Innovation Photovoltaïque) to provide a new solution to increase absorption in ultra-thin crystalline GaSb layers

for hot carrier solar cell application. In 2009, the collaboration continues with the application to ultra-thin CIGS solar cells in the frame of the french project ULTRACIS (ANR HABISOL) and in 2013 with ULTRACIS-M.

This PhD thesis, joint between LPN and IRDEP, has begun in the context of these projects. Our goal was to develop one or several novel light management schemes that can be universally applied to thin-film solar cells regardless of the technology. The nature of this study is therefore exploratory. We have focused in this manuscript on crystalline and poly-cristalline materials in particular: gallium arsenide (GaAs - record conversion efficiency for single junction solar cells), gallium antimonide (GaSb - application to hot carrier solar cells - ANR THRIPV) and copper indium gallium diselenide (CIGS - low-cost, high efficient solar cell - ANR ULTRACIS). The final goal of our study is to reduce the absorber thickness of these devices to pave the way toward ultra-thin solar cells (thickness of 25-250 nm). The philosophy of my approach has been influenced by both laboratories: in one hand the will is to propose a novel light-trapping structure that breaks the standards of PV in order to push toward the study of ultra-thin solar cells (25-100 nm) on a mid/long term scope and on the other hand the necessity to develop structures able to solve dedicated issues on existing PV devices on a short/mid-term scope.

Organization of this manuscript

This manuscript is structured is three parts:

- Part 1 includes three chapters providing an introduction to the study. In Chapter 1, a general introduction on photovoltaics is given in order to motivate our study. In particular, we show that ultra-thin solar cells are a promising solution to lower cost, to solve manufacturing issues and to allow the development of novel concepts in PV. Chapter 2 provides an overview of the strategies proposed in the literature to manage light in solar cells and ultra-thin solar cells in particular. In chapter 3, we introduce the nanophotonic tools and concepts used in this manuscript. Especially, we present the metal/insulator/metal structure as well as the numerical code used in this work

- In Part 2, we present an original light-trapping structure, called nano-cavity array design, applied to an ultra-thin (25 nm) GaAs absorber layer. Chapter 4 focuses on the numerical analysis, design rules and optimization of the structure to achieve broadband, multi-resonant absorption inside the semiconductor layer. Chapter 5 is dedicated to the fabrication and optical characterization of GaAs proof-of concept samples.

- In Part 3, we propose solutions for GaSb and CIGS ultra-thin structures.

Chapter 6 presents the adaptation and optimization of the nano-cavity array design to both materials along with the results obtained in the frame of ANR THIRPV and ANR ULTRACIS. For CIGS especially, two case are studied: a 45 nm CIGS ultra-thin layer and a more complete 100 nm CIGS solar cell. Alternatively, we propose a third CIGS design for flat solar cells in the 100-400 nm thickness range based on a back metallic grating. The key technological steps of the production of ultra-thin, nano-structured CIGS solar cell are presented in Chapter 7. In particular, an innovative way to process back metallic grating suitable for various flat solar cell structures is presented in the case of CIGS solar cells.

Contributions

I would like to precise here my contribution to the work presented in this manuscript. The numerical calculations have been performed by myself with the Reticolo code supplied by Philippe Lalanne from LP2N and Christophe Sauvan from Laboratoire Charles Fabry, IOGS (Institute of Optics Graduate School). Originally, the idea of 1-dimensionnal MIM design for a 25 nm-thick GaAs layer had been numerically proposed by Stéphane Collin (LPN). I have studied a 2-dimensionnal polarization independent design with the support of the Reticolo code, added some functionality and proposed guidelines for the optimization of the optical response.

For the experimental work of Chapter 5, I have devoted a large amount of time to the production of GaAs proof-of-concept demonstrators. By the end of Ph.D I have the chance to be trained and independent on a large number of steps of the process, except for the epitaxy of GaAs (Aristide Lemaitre and Elisabeth Galopin, LPN) and electron-beam lithography (Nathalie Bardou, Edmond Cambril and Luc Le Gratiet, LPN). I have of course to acknowledge several peoples from the LPN clean-room for technological supports and trainings. In particular, I must cite Nicolas Peré-Laperne, Christophe Dupuis and Andrea Cattoni (LPN) for their precious help. The optical measurements have been realized by myself (reflectometer, normal incidence if the $\lambda = 200 - 970$ nm range) or by Stéphane Collin and Petru Ghenuche (LPN) on the FTIR setup described in Chapter 5.

For Chapter 6, I have conducted all the optical simulations and optimizations. The theory and conversion efficiency evaluation of GaSb hot carrier solar cells have been done by Arthur Le Bris and Jean-François Guillemoles (IRDEP).

In Chapter 7, the samples presented at the end of the chapter have been mainly processed by myself, in collaboration of many people of the ANR ULTRACIS collaboration. The production of ultra-thin, nanostructured CIGS solar cell is an ambitious and exciting objective, yet the process development has required the time and skills of people from distinct origins. In my case, the growth of CIGS on Mo/glass substrate has been realized by ZSW. I have realized the etching of the

CIGS absorber with the collaboration of Dimitri Mercier and Isabelle Gérard at the Institut Lavoisier de Versailles (ILV). Isabelle has realized also atomic absorption spectroscopy measurements on the samples. The polishing of CIGS surfaces has been realized by Nicolas Peré-Laperne, Christophe Dupuis and I at LPN. I have realized the CIGS superstrate transfer at IRDEP with the collaboration of Zacharie Jehl and Benoit Fleutot. The cadmium sulfide chemical bath deposition has been realized by Nicolas Loones and Valérie Bockelee (IRDEP). The zinc oxyde sputtering has been realized by Gilles Renou and Marie Jubault (IRDEP). I have participated in the development the nano-imprint lithography process of metallic nanostructures (lift-off and back structure) with Andrea Cattoni (LPN). The IV and EQE measurements have been realized by Enrique Leite and Laurent Lombez (IRDEP) and atomic force microscopy by Gulnar Dagher and Ngoc Quach-Vu (LPN).

Chapter 1

Photovoltaics status and trends: toward ultra-thin solar cells

Outline

1.1 Overview of the photovoltaic situation 6
1.2 Inorganic photovoltaic conversion 7
1.2.1 Solar spectrum and Standard Test Conditions 7
1.2.2 Photo-generation of carriers 8
1.2.3 Carrier separation 9
1.2.4 Carrier collection and recombination processes 11
1.2.5 Device operation and J-V characteristic 11
1.3 Selective solar cell technologies overview 14
1.3.1 Crystalline silicon solar cells 15
1.3.2 GaAs and III-V solar cells 16
1.3.3 Thin film technology 17
1.3.3.1 $Cu(In, Ga)Se_2$ 18
1.3.3.2 $Cu(In, Ga)Se_2$ device structure 18
1.4 Toward ultra-thin solar cells : opportunities and challenges 22
1.4.1 A cost-driven research 22
1.4.1.1 Availability in raw materials 23
1.4.1.2 Throughput 23
1.4.2 Electronic transport 24
1.4.2.1 Carrier collection 24
1.4.2.2 Open-circuit voltage 25
1.4.3 Light absorption in ultra-thin solar cells 25
1.4.4 Case study : current status in thinning CIGS solar cells . . 26

1.5 Conclusion 30

1.1 Overview of the photovoltaic situation

The energy transition has become a major concern of developed countries for several years. To meet its energy needs, each country uses its available energy in various proportions. Since the 19th century, the energy sources used to meet global demand have been mostly fossil fuels. Nowadays, in a concern of long-term supplies and environment consideration, the energy mix has to be diversified. The challenge of society is to be able to supply low-cost, environmentally friendly energy sources that can meet the growing demands and the terawatt level development. On paper, photovoltaic power has the potential to meet these needs. The average sun power density available at the earth surface is 198 $W.m^{-2}$. This represents 885.000.000 TWh available per year, which is nearly 6.400 times the global human energy consumption in 2008 [5].

However, the human needs of 140.000 TWh in 2009 are expected to grow to 200.000 TWh by 2030 due to world population growth, the increasing demand of developing countries and assuming that energy policies remain the same [6]. Solar energy is the fastest growing energy sector, yet it is still limited on the global energy market. The total capacity installed worldwide has raised from 40 GW in 2010 to 100 GW in 2012.

The cost of photovoltaic, although relatively higher than other renewable and non-renewable energy resources, is not the first challenge to face. As a matter of fact, the grid parity has already been achieved in some regions and might be reached worldwide by 2020 thanks to scale effects in industrial developments [7]. In a nutshell, the important factors are the following for the development of photovoltaic technologies: high throughput is essential for large scale development; material consumption should be lowered to avoid shortages (CIGS, CdTe) and reduce materials costs; efficiencies have to be high to ensure low costs for the overall system. To meet the two first requirements, a possible solution is to reduce the thickness of solar cells. Thin and even ultra-thin solar cells (i.e. around 100 nm for direct band gap material) are hot topics in the PV research field today. The main limitation however has turned out to be the light management. This problematic is the subject of this manuscript.

1.2 Inorganic photovoltaic conversion

The photovoltaic effect corresponds basically to the conversion of light into electricity. It has been discovered in 1839 by Alexandre Edmond Becquerel [8]. However, first solar cells made of silicon able to supply energy to electric load with an efficiency of conversion of 5 % were obtained by the Bell Telehone company in 1954 [9]. The photovoltaic conversion consists of three steps: carrier generation by photon absorption, carrier separation and carrier collection. These steps are described schematically in the next subsections. First, we present the sun as a optical source for our study.

1.2.1 Solar spectrum and Standard Test Conditions

For solar panels testing, we refer to the solar spectrum with the notion of *Air Mass*. The Air Mass is a measure of how far light travels through the Earth's atmosphere. Fig. 1.2.1 represents the schematic of the different solar irradiance spectra received on Earth from the sun and the spectral irradiances AM0 and AM1.5G as a function of the wavelength. Air mass zero (AM0) describes solar irradiance in space, where it is unaffected by the atmosphere. One air mass, or AM1, is the thickness of the Earth's atmosphere. Air mass 1.5 (AM1.5) is the absolute air mass at a solar zenith angle of 48.19 °. To make the standard spectrum representative to as many PV applications as possible, it is not derived from a particular measured spectrum, but it is calculated from the reference AM0 spectrum under representative geometric and atmospheric conditions (Rayleigh scattering, particle diffusion, temperature, pressure, absorption of air and water) [10]. Two standards are defined for terrestrial use. The AM1.5G (Global) spectrum is designed for flat plate modules and has an integrated power of 1000 W/m2 (100 mW/cm2). The AM1.5D (Direct+circumsolar) spectrum is defined for solar concentrator work. It includes the direct beam from the sun plus the circumsolar component in a disk 2.5 degrees around the sun. The direct plus circumsolar spectrum has an integrated power density of 900 W/m2.; the power density of AM0 light is about 1,360 W/m^2.

For PV testing (terrestrial use), the Standard Test Condition (STC) is to predict the performance of a device defined at one sun, at 25 °C and with a solar spectral distribution equivalent to global AM1.5G, by the standards ASTM G173-03 and IEC 60904-3 [11]. For our solar cell performance simulation, we use AM1.5G solar spectrum if not precised otherwise. More details, reference and tables can be found on the website of the American Society for Testing and Materials (ASTM)-Terrestrial Reference Spectra for Photovoltaic Performance Evaluation [12].

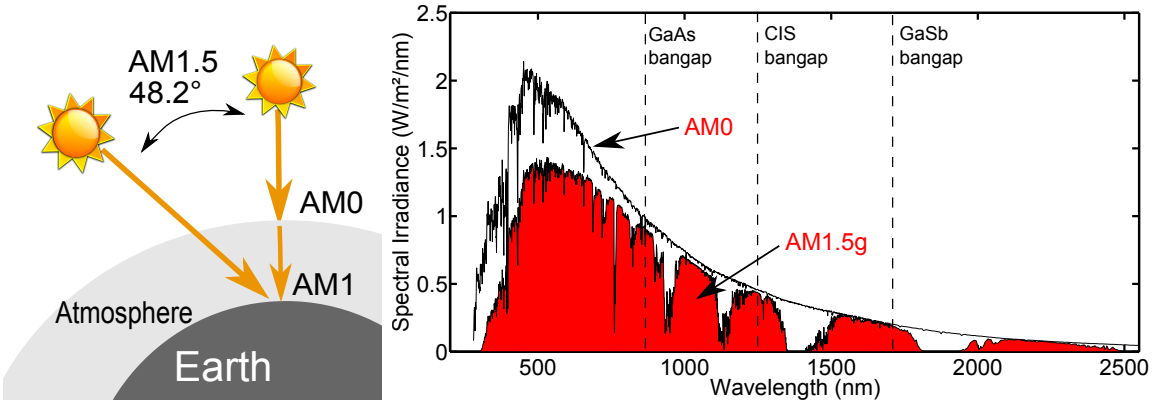

(a) (b)

Figure 1.2.1: (a) Schematic of the different solar irradiances received on Earth from the sun. (b) Spectral irradiance AM0 and AM1.5G as a function of the wavelength (tables from [12]). The values of the band gaps of gallium arsenide (GaAs), copper indium diselenide (CIS) and gallium antimonide (GaSb) are also represented by three dashed lines.

1.2.2 Photo-generation of carriers

The purpose of a solar cell is to convert incident sunlight to electrical power. A single-junction photovoltaic device is a two band system device as depicted in Fig. 1.2.2. In the case of inorganic solar cells made of semiconductors, the ground state is the valence band and the excited state is the conduction band. The two states are separated by an energy band-gap E_g, characteristic of the semiconductor.

When an incident photon of energy $E = \frac{hc}{\lambda}$ (h is Planck's constant, c is the velocity of light and λ the photon wavelength) hits a solar cell, there are several possible outcomes. First, it can simply be reflected on the surface. Second, as shown in Fig. 1.2.2, if the energy of the photon is lower than the band-gap of the semiconductor ($E < E_g$), it passes through the semiconductor without absorption. If the energy of the photon is higher or equal than the band-gap of the semiconductor ($E > E_g$) then it can be absorbed by the semiconductor, exciting an electron from the valence band to the conduction band and generating an electron-hole pair. When the photon energy is higher than the band-gap, the carriers relax rapidly towards the band edges through electron-phonon interactions and the excess energy is lost as heat. This thermalization process is classically much faster than any electron-hole pair separation process. Therefore, we assume in this manuscript that all the generated electron-hole pair has an energy equal to the band-gap energy regardless the energy of the absorbed photon.

In this first step of photovoltaic conversion, there is already three potential losses limiting the efficiency: the reflection of photons on the surface of the cell, the non-absorption of photons of energy $E < E_g$ and the thermalization of photo-generated carriers.

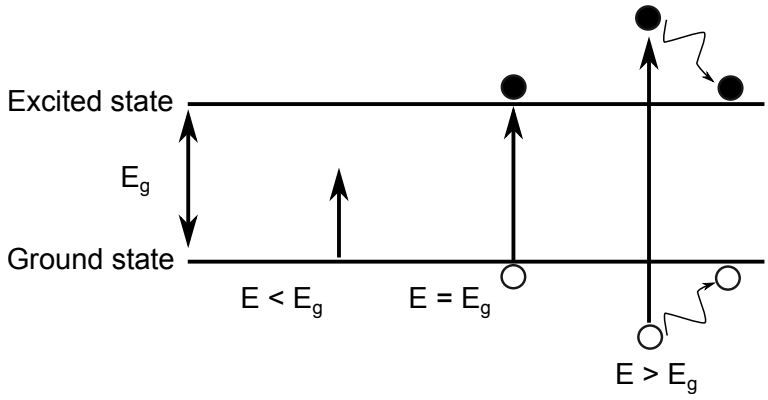

Figure 1.2.2: Simplified schematic of a semiconductor system with two energy states. If the incoming photon has an energy $E < E_g$ (E_g is the band gap value of the semiconductor), it is not absorbed by the material. If $E \geq E_g$, the photon can be absorbed and can give rise to an electron-hole pair. The excess energy is quickly lost by relaxation of the carriers to the band edges.

1.2.3 Carrier separation

After an electron-hole pair is generated, the electron and the hole must be separated and driven to collection at separate electrodes to prevent recombination. The most common separation mechanism is the p-n junction. Such a junction is formed when a n-type semiconductor is contacted to a p-type semiconductor. When the two semiconductors have the same band-gap energy, this junction is called an homo-junction by opposition with an hetero-junction. In the following, we give a brief description of this homo-junction separation mechanism.

The n-type doped layer has a higher electron density. The p-type doped layer has a higher hole density. As a consequence, the Fermi level of the n-doped/p-doped layer is closer to the conduction/valence band than the Fermi level of the intrinsic semiconductor, respectively. At equilibrium, the Fermi level must be the same in the entire junction. It leads to a bending of the energy bands at the junction and the creation of a potential barrier. The height of the potential barrier is equal to qV_{bi} , with V_{bi} the built-in voltage of the junction and q the electron charge. V_{bi} is a function of the doping levels N_a (density of acceptor atoms), N_d (density of

donor atoms) and n_i (intrinsic doping):

$$V_{bi} = \frac{k_b T}{q} ln \left(\frac{N_a N_d}{n_i^2} \right) \tag{1.2.1}$$

where k_b is the Boltzmann constant and T the temperature.

The asymmetry in the electronic structure of the n-type and p-type semiconductors is the basic requirement for the photovoltaic energy conversion. Fig. 1.2.3 shows a schematic band diagram of an illuminated idealized solar cell structure. The quasi-Fermi level for electrons, E_{FC}, and the quasi-Fermi level for holes, E_{FV}, are used to describe the illuminated state of the solar cell. Upon illumination, the quasi-Fermi level splits, giving rise to a chemical potential $\Delta\mu$ defined by:

$$\Delta\mu = E_{Fn} - E_{Fp} \tag{1.2.2}$$

The higher the light intensity the more they split. Close to the electrode both quasi-Fermi levels collapse toward the majority quasi-Fermi level, where they are connected to the metal Fermi level. According to the work of Peter Wurfel [13], the driving force of charge separation is the gradient in the quasi-Fermi levels of the carriers, or in other words, the chemical potential $\Delta\mu$. Electrons flow from the p-type into the n-type region and holes from the n-type into the p-type region. The flow of the photo-generated carriers causes the so-called photo-generation current, J_{ph}. The output power of the cell corresponds to the electrical potential energy of the photo-generated carriers: $\Delta\mu = qV$ with V the voltage drop across the junction. The electrical work extracted depends on the quasi-Fermi level splitting and thus on the semiconductor material used and the doping levels.

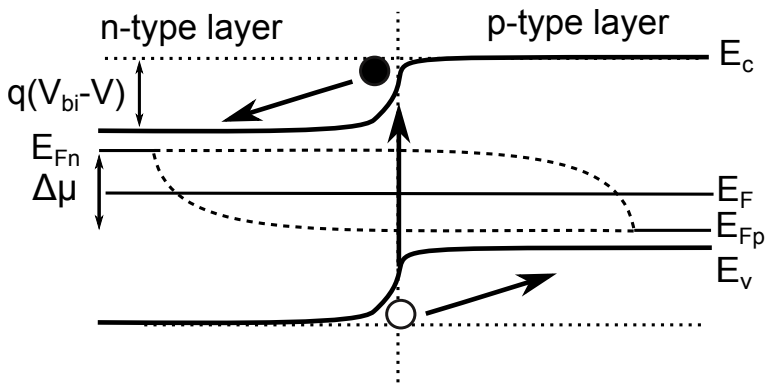

Figure 1.2.3: Schematic energy band diagram of a p-n homojunction under illumination

1.2.4 Carrier collection and recombination processes

After charge separation, the carriers are collected at the electronic contacts, chosen to form an ohmic behavior with the homo-junction. Several recombination processes limit however the collection:

Radiative recombination: the radiative recombination process can be thought of as the inverse of the generation mechanism. An electron in the conduction band loses its energy by the spontaneous emission of a photon and recombines with a hole in the valence band.

Auger recombination: Auger recombination occurs occasionally when two electrons (or two holes) collide. One is excited to a higher energy level while the other one loses its energy to recombine with a hole (or an electron) in the valence (conduction) band. Auger recombination is a non-radiative recombination process. As it requires the interaction of three particles (two electrons and one hole or two holes and one electron), it is more likely to happen at high excess carrier densities (doped layers, high injection level).

Shockley-Read-Hall recombination: another non-radiative recombination process is due to the presence of defects (or traps) in the band gap. The energy lost is given up as heat.

Trap assisted recombination can be particularly important at surfaces and interfaces (for multi-crystalline materials and hetero-structures) because of the high density of surface defects. Surface recombination can be limited by the use of surface passivation. Generally, surface passivation is ascribed to two strategies: reducing interface defect density (chemical passivation) or reducing either electrons or holes concentration at the surface (field effect passivation).

1.2.5 Device operation and J-V characteristic

A solar cell can be described as an ideal current generator, delivering a current J_{ph} under an applied voltage V. The collection efficiency of the photovoltaic conversion process is limited by several sources of losses that can be taken into account in the electric circuit equivalent to a realistic cell as shown in Fig. 1.2.4:

Shunt resistance: leakage currents in the cell are modeled by a shunt resistance R_{sh} in parallel with the current generator.

Series resistance: resistance that arises from the semiconductor resistance when a current is flowing through the cell and from the contact. It is modeled by a series resistance R_s. Series resistance is particularly important in the case of high injection levels, as for concentrated light.

Diode model: All recombination mechanisms are taken into account with a current flowing through a parallel diode, which is the current in the solar cell under applied bias without illumination.

The so-called dark current can be expressed as a function of the voltage:

$$J_d(V) = J_0 \left(exp\left(\frac{qV}{nk_BT}\right) - 1 \right) \tag{1.2.3}$$

where J_d is the current flowing through the diode, J_0 saturation current, V the applied voltage to the diode, k_B the Boltzmann's constant. n is the ideality factor of the diode. Its value, between 1 and 2, reflects the recombination mechanisms in the material. An ideal solar cell has an ideality factor equal to 1. A two diode model can be used to take into account more accurately the different recombination mechanisms.

Under illumination, the Eq. 1.2.3 becomes [14]:

$$J(V) = \left(J_0 exp\left(\frac{q(V - R_sJ)}{nk_BT}\right) - 1 \right) + \frac{V - R_sJ}{R_{sh}} - J_{ph} \tag{1.2.4}$$

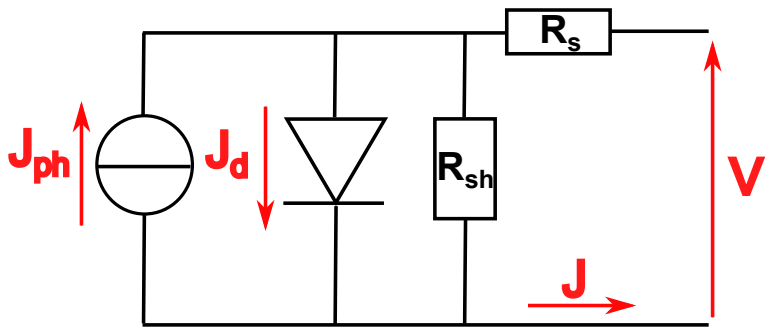

Figure 1.2.4: Diode model: equivalent circuit of a realistic photovoltaic device including series and shunt resistances.

A standard characterization of photovoltaic devices is the current-voltage (I-V or J-V curve) curve. As the generated photocurrent J depends on the illuminated area, it is common to use the current density J, usually expressed in mA/cm^2. Fig. 1.2.5 shows a typical J-V curve. Working in the dark allows to determine J_0 and n. Working under illumination, three points are of importance:

- when no current flows, the voltage is equal to the open-circuit voltage V_{oc}. The open-circuit voltage is limited by the band-gap of the material E_g.
- when there is no voltage, the current density equals the short-circuit current density J_{sc}. We can consider that $J_{sc} \simeq J_{ph}$.

- the maximum power point (V_{max}, J_{max}). It corresponds to the operating point of the cell, which determines the conversion efficiency of the cell.

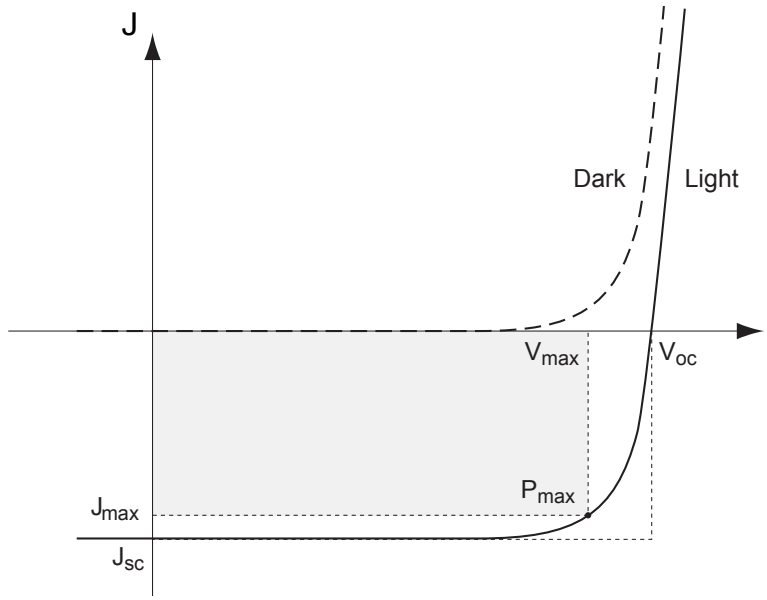

Figure 1.2.5: Current-voltage characteristics of a solar cell in dark (dotted line) and under illumination (solid line). The open circuit voltage (V_{oc}), short circuit current (J_{sc}) and maximum power point (P_{max}) are indicated.

The energy conversion efficiency is defined by Equation 1.2.5:

$$\eta = \frac{V_{max} J_{max}}{P_{in}} = \frac{V_{oc} J_{sc} FF}{P_{in}} \tag{1.2.5}$$

where P_{in} is the total radiation incident on the solar cell and FF the fill-factor. High series resistance, high shunt conductance or high diode current result in poor FF.

The external quantum efficiency (EQE) is defined as the probability that a photon incident on the solar cell contributes to the external photo-current, as a function of the photon wavelength. It can be regarded as the product of $A(\lambda, x)$, the wavelength- and position-dependent probability for absorbing a photon (or thereafter the absorption spectrum in the active region of the solar cell) and a parameter f_c that is the probability that a generated electron-hole pair contributes to the photo-current:

$$EQE(\lambda) = \int A(\lambda, x) f_c(x) dx \tag{1.2.6}$$

An EQE measurement often provides valuable information on the optical properties of the solar cell. Moreover, it can be noted that the EQE can be used to calculate the short-circuit current (expressed in mA/cm^2):

$$J_{sc} = q \int_0^\infty \phi_{1.5G}(\lambda) EQE(\lambda) d\lambda \tag{1.2.7}$$

where q represents the charge of the electron and $\phi_{1.5G}(\lambda)$ the spectral irradiance AM1.5G.

f_c includes all the recombination processes likely to occur in a solar cell (Shockley-Read-Hall, Auger, radiative, ...). Supported by experimentation and simulations, we can also make the approximation that $f_c \approx 1$ for a optimized devices (such as GaAs solar cells). $A(\lambda)$ can be determined for each layer, in the frame of this manuscript, with an electromagnetic simulations. With the previous approximations, the theoretical upper value of the short-circuit current (now noted J_{th}) can be expressed:

$$J_{th} = q \int_0^\infty \phi_{1.5G}(\lambda) A(\lambda) d\lambda \tag{1.2.8}$$

This theoretical value gives us a fair estimation of the effective short-circuit current, or at least an upper limit. In this manuscript, we take Eq. 1.2.8 to estimate the performance of our solar cell design and to compare different structures.

The voltage across an unloaded solar cell is called the open circuit voltage, V_{oc} (see Fig. 1.2.5). V_{oc} corresponds to the separation of the Fermi levels between the front and back contact. In the diode model of Eq. 1.2.4, the V_{oc} can be expressed as:

$$V_{oc} = \frac{k_B T}{q} ln \left[\frac{J_{sc}}{J_0} + 1 \right] \tag{1.2.9}$$

Theoretically this separation is limited by the band gap of the active layer in most of the case we are interested in. In practice, the V_{oc} is lower than the band gap because of the recombination processes (contained in J_0).

1.3 Selective solar cell technologies overview

We propose here selective survey of the different solar cell technologies. In this section, extra details are given in particular for the two technologies studied in this manuscript: gallium arsenide (GaAs) and $Cu(In, Ga)Se_2$ (CIGS). Table 1.1 lists the latest record efficiencies for cells and modules for each major technology.

Technology	Record cell efficiency	Record module efficiency
c-Si	25 % (UNSW)	22.9 % (UNSW)
a-Si:H	10.1 % (Oerlikon)	10.5 % (LG Electronics)
CdTe	19.6 % (GE Global Research)	16.1 % (First Solar)
GaAs	28.8 % (Alta Devices)	24.1 % (Alta Devices)
CIGS	20.4 % (EMPA)	18.7 % (SolarFrontier)
Organic	11.1 % (Mitsubishi Chemical)	

Table 1.1: Latest record efficiencies for cells and modules for each major technology in PV. The values extracted from the solar cell efficiency tables of Green *et al.* [15] and the latest efficiency chart from NREL (2013). Please note that the record module efficiency for a-Si:H technology is for tandem a-Si/Si-Ge/nc-Si cells.

1.3.1 Crystalline silicon solar cells

Over 90 % of the solar cell modules sold today is based on crystalline or polycrystalline silicon (Si). A number of reasons have led to this great success. High performance and good long-term stability are probably the most important ones. Also the huge available amounts of Si, which represents around 20 % of the earth crust, are to the benefit of this technology. However, crystalline silicon solar cells also have disadvantages, which lead to an increased cost for the generated electricity. This is mainly due to the fact that Si is a relatively weak absorber, requiring 100 - 200 µm of semiconductor material to fully absorb the incident sunlight. This c-Si must be high quality and defect free so that the generated carriers are not lost before collection. There is therefore a very high energy demand for purifying SiO2 to Si, which in combination with a rather low material yield during fabrication leads to a relatively high production cost. In the fabrication of crystalline Si solar cells, a so-called wafer technology is used, which means that individual solar cells, made from Si wafers, need to be soldered together to form a solar cell module. This adds complexity to the production process and thereby increases the production costs further. For c-Si approximately 50 % of the total cost is due to the cost of the materials themselves [16].

However, the growing industrialization of crystalline silicon PV technology tends to lower the costs of the overall process, making it still today the leading technology on the solar energy market, although thin-film solar cells are gaining an increasing market share.

1.3.2 GaAs and III-V solar cells

GaAs has been extensively studied since the 50's and now its growth, its processing and its optical and electronic properties are for the most part mastered and known. GaAs is a III-V compound with a direct band-gap of 1.42 eV, widely used in infrared LED and LASERs, fiber optic drivers and receivers, high speed microelectronics devices and high efficiency solar cells. GaAs has some electronic properties which are superior to those of Si [17]: it has a higher electron saturation velocity and a higher electron mobility. However, Si still has some major advantages over GaAs, such as its cheaper price, larger substrate diameter (up to 12"), the possibility to use SiO2 as an insulator or as an excellent gate oxide and higher hole mobility. Despite some drawbacks in the fabrication of microelectronic devices, GaAs has far superior potential than Si in the fabrication of solar cells: the direct band-gap of GaAs allows the absorption of the entire solar spectrum in less than a thickness of 3 µm. Theoretical calculations [18, 19] have shown that the optimum band gap that a single junction solar cell should have in order to reach the best conversion efficiency is about 1.34 eV. This place GaAs solar cells as the top of the list choice for single-junction solar cells.

Being much more difficult to grow and to optimize compared to Si, III-V semiconductors have experienced a slower development until the 1980's and the extent use of molecular beam epitaxy (MBE) and metalorganic vapour phase epitaxy (MOVPE). Today, GaAs solar cell technology holds the record conversion efficiency for single junction solar cells (28,8 % Alta Devices [20, 21]). Despite some promising technological advances in terms of cost reduction and substrate recycling (Epitaxial Lift-Off ELO [22, 23] and controlled spalling technology [24, 25]), single-junction GaAs solar cells remain mainly at space applications or at the pre-industrial state (Alta Devices). Nevertheless, given its ideal properties, it remains a system of choice for research on solar cells in laboratories.

Currently, the great potential of III-V compounds in photovoltaic is their use in multi-junction solar cells. Nowadays, III-V semiconductor devices have almost completely replaced Silicon as the main component for space flat PV modules and in terrestrial applications in concentrated PV thanks to their far greater efficiency, low weight and better radiation resistance. Since substrate lattice matching is yet another limiting condition, the material of choice for the realization of multi-junction solar cells is represented by III-V arsenides (GaAs) and phosphides (InGaP). The record is hold by Sharp and its 37.7 % efficient InGaP/GaAs/InGaAs multi-junction device [26].

1.3.3 Thin film technology

As the name hints, thin film solar cells are normally composed of several thin films, with total thicknesses in the order of 10 µm or less, deposited generally onto a low cost substrate. One advantage with this technology is that a complete, large area, solar cell module can be fabricated in "one piece" (so called monolithic integration). In combination with the low amounts of active material needed, the production cost of thin film solar cells can potentially be significantly lower, compared to crystalline Si solar cells. The development of thin film solar cells started in the 1970s and almost since it has been said "within 5 years the thin film technology will take over the solar cell market". The fact is that in 2013, thin film solar cells still had less than 18 % of the solar cell market, but with an ever increasing market share. One major disadvantage with thin film solar cells is that the efficiencies obtained are not as high as for crystalline silicon solar cells. Mainly three thin film technologies are candidates for large-scale production. These are based on amorphous silicon (a-Si), cadmium telluride (CdTe) and copper indium gallium diselenide Cu(In,Ga)Se2 (CIGS). Additionally, we can mention dye-sensitized solar cell (DSSC) and other organic solar cells.

a-Si solar cells have the longest commercial history in the thin film technology. It has diversified in multijunctions including various other active layers such as micro-crystalline Si (µc-Si) or hydrogenated amorphous silicon germanium (a-SiGe:H). However, commercial single junction a-Si:H solar cells have low efficiencies, from 6 % to 7 % [27]. Combined with high capital costs, these lower efficiencies have limited the implementation of thin-film Si modules to date, and improvements in both efficiency and cost are necessary.

The industrial activity for CdTe-based thin film solar cells is carried by the leader by far in thin film technology, First Solar. By 2013, CdTe had reached recently extremely encouraging production costs as low as $0.64/W, with record efficiencies of 16.1 % total area module efficiency [28]. However, except for First Solar, the CdTe technology is not progressing in terms of market share. Besides technical problems, a major reason for this is a lack of market acceptance related to the relatively large amounts of the toxic element Cd and the rare element Te included in these devices.

Cu(In,Ga)Se2-based solar cells are the thin film technology that results in the highest conversion efficiency and is seen as the most promising solar cell technology for the near future. It has the fastest growing market share and is expected to be the leader in thin-film technology by 2016 according to Fig. 1.3.1, representing the thin-film PV base forecast market value and production from a recent GTM report [29].

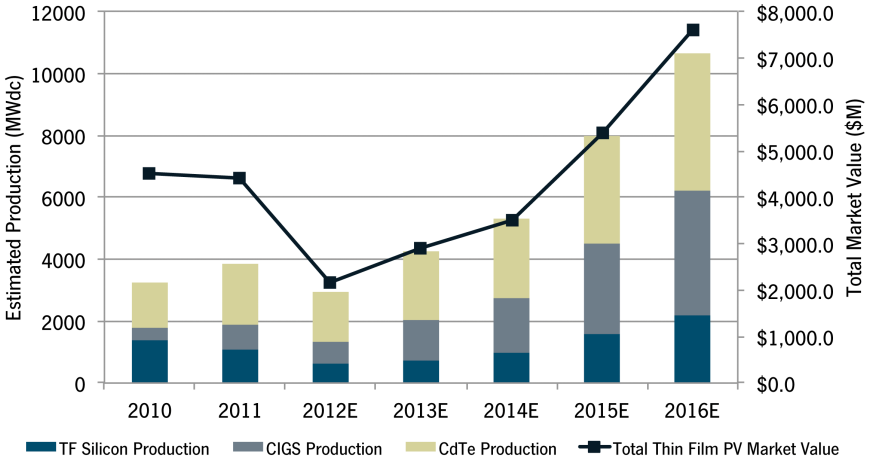

Figure 1.3.1: Thin-film PV base forecast market value and production from a 2012 GreenTech Media report [29]

1.3.3.1 $Cu(In, Ga)Se_2$

First to use $CuInSe_2$ (CIS) as a photovoltaic material were Wagner and co-workers, who in 1973 fabricated a solar cell device with a single crystalline $CuInSe_2$ absorber, which had an efficiency of 12 % [30]. During the early 1980's, Boeing Corporation made large progress in the development of thin film polycrystalline $Cu(In, Ga)Se_2$ (CIGS) solar cells. Efficiencies above 10 % were achieved using a three-sources co-evaporation process [31]. To this date, the highest conversion efficiency for CIGS based thin film solar cells is 20.8 % on glass substrate (ZSW 2013 [32]) and 20.4 % on flexible substrate announced in 2013 by Tiwari's group at EMPA[33].

The current industrial leader is Solar Frontier. They have recently announced that they have achieved a world-record energy efficiency of 19.7 % for a cadmium-free CIS solar cell (approx. 0.5 cm^2), the world's highest aperture area efficiency of 17.8 % for a 30 cm x 30 cm CIS sub-module and the 14.6 % conversion efficiency certified record for a 1257 mm x 977 mm CIS module [34]. More recently, Hanergy Solar announced that Solibro's Copper indium gallium (di)selenide (CIGS) technology has taken a step forward by demonstrating 18.7% photovoltaic module efficiency. The device involves a sub-module in 5x5 cm^2 with an aperture area of approximately 16 cm^2 and consists of 4 serially connected cells [35].

1.3.3.2 $Cu(In, Ga)Se_2$ device structure

A sketch of the conventional $Cu(In, Ga)Se_2$-based thin film hetero-structure is shown without anti-reflection coating (ARC) in Fig. 1.3.2a. Fig. 1.3.2b represents a SEM cross section of a CIGS solar cell taken from Chirila *et al.* [36]. The

structure consists of five thin layers deposited on a substrate.

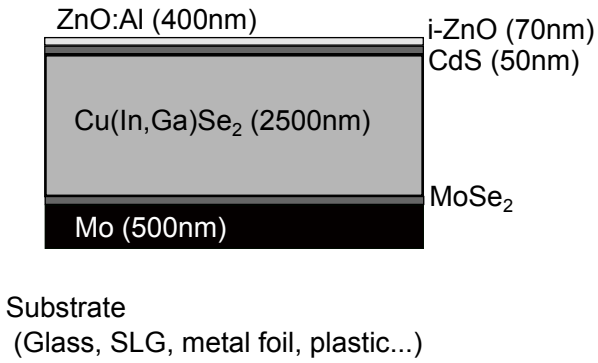

(a)

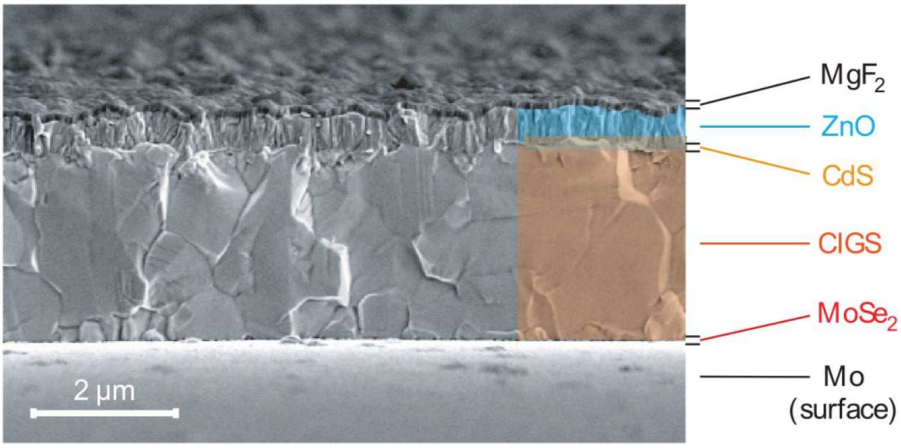

(b)

Figure 1.3.2: (a) Standard structure of a CIGS based thin film solar cell. SEM cross section of a 2.5 µm CIGS solar cell taken from Chirila *et al.* [36]

Substrate: A large improvement of the device performance was observed when the commonly used sodium-free substrates were replaced by soda-lime glass. Indeed, the beneficial effect of sodium, diffusing from the glass to the absorber, is today well recognized. Soda-lime glass substrates are also suitable because of their relatively low cost as well as its good surface quality. Replacing the glass with a flexible substrate, like a plastic or metal foil, is to be advantageous in many ways. So far, excellent results have been obtained by EMPA with record efficiency exceeding 20 % on flexible substrate [33].

Back contact: The criteria for a good back contact material in CIGS based solar cells are, except for being conductive, that it should provide a good ohmic

contact for holes as majority carriers and at the same time provides low recombination for the electrons as minority carriers. It should also be inert during absorber deposition and preferable have a high light reflectance. Molybdenum is so far the best alternative, which also has the special quality of allowing sodium to diffuse from the soda lime glass into the absorber layer [37]. Sodium is an important element that diffuses to the grain boundaries, catalyzes oxygenation and passivation of Se vacancies, favors the formation of a $MoSe_2$ layer [38] and plays the role in the growth of the absorber. The thin $MoSe_2$ layer found at this interface is one reason to explain the good electrical behavior between the absorber and the molybdenum layer. However, one disadvantage with this back contact is its relatively low light reflection and high absorption (see Chapter 6).

Absorber: An absolute need for the absorber in a thin film solar cell is a high absorption coefficient. This is one of the qualities that makes $Cu(In, Ga)Se_2$ suitable as a solar cell absorber. The typical thickness of CIGS is ranging from 1.5 µm to 2.5 µm. Due to the many including elements in ternary and multinary compounds, CIGS have the disadvantage of being relatively complex. However, ternary and multinary semiconductors also have advantages over elementary and binary semiconductors like Si and GaAs to have an off-stochiometric composition and still appear intrinsic. Cu(In,Ga)Se2 belongs to the semiconducting I-III-VI_2 materials that crystallize in the tetragonal chalcopyrite structure [39]. A special quality of the CIGS material is its variable band gap. By changing the x =Ga/(In+Ga) ratio from 0 to 1, the band gap is increased from 1.0 to 1.7 eV. CIGS has a direct band gap. The bandgap dependence on x in eV is of the form $E_g(x) = 1.02+0.67x+0.11x(x-1)$ [40]. Among the large number of possible ways to deposit polycrystalline CIGS layers there are three main approaches that have been more successful than the others, co-evaporation [41, 42], sputtering [43, 44] and electrodeposition [45, 46]. The co-evaporation is a physical vapor deposition technique, where Cu, In, Ga and Se are evaporated in a high vacuum chamber from elemental sources to a heated surface (up to 500-600 °) . The record CIGS devices have absorbers that are made by three-stages co-evaporation [47, 48]. The principle of these three stages is to create a gap grading in the absorber layer that naturally creates a front and a back surface field that are favorable for the device electronic properties.

Buffer layer: Cadmium sulfide (CdS) is the buffer layer so far yielding the highest device performance. The effect of this CdS buffer layer is manifold but not completely understood, which also is illustrated by the difficulty of replacing it with a non-toxic buffer layer [49]. Surface passivation and junction for-

mation are two important tasks fulfilled by this layer. The best results are obtained if a 50 nm-thick CdS layer is deposited with a controlled solution growth process often referred to as chemical bath deposition (CBD) [50, 51]. Devices with less toxic alternative buffer layers such as In_2S_3 and Zn(OH,S) have recently reached similar efficiencies as devices with CdS. These layers can also be deposited by a "dry" high-vacuum process like atomic layer deposition (ALD), which in large-scale production might be beneficial over a "wet" process like CBD in order to preserve the high vacuum chain between absorber and window layer depositions [52]. An intrinsic zinc oxide layer (i-ZnO) is commonly used as a second buffer layer.

Front contact: The front contact of a solar cell has the special requirement that it should be both conductive and transparent as the lateral conductivity of CIGS is rather low. A few different kinds of transparent conductive oxides (TCO) exist, of which zinc oxide doped with aluminum (ZnO:Al) is the most commonly used for CIGS-based thin film solar cells.

The $Cu(In, Ga)Se_2$/CdS/ZnO solar cell is a hetero-junction, i.e. a junction between semiconductors of different band gaps. The model for an ideal hetero-junction has been developed by Anderson [53], which extends the p-n homo-junction model to a defect-free abrupt hetero-junction. In this model the valence and conduction band present discontinuities, due to the different band gaps.

A general description of the Cu(In,Ga)Se2 solar cell band diagram can be calculated with SCAPS software [54] and the material parameters given in reference [55]. Figure 1.3.3 shows the energy band diagram in the dark under zero applied voltage. The absorber presents a band gap gradient, from 1.34 eV at the back contact to 1.08 eV at the front contact.

In the case of CIGS, interfaces, because of their higher defect density, are often region of high SRH recombination. Back contact recombination, occurring when electron reach the metallic back contact, are often neglected for standard CIGS solar cell due to the important thickness of the absorber. However, their influence becomes of major importance for thinner absorber layer, particularly for low energy photons that are absorbed deeper in the CIGS, and thus closer to the back contact. Finally, recombination at the CIGS/CdS interface which are assisted by tunneling can also occur, due to interface defects.

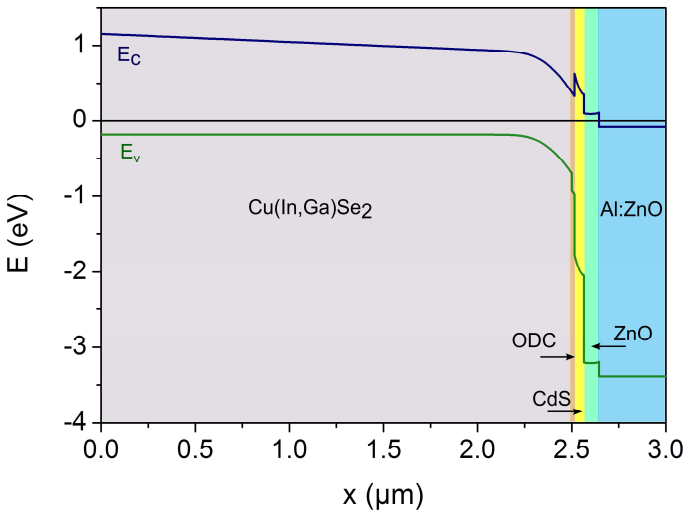

Figure 1.3.3: Energy band diagram of the Cu(In,Ga)Se 2 solar cell according to Petterson *et al.* [55] at zero applied voltage in the dark. Cu(In,Ga)Se 2 bandgap shows a gradient from 1.34 eV at the back contact to 1.08 eV at the front contact. An ordered defect compound layer is included at the absorber surface.

1.4 Toward ultra-thin solar cells: opportunities and challenges

Reducing the thickness of solar cells has been identified as a key issue for the future development of solar cells. Let us get into details about opportunities and challenges concerning ultra-thin solar cells.

1.4.1 A cost-driven research

Thinner layers naturally require fewer raw materials, making the cells less expensive. For c-Si technologies in France however, the cost of the material is approximately 30 % to 50 % of the cost of the total module fabrication cost, which is only about 22 % of the total cost of installation and exploitation on a period 20 years [56]. These cost reductions are significant but not game-changing (although it might be significant for gallium arsenide due to its price [57]). Ultra-thin solar cells must then have other advantages over their thin-film counterparts to be beneficial.

1.4.1.1 Availability in raw materials

One of the main problems of certain current photovoltaic technologies, such as CdTe and CIGS, is the use of rare elements such as Indium (In) and Tellurium (Te). Since these elements are scarce they are usually isolated as by-products of mineral purification for other more common elements; for example, Se and Te are produced largely from Cu mining, and In is produced from Zn mining. As demand increases for these elements in technological applications, such as the use of In for digital displays, the market prices for these rare elements in rising, putting at risk the wide-scale development of these technologies.

Several studies have examined the material abundance limits for the most common thin-film technologies [57–59]. All scenarios of these papers are not the same as the assumptions made for the calculations are not similar (representative efficiencies of the solar cells, representative thickness, material utilization during fabrication, material recycling, PV market growth, CIGS market share growth, Indium price...). All agree though that there may be constraints for Te and In, mostly due to increasing costs in the next few years. All studies are unanimous in the following conclusions: increase cell and module efficiencies, reduce absorber layer thickness (while maintaining the efficiency) and increase material utilization during fabrication (material utilization rate of In in co-evaporation commercial processes is only 34 % [59]).

In the paper of Fhtenakis [59], the probable thickness of CIGS solar cell in 2020 is 1 µm. In his scenario, the CIGS PV production may be limited to 13 to 22 GW/year, which represents a small growth compared to the actual production rate (already 1 GW/year for Solar Frontier). Reducing the thickness of absorber by a factor of ten while conserving the same efficiency with an efficient light management would obviously release all the constraints in terms of feedstock and production by the same factor. Ultra-thin film solar cells along with concentration microcells [60] (providing selective deposition methods)) and absorbers based on abundant elements (such as kesterites) are top of list choices for dealing with material abundance issues.

1.4.1.2 Throughput

Ultrathin-film solar cells, require much shorter deposition times as the layer thickness is reduced, directly improving fabrication throughput and reducing the cost at the industrial level. This is true for every technology, especially for those relying on vacuum and high-vacuum deposition techniques (plasma-enhanced chemical vapor deposition (PECVD) for high quality a-Si:H, co-evaporation for CIGS, epitaxy for GaAs). These deposition techniques have low deposition rates (about 1 nm/s for a-Si:H PECVD), and every factor of reduction in the layer thickness would

improve the manufacturing of solar cells, even for abundant material-based solar cells such as a-Si:H and GaAs.

1.4.2 Electronic transport

1.4.2.1 Carrier collection

Most collection-limited materials would benefit from ultrathin-film devices with optically thick absorption. Materials such as organic polymers, quantum dots, and polycrystalline or amorphous inorganic semiconductors could all benefit from reduced layer thicknesses, particularly if the thickness can be reduced to be comparable to the minority carrier diffusion length. Many cells made from these materials face a trade-off between complete light absorption and carrier collection, limiting the achieved efficiencies. Alternative device architectures have also been used for these materials, including p-i-n drift based devices for thin-film Si and bulk heterojunctions for organic cells, although these devices still have some restrictions on the thickness for complete carrier collection.

Alternatively, for crystalline materials with good electronic properties, what if the thickness of the junction would become much lower than the mean free path of the carriers? The average time between collision events for electron in a semi-conductor can be expressed as [61]: $\tau_c = \frac{\mu_n m_e^*}{q}$ where q is the elementary charge, m_e^* is the electron effective mass and μ_n the mobility of of electrons. For undoped gallium arsenide (GaAs) at 300 °K, the mobility of electrons is $\mu_n = 8800\,\mathrm{cm^2V^{-1}}s^{-1}$ and the thermal velocity of electron is $v_c = 1.10^5\,\mathrm{m/s}$ [62] and the electronic effective mass in GaAs is $m_e^* = 0.067m_e$ [63]. The collision time is therefore equals to $\tau_c = 34\,\mathrm{ps}$. The mean free path is therefore $l = v_c\tau_c = 34\,\mathrm{nm}$. For a GaAs junction thinner than 34 nm, we could face a change of paradigm in electronic transport from the drift-diffusion model to a ballistic model. This is still to be studied and may require different junction designs (and maybe higher doping concentration). Yet, with ultra-thin solar cell, we could tackle new concepts of electronic transport. In hot carriers solar cells for instance, ultra-thin layers have been pointed out as a key factor for the extraction of hot carriers [64, 65] (high-injection regime in a small volume for a sustained hot carrier population, see Chapter 6). One could also think about:

- appropriate filling of intermediate bands for sub-gap absorption (Intermediate-band solar cells).
- up-conversion or down conversion medium and exaltation of quantum cutting effect and photon recycling [66].

On the other hand, if all these points are promising and exciting, the study and realization of ultra-thin junctions are mainly yet to be done. Yet, in a very recent

article, Bernardi *et al.* [67] from MIT have pushed the concept of ultra-thin solar cells towards the nanometer limit. They have studied the feasibility of nanometer-thin solar cells based on MoS_2/graphene systems. They suggest that a stacking of three graphene monolayers and three MoS_2 monolayers with a back metallic contact (for light trapping purposes) could reach 10 % efficiency with a 3 nm-thick active layer. Even if this design is only a concept so far, it shows that research on optoelectronics currently is constantly proposing novel architectures for ultra-thin solar cells.

1.4.2.2 Open-circuit voltage

The open-circuit voltage of a cell can be expressed with the expression of Eq. 1.2.9. The dark current depends proportionally on the volume of material, and so decreasing the thickness can also decrease the dark current. If the photocurrent can remain high in an ultra-thin solar cell due to light trapping, then it is possible for an ultra-thin device to be more efficient than a thicker device due to the increased V_{oc}. Another way to explain this phenomenon without referring to volume recombination is the thermodynamical approach of Brendel and Queisser [68]. In their paper, they claim that thinning the cell at constant short circuit current enhances the minority carrier generation rate per unit volume and hence the steady state carrier concentration. Thermodynamically, an increased carrier concentration is equivalent to a reduction of the entropy production per photon, thus leading to larger voltage.

However, one must also consider the shunt resistance and surface recombination effects that become dominant issues in ultra-thin layers. This increase in V_{oc} can not be realized in all devices. Actually, in sub optimal devices, thinning the absorber could lead to a decrease in V_{oc} due to shunt issues (see the CIGS section 1.4.4).

1.4.3 Light absorption in ultra-thin solar cells

The main assumption in the opportunities in terms of performances and cost reduction listed above relies on the capacity to maintain the short-circuit current while decreasing the absorber thickness. This is of course the most obvious challenge of ultra-thin solar cells and the reason why efficient devices are yet to be produced. A decreasing thickness of absorber leads to absorption losses that mainly affect the short-circuit current. A useful parameter to estimate the thickness of material needed to absorb all the light at a given wavelength is the absorption depth, defined as the inverse of the absorption coefficient: absorption depth $d = 1/\alpha = \frac{\lambda}{4\pi k}$, where λ is the wavelength and k the imaginary part of the dielectric constant of the material. Table 1.2 lists the absorption depth for different materials to absorb all

of the light available under the gap of the material in wavelength. The absorption depth is calculated for a wavelength 50 nm under the band gap of the material to have an idea of the order of magnitude of the typical thickness needed to absorb of the light in a single pass. Reducing the thickness of absorber below this value will increase the losses, especially for the long wavelength photon range. One can note that these values of absorption depth are, for each technology, roughly the thicknesses of the conventional solar cells

	c-Si	a-Si:H	GaAs	CIGS	CdTe
Optical data (n,k)	Palik [69]	SOPRA [70]	Palik [69]	Orgassa (x=0.23) [71]	SOPRA [70]
Band gap wavelength λ_{BG} (µm)	1.100	0.730	0.870	1.180	0.86
Absorption depth at $\lambda_{BG} - 50\,\text{nm}$ (µm)	670	0.48	0.800	2.1	0.2

Table 1.2: Absorption depth for different materials of band gap wavelength λ_{BG}, calculated at $\lambda_{BG} - 50\,\text{nm}$.

Of course, the absorption does not have to occur on a single pass of light across the layer. The role of light trapping is to increase the optical path of light (uppermost in the long wavelength range). This allows reducing the effective thickness of the absorber while conserving constant short-circuit current densities. This concept and its limits are be detailed in the next Chapter.

1.4.4 Case study: current status in thinning CIGS solar cells

When reducing the absorber thickness in the case of CIGS solar cells, the device becomes more sensitive to various parameters such as the material absorption and the increased recombination. In the following, we expose a general overview of previous studies related to thinning the CIGS absorber.

Reducing the absorber thickness of CIGS solar cells has been pointed out as a key priority. Since the late 1990's, many groups have engaged both theoretical and experimental studies on the subject. The first publications on the subject are the papers of Shafarman et al. in 1997 [72] and Negami et al. in 1998 [73]. Since then, the most active groups have been the NREL group [74–76] and the Uppsala University group [77, 78] with extensive studies on this topic. Those two groups submitted the same approach for reducing the absorber thickness, consisting in

directly growing the CIGS layer at a lower rate, thus adapting the existing process to a lower thickness. Table 1.3 reports the record efficiencies of ultra-thin CIGS solar cells overview from literature.

When reducing the absorber thickness of a photovoltaic device, the most expected problem is the reduction of the light absorption and therefore the decrease of the photocurrent generation in the solar cell. Although the absorption coefficient of the CIGS material is very high, all the studies have shown that the amount of light absorbed is strongly affected when decreasing the absorber thickness to the sub-micrometer level.

Moreover, other problems may appear due to the ultra-low scale of the devices. Negami [73] reported that the solar cells were electrically shunted when the absorber thickness became close to 0.5 µm; this was related to the natural roughness of as-grown CIGS layers which was of the same order as the film thickness itself. Shafarman et al. [72] also reported a strong decrease of the parallel resistance when reducing the CIGS thickness, most likely related to an increased shunt effect due to pinholes in the absorber. Gloeckler and Sites [82] also investigated on the properties of very thin and ultra-thin absorber CIGS solar cells from a theoretical point of view. Their simulations indicated that reducing the absorber thickness leads to a reduction of the short circuit current due to a combination of a reduced light absorption and increased back contact recombination. However, when the absorber is fully depleted (thickness lower than the space charge region width), the authors state that the back contact recombination becomes negligible and the current of the cell depends only on the absorption in the CIGS.

In a nutshell, the conclusion of Ramanathan [74] (co-deposition, 3 stage process) and Lundberg [77] is the following. With direct deposition of thin CIGS absorber, it is possible to get down to 500 nm of CIGS without affecting the open-circuit voltage (V_{OC}) and the fill factor (FF). Only the external quantum efficiency and the short-circuit current (J_{SC}) were to suffer a lot from the diminution of thickness. For ultra-thin devices (<400 nm) however, shunting, front and back surface recombination are to limit globally the performance of the device.

Nevertheless, it was noted that an absorber thickness of 1 µm (compared to classic 2 or 2.5 µm-thick CIGS solar cell) was enough to perform excellent conversion efficiency. For instance for Ramamanthan *et al.*, the highest efficiency for a 1 µm CIGS solar cell was achieved for a three stage process absorber with 17.1 % conversion efficiency ($FF = 79.2\,\%$, $V_{OC} = 678\,\mathrm{mV}$ and $J_{SC} = 31.9\,\mathrm{mA/cm^2}$ compared to 2.5 µm-thick CIGS solar cell $FF = 80.3\,\%$, $V_{OC} = 728\,\mathrm{mV}$ and $J_{SC} = 31.87\,\mathrm{mA/cm^2}$). Remarkably, we note no difference in the J_{SC} from 1.8 µm to 1 µm of absorber thickness.

Instead of directly growing the absorber to a thinner scale, which may lead to the problems previously reported, more fundamental studies can be performed by

Reference	CIGS Thickness (nm)	V_{OC} (mV)	J_{SC} (mA/cm^2)	FF (%)	η (%)	Remarks
Ramanathan *et al.* (2006) [79]	1000	678	31.9	79.2	17.1	Direct deposition (3-stage process), no ARC
Ramanathan *et al.* (2006) [79]	400	565	21.3	75.7	9.1	Direct deposition (3-stage process), no ARC
Sharfarman *et al.* (2006) [80]	400	560	23	74	9.5	Etched absorber, no ARC
Jehl *et al.* (2012) [81]	400	630	25.5	63	10.2	Etched absorber, no ARC, gold mirror
Jehl *et al.* (2012) [81]	300	620	26.5	55	9	Etched absorber, no ARC, gold mirror, shunts
Lundberg *et al.* (2003) [77]	150	600	13.6	59	4.8	Direct deposition (co-evaportation), no ARC, shunts

Table 1.3: Record efficiencies of thin and ultra-thin CIGS solar cells overview from literature.

reducing the thickness of a standard absorber by chemical etching. The chemical etching of CISe surface was first introduced by Birkmire and McCandless in 1988 [83], who realized specular CISe surface with this technique. This method was adapted to obtain improved devices made with Cu(In,Ga)Se2 by Canava *et al.* [84], by removing detrimental interfacial layers left after a bromine etch.

Following this trend, Shafarman *et al.* performed a systematic comparative study between etched absorbers and as-deposited absorbers of the influence of the reduction of the CIGS thickness on the photovoltaic parameters of the solar cells. They reported an overall similar behavior, with a slightly better value for V_{oc} of chemically etched samples.

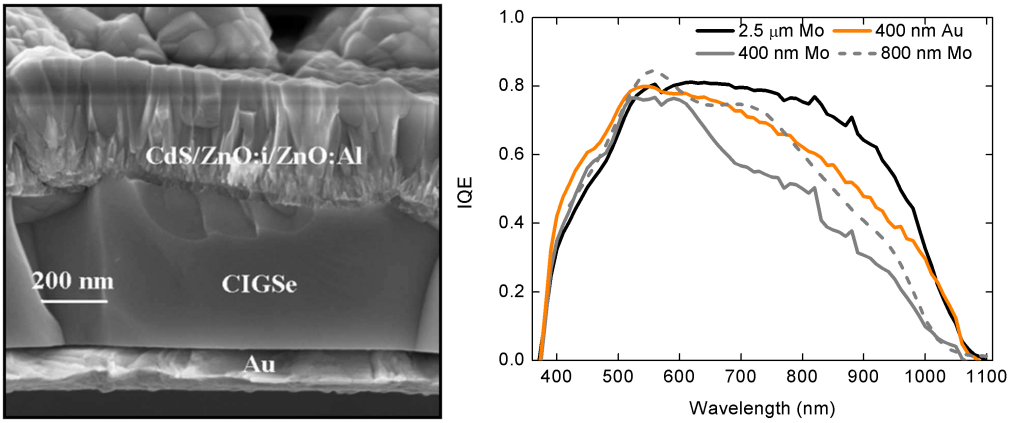

(a) (b)

Figure 1.4.1: (a) SEM image of the cross section of the 10.2 % efficient 400 nm-thick CIGS solar cell on a gold back substrate. (b) Measured internal quantum efficiency spectra for different configuration of CIGS solar cells. From Jehl *et al.* [85].

In this dynamic, the french ANR HABISOL project ULTRACIS was launched in 2009 [81, 85–88]. The goal was to test the feasibility of sub-micronic CIGS films down to 100 nm while keeping the same efficiency through several milestones:

- The systematic production of non-shunted thin and ultra-thin (down to 100nm-thick) CIGS layer by chemical etching.
- A deeper comprehension and engineering of the front contact (for instance, replacing the CdS by a ZnS layer).
- An optimization of the back contact (alternative back contacts).
- Suggest a new solution of photon management to prevent the drop in short-circuit current for ultra-thin solar cells.

One of the main achievements of the project was the development of a process of substrate transfer of chemically etched CIGS layer on alternative substrate [81, 87]. This has led to a 10.2 % efficient 400 nm-thick CIGS solar cell on a gold back substrate [85], the most efficient CIGS solar cell for this thickness range so far. Fig. 1.4.1 shows an SEM image of the cross section of the cell and its measured internal quantum efficiency spectrum. Among other results, this realization is an example of a doubling of the optical path thanks to an efficient mirror (same IQE spectra for 400 nm Au and 800 nm Mo).

The project has also lead to the characterization of solar cells of different CIGS thicknesses in order to determine the influence of this parameter of the electronic parameters of the solar cell [85]. The conclusion of this work in 2011 with etched and transferred solar cell is the same as for ultra-thin grown CIGS solar cell: the IV parameters are constant down to thickness of 400 nm (except the short-circuit current) but below this limit, both shunts and increased recombination limit the open-circuit voltage and the fill factor. Moreover, the project has led to an optical characterization of the $MoSe_2$ interface [86] and a solution to enhance the absorption in CIGS through a theoretical electromagnetic simulation of the CIGS solar cells [88]. One of the motivations of this manuscript is to pursue those results and this process to fabricate proof-of-concepts of nano-patterned ultra-thin CIGS solar cells.

In conclusion, not many papers report CIGS solar cell thinner than 500 nm. This is due to the extreme complexity to obtain an non degraded device due to the material property. For once, insufficient light-trapping is not the main limitation to tackle 100 nm-thick solar cells, but still a close second. The main care should be brought to the routine production of flat pinhole free layers.

1.5 Conclusion

Photovoltaic is a major actor of the energy mix. In particular, thin-film technologies have an increasing market share each year. For now, their efficiencies are however lower than c-Si solar cells. A thickness reduction of a factor at least 10 compared to the standard commercial thickness for the considered technology would unlock the issues of manufacturing cost and availability in scarce materials. This tenfold reduction in thickness is our goal in this manuscript. A solar cell with this thickness reduction is qualified in this manuscript as «ultra-thin».

Ultra-thin devices are both an exciting and a challenging topic. If the thickness becomes close to the scattering length of the material for instance, we can reach a new paradigm for electronic transport. Being ultra-thin has been pointed out to be one of the milestones of several new concepts in PV such as hot carrier solar cells for instance. On the other hand, many more studies are needed to reach an

optimized ultra-thin devices, in the case of CIGS for instance. Both requirements are taken into account in this manuscript.

Another challenge lies in the light management of these ultra-thin solar cells. We are aiming to thicknesses around ten times thinner than the absorption depth of the absorbers. This issue is at the heart of this manuscript. In the next chapter, we give an overview of the light management in solar cells and of novel solutions aimed at ultra-thin devices in particular.

.

Chapter 2

Light management in solar cells: state-of-the-art

Outline

2.1 Introduction . . . 33
2.2 Decreasing the reflection losses . . . 34
2.3 Interface texture . . . 35
2.3.1 Ergodic limit . . . 36
2.3.2 The case of thin-films . . . 36
2.4 Periodic nanophotonic structures for PV . . . 37
2.5 Plasmonics for photovoltaic . . . 39
2.5.1 Introduction to plasmonics . . . 39
2.5.1.1 Surface plasmon polaritons . . . 40
2.5.1.2 Localized surface plasmon resonance . . . 41
2.5.2 Plasmonic scattering . . . 42
2.5.3 Local absorption enhancement . . . 43
2.5.4 Coupling to waveguide mode . . . 43
2.6 Review of novel light management in the case of GaAs and CIGS solar cells . . . 45
2.7 Conclusion and discussion . . . 48

2.1 Introduction

The main effects limiting an ideal absorption of light by a solar cell structure are depicted in Fig. 2.1.1a. We consider a slab of material of thickness d, of refractive

index n_2+ik_2 and absorption coefficient $\alpha = \frac{4\pi k_2}{\lambda}$, where λ is the wavelength of the incident light coming from a medium of refractive index $n_1 + ik_1$. The principal optical losses are: reflection at the front of the slab and non-absorption of long wavelength photons. Fig.2.1.1b represents two classic light trapping techniques that are used to deal with those losses: anti-reflection coating (ARC), a scattering element and a mirror. These elements are presented in the following paragraphs.

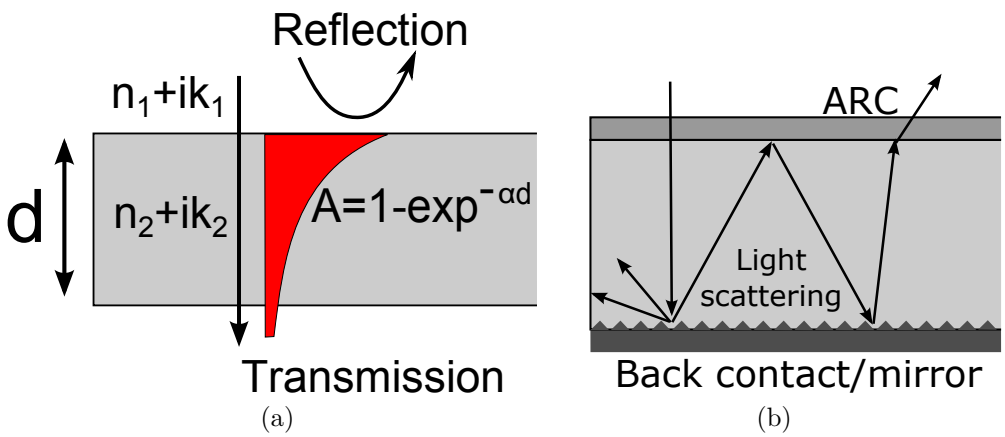

Figure 2.1.1: Schematic of a slab of material of thickness d, of refractive index n_2+ik_2 and absorption coefficient $\alpha = \frac{4\pi k_2}{\lambda}$, where λ is the wavelength of the incident light coming from a medium of refractive index $n_1 + ik_1$. (a) Main optical losses: reflection at the front of the slab and transmission losses. (b) Classical light trapping techniques for solar cells: anti-reflection coating (ARC), a light scattering layer and a mirror. Note that the textured layer can be located at the front or at the bottom of the solar cell.

2.2 Decreasing the reflection losses

Reflection losses can be calculated with the Fresnel coefficient of reflection of light at a flat interface and normal incidence between two media of refractive indices $n_1 + ik_1$ and $n_2 + ik_2$ respectively:

$$R = \left| \frac{n_1 + ik_1 - n_2 + ik_2}{n_1 + ik_1 + n_2 + ik_2} \right|^2 \tag{2.2.1}$$

For instance, at $\lambda = 400\,\text{nm}$ for an interface air/GaAs , the reflection coefficient is $R = 40\,\%$ (c-GaAs data are taken from Palik [69]). That means that only $60\,\%$ of light effectively enters the active material due to a high contrast of the real part

of the refractive index between air and GaAs. This phenomenon is true for any solar cell.

Thin film anti-reflection coatings greatly reduce this light loss by making use of phase changes (and the dependence of the reflectivity on index of refraction). A single quarter-wavelength coating of optimum index can eliminate reflection at one wavelength. The idea is that the creation of a double interface by means of a thin film gives two reflected waves. If these waves are out of phase, they partially or totally cancel. If the coating is a quarter wavelength thickness and the coating has an index of refraction lower than the substrate then the two reflections are 180 degrees out of phase. Multi-layer coatings can reduce the loss over the visible spectrum. Practically, ARCs in solar cell rarely stack more than 2 layers.

The challenge is to find the optimum ARC on the larger spectral range for each PV material. For instance for silicon that already has a rather low refractive index ($n = 3.5$ at $\lambda = 500\,\text{nm}$), the most common ARC for silicon solar cell are silicon nitride because of its attractive cost. New solutions have been studied such as single layers of mesoporous silica nanoparticles with refractive indices as low as 1.12 [89]. One of the most effective ARC on GaAs based solar cells is the couple MgF_2/ZnS [90–92]. For a-Si:H and CIGS, the front contact ZnO:Al can be considered as an ARC along with MgF_2.

Surface texture, either in combination with an anti-reflection coating or by itself, can also be used to minimize reflection. Any "roughening" of the surface reduces reflection by increasing the chances of reflected light bouncing back onto the surface, rather than out to the surrounding air. Finally, one can use nano-textures that provide a gradual change in the effective index of refraction, the latter being inspired from natural moth eye textures [93].

2.3 Interface texture

Classically, following the Beer-Lambert law, the absorption of a media of fixed thickness d is a decreasing function $A = 1 - exp^{-\alpha d}$. This means that low energy photons tend not to be absorbed by the active media when one decreases the thickness of the active material (see Fig. 2.1.1).

One would therefore try to increase the optical path of light in the structure (i.e. the distance that an unabsorbed photon may travel within the structure before it escapes). The first solution is to place a mirror at the back of the solar cell in order to reflect the non-absorbed light and therefore to double the optical path.

In addition, the other main light trapping scheme used in solar cell is to texture one or several layers of the solar cell (at the bottom or at the top of the structure) to induce light scattering that increase the optical path. Ideally, the texture is optimized so as the oblique scattered light is eventually «trapped» by total internal

reflection inside the solar cell until it escapes the structure when reflected within the escape cone. This is represented on Fig. 2.1.1b. In this case, the scattered incident photon is reflected once at the top of the solar cell before escaping the structure.

2.3.1 Ergodic limit

The limit of the ray-optic light trapping has been studied by Yablonovich [94] in 1982 in the case of thick ($d \geq \lambda/2n$) solar cells. In the case of Fig. 2.1.1b, let's consider for instance a lambertian surface at the bottom of our system. A Lambertian surface is a perfectly randomising surface that scatters light isotropically, which means that all reflected angles have the same probability. For incident light at normal incidence, the maximum enhancement ratio of the path length (and therefore of the absorption) can be demonstrated to be $e = 4n_2^2$ (with respect to a planar structure) for the case of a Lambertian surface used as a back reflector. This is known as the Yablonovich limit.

In the case of c-Si, the enhancement can reach a factor of 50 at normal incidence. Textured c-Si can be obtained by anisotropic etching of a (100)oriented crystalline silicon wafer using a diluted potassium hydroxide solution (KOH) which gives a randomly pyramidal textured surface [95].

However, this ergodic limit is obtained under strict assumptions: low absorption in the material (near the band edge for instance), a thick layer (compared to λ/2n) to lose the phase coherence and wave-optics effects, perfect lambertian surface and perfect back mirror. This limit is not relevant for the study of light management in ultra-thin solar cells.

2.3.2 The case of thin-films

Obviously it is still possible to use a scattering layer to increase the absorption in a thin-film layer. For a-Si:H solar, the front TCO can be randomly textured either by a wet chemical etching [96]. Periodic textures have also been developed with the possibility of using low-cost and large-area patterning processes such as nano-imprinting [97] and nanomoulding [98]. The range of shapes and sizes of random textures available being limited, this solution offers the possibility to design morphologies with a large-angle scattering. However, no experimental studies have shown that periodic texture can outperform random texture [99].

For CIGS solar cell, the natural roughness of the CIGS layer plays the role of effective and costless scattering texture. Interestingly, if a texture is applied on the front contact, it also acts as a moth eye ARC, achieving two light trapping techniques at the same time. Ultimately, the size of the grains can be optimized [100] for the anti-reflection effect. Alternatively, more theoretical studies have

been performed in the case of CIGS solar cells. For instance, a study of Dahan *et al.* [101] has been done to quantify the absorption enhancement induced by a Lambertian back reflector for a CIGS solar cell using radiative transfer equation theory.

In the case of thin-films, the difference with the case studied by Yablonovich is that we have to consider the light as a wave. If the coherence of the light is maintain over the film thickness, it may experience interference effects, at least for flat surfaces. The film can therefore act as a Fabry-Pérot cavity and light can be resonantly absorbed.

Eventually, alternative solutions have been proposed as an efficient light trapping in thin or ultra-thin solar cells: nanophotonic concepts in general and plasmonic designs in particular. Considering these aspects, some teams have proposed or reviewed some of the upper limits in terms of absorption enhancement that can be found in the case of thin-films by contrast to the ergodic limit of Yablonovich. We can cite for instance the work of the team of Shanhui Fan [102, 103], Harry Atwater [104–106] or Kylie Catchpole [107] which provides review depending on the assumptions and the analysis used. A condensed overview of these considerations is given in the two next sections.

2.4 Periodic nanophotonic structures for PV

Recently, progress in solar cells as pointed out the need to control the light at the wavelength scale (i.e. the nanometer scale in the visible). New solutions have emerged from other communities to propose a panel of solutions such as diffraction gratings [108, 109], photonic crystals [1, 110–115], or nanowires [3, 116].

1D or 2D dielectric diffraction gratings present a great potential for solar cells. They can be used first as advanced back reflectors to diffract light that can be coupled in quasi-guided mode inside the thin film. This increases both the path length and the spectral density of optical modes a long wavelength [109, 117, 118]. They can be used also as front ARC to decrease the global reflection and to enhance transmitted grating order [116, 119–121] Double-sided designs have recently been proposed to obtain a broadband absorption enhancement [115, 120–122].

The next example is important for this manuscript as it tackles the rare problematic light management for ultra-thin crystalline materials at the center of this manuscript: the broadband, wide-angle absorption in an ultra-thin (50 nm) layer of GaSb. The sawtooth dielectric grating design proposed by Esteban, Laroche and Greffet [123] and the plot of the absorption averaged over the numerical aperture are represented in Fig. 2.4.1. The absorption is explained by resonant modes that lead to very interesting performances: the layer absorbs 66 % of the incident solar photons above the band gap for a concentration equivalent to a numerical

aperture $NA = 1/\sqrt{2}$. Such features are very interesting for application to ultra-thin solar cells. However, the geometry of the sawtooth dielectric grating makes it difficult to fabricate with actual clean-room processes.

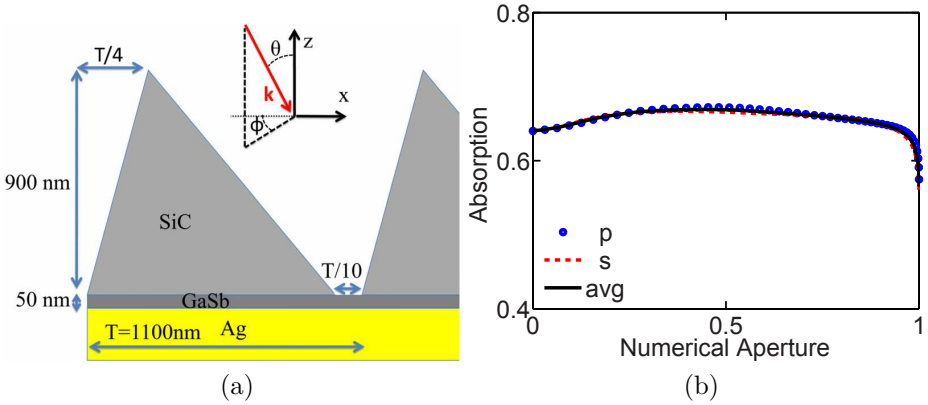

(a) (b)

Figure 2.4.1: (a) Sawtooth dielectric design proposed by Esteban, Laroche and Greffet for enhance the absorption in a 50-nm thick GaSb layer [123]. (b) Absorption in the GaSb layer of (a) as the function of the numerical aperture.

Photonic crystals (PC) [124, 125] are a structure in which the refractive index is periodically modulated, with a lattice constant in the same range of the incident wavelength. They have been proposed as a promising approach to enhance light absorption in ultra-thin solar cells a few years ago [118]. The principle is to use one, two or three dimensional (1D, 2D or 3D) periodic structures which exhibit a wide variety of light control effects. Let's consider for instance the structure fabricated by Meng et al. in Fig. 2.4.2. It consists a ultra-thin (100 nm) hydrogenated amorphous silicon solar cell designs with a 2D photonic crystal. The planar PC is used to couple incident light into slow Bloch modes standing over the light line in the amorphous silicon layer. This has been fabricated experimentally by holographic lithography and an absorption enhancement of 28 % compared to an unpatterned cell has been obtained [1]. This approach has also been successfully applied to organic solar cells [126, 127].

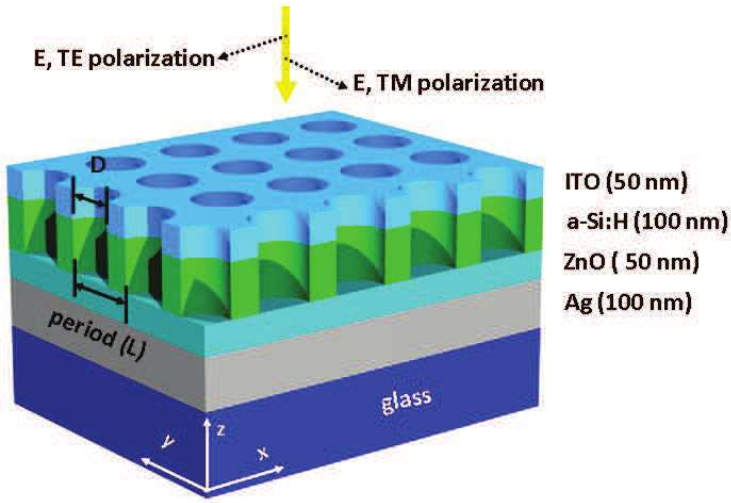

Figure 2.4.2: Design of a 2D-PC ultra-thin (100 nm) hydrogenated amorphous silicon solar cell to control the photon lifetime in the case of a a-Si:H solar cells (from Meng *et al.* [1]).

2.5 Plasmonics for photovoltaic

2.5.1 Introduction to plasmonics

The use of plamonics and metallic nano-particles can be retraced as early as the 4th century in the case of the Lycurgus Cup, identified as such in 1958. The field of plasmonics has been theorized at the beginning of the 20th century and has experienced a vast expansion with the development of fabrication and numerical analysis methods in the late 90's. The ability of plasmonic structure to control and confine light at the nanoscale has open new perspectives in modern physics [128].

Some recent articles have reviewed the application of plasmonics to photovoltaic devices [105, 129–131]. Atwater and Polman [129] have proposed a classification of solutions and guidelines for the use on metallic solutions to enhance the active absorption. These solutions are depicted in Fig. 2.5.1, namely (a) scattering metallic nanoparticles (b) metallic nanoparticles for local absorption enhancement and (c) metallic grating and excitation of SPP guided mode. In the following, we first describe the properties of surface plasmons and then evaluate the potential and limitations of these solutions for photovoltaic application. Eventually, examples in the case of GaAs and CIGS solar cells are described further and compared.

Plasmonics relies on the coherent oscillation of electrons of a metal, induced and coupled to the incident light. We focus here on two forms of plasmonic interac-

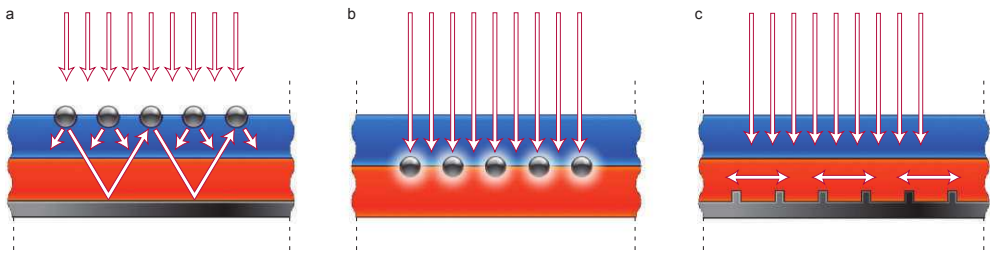

Figure 2.5.1: The three solutions proposed by Atwater and Polman [129] for plasmonics for photovoltaic: (a) scattering metallic nanoparticles in the front of the solar cells (b) metallic nanoparticles for local absorption enhancement and (c) metallic grating at the back of the solar cell to couple incident light to waveguide mode.

tion: *surface plasmon polaritons* (SPP) and *localized surface plasmon resonances* (LSPR).

2.5.1.1 Surface plasmon polaritons

A surface plasmon polariton is an electromagnetic wave that propagates at the interface between a metal and a dielectric (or a semi-conductor), coupled to the oscillation of the free electrons of the metal as sketched in Fig. 2.5.2. The existence of these modes is directly linked to the negative sign of the real part of the dielectric constant of the metal ϵ_2 (with $n_2 = \sqrt{\epsilon_2}$), the refractive index of the metal). These modes conform to the dispersion relation $k_{SPP}(\omega)$, where k_{SPP} is the component of the wave vector of the SPP in the direction of propagation and ω is the wave frequency. At the interface between two semi-infinite dielectric and metallic media of dielectric permittivity $\epsilon_1$and ϵ_2, the dispersion equation of a SPP is:

$$k_{SPP} = \frac{k_0}{\sqrt{\frac{1}{\epsilon_1} + \frac{1}{\epsilon_2}}} \tag{2.5.1}$$

with $k_0 = \frac{\omega}{c} = \frac{2\pi}{\lambda}$ the wave vector of light in vacuum. The effective index of the propagating mode can be defined as $n_{eff} = \frac{k_{SPP}}{k_0}$.

A SPP is an electromagnetic wave that is polarized transverse-magnetic TM (or S-like), i.e. the magnetic field $\mathrm{H_i}$ in the medium i is parallel at the interface metal/dielectric and can be written in the basis of Fig. 2.5.2 as:

$$\mathbf{H}_i = \mathbf{H}_{0i} exp[i(k_{SPP}x + k_{zi}z - \omega t)]\mathbf{u_y} \tag{2.5.2}$$

The wave vector k_{SPP} in the direction $\mathbf{u}_x$ is a complex number that can be written as $k_{SPP} = k'_{SPP} + ik"_{SPP}$. In a metal, the real part of dielectric constant is negative and from the Eq. 2.5.1:

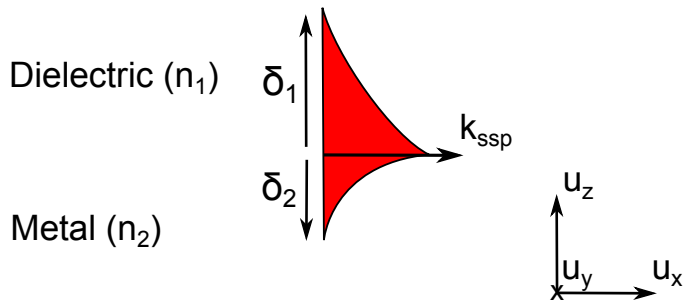

Figure 2.5.2: Schematic of a surface plasmon polariton propagating at the interface of two semi-infinite media (dielectric and metal).

$$|k_{SPP}| > k_0 \tag{2.5.3}$$

The components of the wave vectors k_{SPP} and k_{zi} are linked by the relation:

$$k_{zi} = \sqrt{\epsilon_i {k_0}^2 - {k_{SPP}}^2} \tag{2.5.4}$$

As k_{SPP} and k_0 are complex, k_{zi} is complex and can be written $k_{zi} = k'_{zi} + ik"_{zi}$. The amplitude of the magnetic field can therefore be written as:

$$|\mathbf{H}_{SPPi}(x,z)| = \mathbf{H}_0 exp(-k"_{SPP}x) exp(-k"_{zi}z) \tag{2.5.5}$$

The magnetic field of an SPP field is evanescent: because of the loss in the metal, the field is also decreasing exponentially during the propagation. The Eq. 2.5.5 allows us to extract two important characteristics of the damping of the SPP: its propagation length Λ along the axis x and its confinement δ_i along the axis y in the medium i defined in amplitude as follows:

$$\Lambda = \frac{1}{k"_{SPP}} \tag{2.5.6}$$

$$\delta_1 = \frac{1}{|k"_{z1}|} \text{ and } \delta_2 = \frac{1}{|k"_{z2}|} \tag{2.5.7}$$

Characteristic values and properties about SPP in the particular cases of our manuscript are discussed further in Chapter 3.

2.5.1.2 Localized surface plasmon resonance

On the other hand, localized surface plasmons are non-propagating excitations of the electrons in the metal [132]. In the case of a metallic nano-particle, upon application of an electromagnetic field, a resonant dipole moment is induced inside

the nanoparticle. At its resonance wavelength, the nanoparticle dipole induces a field enhancement in the vicinity of the particle as well as an enhancement of the scattering and absorption efficiencies. The scattering and absorption cross-sections can be expressed as follows [132, 133]:

$$\sigma_{scat} = \frac{1}{6\pi}\left(\frac{2\pi}{\lambda}\right)^4 |\alpha|^2 \tag{2.5.8}$$

$$\sigma_{abs} = \frac{2\pi}{\lambda}\Im\left[\alpha\right] \tag{2.5.9}$$

where α is the polarizability of the particle. The polarizability and resonance wavelength are a function of the shape, the size and the nature of the particle. For instance, for a spherical nano-particle, scattering and absorption cross-sections can be expressed as a function of the radius r of the particle as $\sigma_{scat} \propto \frac{r^6}{\lambda^4}$ and $\sigma_{abs} \propto \frac{r^3}{\lambda}$. For the smallest particles, the absoption mechanism is dominant. However, when the size of the nanoparticle approaches λ, multipolar modes contribute mainly to the particle's scattering cross section

2.5.2 Plasmonic scattering

Fig. 2.5.1a represents the simplest architecture for a solar cell employing scattering objects: a conventional thick device with a sparse array of sub-wavelength metal scatterers deposited on the top and a mirror at the back. The scattered light acquires an angular spread in the semi-conductor that effectively increases the optical path length. Moreover, the light scattered at an angle beyond the critical angle for reflection remains trapped in the cell. In addition light reflected towards the surface couples to the nanoparticles and are partly re-radiated into the semi-conductor by the same scattering mechanism.

The front scattering approach has already been applied to a-Si:H [134–136], GaAs [137–139], quantum well [140] and even CIGS [141] solar cells. However, the effect of the geometry (sphere, hemisphere, cylinder), the size, the nature (Cu, Ag, Al, Au) and the density of the nano-particles on the efficiency of this light trapping architecture is still studied theoretically today. The first requirement is obviously to obtain $\sigma_{scat} \gg \sigma_{abs}$ even if metal nanoparticles placed at the front of the solar cell always induce parasitic absorption losses. The second requirement is to optimize the fraction of light scattered in the semi-conductor (instead of being back scattered in free space). Eventually, one has to optimize the path length enhancement induced by the metallic scatterers. Theoretical studies have shown that hemispherical would be beneficial over sphere both for path length and a fraction of light scattered in the semi-conductor enhancement [142].

The advantage of this front approach offers the advantage of depositing the metal nanoparticles at the end of the fabrication process. This advantage makes this approach easily adaptable for various structures of solar cells. The deposition method of the metal scatterers can be done either in a random way (ultra-thin metallic film annealing [139] or pulsed laser deposition [141, 143]) or by large-area patterning processes: self-assembly of metal islands [144–146], hole-mask colloidal lithography [147] and conformal imprint-lithography (SCIL) [136, 148].

Another approach can be considered to avoid the parasitic absorption of the particles on the top of the solar cell. The idea is to place the film of nano-particles at the back of the solar cell, decreasing the parasitic absorption in the region of solar spectrum that is absorbed through a single pass. This solution have been used for a-Si:H [146, 149] and organic [150–152] solar cells. However, this geometry generally implies that the active material is grown on the metal nanoparticles which exclude crystalline materials and can induce defects that can be detrimental for the V_{OC} and fill factor of the device for a-Si:H solar cells [153]. Recent publications have applied this concept to thin c-Si solar cells [154, 155].

2.5.3 Local absorption enhancement

A second plasmonic architecture for enhanced absorption results from high near-field intensities associated with the localized plasmonic resonance of the particle embedded directly in the active material (Fig. 2.5.1b). Since the optical absorption is proportional to the electric field intensity, high local fields lead to increased absorption (see for instance a numerical study [156]). In this case, the metallic nanoparticles are small (20-50 nm of radius) i order to have $\sigma_{scat} \ll \sigma_{abs}$.

This solution has been tested in organic and dye-sensitized [157] and organic [150–152] solar cells. The embedding of metal nanoparticles in the active layer is however unthinkable in inorganic photovoltaics technology. Moreover absorption also occurs in the metallic particles, limiting the efficiency of this approach.

2.5.4 Coupling to waveguide mode

The last approach is the use of metallic gratings. In the case of Fig. 2.5.1c for instance, we consider an active material with a back metallic nano-structured mirror. This solution is used to couple the incident light into wave-guided mode inside the absorber layer.

A schematic vision of the mechanism is to consider that the metallic grating acts as a diffraction grating as described above in this chapter: incident light can be trapped in the active material if the periodicity of the array is chosen so the angle of the diffracted light is superior to the critical angle of reflection at the upper interface.

When the solar cell becomes really thin, a wave behavior is required to describe the light-trapping mechanism. For an array of period d shone by a plane wave with an angle of incidence θ, the relation of dispersion of the diffracted light can be written according to the Floquet-Bloch theory along the direction x of the plane of the absorber as:

$$\Re\left(k_x^{(p)}\right) = k_0 sin\theta + p\frac{2\pi}{d} \qquad (p = 0,\ \pm1,\ \pm2...) \tag{2.5.10}$$

where $k_x^{(p)}$ is the component of the wave vector parallel to the interface of the wave diffracted in the order p. In other words, the grating gives the extra momentum in the plane direction needed for the excitation of a photonic mode than can propagate inside the absorber layer with an effective index defined as $n_{eff} = \frac{k_x}{k_0}$. In this case, the path of incident light in the solar cell is rotated by 90 °. The light trapping condition is in this case typically depending on the incident light angle.

The form of this photonic mode is generally complex, depending on the geometry of the structure, as it can be the result of the superposition of different mode. For instance, a metallic grating offers the possibility to excite SPPs modes at the back metallic interface. Owing to the momentum mismatch between the incident light and the in-plane SPPs (see Fig. 2.5.2), a light coupling structure must be integrated in the metal/active material interface. A SPP mode can be excited along metallic arrays with a plane wave with an angle of incidence θ when:

$$k_{SPP} \approx k_x^{(p)} \tag{2.5.11}$$

At normal incidence, the Eq. 2.5.11 and Eq. 2.5.10 gives a condition on the period of the grating for the creation of the SPP mode.:

$$d = \Re\left(\sqrt{\frac{1}{\epsilon_1} + \frac{1}{\epsilon_2}}\right) p\lambda \qquad (p = 0,\ \pm1,\ \pm2...) \tag{2.5.12}$$

This back metallic design has been principally used with a-Si:H structure (non-planar layers) to increase both absorption and the short-circuit current. Fig. 2.5.3 represents for instance the 160 nm-thick, 6.6 % efficient a-Si:H of Ferry *et al.* [4, 158] with 46 % enhancement in short-circuit current. We can also cite the nanocone design of Zhu *et al.* *[3]* or the study of Soderstrom *et al.* [2, 3, 159].

For GaAs, Ferry *et al.* [104, 105] have also proposed numerically subwavelength ridges in the metallic back mirror to enhance the performances of GaAs solar cells (thickness=50-200 nm). They have predicted numerically an absorption enhancement factor between 1.4 and 1.6 near the band edge (880 nm) with respect to absorption in a identical film without a groove.

The metallic grating can be placed on the front of a solar cell structure to couple incident light to waveguide modes. The applications to c-Si plane layers [160, 161]

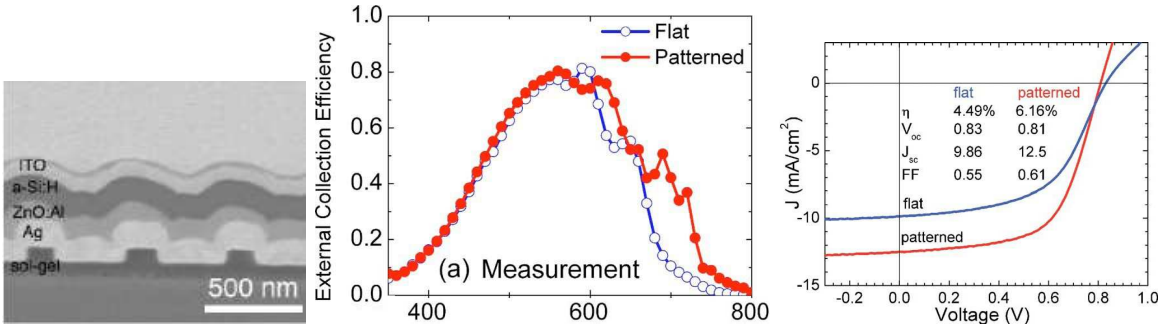

(a) (b) (c)

Figure 2.5.3: (a) Example of a back metallic grating from Ferry *et al.* [158] for ultra-thin a-Si:H solar cells; Compared measured EQE (b) and I-V curves (c) of patterned and un-patterned 160nm-thick a-Si:H solar cell [4]. The 46 % enhancement in short-circuit current (red part of the EQE measurement) leads to a 6.6 % efficient solar cell.

or to to ultra-thin a-Si:H solar cells submitted by Massiot *et al.* [162, 163] at LPN illustrate this possibility.

2.6 Review of novel light management in the case of GaAs and CIGS solar cells

We focus in this section on the materials that are specifically studied in this manuscript: gallium arsenide (GaAs) and $Cu(In, Ga)Se_2$ (CIGS). The section tries to review all available attempts of plasmonics design adapted to these technologies. The results of overall enhancements in photo-current and efficiencies of these papers are reported on Table 2.1.

For CIGS solar cells, we can cite the structure of Baraldi *et al.* [141] where they apply a pulsed laser deposition technique to the fabrication of plasmonic structures made of Ag nanoparticles embeded in an Al_2O_3 layers in the case of CIGS solar cells. The structure is depicted in Fig. 2.6.1a. The principle is to use a front scattering approach to enhance the short-circuit current. In their case, no short-circuit current enhancement have been experimentally observed compared to a reference solar cell without nanoparticles. On the contrary, this extra $Ag - Al_2O_3$ contributes to the diminution the global performances.

The front metallic nanoparticles scattering approach has also been applied for GaAs. Fig. 2.6.1b represents a 1.5 µm-thick GaAs solar cell «decorated» with size-controlled Ag nanoparticles fabricated by masked deposition through anodic alu-

Reference	Material	Technique	Absorber thickness	Best J_{SC} enhancement (relative enhancement)	Best efficiency enhancement (relative enhancement)	Remarks
Baraldi *et al.* (2011) [141]	CIGS	Ag nano-particles front scattering	2.3 µm	- 0.9mA/cm² (-3 %)	-1.2 % (-9 %)	Experimental, Cu/(In+Ga) ratios of 0.62
Nakayama *et al.* (2008) [137, 138]	GaAs	Ag nano-particles front scattering	1.5 µm	+0.9 mA/cm² (+8 %)	+1.2% (+20%)	Experimental, enhancement in V_{OC} and FF due to annealing
Liu *et al.* (2011) [139]	GaAs	Ag nano-particles front scattering	150 nm	+1 mA/cm² (+14.2 %)	N/A	Experimental
Grandidier *et al.* (2012) [164]	GaAs	Whispering gallery modes of dielectric nanospheres	100 nm	+2 mA/cm² (+11 %)	N/A	Numerical

Table 2.1: Proposition of nano-photonic light-trapping for GaAs and CIGS solar cells.

minum oxide templates (Nakayama *et al.* [137]). The strong scattering by the interacting surface plasmons in densely formed high aspect-ratio nanoparticles effectively increases the optical path of the incident light in the absorber layers resulting experimentally in an 8 % increase in the short-circuit current density of the cell. The nanoparticle array sheet conductivity also reduces the cell surface sheet resistance evidenced by an improved fill factor.

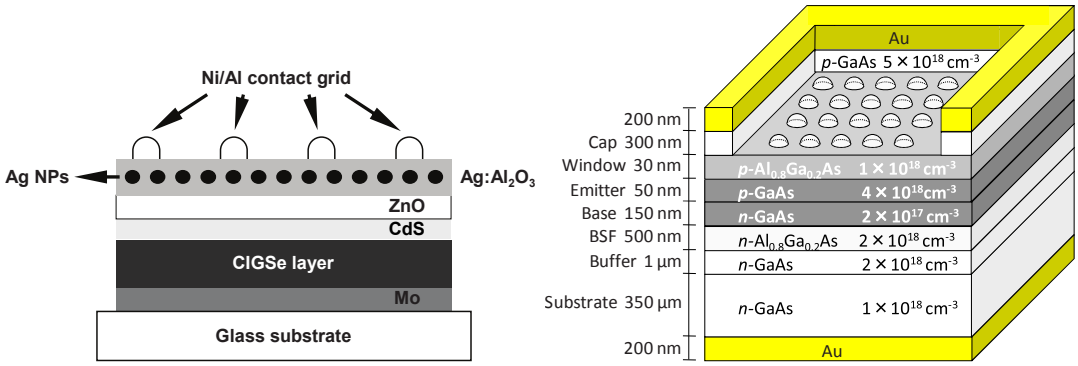

Figure 2.6.1: Example of a front metallic nanoparticles scattering approach to enhance the short-circuit current in (a) 2.3 µm-thick CIGS solar cells in the case of Baraldi *et al.* [141] and (b) for a 1.5 µm-thick GaAs solar cell in the case of Nakayama *et al.* [137, 138].

For a similar approach but thinner GaAs solar cell, we can cite the work of Liu *et al.* [139]. They performed a systematic study of LSPR on 150 nm-thick GaAs solar cells with different sizes of Ag nanoparticles on the surface. The nanoparticles were fabricated by annealing E-beam evaporated Ag films in a N_2 atmosphere. They report a best short-circuit enhancement of 14.2 % over that of the untreated solar cell.

Different approaches have been proposed numerically for ultra-thin GaAs solar cells. We have already cited the subwavelength ridges in the metallic back mirror Ferry *et al.* [104, 105] to enhance the performances of GaAs solar cells (thickness = 50-200 nm) leading to an absorption enhancement factor between 1.4 and 1.6 near the band edge.

Fig. 2.6.2 represents a schematic of an original dielectric nano-spheres structure for in a 100 nm-thick GaAs layer and its simulated absorption spectrum in GaAs weighted by the solar irradiance spectrum (Grandidier *et al.* [164]. The absorption enhancement is explained by the use of whispering gallery mode in the spheres. They have calculated a theoretical short-circuit current of $J_{th} = 18.14\,\mathrm{mA/cm^2}$ for their structure compared to $J_{th} = 16.4\,\mathrm{mA/cm^2}$ for the flat structure composed

of a DARC. The dielectric nano-spheres enhance the absorption very locally and the enhancement compared the flat structure in terms of theoretical short-circuit current is 10 % .

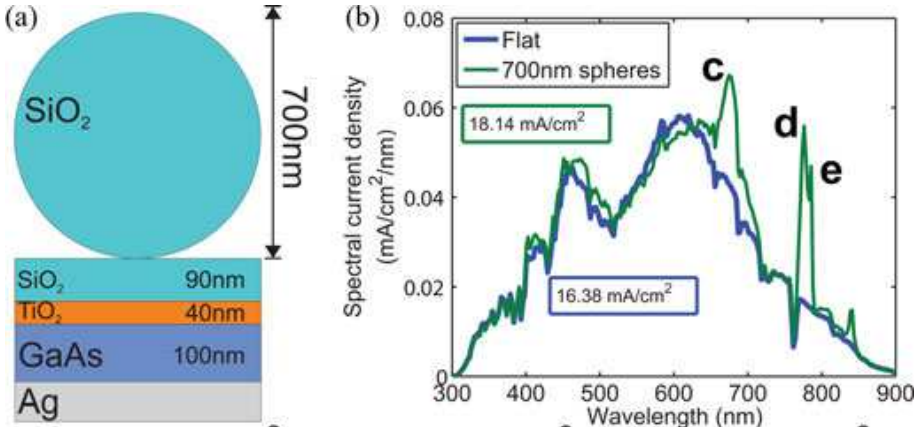

Figure 2.6.2: (a) Schematic of the dielectric nano-spheres structure of Grandidier *et al.* composed of a 100 nm-thick GaAs layer and (b) its absorption spectrum weighted by the solar irradiance spectrum [164].

2.7 Conclusion and discussion

In this chapter, we have presented the existing approaches for light trapping in thin and ultra-thin film solar cells. The first observation is that most of the proposed strategies have not been implemented for 100 nm-thick absorber layers yet. The second observation is that most of the literature concerning novel light management solutions for ultra-thin solar cells deals with materials that can be deposited on non-plane surface (OPV, DSSC, a-Si:H, µc-Si). Very few paper reports design dedicated to planar crystalline and poly-crystalline solar cells as they do not face classically the same issue in efficiency compared to amorphous silicon solar cells for instance. However, to go towards ultra-thin solar cells, new needs in light management are required for these materials. This is the main motivation of this manuscript.

Metallic gratings appear as one of the most promising candidate for absorber layers thickness below 100 nm. This solution is at the center of this manuscript. However, a certain number of constraints exist with this design, especially with the SPP modes than can be induced with such structures:

- A part of the SPP wave decays in the metal, inducing parasitic losses. The parasitic absorption losses should not be superior or equal to the absorption enhancement in the active material to justify the investment.

- The solar spectrum is broadband. The light-trapping scheme should be ideally effective on the whole spectrum below the effective band gap of the active material (in wavelength). If different geometries are available, one should optimize the system and maximize the absorption where the maximum of photons are available in order to increase the short circuit current.

- The sun is an unpolarized source and light management approaches should be independent of the polarization. However, SPPs do not exist for a transverse electric polarization. This implies classically to use a 2D geometry which is by definition independent from the incident polarization at normal incidence.

- AM1.5G spectrum takes into account light incoming from a large aperture angle yet SPP modes induced by a metallic grating are dispersive and thereby sensitive to incident light angles. One must try to propose the most angle independent absorption spectrum, at least on average.

In this manuscript, we endeavor to propose light management schemes that keep the ultra-thin absorber flat for application to crystalline materials. As stated before, this approach to crystalline solar cells is relatively new and original in literature. In particular, we are interested in three materials: GaAs for highly efficient single-junction solar cells, CIGS for application to low-cost high efficient solar cells and GaSb for application to hot carrier solar cells. Several studies are needed since the band gap and the deposition/growth method of these materials are very different from what exists in literature in the case of amorphous silicon.

Our first strategy is to use a combination of metallic grating and localized plasmonic resonance. The base of our design is the so-called metal/insulator/metal structure. This structure is described in the following chapter and adapted for photovoltaic application in Chapter 4 and 6.

Chapter 3

Nano-photonic and plasmonic: tools and concepts

Outline

3.1 Introduction 51
3.2 Metal/Insulator/Metal (MIM) nano-cavity array structure 52
3.2.1 Presentation of the structure 52
3.2.2 Optical response of MIM nano-cavity array 53
3.2.3 Resonance mechanism 53
3.2.4 Critical coupling condition and achievement of perfect optical absorption 54
3.2.5 State-of-the-art: 2D - Metal/insulator/metal (MIM) structure and omnidirectional total absorption 56
3.3 Plasmonic in the visible for gallium arsenide and silver 57
3.4 RETICOLO code: exact Maxwell equation solver 58
3.4.1 Principle 59
3.4.2 Input parameters 60
3.4.3 Application to this manuscript 60
3.5 Conclusion 61

3.1 Introduction

The aim of this chapter is to describe the tools and concepts that are necessary for the study of this manuscript. The first part of this chapter concentrates on the fundamental aspects of the metal/insulator/metal structure. This structure and

its properties are used several times in this manuscript to describe and analyze our results. As it involves surface plasmon polariton, we present in a second part the optical properties in the visible range of the of a GaAs/Ag interface. Considering the dimension of the structures, the optical analysis requires a specific numerical tool. The Reticolo code, at the origin of each simulation results in this manuscript, is described in the last section of this chapter.

3.2 Metal/Insulator/Metal (MIM) nano-cavity array structure

3.2.1 Presentation of the structure

In this section, we present the optical properties of MIM nano-cavity arrays through the particular case of the paper of Cattoni et al. [165] at LPN. The structure is represented in Fig. 3.2.1. It is made of a lower semi-infinite gold metallic mirror, a dielectric layer made of silica of thickness $t_l = 20$ nm and an upper gold metallic nanoparticle or nanowire thickness $t_M = 20$ nm and width $w = 200$ nm. This basic element is assembled in periodic arrays of 1D wires or 2D nanoparticles (bottom) with a period of $p = 400$ nm.

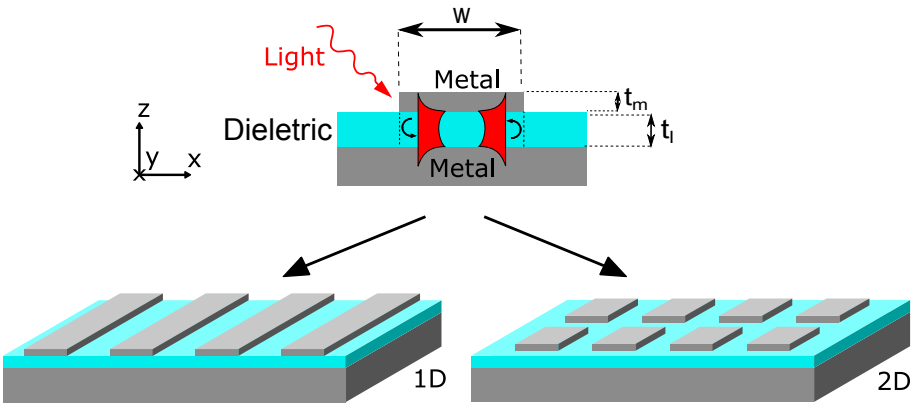

Figure 3.2.1: Schematic of the metal/insulator/metal (MIM) structure. Top: basic element of the optical array. The MIM structure is composed by a lower thick metal film, a thin dielectric layer of thickness ($t_l = 20$ nm) forming the gap of the structure and an upper thin metal film of thickness $t_M = 20$ nm and width $w = 200$ nm. It is assembled in periodic arrays of 1D wires or 2D nanoparticles (bottom) with a period of $p = 400$ nm. From Cattoni *et al.* [165].

3.2.2 Optical response of MIM nano-cavity array

Reflection measurements (R) were performed in the 3-60 ° angular range in TM polarization (magnetic field along the y direction) and are reported in Fig. 3.2.2a as a (1-R) spectrum. The reflection signal was normalized with the reflection of a flat gold mirror. The structure leads to a nearly perfect absorption at $\lambda = 1280\,\text{nm}$, independent from the incident light angle. Another resonance is found at $\lambda = 700\,\text{nm}$, reaching its maximum at $\theta = 45\,°$. Fig. 3.2.2a also represents the simulations showing the magnetic field intensity below the metal wires for both resonances ($\lambda = 1280\,\text{nm}$ at $\theta = 0\,°$ and $\lambda = 700\,\text{nm}$ at $\theta = 30\,°$), under plane wave illumination. Fig. 3.2.2d represents the angular diagram of the maximum absorption of the two resonances between 3 ° and 60 °. The absorption peak at $\lambda = 1280\,\text{nm}$ is nearly independent from the angle of incidence.

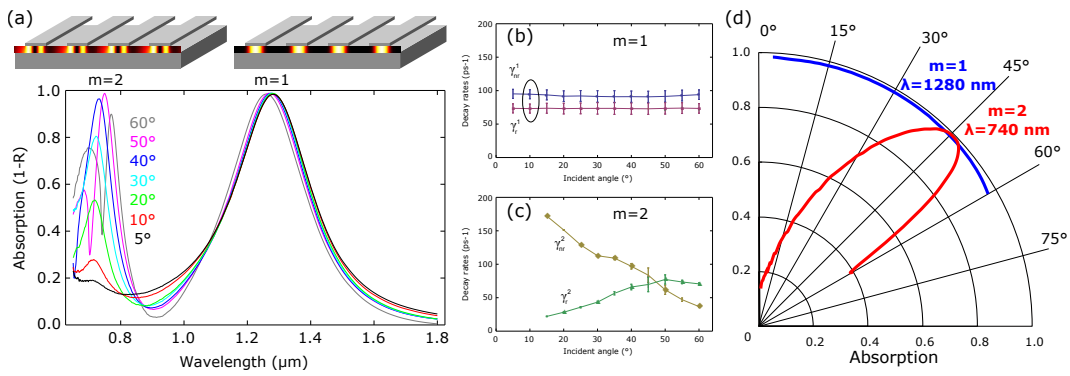

Figure 3.2.2: Summary of the results obtained for the structure of Fig. 3.2.1. (a, top): simulations showing the magnetic field intensity below the metal wires for the fundamental ($m = 1$, $\theta = 0\,°$) and second-order mode ($m = 2$, $\theta = 30\,°$), under plane wave illumination. (a, bottom): experimental absorption spectra of the MIM resonators measured under TM polarization (magnetic field parallel to the wires) at different angles of incidence. (b,c) Determination of the radiative and non-radiative losses γ_r and γ_{nr} at several angles for $m = 1$ (b) and $m = 2$ (c). (d) Experimental angular diagram of the maximum absorption of the two modes between 3 ° and 60 °. From Cattoni *et al.* [165].

3.2.3 Resonance mechanism

When two dielectric/metal interfaces are close together, the two SPPs propagating at each interface can couple together if the dielectric gap between the two metals is small enough as sketched in Fig. 3.2.1. The upper metallic nano-particle of

finite width w supports a localized surface plasmon resonance (LSPR) . We have seen in Chapter 2 that such a single particle displays several LSPR resonance modes, depending on the particle aspect ratio, volume, and surrounding medium permittivity [166]. When brought close to a metallic interface, this LSP mode couples to a plasmonic mode of the lower interface. Contrary to a plane interface, this coupling from a plane wave to this plasmonic mode is possible and happens independently from the angle of incidence for the fundamental mode [167, 168]. In this case, the plasmonic wave propagates now along the x direction, and is reflected at the ends of the wire [167, 169–171]. The nanostructure forms a horizontal cavity of size w that resonates at a given wavelength. It is modeled has a Fabry-Perot resonator and is referred to as the MIM resonator.

The excitation of the fundamental mode (m = 1) of the MIM resonator leads to a resonant absorption peak at $\lambda = 1280\,\text{nm}$, resulting in a completely localized lobe on the magnetic field intensity map of Fig. 3.2.2a. The effective index of the mode is calculated numerically with a finite element method and is found to be a 2-fold enhancement of the mode effective index ($n_{eff} \approx 2.9 + 0.07i$ at $\lambda = 1.3$ µm) as compared to the optical index of silica (1.45). This is a key for the design of optical antennas much smaller than the wavelength: $w = \lambda/6.4 = \lambda/(2n_{eff})$. The non-perfect agreement between the width of the cavity and the simple Fabry-Perot model is attributed to phase shifts at the edges of the stripe. Hence, the resonant wavelength is mainly determined by the wire width w and by the layer thicknesses (t_l) to a lesser extent.

The second order is also in good agreement with the Fabry-Perot model. We can distinguish in the magnetic field intensity map the two lobs of a Fabry-Perot mode. However, due to the symmetry of the structure, the second-order mode can not couple to the structure at normal incidence.

3.2.4 Critical coupling condition and achievement of perfect optical absorption

In the previous section, we have described the resonance mechanism. In this section, we give an explanation of the perfect optical absorption at the resonance wavelength. With a diffraction grating, diffracted light have maxima at angles given by $\theta_m = \arcsin(\frac{m\lambda}{d} - \sin\theta_i)$ where m is the order of the diffracted wave, λ the incident wavelength, d the period of the grating and θ_i the incident angle. For a strongly sub-wavelength grating, all but the zero order wave are evanescent at normal incidence. This means that a lot of potential loss channels (diffraction back into the air) are suppressed. A way to explain the resonant total absorption is to consider the temporal coupled-mode theory. This approach used in the following for resonant modes coupled to plane waves was primarily developed by H. A. Haus

[172] and extended by S. Fan *et al.* [173]. This is a powerful tool to analyze resonant nanostructure array.

Let us consider first a resonant single mode optical system coupled to N input/output channels (monochromatic input wave, time dependence $e^{i\omega t}$). The width of the resonance is assumed to be much smaller than the resonance frequency. The temporal variation of the mode amplitude is written as a function of energy dissipation (with a decay rate γ), a dephasing term ($j\omega_0$) and of the input wave amplitude I_n coupled to the system with the coupling coefficient α_n^i as:

$$\frac{da}{dt} = (j\omega_0 - \gamma)a + \sum_n \alpha_n^i . I_n$$

The amplitude a is defined such that $|a|^2$ is the energy in the resonant mode and with this notation, the total decay rate of the energy stored in the system is 2γ. Under illumination, our system can either absorb light (non-radiative loss channel, radiative decay rate γ_{nr}) or scatter light in the whole upper half-space (radiative loss channels). In ensembles of resonant nano-particles with subwavelength period, all but one radiative loss channels are suppressed. Then the two only loss channels are absorption (non-radiative decay rate γ_{nr}) and specular reflection (radiative decay rate γ_r). Following the derivation from S. Fan *et al.* [173], the temporal coupled mode theory gives the absorption intensity in the slab as a Lorentz function:

$$A(\omega) = \frac{4\gamma_{nr}\gamma_r}{(\omega - \omega_0)^2 + (\gamma_{nr} + \gamma_r)^2} \tag{3.2.1}$$

Perfect optical absorption is achieved when the *critical coupling condition* $\gamma_{nr} = \gamma_r$ is fulfilled.

This theory can be applied to the asymmetric resonator (no transmission) case of Cattoni e*t al.* If we control the coupling of the incoming and out-coming waves, it is possible to put these waves in phase opposition for the same amplitude, leading to a perfect absorption. The free-space (radiative) coupling can be tuned by the fill factor w/d in order to fulfill this condition.

The fundamental (m = 1) and second-order (m = 2) absorption resonances can be fitted by the Lorentzian function of Eq. 3.2.1 and the radiative and non-radiative decay rates can be determined for each angle of incidence. The experimental results are plotted in Fig. 3.2.2b,c. For the fundamental mode (m=1), γ_{nr} and γ_r are nearly equal. This illustrates the nearly perfect absorption achieved at any incidence angle (3 °-60 °), as shown in the angular diagram. For the the second-order resonance, the critical coupling condition γ_{nr}=γ_r is obtained between 45 ° and 50 °. The angular diagram shows the high-directivity absorption exhibited by the second-order mode.

3.2.5 State-of-the-art: 2D - Metal/insulator/metal (MIM) structure and omnidirectional total absorption

The experimental validation of omnidirectional, polarization independent optical total absorption for 2D-MIM structures has been reported in the paper of Cattoni *et al.* [165] but also in the paper of Liu et Giessen [167] for instance. Fig. 3.2.3b and Fig. 3.2.3a represents their respective structures and the associated optical response as the function of the angle and the wavelength. The structures display very intense measured peaks of absorption (absorption superior to 90 %) that are independent from the polarization and from the angle of incidence (in particular, the results of the TE polarization are displayed in Fig. 3.2.3.

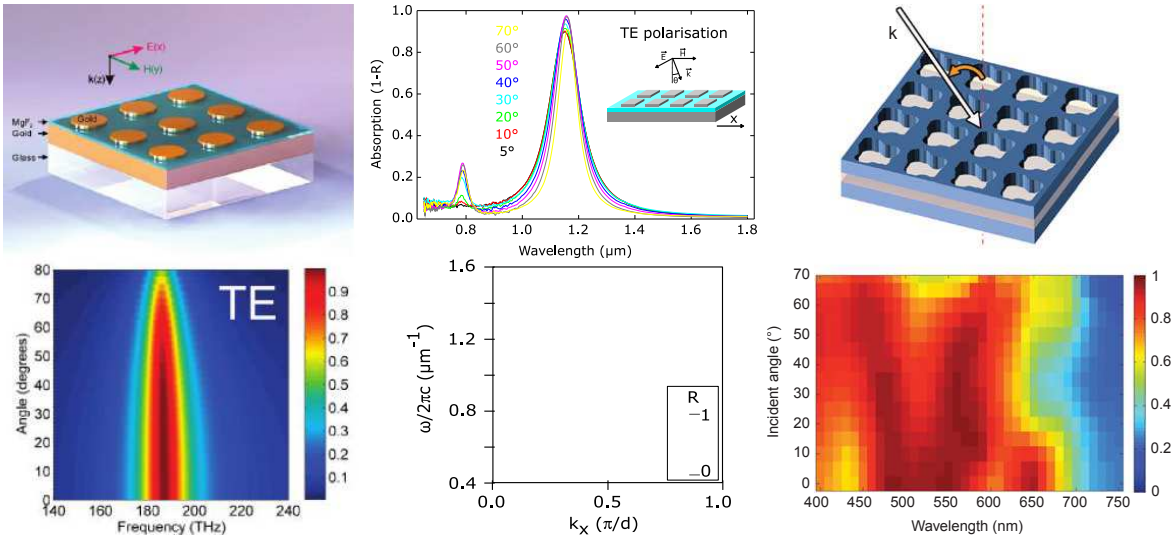

(a) (b) (c)

Figure 3.2.3: Example of 2D-MIM structure (a) from Liu et Giessen [167] and its absorption spectrum as a function of the angle of incidence and the frequency in TE polarization; (b) from Cattoni *et al.* [165] at LPN in inset, with the reflectivity spectrum as a function wavelength and as a function of the frequency and the wave vector in TE polarization; (c) from Aydin and Atwater [174] and its calculated broadband total absorption spectrum as the function of the polar angle and the wavelength.

A 2D crossed-grating MIM design that displays a broadband absorption spectrum is the proposition by Aydin and Atwater [174] in Fig. 3.2.3c. In their case, the structure is a 2D-crossed trapezoidal silver array (100 nm-thick) / SiO_2 (60 nm-thick) / silver mirror stacking. It features a high broadband absorption spectrum

in the visible range, independent from the polarization and the angle of incidence. The broadband and polarization-independent resonant light absorption over the entire visible spectrum has a measured average of 0.71 and simulated average of 0.85 in the $\lambda = 400$–$700\,\text{nm}$. All the absorption occurs in the metal in this case and the structure allows strong absorption in very small volumes. This structure features properties interesting for solar cell application.

3.3 Plasmonic in the visible for gallium arsenide and silver

In the previous section, we have detailed a certain number of properties of MIM nano-cavity arrays. Let's now take a closer look to the optical properties of GaAs and silver in the visible range. The main difference compared to the previous sections is that the dielectric ($k \simeq 0$) is replaced by a semi-conductor (*a priori* absorbing). Now, while the SPP propagates, light is also absorbed in the semi-conductor.

Let us consider the couple gallium arsenide and silver (GaAs/Ag). The refractive indices are taken from [69] and [175], respectively. Fig. 3.3.1 represents the real part of the effective index $n_{eff} = \frac{k_{spp}}{k_0}$ (k_{spp} as defined in Eq. 2.5.1) as a function of the wavelength for three cases: a vacuum/Ag interface, a GaAs/Ag interface and a Ag/GaAs/Ag guide (this last case is calculated with the analytical formula of [176] for a gap of $t = 50\,\text{nm}$ and $t = 25\,\text{nm}$). The effective index increases strongly from the vacuum/Ag interface to the a GaAs/Ag interface. For the GaAs waveguide case, the smaller the waveguide, the stronger the plasmon coupling and the higher the effective index. In the GaAs/Ag case, the plot displays a pike for the real part of the effective index at $\lambda = 600\,\text{nm}$. Practically, the SPPs do not exist below this wavelength for the GaAs/Ag interface.

For the couple GaAs/Ag, Eq. 2.5.6 and Eq. 2.5.7 allows us respectively to calculate the propagation length and the confinement of the SPP at λ =760 nm, the values are $\Lambda_{GaAs/Ag} = 400\,\text{nm}$, $\delta_{GaAs} = 32\,\text{nm}$ and $\delta_{Ag} = 16\,\text{nm}$.

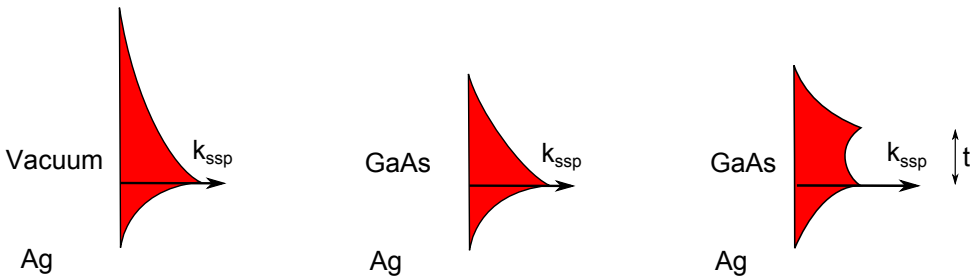

(a)

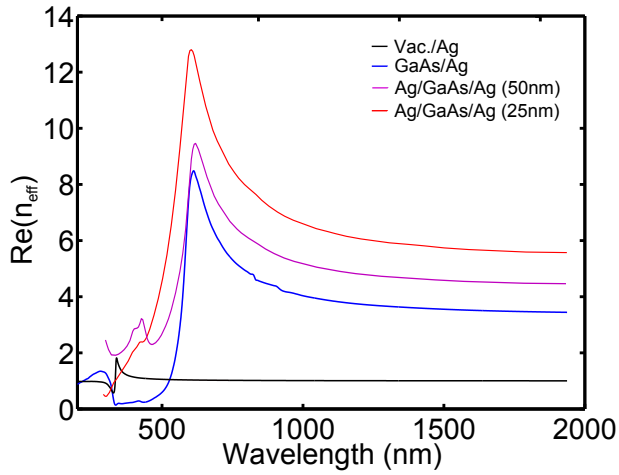

(b)

Figure 3.3.1: (a) Three cases: a vacuum/Ag interface, a GaAs/Ag interface and a 25nm-thick Ag/GaAs/Ag guide (b) Real part of the effective index ($n_{eff} = \frac{k_{SPP}}{k_0}$) of the SPP mode as the function of the wavelength for the three cases described in (a).

3.4 RETICOLO code: exact Maxwell equation solver

Electromagnetic simulation of sub-wavelength metallic grating takes a great space in this manuscript. In our case, numerical calculations are performed with the software developed by P. Lalanne and J.P. Hugonin at the Institut d'Optique. This is a software written in the MATLAB language. Our version of Reticolo has been provided by Philippe Lalanne and Christophe Sauvan for applications to 2D MIM nano-cavity array solar cells.

3.4.1 Principle

Reticolo software relies on the determination of electromagnetic fields from Maxwell equations. In brief, the software implements a frequency-domain modal method known as the Rigorous Coupled Wave Analysis (RCWA) developed by Moharam and Gaylord [177–179]. The structure of the problem, represented in Fig. 3.4.1, is defined by a stack of n layers on a substrate. Each layer can be structured in the x and y directions. All gratings have all identical periods in the x- and y-directions.

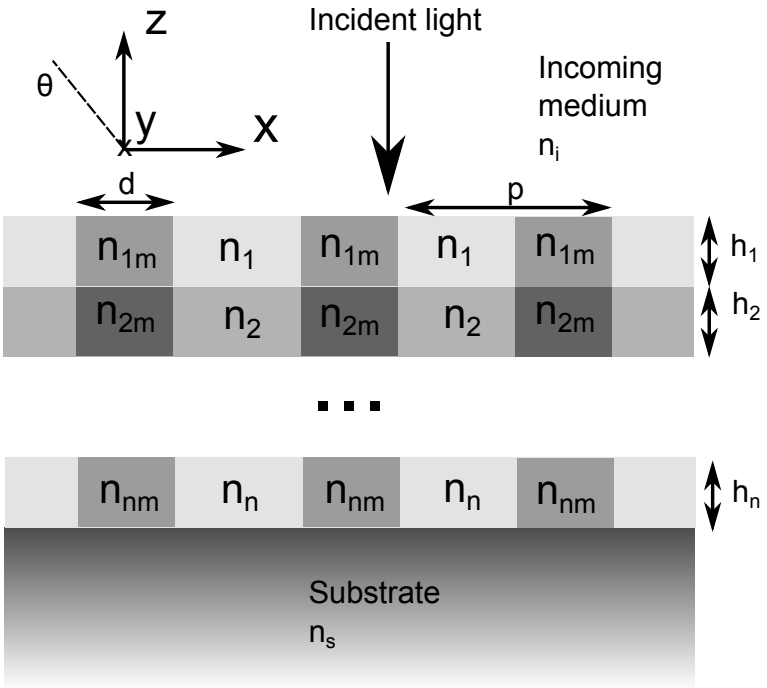

Figure 3.4.1: Schematic of the RETICOLO input structure.

The RCWA relies on the computation of the eigenmodes in each layers of the grating structure in a Fourier basis (plane-wave basis) [180]. Once the eigenmodes are known, the mode amplitudes in the different layers are calculated using a scattering matrix approach. The Reticolo code then calculates the absorption fraction in each layer of the system but it also provides electromagnetic field calculations in each point of the structure [181].

The RCWA is a relatively straightforward technique for obtaining the exact solution of Maxwell's equations for the electromagnetic diffraction by grating structures. It is a deterministic technique utilizing a state-variable method that converges to the proper solution without inherent numerical instabilities. The accuracy of the solution obtained depends solely on the number of terms in the field space-harmonic expansion, with conservation of energy always being satisfied.

3.4.2 Input parameters

Fig. 3.4.1 shows an example of a multilayer structure that can be simulated with Reticolo. The first parameter needed is the number of layers n in the stack. For the version of Reticolo code used during this thesis, n was limited between 1 and 6. Once the number of layers is defined, we have to enter the thickness of each layer in the stack (h_1, h_2,..., h_n).

Each layer can be structured or not. For each layer a, the optical constants n_a and n_{am} are required. The grating is also characterized by its geometry (1D or 2D) and its geometrical parameters (period p and diameter d of the structured zone). The wavelength range, the incident light angle (from 0 to 90 °) in either the (x,z) or the (y,z) plane as well as the polarization (TM or TE) are also input parameters. Finally, we have to give the number of Fourier harmonics along x (M_x) and y (M_y) axes retained for the computation. This parameter is very important in particular for 2D structures where more Fourier modes are determinant for the accuracy of the solution. An option allows to choose between the following calculations: 1) total reflection (R0) only; 2) R0 and absorption fraction in each layer; 3) electromagnetic field intensity calculation on each point of the structure.

3.4.3 Application to this manuscript

In our case, the principal use of RETICO is to simulate 2D MIM nano-cavity array solar cells, similar in structure to Fig. 3.2.1. The most standard calculation is to determine the absorption in each layer of the stack. In particular, it allows to compute the absorption fraction within the semiconductor absorber layer as the function of the wavelength and to calculate the predicted short-circuit current density of the cell. The values of the absorption fraction in each material of the system also enables an analysis of the absorption losses in the solar cell and to distinguish the different sources of losses: spacing layers, doped layers, metallic grating, back mirror.

In our study, we consider periods as small as 150 nm. RETICOLO is probably one of the only code able to converge for this kind of structures. All the calculations presented in this manuscript were made for 25 or more Fourier terms along the grating direction(s) to ensure the convergence of the calculation. As implicitly said in the previous section, we limit ourselves to geometries symmetric in both x and y direction to accelerate the performance and the stability of the calculation [182]. With my computer (8 core at 2.3 GHz, 24 Gb of RAM), the standard absorption calculation with 25 Fourier terms take about 68 seconds per wavelength at normal incidence. For a standard spectrum of 100 points, this means a bit less than two hours per spectrum. It has two consequences. First, considering the number of parameters, we can hardly use an optimization routine (genetic

algorithm for instance) for our structures. Second, we limit ourselves to square nano-particles and do not consider in a first intention exotic geometries such as trapezoidal particle, although undoubtedly interesting for our application (see for instance the paper of Aydin and Atwater [174]).

3.5 Conclusion

This chapter has highlighted some of the properties of the SPPs and the MIM structure. This study is the building block for the construction of our designs and for the Ag/GaAs/Ag metal/semi-conductor/metal structure studied in Chapter 4 in particular. The periodicity of the array is critical for the absorption mechanism. For instance, the array should be strongly sub-wavelength to cancel the propagation of all but zero-order diffracted light, an important aspect to fulfil the critical coupling condition. The thickness of the semiconductor layer is also very important, as it allows us to vary strongly the effective index of the coupled SPP mode. For an Ag/GaAs/Ag, the effective index reaches interestingly high values for low thickness of GaAs (typically 25 nm). In the next chapter, we apply the MIM structure to an ultra-thin GaAs layer.

Chapter 4

Metal/Semi-conductor/Metal (MSM) nano-cavity arrays for broadband multi-resonant absorption in ultra-thin GaAs layer

Outline

4.1 Introduction 64
4.2 Optical indices and approximations 64
4.3 Reference GaAs solar cell 65
4.4 One-dimensional (1D) nano-cavity array structure 68
4.4.1 Description of the structure 68
4.4.2 Absorption spectrum for the one-dimensional array 68
4.5 Resonant absorption mechanisms analysis 70
4.5.1 The Fabry-Perot model 70
4.5.2 Resonance C: horizontal Fabry-Pérot MSM cavity 72
4.5.3 Resonance A et B: vertical Fabry-Perot cavities. 75
4.5.4 Influence of the wire width 76
4.5.5 Influence of the GaAs thickness 76
4.5.6 Summary 77
4.6 Fundamental properties of the structure 78
4.6.1 Critical coupling condition 78
4.6.2 Absorption in metal 82
4.6.3 Flexibility and optimization 85
4.6.4 Study of the angular dependence 87
4.7 From 1D to 2D structures: polarization independence 90

4.8 Performances and comparison to literature 92
4.9 Conclusion 93

4.1 Introduction

To introduce the metal/semi-conductor/metal (MSM) nano-cavity arrays for light trapping (in reference to metal/insulator/metal - MIM resonator of Chapter 3), we use a model material to play the role of the active medium in our structure. In our case, this material is gallium arsenide (GaAs). The main reasons being its ideal character to make solar cell (low volume recombination rate, adapted band gap for single junction solar cell) and the extent of data (both optical and electronic) and expertise (technological knowledge in growth and process of III-V materials at LPN) about GaAs.

The principle of our light management scheme is to use multi-resonant periodic metallic arrays based on localized resonances. In this chapter, based on numerical electromagnetic calculations, we are evaluating the potential of this MSM nano-cavity array design in the case of a ultra-thin GaAs layer as a light management for ultra-thin solar cell. The goal of the electromagnetic simulations in this chapter are enlightening three main points:

- The performance of this design as an efficient light trapping for solar cells.
- The rules, models and guidelines to optimize this design.
- The unique properties in terms of nano-photonic concepts.

The nature of this study is ambitious, both from a solar cell application and from a nano-photonic point of view. We focus here first on an optical point-of-view and not on a complete device simulation. Therefore, the structures in the following sections do not always describe actual solar cells as we aim deliberately towards ultra-thin semi-conductor layers. This approach is against the tide of the classic light management approach on solar cells. These structures give access nonetheless to results, explanations, properties and rules of optimization about this broadband absorption design that can be later adapted to real solar cells.

4.2 Optical indices and approximations

We need to select the refractive index of the different materials included in a GaAs solar cell. These indices affect the electromagnetic fields in the structures

and therefore the absorption mechanisms. Nevertheless, the choice is arbitrary as we are not immediately trying to fit experimental measurements. For the following paragraphs, common refractive indices are used to ease the comparison between different studies:

- Gold (Au) and silver (Ag) from Johnson and Christie [183].
- Zinc sulfide (ZnS - cubic), magnesium fluoride (MgF_2 - tetragonal, ordinary index) and cubic gallium arsenide GaAs from Palik [69].

To simplify and to exploit efficiently an already optically complex structure, we are considering a simple model for the GaAs solar cell. In this study, the GaAs region is considered as a homogeneous intrinsic medium with no barrier layers nor doped layers. The absorption in these layers do no contribute to effective carrier generation and have optical data similar to GaAs (optically negligible change if we do not consider in a first approximation the bandgap shift due to doping). Consequently, the theoretical short-circuit current is here calculated from the absorption in the GaAs layer.

Moreover, some electric contacts are absent of the described solar cell structure. This last point however, is consistent with the fact that the typical periods of the metallic arrays described below are much smaller than the period of a solar cell grid. Hence, the two elements have a very limited interaction optically. Finally, each component of the structure is considered as ideal and non-oxidized.

4.3 Reference GaAs solar cell

The purpose of this section is to build a reference for this study. The idea is to simulate state-of-the-art record GaAs solar cell and to evaluate its theoretical short-circuit current. Afterward, the impact of a thickness reduction on the theoretical short-circuit current is evaluated in order to give a basis for future results.

The reference GaAs solar cell structure depicted in Fig.4.3.1 is considered: a GaAs thin-film on a Au back mirror with an anti-reflection coating composed of 109 nm-thick MgF_2 and 63 nm-thick ZnS layers. The two last layers act as a double-layer anti-reflection coating (DARC). Gold acts as an efficient mirror in the visible range and as a good ohmic contact with GaAs.

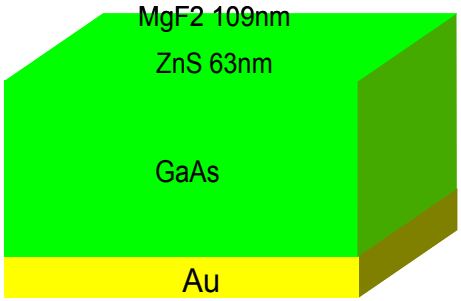

Figure 4.3.1: Structure of the reference GaAs solar cell. It is composed of an active region of GaAs of thickness ranging from 1 µm to 25 nm. The back mirror is composed of gold and the double-layer anti-reflection coating (DARC) is composed of 109 nm-thick MgF_2 and 63 nm-thick ZnS layers.

The GaAs thickness is now taken from 1 µm (in reference to conventional GaAs solar cell) to 25 nm and we compare the performance of the different structures. Fig. 4.3.2a shows the absorption spectra in the GaAs for each absorption thicknesses. These simulations are compared to the external quantum efficiency of the record GaAs solar cell from Alta Devices (dashed black curve, data extracted from [184]). The table of Fig. 4.3.2b lists the calculation of the theoretical short-circuit currents for each thickness of GaAs. Note that the DARC thicknesses have been optimized for the thickest (1 µm-thick) GaAs structure in order to give the highest short-circuit current. Each thickness of GaAs would naturally need a proper optimization of the DARC. However, for comparison purpose, we keep this geometry for all GaAs thicknesses.

1 µm of GaAs can absorb most of the light available under the maximum of the solar spectrum (over 95% absorption in the 450-800 nm range). This is consistent with the fact that the absorption depth for GaAs below $\lambda = 870$ nm is always inferior to twice the GaAs thickness (2 µm, back and forth in the GaAs here) as seen in Fig. 6.1.2. We note here also that the absorption in the GaAs layer strongly decreases below $\lambda = 450$ nm. This is due to the parasitic absorption of the DARC. The 1 µm-thick GaAs structure a calculated value of $J_{th} = 30.5\,\mathrm{mA/cm^2}$. This value is in the same range than the value of record GaAs solar cell [21, 23]. The red simulated curve is also in quantative agreement with the EQE of the record GaAs solar cell from Alta Devices. In GaAs solar cells, the collection of charges is excellent. This legitimates the assimilation of the EQE to the absorption spectrum for the calculation of the short-circuit current on our study.

When the thickness decreases to 500 nm, the absorption spectrum drops of an

average 15 % for wavelength over $\lambda = 750\,\mathrm{nm}$ but stays in average the same below. The theoretical short-circuit current reaches value of $J_{sc} = 27.7\,\mathrm{mA/cm^2}$. The gold back mirror allows to double the optical path in the structure. Yet, some photons in the red part of the spectrum are not absorbed.

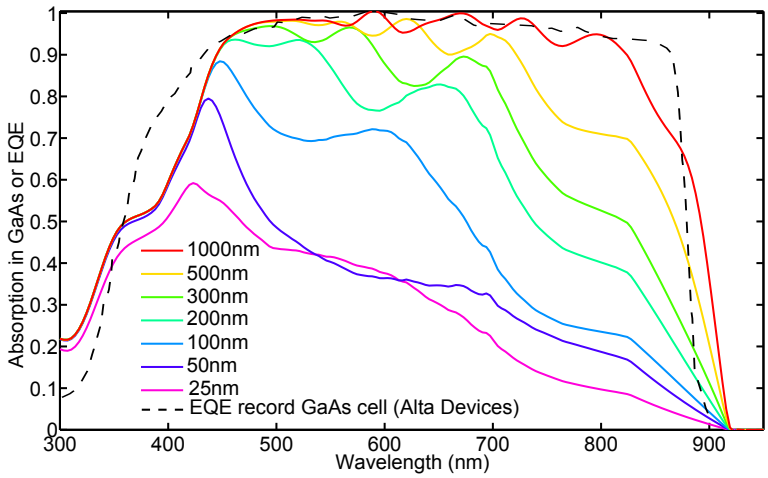

(a)

Thickness (nm)	J_{th}(mA/cm^2)
1000	30.5
500	27.7
300	24.5
200	21.7
100	16.6
50	11.6
25	9.5

(b)

Figure 4.3.2: (a) Absorption spectrum in the GaAs region for the structure depicted in Fig. 4.3.1. Each colored curve represents an absorption spectrum for a given GaAs thickness, ranging from 1 µm to 25 nm. These simulation are compared to the external quantum efficiency of the record GaAs solar cell from Alta Devices (dashed black curve, data extracted from [184]) (b) Table of the theoretical short-circuit current calculated from each absorption spectrum of (a).

The absorption spectrum begins to drop severely for thicknesses thinner or equal to 100 nm. For a 25 nm-thick GaAs layer, the absorption reaches a maximum of 50 % and the short-circuit current has dropped down to $J_{sc} = 9.5\,\mathrm{mA/cm^2}$. This is diminution of 70 % in the short-circuit current value compared to the 1 µm-thick

structure. For this range of thickness, the active region is simply too thin to absorb light efficiently.

4.4 One-dimensional (1D) nano-cavity array structure

4.4.1 Description of the structure

To demonstrate the multi-resonant absorption in a 25 nm-thick GaAs layer, the structure depicted in Fig. 4.4.1 is considered. It is composed of a 25 nm-thick GaAs layer on a silver mirror. The array is made of a periodic repetition of silver wires (supposed infinite along their length and the y axis). In the following section, a reference set of geometrical parameters is taken: period $p = 200\,\text{nm}$; width $w = 100\,\text{nm}$; thickness $t = 15\,\text{nm}$. The term «fill factor» of the grating is define by: $\text{fill factor} = \frac{\text{width}}{\text{period}}$. This set of array is the result of optimization, discussed later in this chapter, whose objective is maximize the theoretical short-circuit current. This 1D array is the first «brick» of our light trapping structure and is the simplest design to explain. It is the first step to the comprehension of the absorption mechanisms at stake. This structure is polarizing but it is generalized to a 2D structure later in this chapter. First, we only consider the TM polarization.

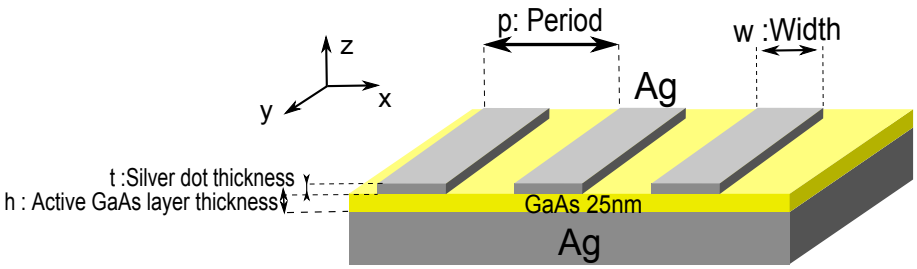

Figure 4.4.1: 1D MSM nano-cavity array structure. It is composed of a 25 nm-thick GaAs layer, a silver mirror and a metallic array of one dimensional (i.e. infinite along their length and the y axis) silver wires array. The parameters of the array are: period $p = 200\,\text{nm}$; width $w = 100\,\text{nm}$; thickness $t = 15\,\text{nm}$.

4.4.2 Absorption spectrum for the one-dimensional array

The absorption spectra of the 1D GaAs structure is plotted in Fig. 4.4.2 in TM polarization (magnetic field parallel to the y axis) and normal incidence. The blue and the red curves represent the total absorption and the absorption in the

GaAs layer, respectively. The difference between these two curves represents the absorption in the other layers, i.e. in metal. It is compared to the absorption of the reference 25 nm-thick GaAs solar cell of Fig. 4.3.1 (in black) and to the absorption in a 25 nm-thick GaAs film on a silver mirror with no structures (dashed line). The solar irradiance spectrum is plotted in gray. The electronic band gap of GaAs is represented in gray at $\lambda \geqslant 870\,\text{nm}$.

The absorption spectrum is multi-resonant. One can distinguish mainly three absorption peaks at $\lambda = 560\,\text{nm}$ (resonance E), $\lambda = 675\,\text{nm}$ (resonance D) and $\lambda = 760\,\text{nm}$ (resonance C). Here are listed the main properties of this spectrum:

- The absorption in GaAs is above 70 % in the $\lambda = 500 - 800\,\text{nm}$ range due to the multi-resonant mechanisms, right under the maximum of the solar spectrum. Despite their relative sharpness, three different resonances next to each other to broaden and raise the absorption spectrum compared to the reference solar cell.

- The absorption in the metal remains very low (maximum $< 15\,\%$) over the whole absorption spectrum, even with the presence of metallic nanoparticles on the front of the structure.

- Without any anti-reflection coating, there is almost no reflection at the resonant wavelength. This means that the structure allow an optimal coupling of light from the free space to the structure.

- The low absorption occurring between $\lambda = 300\,\text{nm}$ and $\lambda = 400\,\text{nm}$ is mainly due to the fact that the reflection coefficient between air and gallium arsenide is high at this wavelength ($R = \left|\frac{n_{GaAs}-n_{air}}{n_{GaAs}+n_{air}}\right|^2 \approx 0.50$ at $\lambda = 350\,\text{nm}$). In this region, no mechanism is present to reduce the reflectivity, yet.

Moreover, in this process, compared to the reference solar cell, the maximum of absorption has moved from $\lambda = 450\,\text{nm}$ to beneath the maximum of the solar irradiance spectrum, yet still below the gap of the gallium arsenide. The maximum of the structure match spectrally with the peak that appears on the dashed black curve at $\lambda = 650\,\text{nm}$. In the case of the sole GaAs layer on the silver mirror, this resonant phenomenon is well known: the GaAs acts as a cavity that resonates accordingly the thickness of the layer. The 1D GaAs structure displays however two additional peaks that are not yet explained.

The design displays a surprising absorption spectrum. It offers a significant increase in absorption compared to the reference GaAs solar cell and compared to a simple GaAs layer on a silver mirror. We now look deeper in the analysis of the absorption mechanisms to understand the origin of the multi-resonant absorption mechanism.

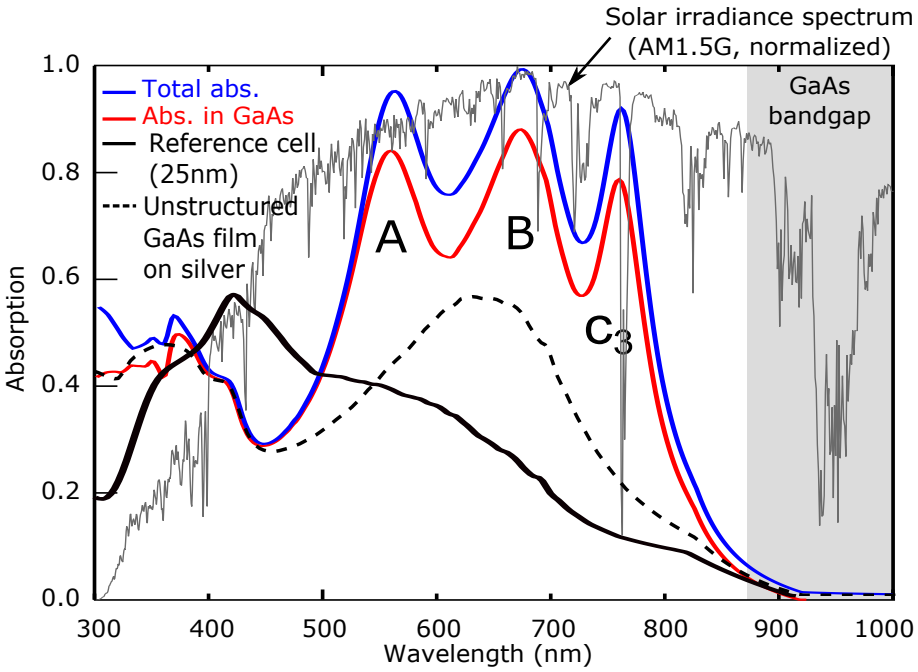

Figure 4.4.2: Simulated optical absorption in the 25 nm-thick GaAs active layer design depicted in Fig. 4.4.1, in TM polarization and at normal incidence. The blue and red curves represent the total absorption and the absorption in GaAs respectively. The difference between these two curves represents the absorption in the other layers, i.e. in the metal. It is compared to the absorption in GaAs of the reference 25 nm-thick GaAs solar of Fig. 4.3.1 (in black) and to the absorption in a 25 nm-thick GaAs film on a silver mirror with no structures (dashed line). The solar irradiance spectrum is plotted in gray. The electronic band gap of GaAs is represented in gray at $\lambda \geqslant 870$ nm.

4.5 Resonant absorption mechanisms analysis

Let us analyze the origin and the nature of the three resonance peaks.

4.5.1 The Fabry-Perot model

To model this multi-resonant spectrum, we describe each resonance as a Fabry-Pérot cavity of size h as depicted in Fig. 4.5.1. In this model, λ is the wavelength, $(n + ik)$ the complex refractive index of the mode, r_1 and r_2 are the reflection coefficients at the boundaries of the resonator and ϕ_1 and ϕ_2 the phases induced by these two reflections ($\phi_1 = arg(r_1)$, ...). The resonance condition for a Fabry-

Pérot resonator can be expressed as follows: $1 - r_1 r_2 e^{2ik_{fp}h+\phi_1+\phi_2} = 0$ where $k_{fp} = 2\pi(n + ik)/\lambda$ is the wave vector. The resonance condition can be expressed as: $4\pi hn/\lambda + \phi_1 + \phi_2 = 2\pi p$ where p is a integer (p=0, ±1, ±2...). For a given resonance wavelength λ_{res}, the size h of a resonator is therefore given by the expression:

$$h = \lambda_{res} \frac{2\pi p - (\phi_1 + \phi_2)}{4\pi n} \tag{4.5.1}$$

For a symmetric non-absorptive Fabry-Pérot resonator, we have $\phi_1 = \phi_2 = 0$ for a resonator surrounded by air and $\phi_1 = \phi_2 = \pm\pi$ when surrounded with an «ideal» metal. In these cases, the resonance condition gives $h = \lambda_{res}\frac{p}{2n}$.

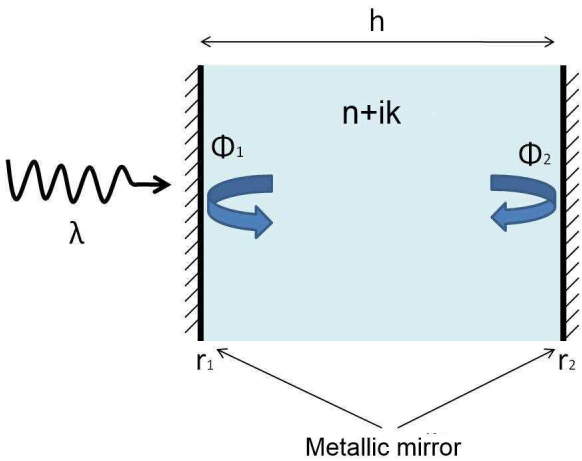

Figure 4.5.1: Schematic of a Fabry-Pérot cavity of size h. $k_{fp} = 2\pi(n + ik)/\lambda$ is the wave vector, λ is the wavelength, $(n + ik)$ the complex refractive index of the mode, r_1 and r_2 are the reflection coefficients at the boundaries of the resonator and ϕ_1 and ϕ_2 the phases induced by these two reflections.

We first consider a Ag/GaAs/Ag resonator. To resonate around $\lambda_{res} = 700\,\text{nm}$ for an refractive index of $n = 3.5$ (GaAs), the size of resonator should be at least of $h = 100\,\text{nm}$ for the first-order resonance ($p = 1$). This does not fit with our 25 nm-thick GaAs layer. To explain this in the Eq. 4.5.1, we need either to increase the refractive index or to take into account the real phase at the reflection to decrease the size of the resonator.

Moreover, for a size of resonator of $h = 100\,\text{nm}$, the first-order effectively resonates at $\lambda_{res1} = 700$ nm and the second-order resonates at $\lambda_{res2} = 350\,\text{nm}$. We see that the large separation between the two resonances of this mechanism cannot explain the multi-resonant absorption spectrum of Fig. 4.4.2. There must be three different cavities to induce such close absorption peaks.

The first apprehension of this simple model has highlighted paradoxes in this structure: a cavity that small should not resonate at this range of wavelength and should not display such close resonance peaks in this range of wavelength. In the next sections, some refinements are given to explain this phenomenon.

4.5.2 Resonance C: horizontal Fabry-Pérot MSM cavity

The resonance mechanism at $\lambda = 760\,\text{nm}$ is very similar to the MIM resonator described in Chapter 3 and sketched in Fig. 4.5.2a. It is based on two surface plasmons at the two GaAs/Ag interface that couple together. In this case, the wave vector becomes high and we can define the effective index of this mode as $n_{eff} = \frac{k_{SPP}}{k_0}$ with $k_0 = \frac{\omega}{c} = \frac{2\pi}{\lambda}$ and k_{SPP} the wave vector of the plasmonic mode. The closer the two metallic interfaces are, the higher the effective index. We can compute the effective index n_{eff} of the coupled plasmons (in the configuration Ag/GaAs/Ag) mode as a function of the wavelength to estimate the size of the resonator (seen in Chapter 3 and recalled in Fig. 4.5.2b). At $\lambda = 760\,\text{nm}$, $n_{eff} \approx 10$ for this mode and stays very high ($n_{eff} \approx 6$) in the near infra-red region. The confinement and the coupling of the two plasmons increase the effective index of the mode and therefore decrease the size of the cavity in Eq. 4.5.1.

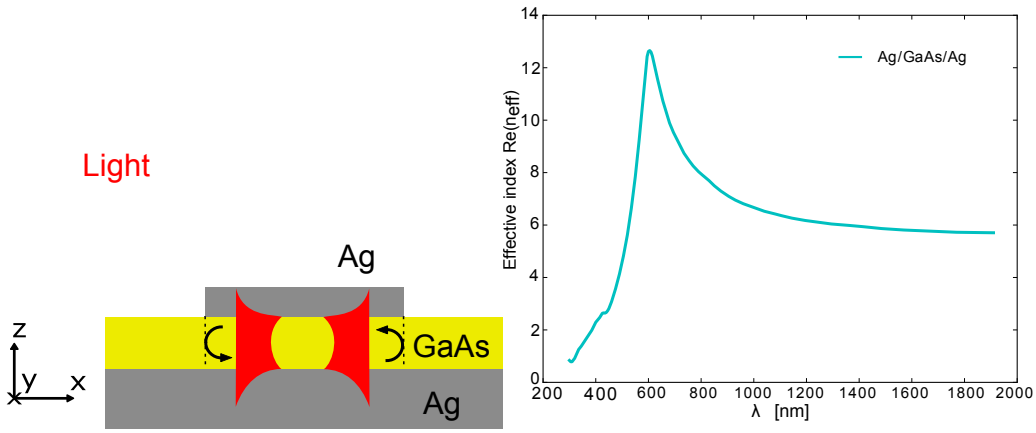

(a) (b)

Figure 4.5.2: (a) Schematic of the horizontal Fabry-Pérot MSM cavity. (b) Effective index n_{eff} of the coupled plasmons mode (in the configuration Ag/GaAs/Ag waveguide) as the function of wavelength for a 25nm-thick GaAs film.

The coupled mode propagates along the interfaces and is partly reflected at the end of wire, forming a cavity. The size of the wire is the size of the Fabry-Pérot

resonator. Contrary to Chapter 3, the spacer is not a dielectric but a absorptive media. Therefore, we expect to have a significant absorption in the GaAs layer. In a first approximation, we take $\phi_1 = \phi_2 = 0$. For $p = 3$, Eq. 4.5.1 gives a size of resonator of $h = 110\,\text{nm}$ at $\lambda_{res3} = 760\,\text{nm}$, which is consistent for our geometry (the wire width is about 100 nm). The non-perfect agreement between the width of the cavity and the simple Fabry-Perot model is attributed to phase shifts at the edges of the wire. Using the same calculation the second-order ($p = 2$) and first-order ($p = 1$) are expected at $\lambda_{res2} = 880\,\text{nm}$ (for $n_{eff} \approx 8$) and $\lambda_{res1} = 1540\,\text{nm}$ (for $n_{eff} \approx 7$), respectively.

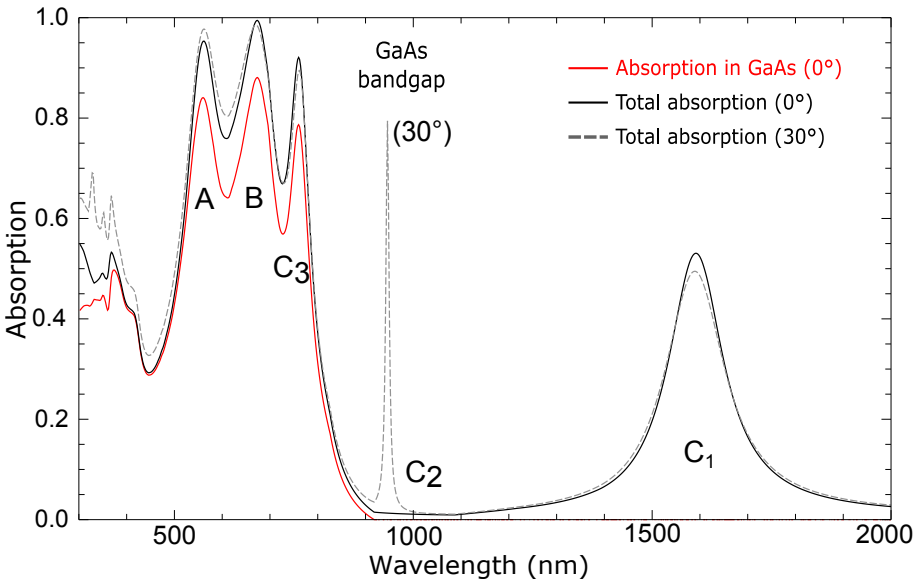

Figure 4.5.3: Total absorption of the structure depicted in Fig. 4.4.1 at normal incidence (plain black) and 30° incidence angle (dotted black). The red curve represents the absorption in GaAs at normal incidence. We can labeled two extra absorption peaks above the gap of the GaAs: C_2 at $\lambda = 945\,\text{nm}$ and resonance C_1 at $\lambda = 1590\,\text{nm}$.

There are indeed three similar MIM resonances in the structure. Fig. 4.5.3 represents a larger spectral view (in particular the region of energies below the gap of the GaAs) of the absorption spectrum plotted in Fig. 4.4.2, for normal incidence and a 30° incidence angle. In particular, two additional resonances are present above the GaAs band gap: C_2 at $\lambda = 950\,\text{nm}$ (only appearing at off normal incident angles) and C_1 at $\lambda = 1590\,\text{nm}$. These values are coherent to those expected from the Fabry-Pérot model. In Fig. 4.5.4, schematics of the different resonant mechanism are presented for each resonance wavelength. Moreover, the $|H|^2$ (magnetic) and $|E|^2$ (electric) field intensity map are represented at each resonant wavelength.

Either $|E_x|^2$ or $|E_z|^2$ field intensity map is added depending on the vertical or horizontal nature of the resonance, respectively. Each field intensity map is calculated at normal incidence except for the C2 resonance, calculated at 30°. Additional electromagnetic field intensity maps can be found in the appendix. We verify from the magnetic field intensity maps in Fig. 4.5.4 that resonances C1 ,C2 and C3 fit the description of the orders 1,2 and 3 respectively of the same Fabry-Pérot mode ($p = 1, 2, 3$ corresponding to the number of lobes in the $|H|^2$ field intensity map). Moreover, the main contribution to the global electric-field is made on the vertical direction ($|E_z|^2$), indicating the horizontal propagation of the mode. Resonances C1 and C2 are similar to the two resonance of the MIM structure described in Chapter 3. Due to the mirror symmetry of the antenna in the x direction, the resonant modes either have an even ($m = 1$) or an odd ($m = 2$) amplitude profile. At normal incidence, the incident plane wave has an even amplitude profile and cannot couple to the second-order mode: the radiative decay rate vanishes at $\theta = 0$ ° for $m = 2$.

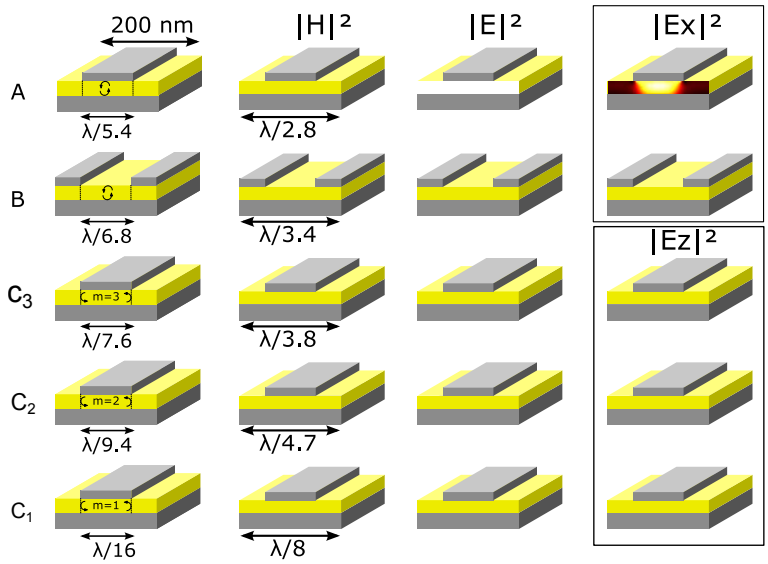

Figure 4.5.4: Schematic of the absorption mechanism (left column) and electromagnetic ($|E|^2$ and $|H|^2$) field intensity maps at the resonant wavelength of each peaks plotted in Fig. 4.5.3. Either $|E_x|^2$ or $|E_z|^2$ field intensity map is added depending on the vertical or horizontal nature of the resonance, respectively. Each field intensity map is calculated at normal incidence except for the C2 resonance, calculated at 30°.

4.5.3 Resonance A et B: vertical Fabry-Perot cavities.

We group here the study of resonances A (at $\lambda = 560\,\text{nm}$) and B ($\lambda = 675\,\text{nm}$) as their resonant mechanisms are similar. Even without the metallic array, the absorption spectrum of a 25 nm-thick GaAs exhibits already a resonance around $\lambda = 650\,\text{nm}$ (see the dashed line in Fig. 4.4.2 representing the absorption of a 25 nm-thick GaAs film on a silver mirror). As stated before, the resonant absorption can be modeled as a Fabry-Perot cavity inside the 25 nm-thick GaAs layer. However, this is counter intuitive as we have seen that we expect the smallest resonator to be classically of a size of 100 nm in order to resonate around 600/700 nm.

To explain this phenomenon, let us take a look at the phase shift calculated analytically of the electric field a the GaAs/Ag interface, plotted in Fig. 4.5.5 as a function of the wavelength. The phase shift value at $\lambda = 600\,\text{nm}$ is around $\phi = -2\pi/3$ instead of $\phi = -\pi$ that was taken before for an assumed ideal metal (this assumption is true in the infrared region). In this case, if we assume no changes for the other interface (Air/GaAs and $\phi = 0$), the resonance condition gives $h = \frac{\lambda}{8n_{eff}}$ for $p = 1$. At $\lambda = 600\,\text{nm}$, a GaAs resonator thickness of about $h = 22\,\text{nm}$ is found, matching with our current structure.

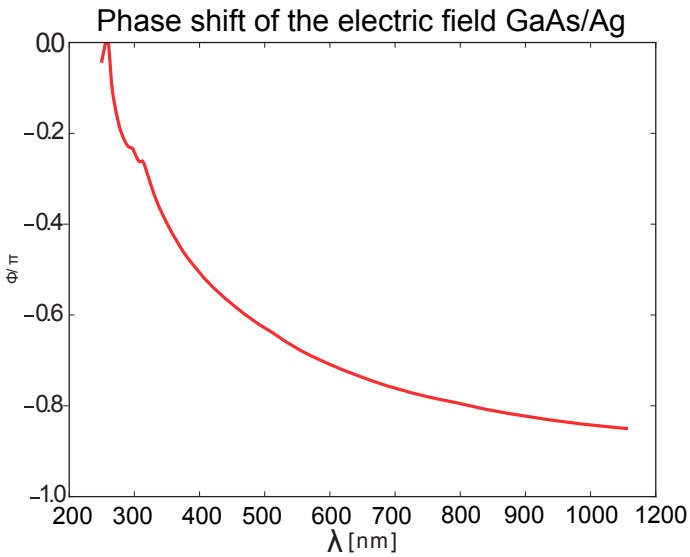

Figure 4.5.5: Phase shift ϕ/π of the electric field at a GaAs/Ag interface as the function of the wavelength.

With the metallic grating, this cavity is in principle still present. Around $\lambda = 600\,\text{nm}$ however, two distinct peaks can be observed. When we calculate and plot the electromagnetic field intensity maps (see Fig. 4.5.4 for resonance A and B), we observe that here is in fact two different behavior A (at $\lambda = 560\,\text{nm}$) and B

($\lambda = 675\,\mathrm{nm}$) with a maximum of the electromagnetic field located in the GaAs layer.

The first resonator correspond to the vacuum/GaAs/Ag cavity, located between the metallic stripes at $\lambda = 775\,\mathrm{nm}$ (as represented in the schematic of Fig. 4.5.4 labeled here resonance B). The mode is completely localized and confined and displays one lobe as expected. The main contribution to the global electric-field is the horizontal component ($|\mathrm{E_x}|^2$), justifying the fact that the mode resonates vertically inside the GaAs layer.

The other resonance (A at $\lambda = 560\,\mathrm{nm}$) is of the same nature as resonance B (see in Fig. 4.5.4). The maximum of the electromagnetic field is localized directly below the metallic wires in an Ag/GaAs/Ag cavity. The resonator is modeled schematically as before with a different upper boundary condition. This increase in the phase value make the absorption peak blue-shift for the same size of resonator according to the equation 4.5.1. This is indeed what we observe in the absorption spectra between resonance B and A. The main contribution to the global electric-field is also made on the horizontal direction ($|\mathrm{E_x}|^2$).

4.5.4 Influence of the wire width

To go further, the wire width w is varied to study the behavior of the resonance peaks. In Fig. 4.5.6, the spectral position in energy of the maximum of each resonance peak is reported as a function of the silver wire width w. The blue peaks (C_1 ,C_2 and C_3) shift accordingly to the variation of the wire width (i.e. the size of the resonator) contrary to resonances A and B. This is compatible with the model of Fabry-Pérot MSM cavity mode that propagates horizontally in the GaAs film. Higher orders of the MIM ($p = 4, 5$) also appear for larger wires (>140 nm).

The ratio of the spectral position of the peak C_3 compared to the wire width reaches in this case a maximum of $\tau = 5\,\mathrm{nm/nm}$. This is a acceptable tolerance for future technological fabrication of the array by electron beam lithography (nanometer resolution, see Chapter 5).

As expected, we see that resonance A and B are nearly independent of the wire width. This parameter (coupled with the fill factor) only confines more or less the mode of resonances, affecting slightly the spectral position of the peaks.

4.5.5 Influence of the GaAs thickness

Fig. 4.5.7 represents the spectral position of the maximum of the absorption peaks as a function of the GaAs thickness. In this figure, the MSM resonances C_1 ,C_2 and C_3 do no shift much with the variation of the GaAs thickness. The thickness of the GaAs layer is not a parameter of the condition of resonance C but a thicker GaAs thickness decrease the coupling of the two plasmons and the effective index,

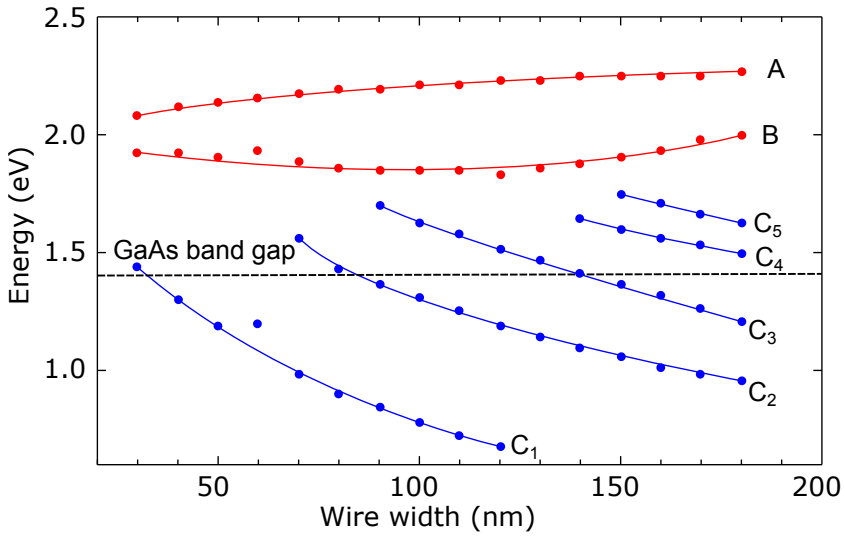

Figure 4.5.6: Parametric study. Spectral position of the maximum of the absorption peaks as a function of the silver wire width w at a fixed period of $p = 200\,\text{nm}$. The red and the blue curves correspond the resonances A/B and C1/C2/C3/C4/C5 ($p = 1, 2, 3, 4, 5$ orders of the MSM resonance), respectively.

leading to a blue shift of the resonance peak. If the gap between the two metallic interfaces becomes too important (typically over twice $2\delta_{GaAs}$ the confinement of the plasmon in energy, so here twice 50 nm), the coupling of the two SPPs is probably lost and the MSM resonance no longer exists.

On the contrary, the spectral position of resonances A and B shifts in accordance with the GaAs thickness, that is the size of the resonator. The ratio of the spectral position of the peak B compared to the GaAs thickness reaches in this case a maximum of $\tau = 16\,\text{nm/nm}$. This gives also a good tolerance for further epitaxial growing (molecular beam epitaxy resolution in thickness is below the nanometer).

4.5.6 Summary

The nano-cavity array structure induce the resonance of three distinct cavities:

- A plasmonic MSM resonance whose spectral position is defined by the wire width.
- Two disctinct resonances in the GaAs layer, forming a cavity. Adding the metallic array allows a splitting of a Fabry-Pérot resonant mode taking place in the 25 nm-thick GaAs layer. This allows to broaden the absorption spec-

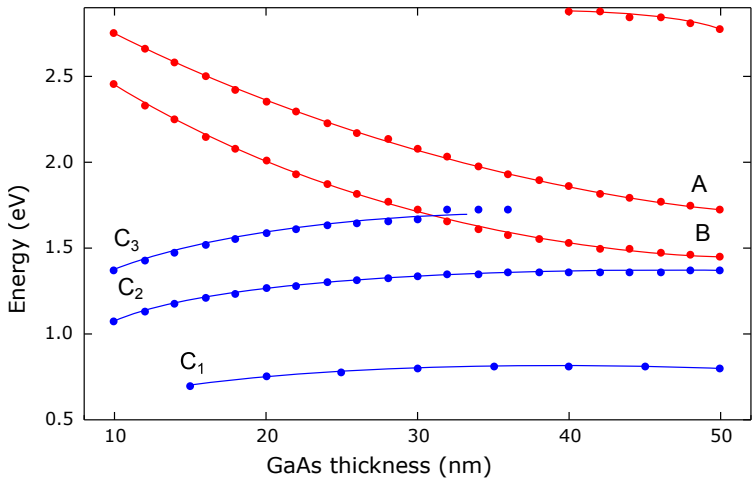

Figure 4.5.7: Parametric study. The plotted curves correspond to the spectral position in energy of the maximum of the absorption peaks as a function of the GaAs thickness. The red and the blue curves correspond the resonance A/B and C1/C2/C3 ($p = 1, 2, 3$ order of the MSM resonance), respectively.

trum locally and to achieve a higher absorption. The spectral position of these peaks is defined by the GaAs thickness.

In conclusion, each cavity is dependent of a single geometrical parameter and is weakly (or a least dependent at the second order) of the others geometrical parameter. With this simple model, it is possible to place each resonance to a desired spot simply in order to build a broad absorption spectrum. This method allows to design quickly a preliminary draft of the structure. Of course, the other geometrical are also of importance. A discussion about the full optimization process is given in the next section.

4.6 Fundamental properties of the structure

4.6.1 Critical coupling condition

In the previous parts, we have analyzed the different resonance mechanisms. In this section we use the model of the temporal coupled-mode theory to understand the nearly total absorption seen at each resonance wavelength. In section 3.2.4, we have introduced this notion. Our array is sub-wavelength in the visible range, which means that at normal incidence, all but the zero-order diffracted wave are evanescent. We have therefore two loss channels in our resonant system: non ra-

diative losses (absorption, decay rate γ_{nr}) and radiative losses (reflection, decay rate γ_r). For a resonant system that has only two dissipation channels, the temporal coupled mode theory provides the absorption intensity in the system with the equation:

$$A(\omega) = \frac{4\gamma_1\gamma_2}{(\omega - \omega_0)^2 + (\gamma_1 + \gamma_2)^2} \tag{4.6.1}$$

where ω is the frequency and ω_0 the resonance frequency.

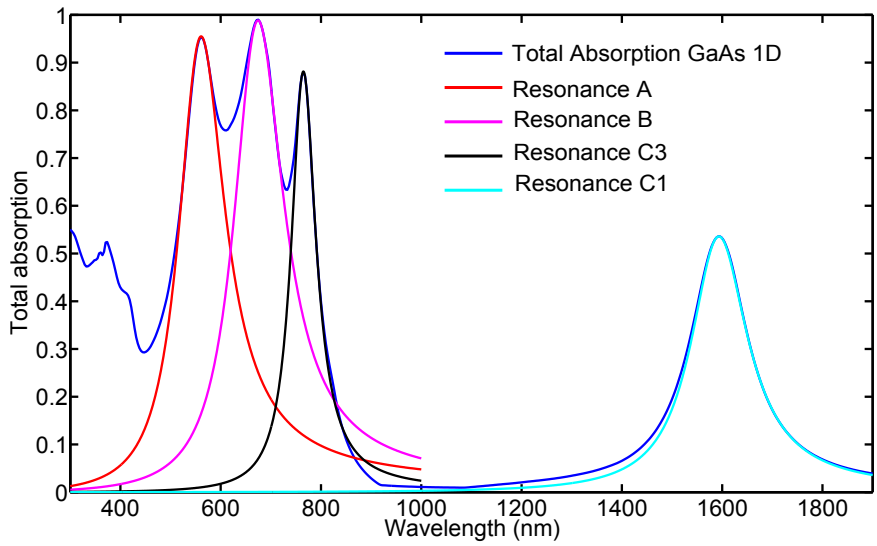

Figure 4.6.1: Total absorption spectrum (blue) at normal incidence, TM polarization of the structure depicted in Fig. 4.4.1. The additional curves correspond to the Lorentz fits of Eq. 4.6.1 for each resonance (A,B,C_3 and C_1).

We can now try to fit the resonant absorption peaks of Fig. 4.5.3. In our case, the

radiative and non radiative losses γ_1 andγ_2 play the same role within the equation. Normally, the equation is only valid for spaced out resonances. This nevertheless allows to have an idea of the decay rates of each loss channel.

Let us start first with the total absorption spectra, as we treat the system in its totality (we do not distinguish the absorption in the metal and in the GaAs). Fig. 4.6.1 corresponds to the four Lorentz fits for each resonance (A,B,C3 and C1) compared to the total absorption spectrum of 25 nm-thick GaAs structure (normal incidence, TM polarization) of Fig. 4.5.3.

	Resonance wavelength $\lambda = \frac{2\pi}{\omega_0}$ (nm)	γ_1 (ps^{-1})	γ_2 (ps^{-1})
Resonance A	561	205	133
Resonance B	675	140	113
Resonance C3	765	65	32
Resonance C1	1594	43	8

Table 4.1: List of parameters γ_1, γ_2 and ω_0 of the Lorentz fits of Fig. 4.6.1 for each resonance (A, B, C3 and C1).

First, we see that the resonant peaks are well fitted the coupled-mode theory model. To have nearly perfect absorption for our three resonances means that we are close to the critical coupling condition (i.e. $\gamma_1 = \gamma_2$) for each resonance. Achieving this critical condition is a key element of our structure from a nano-photonic point of view. To go further, we extract the decay rates of Eq. 4.6.1 for each resonance (listed in Table 4.1). Acting on this decay rates with our geometry is one of the goal of our structure.

To carry out this study to the end, we should distinguish γ_{nr} in two components: absorption in GaAs and absorption in metal with decay rates γ_{GaAs} and γ_{Ag} respectively. If we focus on the absorption spectrum in the GaAs layer, the absorption intensity in GaAs can be written as:

$$A_{GaAs}(\omega) = \frac{4\gamma_{GaAs}\gamma_r}{(\omega - \omega_0)^2 + (\gamma_{nr} + \gamma_r)^2} \tag{4.6.2}$$

The three different peaks can be fitted with Eq. 4.6.1 with the decay rates present in Fig. 4.6.2. However, we need now the same type of analysis for the absorption in the metal. However, the resonance in the metallic parts is very low and it is difficult to fit the peaks properly. We lack therefore a method to discriminate the different components of the non radiative decay rate and to finish this work.

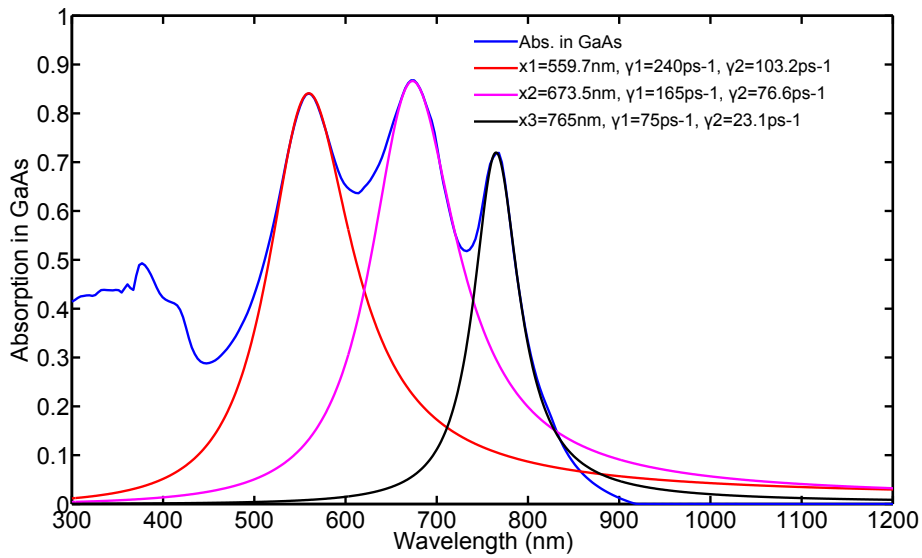

Figure 4.6.2: Absorption spectrum in GaAs (blue) at normal incidence, TM polarization of the structure depicted in Fig. 4.4.1. The additional curves correspond to the Lorentz fits of Eq. 4.6.1 for each resonance (A,B and C3).

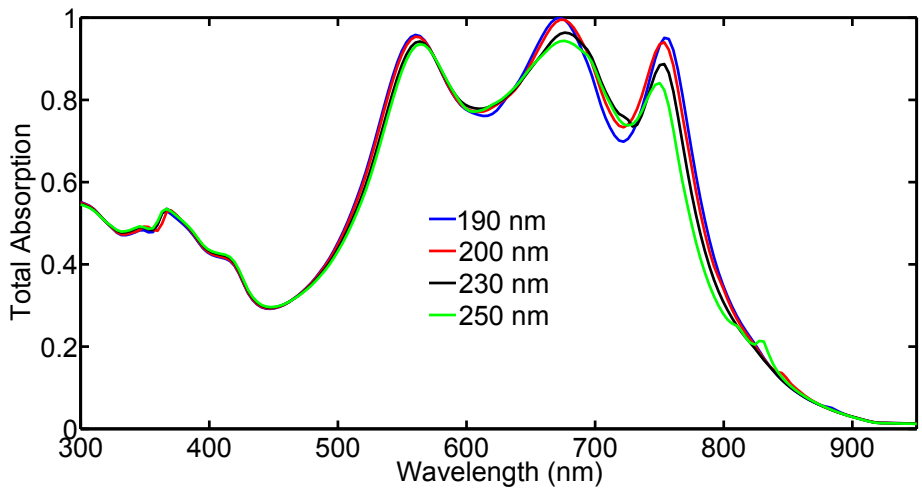

Figure 4.6.3: Total absorption spectra of the 1D GaAs structure at normal incidence and TM polarization calculated for different periods (190 nm to 250 nm) of the array at fixed width of the particle $w = 100$ nm.

Anyhow, the dependence of the different decay rates as a function the different geometrical parameters is crucial. For instance, modifying the fill factor have also another consequence as seen in Chapter 3 as it allows to tune the free-space

(radiative) coupling of the MSM resonance. This aspect is illustrated in Fig. 4.6.3: the total absorption spectra of the 1D GaAs structure at normal incidence and TM polarization are calculated for different periods of the array at fixed width of the particle $w = 100\,\text{nm}$. As the width of the particle is fixed, the spectral position of the peaks are constant. However, modifying the period has an effect on the maximum of the MSM resonance: with a shift of 50 nm in period, the maximum of the resonance increases of 10 %. This is just an example of the possibilities. This study would be a very interesting study to pursue. We would have a better control on the critical coupling condition and we would be able to understand better the optimization of total resonant absorption.

4.6.2 Absorption in metal

We have seen that we take advantage of mechanisms that induce extremely high confinement of light (high enhancement of the electromagnetic field) near metallic parts. Quantifying, understanding and controlling the losses in the metal is really important. In the spectrum of Fig. 4.4.2, the absorption in the metal remains constantly inferior to 15 % on the whole spectrum. This is a remarkable and surprising result: in literature, plasmonic structures often absorb all the light in the metal ([167, 174]).

Fig. 4.6.4 represents the absorption spectra in each region of the 1D GaAs structure and in the metallic parts in particular. In fact, the absorption in metal is also multi-resonant even though the two components (array and mirror) compensate somehow in an average value. Resonance peak A at $\lambda = 560\,\text{nm}$ for instance has been modeled as a vertical cavity below the metallic wires (Ag/GaAs/Ag resonator). It is therefore logical to find a corresponding peaks of absorption in the the array and in the mirror of the same amplitude for this particular wavelength. Resonance peak B at $\lambda = 675\,\text{nm}$ on the contrary is localized between the metallic wires. We can verify indeed that the absorption in the array does not display any peak at this wavelength compared to the absorption in the mirror. Eventually, it is harder to settle to a clear conclusion for resonance C at $\lambda = 760\,\text{nm}$. For an ideal infinite Ag/GaAs/Ag waveguide (i.e. semi-infinite Ag on both side), we would have expected the same amount of absorption in both Ag regions. Here, the absorption is superior in the array. A supposition is that, in our case, the tail of the SPP of the upper Ag/GaAs boundary may be slightly affected by the edge of the Ag wire, leading to an increased absorption in the array.

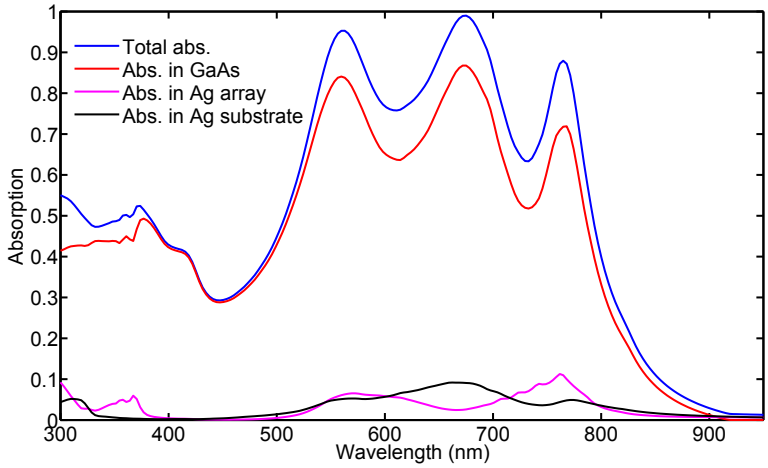

Figure 4.6.4: Absorption spectra for the GaAs 1D structure depicted in Fig. 4.4.1 as a function of the wavelength. Blue: total absorption. Red: absorption in the GaAs. Magenta: absorption in the Ag array. Black: absorption in the Ag mirror (substrate).

In this design, we take advantage of several factors to limit the absorption in the metal. First, the coefficient of refraction of silver is very high in the 500-800 nm range and the imaginary part of the dielectric permittivity of silver is remarkably low for a metal leading to relatively low absorption (at least for the data of Johnson & Christy [183]:$\Im(\epsilon) \leq 1.8$ on the 300-1000 nm range).

However, let's consider for instance a Ag/GaAs/Ag cavity. We can calculate the losses at the reflection at the interface GaAs/Ag $A_{refl} = 1 - R \simeq 10\%$ at $\lambda = 600$ nm with R the Fresnel coefficient of reflection given in Eq. 2.2.1. If we compare this value to the amount of absorption during the travel of light through $t = 25$ nm of GaAs: $A_{travel} = 1 - exp^{-\alpha t} \simeq 10\,\%$, which is approximately the same value. This means that inside the resonator, the absorption of light in the GaAs and the metal should be equal according to this simple calculation. This is however not the case in our simulation of resonance B. The reason is not very clear and would need a deeper study.

Second, concerning resonance C, we have seen in section 3.3 that the confinement length of the plasmon in the GaAs is twice the confinement in the Ag (due to a high index contrast). This tend to localize more the absorption in the GaAs and to diminish the absorption in metal. Nevertheless, the absorption in the metal for this resonance is surprisingly low.

Another surprising point, the absorption in metal at $\lambda = 450$ nm is almost equal to 0. Fig. 4.6.5 represents the ϵ". $|E|^2$ map (proportional to the absorption, where ϵ" is the imaginary part of the dielectric constant) for the 1D-GaAs structure at $\lambda = 450$ nm. We can notice that around $\lambda = 450$ nm, the absorption in metal

is very low. This means that the array is almost transparent at this wavelength. The reason of this low absorption in the metal is therefore not extremely clear and further study are needed for a good comprehension. One hypothesis is that we use a very thin array of silver on the front of our structure compared to other MIM studies [174].

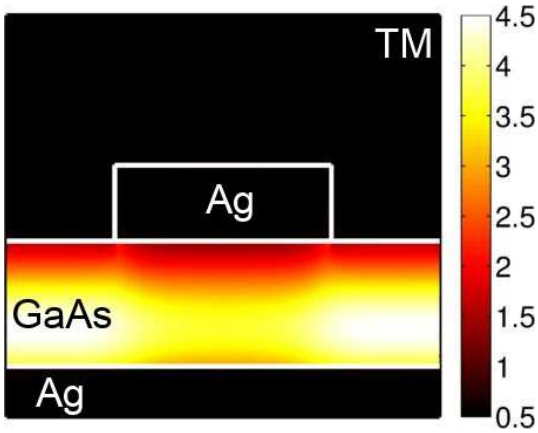

Figure 4.6.5: Absorption map ϵ". $|E|^2$ for the 1D-GaAs structure at $\lambda = 450\,\text{nm}$ calculated at normal incidence and TM polarization (arbitrary units).

However, using the data from Johnson & Christy [183] for silver is controversial for applications to PV systems. As a matter of fact, they lead to sensibly less parasitic losses in the metal compared for instance to data from Palik[69]. Fig. 4.6.6 illustrates this issue by comparing the absorption spectra for the 1D GaAs structure for silver data coming either from Johnson & Christy or Palik. The index of Palik slightly modifies the position of the absorption peaks. Therefore, we have changed a little the geometrical parameters of the structure to re-align them on to ease the comparison (GaAs thickness $h = 24\,\text{nm}$; period $p = 200\,\text{nm}$; width $w = 90\,\text{nm}$; thickness $t = 15\,\text{nm}$ for Palik data). This calculation shows that the absorption in metal is doubled for Palik's data compared to the Johnson & Christy case. Consequently, the absorption in GaAs in the Palik case is sensibly lower than for the J&C case (with no new optimization however) at the resonance wavelengths. This is particularly true for resonance C_3 where the electromagnetic field is strongly confined.

For this particular peak however, the total absorption is also pretty low. This is due to a poor coupling for this resonant mode. As a matter of fact, according to achieve the critical coupling condition of Eq. 3.2.1, we ought to have $\gamma_r = \gamma_{nr}$. γ_r is given by the geometry of the array and does not change much in this case. However, the losses in the metal are increased in the Palik case. Therefore, the non-radiative decay rate is increased, impacting the absorption intensity. A complete

re-optimization of the geometrical parameters for the Palik case is necessary to compare properly the two systems. Nevertheless, this stresses the importance to have the less absorptive silver during fabrication. This problem is addressed in Chapter 5.

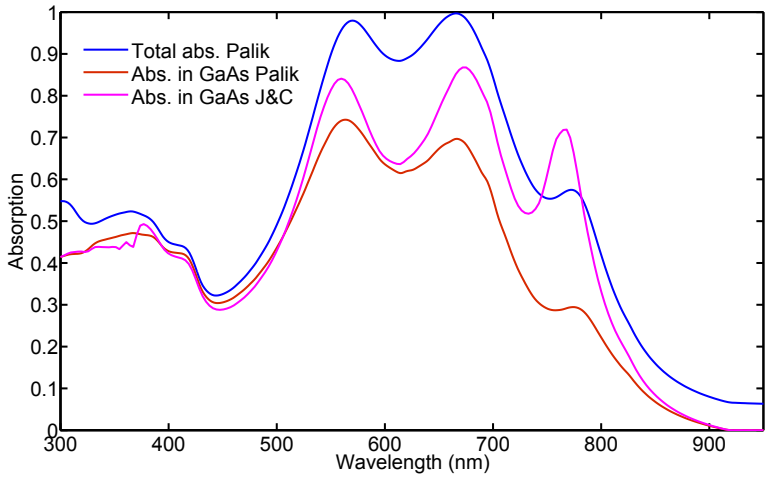

Figure 4.6.6: Comparison of the absorption spectra for the GaAs 1D structure with either Ag data coming from Johnson & Christy [183] or Palik [69]. The blue and the red curve are the total absorption and the absorption in the GaAs, respectively, for Palik data and for the following set of parameters: GaAs thickness = 24 nm; period $p = 200$ nm; width $w = 90$ nm; thickness $t = 15$ nm. The magenta curve represents the absorption in GaAs for the J&C data and for the set of parameters of Fig. 4.4.1.

The conclusion of this section can be generalized to different metals. Gold and aluminum are two candidates to replace silver in our system: the first to obtain a electronic contact with GaAs and the other one for cost and stability reasons (compared to silver). However due to higher imaginary parts of their dielectric permittivity, their use increases the parasitic losses in the metal (at least 20% more losses for gold). Silver is so far the best metal for our design, at least as far as our simulations go. We give silver the priority in our experimental fabrication. The replacement of silver, if inevitable for stability or electronic reasons, calls for further development and optimization from the optical point of view.

4.6.3 Flexibility and optimization

We have seen with the parametric optimization of Fig. 4.5.6 and Fig. 4.5.7 that it is possible to tune the position of each absorption peak by adjusting a single

geometrical parameter (GaAs thickness for resonances A and B and the wire width for resonance C). Moreover, we have seen that the two main absorption mechanisms are relatively independent from each other. This means that we can place the absorption peaks at our convenience, i.e right next to each other, under the maximum of the solar spectrum and below the gap of GaAs. There are enough degrees of freedom to carry out a efficient optimization.

There are nevertheless a few limitations. For instance, it is impossible to bring the MSM resonances at low wavelengths. We have seen in Chapter 3 that for the GaAs/Ag interface, no plasmonic mode can exist below the value of $\lambda = 670\,\text{nm}$. Moreover, it is difficult to control resonances A and B independently as they depend on the same geometrical parameter. We list a few parameters that can help in controlling the splitting amplitude of the two resonance for a deeper optimization:

- Replacing the surrounding medium (vacuum) by another material influence in principle only the resonance B as the phase value of its upper boundary varies.
- Changing the thickness of the wire width may affect the phase value at the upper boundary for the resonance peak A, causing it to shift accordingly. This parameter will also affect the MIM resonator as a plasmon propagates as the Ag/GaAs interface of the wire. Anyhow, if the wire thickness is greater than the evanescent tail of the plasmon in silver (confinement $\delta_{Ag} = 16\,\text{nm}$), we can consider that the plasmon is no longer affected.
- Modifying the fill factor tends to favor the resonance A or B and conversely. If one of this two modes is strongly confined, it may cause a shift of the resonance wavelength.

To improve the control over the resonances, the other geometrical parameters are also of importance. The period for instance must be subwavelength and (at fixed wire width) is essential to ensure the critical coupling condition as seen in the previous sections.

We have shown that with a simple structure, we were able to induce a strong enhancement of absorption in an ultra-thin GaAs layer. Here, we can add that the design of the geometry can be done for the most part intuitively by using the Fabry-Pérot model. The other geometrical parameters allow to go deeper in the optimization as the resonance mechanisms are slightly interlocked with each other. Anyhow, an effective optimization can be done very quickly and visually with these few models and construction rules.

Practically, the set of parameter presented here-above is itself the result of an optimization. If more absorption peaks could be induced (especially higher order

modes of the MSM resonance), the main criteria is to obtain the largest theoretical short-circuit current possible (i.e the broader and higher absorption spectrum in accordance with the solar irradiance spectrum). There is always room for further optimization. Here, the optimization has been realized by a sequential variation of the geometrical parameters, mainly relying on the physical comprehension of the mechanisms at stake to submit a simple model and guidelines for optimization. We assume that a multiple parameter optimization with a specified routine (genetic algorithm for instance) would give a better structure in terms of performance but also a far greater calculation time.

The simplicity of the optimization process offers a welcome flexibility. This has two consequences. We have seen that the structure is tolerant to potential variation of the geometrical parameters and of the refractive indices during fabrication, for instance. Moreover, a re-optimization of the geometrical parameters can be done quickly to take into account the potential variations during fabrication in a second run. This is a very important property that leads to the second point. If this structure is made of GaAs, the absorption mechanisms does not depend fundamentally on the actual refractive index of GaAs as the fine tuning of the absorption peaks is made by according geometrical parameters. This means that it is possible to imagine this design for other materials (with refractive indices in the same range of GaAs) by means of another optimization of the geometrical parameters. Further developments and application to GaSb and CIGS are presented in Chapter 6.

4.6.4 Study of the angular dependence

We have stressed before the importance of angle independence for solar cell applications. One can investigate this attribute by calculating and plotting the GaAs absorption of the 1D GaAs structure as a function of the incident angle in TM polarization (see Fig. 4.6.7). The three absorption peaks are nearly independent of the angle of incidence, up to at least 60 °. A small blue shift appears (40 nm) for resonance A and B. One can also note the apparition of the second-order mode of the MIM resonance (C_2) at $\lambda = 945$ nm.

For incident light angles of 40/50 °, the absorption spectrum seems to broaden. Fig. 4.6.8 represents the angular diagram of the theoretical short circuit current (in mA/cm^2) for the 1D 25 nm-thick GaAs structure in function of the incident light angle (in degrees). As expected, the J_{th} increases with the angle. Overall, the performances of the solar cell are omnidirectional.

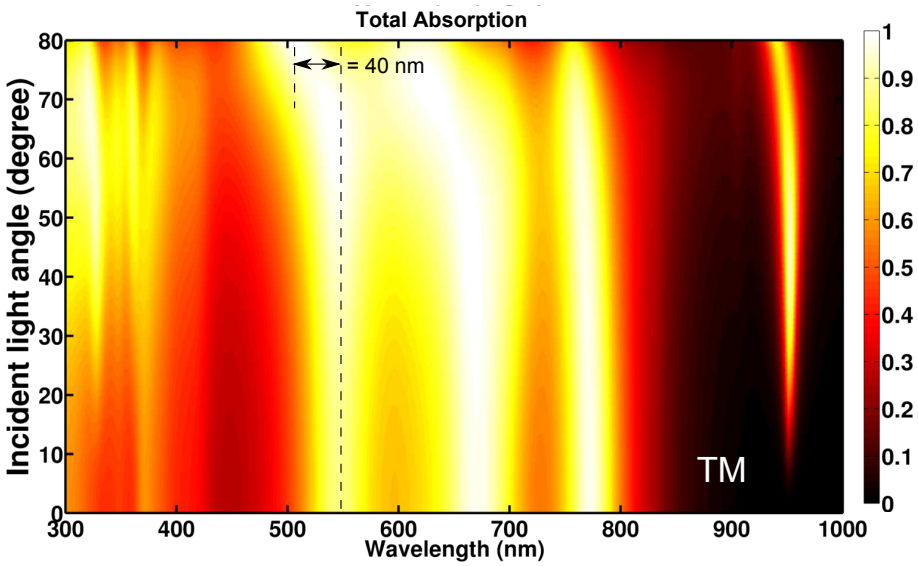

Figure 4.6.7: Total absorption spectrum of the 1D 25nm-thick GaAs structure in function of the incident light angle (rotating around the y axis) and TM polarization.

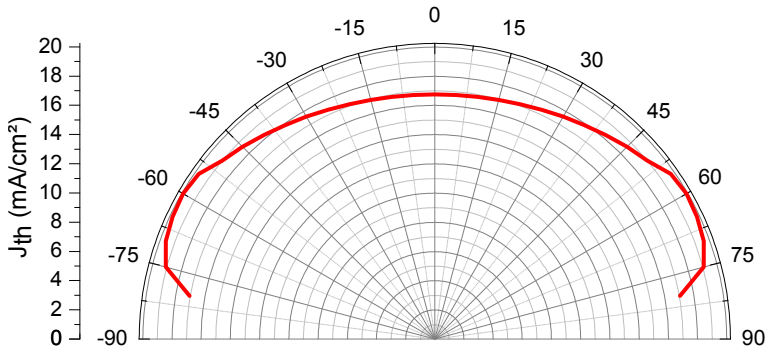

Figure 4.6.8: Angular diagram of the theoretical short circuit current (in mA/cm²) for the 1D 25 nm-thick GaAs structure in function of the incident light angle (in degree).

All the absorption mechanisms of the 1D GaAs structure are localized modes. This property generally induces an omnidirectional behavior of the absorption. To give a partial explanation of this phenomenon, let us take into consideration this question: do we have to be ultra-thin to have this interesting property?

For resonance A and B for instance, we have considered the model of a 25 nm-thick GaAs Fabry-Perot resonator only at normal incidence. For angle of incidence θ, the structure of the Fabry-Perot can be depicted as in Fig. 4.6.9. In this model, the difference of phase between two successive rays is given by:

$$\Delta\phi(\theta) = k_0\, 2\, n\, t \cos\theta \tag{4.6.3}$$

where $k_0 = \frac{2\pi}{\lambda}$ is the wave vector, n the refractive index of the layer (here GaAs), t the thickness of the layer, and θ the angle of the ray inside the structure. Furthermore, $\cos\theta$ can be written as a function of θ_0 with the Snell-Descartes law as:

$$\cos\theta = \sqrt{1 - \left(\frac{n_{vacuum}}{n}\right)^2 (1 - \cos(\theta_0)^2)} \tag{4.6.4}$$

The resonance condition of Eq. 4.5.1 can therefore be simplified to the expression $\lambda = t8n\sqrt{1 - (\frac{n_{vacuum}}{n})^2(1 - \cos(\theta_0)^2)}$ for resonance A for instance. For a 25 nm-thick GaAs cavity, the variation of θ_0 from 0° to 80° only induces a blue shift of $\Delta\lambda = 35$ nm. We can actually see this shift in Fig. 4.6.7 for resonance A and B. With such a small shift, the resonance can be considered angle independent. Of course, the spectral shift increases for larger cavity thickness.

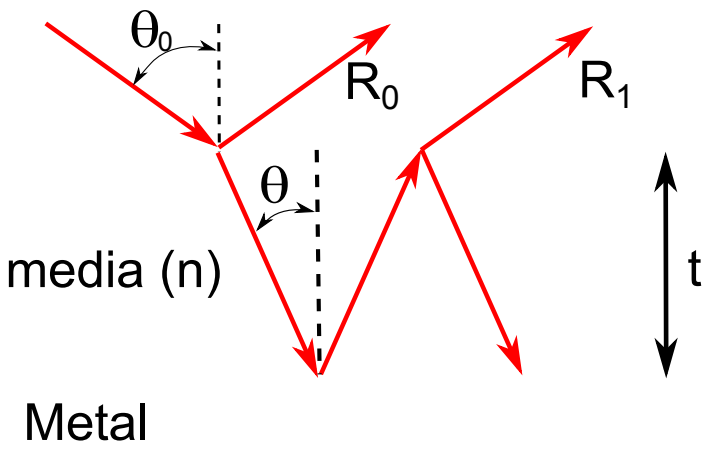

Figure 4.6.9: Schematic of the basic principle of a Fabry-Perot resonator. n is the refractive index of the layer, t the thickness of the layer, θ the angle of the ray inside the structure and $\theta_0$the incident angle

For peak C, the mechanism is different and directly linked to the MIM structure. The study of Cattoni *et al.* (reported in Chapter 3) have already reported that a MIM resonance is mostly independent from the angle of incidence at least for impair orders. This is due to the fact that the superposition of the incident plane wave and the MSM mode is efficient regardless of the angle: the direction of the magnetic field of the incident light remains unchanged with various incident

angles and it can efficiently drive the circulating currents at all angles of incidence as explained in references [167, 168]. The angle independence of this mode is therefore guarantied as long as the mode exists, i.e. for ultra-thin layer thicknesses with coupled plasmons.

4.7 From 1D to 2D structures: polarization independence

Previously, we have only considered the TM polarization, i.e. half of the incoming light because the structure is polarizing. Now, we study the 25 nm-thick GaAs two-dimensional structure, depicted in Fig. 4.7.1a. The structure is the same as for the 1D structure, except that the metallic dots are square and the periodicities along the two directions are equal. The parameters of the array are: period $p = 180\,\text{nm}$; width $w = 108\,\text{nm}$; thickness $t = 25\,\text{nm}$.

The comparison of the absorption spectra in the GaAs of the 1D (blue) and 2D (red) structure is plotted in Fig. 4.7.1b. The absorption spectra are compared to the absorption spectra in GaAs of the reference 25 nm-thick solar cell (black), to the solar spectrum density (gray) and the gap of the GaAs (at 870 nm). The 2D spectrum is similar to the 1D spectrum and displays the same three resonances. A small peak appears nonetheless at $\lambda = 730\,\text{nm}$.

The electromagnetic analysis of the different peaks confirms that three peaks are identical to the 1D structure at normal incidence. The small peak however is yet unexplained in our model, but harmless from a performance point of view. The theoretical short-circuit current change from $J_{th-1D} = 17.2\,\text{mA/cm}^2$ to $J_{th-2D} = 18\,\text{mA/cm}^2$ (plus here, we consider the totality of the incident light).

The main difference from the 1D structure is that the optical is now polarization independent and the electromagnetic field intensity maps are symmetric along both directions. Fig. 4.7.2 represents the total absorption spectrum of the 2D GaAs structure as a function of the incident light angle (rotating around the y axis) with either (a) the magnetic field H parallel to the y axis (TM polarization) or (b) the electric field E parallel to the y axis (TE polarization). Below the band gap of GaAs, the two figures are very similar up to 50 °: all the peaks are angle independent and the absorption efficiencies are stable. Above this value, for the TM polarization, the behavior in 2D is similar to the 1D structure: resonances A and B are broadening and slightly blue shifting.

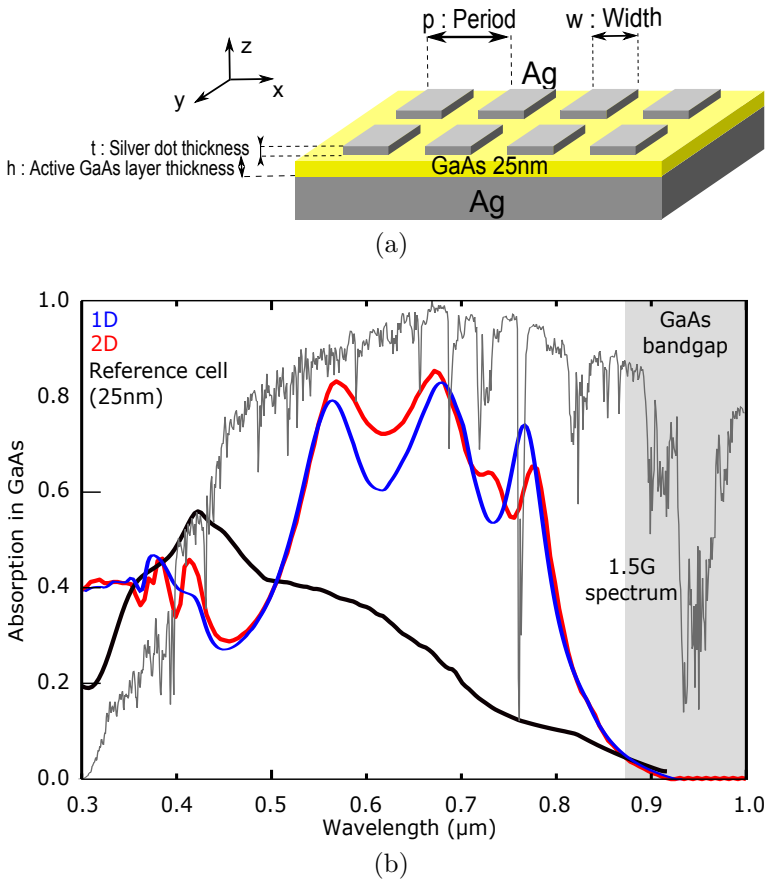

Figure 4.7.1: (a) Sketch of the 2D 25 nm-thick GaAs structure. The metallic dots are square and the periodicity along the two directions are equal. The parameters of the array are: period $p = 180$ nm; width $w = 108$ nm; thickness $t = 20$ nm. (b) Compared absorption spectra in the GaAs layer of the 1D (blue) and 2D (red) structure. The absorption spectra are compared to the absorption spectra in GaAs of the reference 25 nm-thick solar cell (black), to the solar spectrum density (gray) and the band gap of the GaAs (above 870 nm).

For the TE polarization, no shift can be noted and the absorption efficiencies decrease. This is probably due to the fact that the magnetic field cannot drive the circulating currents efficiently at large angles [168] in TE polarization for this structure. We can also note that the second order of the MSM plasmonic resonance C_2 is absent for the TE polarization. From now on, we consider this 2D structure as polarization and angle independent and for theoretical short-circuit current calculation up to an angle of 50 °.

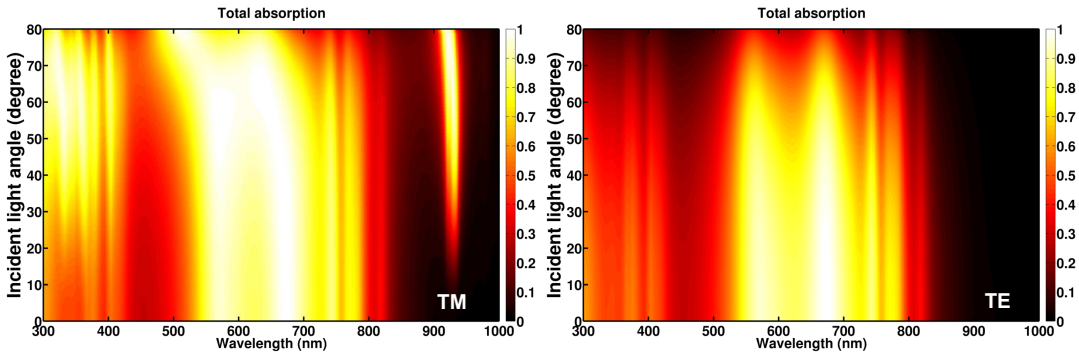

(a) (b)

Figure 4.7.2: Total absorption spectrum of the 2D GaAs structure as a function of the incident light angle (rotating around the y axis) with either (a) the magnetic field H parallel to the y axis (TM polarization) or (b) the electric field E parallel to the y axis (TE polarization).

4.8 Performances and comparison to literature

To conclude on this structure, the performance of this structure is evaluated and compared to literature. Assuming a perfect collection of the photo-carriers, one can compute a value of $J_{th} = 18\,\mathrm{mA/cm^2}$ for the 25 nm-thick GaAs 2D structure. This correspond to a very promising increase of 92 % compared to the reference 25 nm-thick GaAs solar cell ($J_{th} = 9.4\,\mathrm{mA/cm^2}$). It also corresponds to an increase of 45 % compared to the same structure without the metallic array ($J_{th} = 12.4\,\mathrm{mA/cm^2}$)

For GaAs, the only similar numerical structure (in terms of GaAs thickness) is detailed in the paper of Grandidier *et al.* [164] (see Chapter 2). Our structure allows to reach the same value of short-circuit current for a GaAs layer four times thinner. This can be seen in the fact the dielectric nano-spheres enhance the absorption very locally and that the enhancement compared to the flat structure in terms of theoretical short-circuit current is only 10 % (compared to the 92 % enhancement of our structure compared to the reference solar cell).

From a nano-photonic point of view, table 4.2 estimates the confinement ratio of the structure. The absorption depth of GaAs (see Fig. 6.1.2) is compared at each resonance wavelength to the actual GaAs thickness in the structure (25 nm). This simple calculation shows that the confinement ratio reaches a very high value of x24 for the MSM resonance. This confirms high confinement of light with a relatively simple structure.

Resonance wavelength	560 nm	675 nm	760 nm
GaAs absorption depth	15 0nm	300 nm	600 nm
GaAs thickness	25 nm		
confinement ratio	x6	x12	x24

Table 4.2: Comparison between the absorption depth of GaAs at the resonance wavelength (see Fig. 6.1.2), the actual thickness of GaAs in the nano-cavities array structure (25 nm) and their ratio.

4.9 Conclusion

So far in literature, very few papers have proposed nano-photonic solutions (and use of metallic arrays in particular) for crystalline materials. Nano-photonics solutions involving high confinement of light and metallic component have the reputation to induce too much losses induced by the absorption in metal. In this chapter however, we have demonstrated that this type of design can be a remarkable solution for an efficient light trapping with the nano-cavity array design.

In terms of pure absorption of light, this design has exploited the MIM designs of literature (Cattoni *et al.*[165], Liu *et al.* [167] for instance) and had transposed it to the visible range, adapting the geometries and adding the value of a multi-resonant, broadband absorber design. Our design leads to a similar short-circuit current compared to the structure of Grandidier *et al.* [164] but for a fourfold thinner GaAs layer. Another design close to this work is the paper Aydin *et al.*[174] that have demonstrated experimentally also a broadband super-absorber in the visible range with a structure similar to a MSM design. We compare the performances of our design to this paper in Chapter 5, after optical characterizations of our samples.

From a nano-photonic point of view, the design is also very interesting. To have a multi-resonant absorption spectrum in a very sub-wavelength structure is extremely counter intuitive. The strength of these structures is to display several absorption mechanism in a very small volume that are practically independent from one another. The mechanism at stake has been well understood for the most part and described in this chapter. The absorption in the metal, surprisingly low, is also a very good surprise. The reason of this low absorption, however, is not extremely clear and would deserve more study. It is moreover dependent on the nature of the metal. Probably, concessions in the design, multiple re-optimization and significant fabrication efforts are required to go further.

First, from a PV point of view, the design answers to every conditions imposed by the solar irradiance spectrum. The absorption spectrum of the nano-cavities array design is broadband, high below the maximum of the solar spectrum, and

angle and polarization independent. Most important of all (and counter-intuitive), the absorption in the metal remains extremely low, regardless the material and the design concerned. This property is remarkable and imposes this design as a solution of first order for solar cells. Globally, the design allow to reduce strongly the thickness of the absorber and to consider even ultra-thin layers (one or two order of magnitude below the absorption depth) while preserving a high absorption and high theoretical short-circuit current.

From an engineering point of view, the rules of optimization are also easy to establish. Constructing the absorption spectrum is very intuitive as we have enlighten several rules and guidelines to manipulate each absorption peaks. The design can also be applied to different materials from the PV sector. Moreover, in this design, the active media is kept perfectly flat, making it ideal for crystalline materials. Finally, given the flexibility of the design, this solution is very robust to potential fabrication fluctuations in the geometry. This is a very interesting property for the future fabrication developments of chapter 5.

To go further, we could easily imagine some additional ways to improve the absorption spectrum. Here is a small list of ideas to investigate in future developments:

- The structure as presented does not include any anti-reflection coating. Even-though our structure allows total absorption at the resonance wavelength, an ARC would give an extra degree of freedom in our design. A single layer ARC solution is tackled in the next chapter. Yet more efficient and refined inspired from literature could be considered.

- Adding a degree of complexity, we could imagine for instance rectangular instead of square particles. With such particles exposed to depolarized light, we predict the apparition of an extra absorption peak since we would have now two cavity length for the MSM resonance. The optimization of this design seem pretty intuitive as we would simply need to vary independently the two sides of the particle to put the two resonance accordingly.

- Putting things into perspective, it is probable that we could benefit from a break in the symmetry of our system. Our system of symmetry 4 is convenient for relatively quick calculations but is in the end a limitation. Trapezoidal particles, with varying size of the cavity size, would probably be excellent candidates to broaden the MSM resonance. This have been shown in the paper of Aydin *et al.*[174] and their broadband super-absorber (absorption in metal for other applications than PV). This is definitively a idea to investigate, although more time demanding.

Eventually, we have stressed out the fact that the designs of this chapter were mainly to propose optical solutions for solar cells. In fact, a lot a work is remaining

to adapt this design to solar cells structure. We can list a few starting points: take into account the several barrier layers from an optical point of view, use a metal that is the compromise for optical/electronic performance, take into account a real junction thickness. The only subject of ultra-thin junctions is a problem that should be tackled on its own right. A coupling between optical simulations and transport simulations [185, 186] would be a good starting point for the future of the nano-cavities array design.

However, the fabrication and characterization of optical proof of concept is the next step of our work. During this chapter, we have highlighted some points that are to become real challenges to the fabrication of the nano-cavities array design: the transfer of crystalline layers on alternative mirrors, the optical properties of the fabricated silver, the technological development for clean-room process to CIGS. In chapter 5, we tackle these problems encountered during the fabrication of our samples and their characterizations.

Chapter 5

Experimental evidence of broadband multi-resonant absorption in ultra-thin GaAs layers

Outline

5.1 Introduction . . . 98
5.2 Fabrication of GaAs demonstrators . . . 98
5.2.1 Constraints of fabrication . . . 98
5.2.2 Process overview . . . 99
5.2.3 Details of the fabrication process . . . 100
5.2.3.1 Anodic bonding . . . 100
5.2.3.2 Substrate removal . . . 103
5.2.3.3 Electron Beam Lithography and lift-off process . . . 104
5.2.3.4 Metal deposition and lift-off . . . 106
5.2.3.5 ZnO:Al deposition . . . 107
5.3 Optical characterization setups . . . 108
5.4 Optical characterization of Ag/GaAs/Au nano-cavity array demonstrators . . . 110
5.4.1 Optical response of planar GaAs/Au samples . . . 110
5.4.1.1 Measure of the multi-resonant absorption spectrum in ultra-thin Ag/GaAs/Au nano-cavity array demonstrators . . . 111
5.5 Study of the influence of an aluminum-doped zinc oxyde (ZnO:Al) encapsulation layer on the absorption spectrum . . . 113
5.5.1 Role of the extra ZnO:Al layer . . . 113
5.5.2 Optical response of planar ZnO:Al/GaAs/Au samples . . . 114

5.5.3 Multi-resonant and broadband total absorption measurement on the encapsulated nano-cavity array demonstrators 115
5.5.4 Influence of the width of the particle on the total absorption spectrum and discussion about fabrication tolerance 116
5.5.5 Influence of the incident light angle on the total absorption spectrum 117
5.5.6 Comparison to literature 119
5.6 Conclusion 120

5.1 Introduction

The aim of this chapter is to demonstrate the broadband multi-resonant absorption of the 25 nm-thick GaAs design presented in Chapter 4. The first section describes the fabrication process of the GaAs samples, its constraints and the technological approach. The second section reports the results of optical characterizations and the comparison to numerical simulations. Discussions about further characterizations are presented in the conclusion.

5.2 Fabrication of GaAs demonstrators

The objective is to fabricate the structure of Fig.5.2.1. The structure is composed of a 25 nm-thick crystalline GaAs layer grown by epitaxy and transferred on a gold back mirror. The 2D silver array is fabricated by electron beam lithography and embedded in a ZnO:Al layer. The process is described in the next section.

For technological reasons, the fabricated structure is an Ag/GaAs/Au stacking instead of the Ag/GaAs/Ag design studied numerically. As seen previously, the change of back mirror is going to change the optical response and increase the absorption losses in the metal. We also add a encapsulation layer made of ZnO:Al. The role and the thickness of the ZnO:Al layer is discussed later in this chapter.

5.2.1 Constraints of fabrication

The realization of nanophotonic and plasmonic structures requires the use of refined techniques in order to approach the ideal structure of the electromagnetic simulation (Fig. 5.2.1). The control of the geometrical parameters of the array (period, length, thickness of the metal) and of the surfaces quality is critical.

It is important to be able to fabricate large patterned area. For now, we focus on achieving at least 2*2 mm² arrays, a surface that is mandatory for a proper

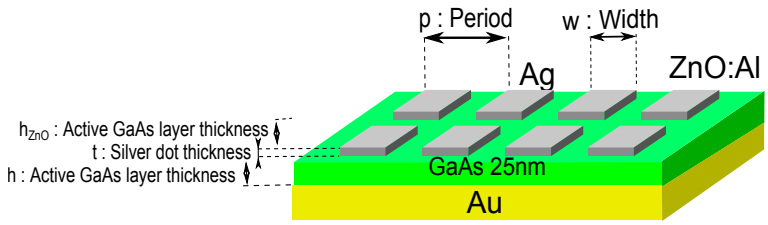

Figure 5.2.1: Schematic of the fabricated structure. The structure is composed of a 25nm-thick crystalline GaAs layer grown by epitaxy and transferred on a gold back mirror. The 2D silver array is fabricated with electron beam lithography and embedded in a ZnO:Al layer.

optical characterization on our experimental setup (reflectivity as a function of the incident angle θ and a resolution of $\delta\theta = \pm 0.5\,°$).

The realization of large patterned areas implies an excellent control of the homogeneity of the sample (size of the dots, period). The process must be also very reproducible and must allow a very low overall roughness (particularly of the metal film). Furthermore, we would like to avoid the use of nucleation or adhesion layer of metal on semiconductor that would change the properties of the modes propagating at this interface (increase of the losses). We would like also to be able to vary and control all the geometrical parameters in order to fit numerical spectra.

5.2.2 Process overview

The fabrication process is based on a layer transfer and a classic lift-off technique. The different steps are represented on Fig. 5.2.2.

- Fig. 5.2.2a: the active region of GaAs is grown on a GaAs substrate by molecular beam epitaxy (MBE) with an additional 300 nm-thick etch-stop layer of $Al_{0.85}Ga_{0.15}As$. The active region is composed of an intrinsic GaAs layer of nominal thickness 25 nm.

- Fig. 5.2.2b: a metal deposition Au/Ti/Al (200 nm / 20 nm / 200 nm) by electron-beam assisted evaporation (PLASSYS MEB 550 SL) is performed on GaAs layer after chemical deoxidation. For GaAs, the classical deoxidation is composed of a 5' HCl bath (concentration = 20 % of the commercial solution), a 5' deionized water rinse and a nitrogen drying. From an optical point of view, only the gold has an optical role as it appears completely opaque to visible light.

- Fig. 5.2.2c: substrate transfer. The sample is bonded to a Pyrex substrate via anodic bonding with the aluminum layer.

- Fig. 5.2.2d: substrate removal. The initial GaAs substrate is chemically selectively wet etched in a ammonium hydroxide/hydrogen peroxide (NH_4OH/H_2O_2) solution down to the etch-stop layer ($Al_{0.85}Ga_{0.15}As$). The etch-stop layer is then removed by chemical etching in hydrofluoric acid (high content of aluminum).
- Electron-Beam Lithography (EBL) and lift-off the mask:
  - deoxidation of the GaAs surface.
  - Fig. 5.2.2e: a 100 nm-thick commercial Poly(methyl methacrylate) (PMMA) layer resist is spin-coated and cured for one hour at 160°. The resist is insulated via electron beam lithography: the electronic beam draws the pattern in the resist.
  - Fig. 5.2.2f: the insulated resist is developed in a buffered methyl isobutyl ketone (MIBK) solution. Residual resist is removed by an O_2 reactive ion etching.
  - Fig. 5.2.2g: metal deposition of a 20 nm-thick silver film (electron-beam assisted evaporation).
  - Fig. 5.2.2h: lift-off of the resist in trichloroethylen solvent.
- Fig. 5.2.2i: a 55 nm-thick layer of ZnO:Al is sputtered to complete the structure. It acts as an encapsulation layer, a transparent conductive oxide and as an anti-reflection coating.

I have fabricated the samples presented in the rest of this chapter following this process by myself, except for the GaAs epitaxy and the EBL resource. Additional details on some critical steps are discussed in the following subsection.

5.2.3 Details of the fabrication process

5.2.3.1 Anodic bonding

Since GaAs is grown by epitaxy on a GaAs substrate, we must perform a layer transfer to obtain the structure of Fig. 5.2.1. There is a large range of techniques to bond efficiently a sample to another substrate. The simplest solution is to stick the sample on a flat substrate such as glass with an adhesive resist (deposited by spin-coating for instance). However, EBL imposes a constraint: the sample to be insulated must be globally flat on a centimeter area. To ensure high resolution, the electron beam is dynamically focused on the surface by a control in height by laser. This height focusing dynamic is limited for a fixed displacement (less than 100 nm for a 10 µm displacement). This constraint imposes a strictly controlled bonding

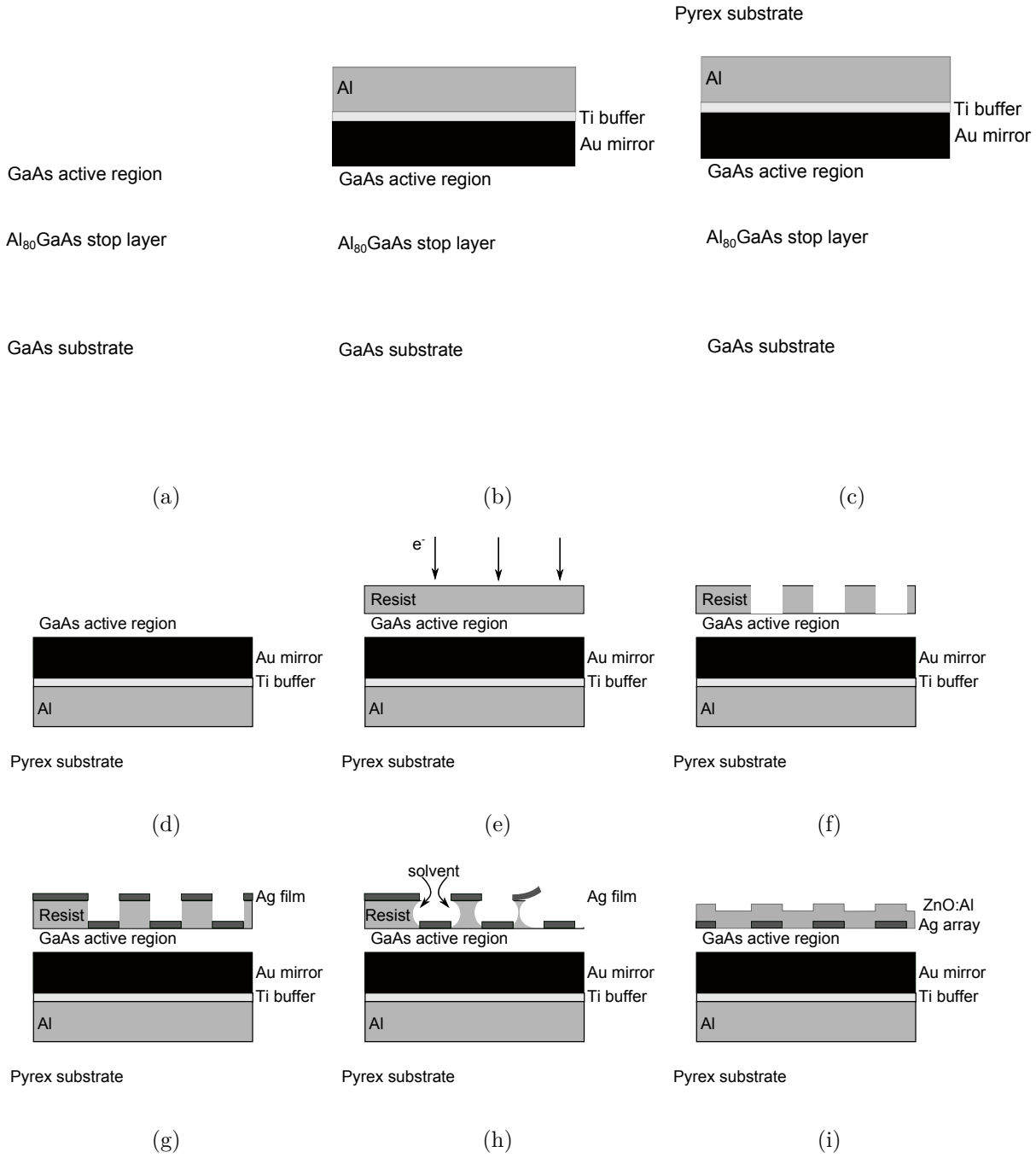

Figure 5.2.2: Overview of the GaAs sample fabrication process: (a) Molecular beam epitaxy (MBE); (b) Metal deposition; (c) Anodic bonding on Pyrex substrate; (d) GaAs substrate removal; (e) Resist spin-coating (PMMA) and electron beam lithography (EBL); (f) Development of insulated resist; (g) Metal evaporation of the 20 nm-thick metallic array; (h) Lift-off; (i) ZnO:Al sputtering.

technique. In this category, one can choose either eutectic bonding [187, 188] or anodic bonding [189, 190]. The second constraint is the temperature. At LPN the temperature of a Au/Au eutectic bonding is around 370 °C, far above the temperature of diffusion of gold in GaAs for instance [191]. For this reason, a relatively low temperature bonding is preferred: anodic bonding.

The anodic bonding is a technique used to perform metal on glass or semiconductor on glass bonding. It has been developed at LPN during the PhD thesis of H. Elfatimi [192] for a bonding between aluminum and Pyrex with strong efforts to decrease the temperature during the bonding process.

In our setup, anodic bonding consists in slightly pressing a glass containing a source of mobile ions (Pyrex Corning 7740) and a metal (Al) at a moderate temperature (160 °C) and a high difference of potential, applied on both sides of the interface (1700V). This potential has for effect to increase the electrostatic forces between the two interfaces.

Pyrex is a sodium-rich glass. It contains sodium oxide Na_2O that can release sodium (Na^+) and oxygen (O^{2-}) ions. When the temperature increases, the mobility of the sodium ions Na^+ rises. The migration of sodium ions towards the cathode induces a depletion region close to the Al/Pyrex interface. All of the applied voltage is dropped in this space charge region. The high electric field increases the electrostatic pressure applied on the two surfaces to be bonded. Once the surfaces are in contact under a high electrostatic force, chemical bonds are created leading to the strong anodic bonding between Al and Pyrex. The electrostatic force intensity depends on the temperature, applied voltage and sodium content in the Pyrex substrate.

The setup has been optimized at LPN over the years. Naturally, the bonding of ultra-thin 25 nm-thick GaAs layers has required additional development to prevent dislocations induced by stress relaxation or the perforation of the layer due to dust particles. For instance, at the start of anodic bonding, only a few contact points exist between the two interfaces. The high electrostatic pressure ensures a local bonding and the process then «diffuse» from these particular points to seal the whole sample. However, the electrostatic pressure also induces a strong local surface deformation that can lead to dislocations. For these reasons, the interfaces should be as clean as possible. Here are the details of current anodic bonding processes at LPN:

- The GaAs surface deoxidized and carefully cleaned with successive thrichloroethylene, acetone and isopropyl alcohol baths before deposition of the mirror. The Pyrex substrate is cleaned with a Piranha solution ($H_2SO_4 : H_2O_2$, 2:1) for 15 minutes and rinsed.

- A 200 nm-thick Al layer is deposited on our chosen mirror. Because of the bonding temperature, a gold mirror is chosen over silver due to the silver

tendency to diffuse at a relatively low temperature in GaAs. For similar reason, a 20 nm-thick Ti layer is deposited to prevent inter-diffusion between gold and aluminum.

- An additional 50 nm multi-directional deposition of aluminum is performed on the edges and the back of our substrate to allow the current to flow between the cathode and the anode during the bonding without damaging the GaAs stack.
- The bonding is performed with a substrate bonder (SUSS MicroTec), at 1700 V and 210 °C for 80 minutes.

5.2.3.2 Substrate removal

After the bonding, the GaAs substrate has to be removed. In our case, the substrate dissolution is performed by wet etching.

The GaAs/$Al_xGa_{1-x}As$ selective etch is made with a ammonium hydroxide/hydrogen peroxide (NH_4OH/H_2O_2) solution. The selectivity of this etch solution, defined as the ratio of the etching rates of GaAs to AlGaAs, is around 30 [193]. This means that the AlGaAs etch-stop layer is etched at a rate of only 10 nm/min. Given the thickness of the AlGaAs layer (300 nm), this etch process allows a controlled etching of the GaAs substrate with a selectivity sufficient in our case.

The AlGaAs is then selectively etched by a hydrofluoric solution (HF, 10 %) for a few second. In Fig. 5.2.3 is reported a (a) SEM cross section image (FEI Magellan) of the 25 nm-thick GaAs layer reported on the Au miror and (b) an optical microscope image of the GaAs surface. The bonding and substrate removal can be successively achieved over 1 cm^2 to 2 cm^2 routinely with a very small amount of defects.

The substrate is totally dissolved and the overall process is extremely costly. However, this is not *a priori* a limiting step. Other substrate removal methods allow to re-use the GaAs substrate for scale-up applications. For instance, the Epitaxial Lift-Off (see for instance Ref. [22]) technique directly dissolves what is in our case the etch stop layer with hydrofluoric acid. However, this technique is currently incompatible with our anodic bonding process (and the presence of aluminum). We would need a new stop layer that can be selectively removed with respect to aluminum or a way to protect the aluminum layer. Another method, the controlled spalling technique [24, 25], allows to separate the active region by inducing a controlled stress in a sacrificial brittle layer especially designed for GaAs based structures and flexible substrate.

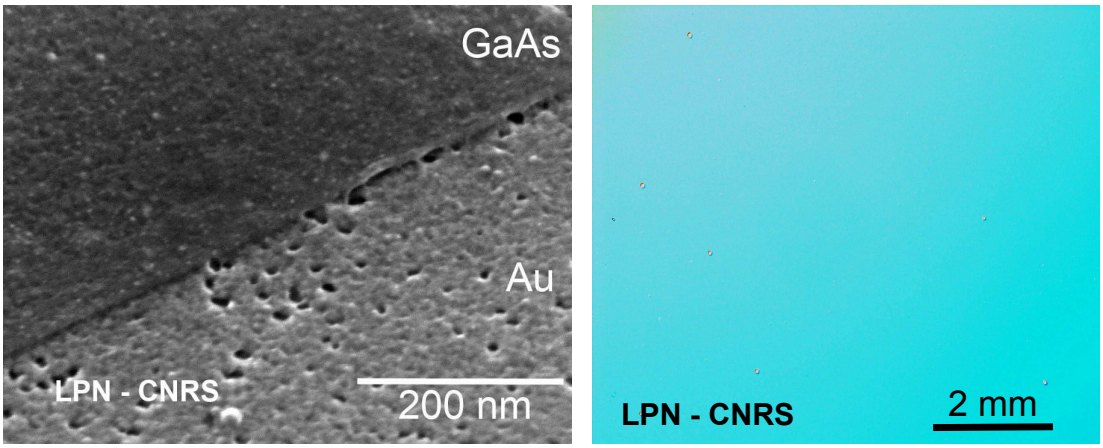

(a) (b)

Figure 5.2.3: (a) SEM image (FEI Magellan) and (b) optical microscope image of a 25nm-thick GaAs layer reported on a gold mirror by anodic bonding.

5.2.3.3 Electron Beam Lithography and lift-off process

The Electron Beam Lithography (EBL) is a common technique in most of technological processes that needs a sub-micron resolution. The other main techniques are nano-imprint lithography (NIL), holographic lithography and bottom-up approach such as colloidal lithography. Schematically, the EBL consists of the scanning of a focus electron beam on electron sensitive resists to draw patterns at the nanometer scale (Fig. 5.2.2e). The setup is constituted of a column, similar to a scanning electronic microscope, equipped with a magnetic or electrostatic refraction beam system. The quality of the setup is determined by the capability to correct aberrations of the beam.

The writing field of the beam being limited to a few hundredths of micrometers, modern EBL setups are also equipped with a holder capable of nano scale displacement assisted by interferometry. This allows an excellent control over the position of the patterns and offers the possibility to obtain relatively large area up to 6”.

The resolution of this technique depends essentially (1) on the diameter and the energy of the electron beam and (2) on the resist. In our case, the resist is PolyMethyl-MethAcrylate (PMMA). We use a commercial PMMA resist (A5 from MicroChem), spin coated at 4000 rpm during 30 s and prebaked in an oven at 160 °C during 80 min. In these conditions, the resist layer has a thickness around 250 nm. The sample is then exposed in a VISTEC EBPG 5000 equipment with a dose of 500 µC/cm^2. The interaction between electrons and the resist causes the rupture of chemical bounds, decreasing the average molecular mass in the

exposed areas in order to dissolve them with to a specific solvent (the so-called development, Fig. 5.2.2f). This type of resist is said positive (like PMMA for instance). We use a mix of methyl isobutyl ketone (MIBK) and isopropyl alcohol (IPA) solvents as a developer. The developer temperature is kept constant at 20 °C with a thermostatically controlled water bath. The resist is developed by immersion in a 3:1 IPA:MIBK solution for 75 s and rinsed in IPA for 10 s.

The resist modification is not due to direct electrons, too energetic. Only the low energy electrons can expose the resist. The electrons lose their energy by electron-electron interaction in the resist and the substrate, deflecting their trajectory [194]. The first consequence is that secondary electrons can be back scattered from the substrate to expose the resist. The size of the pattern is therefore often larger than expected (see Fig. 5.2.4a). The solution is to adjust locally the dose of the electron beam (expressed in µC/cm^2) in order to limit the back-scattering at the edges of the pattern. Commercial software can adjust the exposure automatically according to the pattern and the substrate. However, enough knowledge about the substrate and the resist is often sufficient to adapt the dose of the beam. Moreover, a small downsizing of the mask can be enough to take into account the natural over-sizing of the resulting pattern. In the facts, series of patterns are fabricated on the same sample with different dose in order to chose the correct value after SEM (FEI Magellan) observation.

To prevent charge accumulation, electrons must be driven out from the region of the resist. This is achieved in most cases with a conductive substrate. In our case where the sample is transferred on Pyrex, a thin film of aluminum (50 nm) is deposited on the resist to enable charge evacuation and is then removed in a sodium hydroxide solution. It also has another advantage. The focusing of the electron beam is controlled in height by a laser beam. If the surface is not reflective enough, some problems of focusing can appear, resulting at best to a loss of resolution or to a system error.

A classic step of lift-off after lithography is performed to complete the fabrication of the 2D metallic array. The metal is deposited anisotropically (see Fig. 5.2.4b) to reach a thickness at least three times smaller to the resist thickness. The resist and extra metallic parts are removed in an appropriate solvent (thrichloroethylene). The natural undercut the resist is a strong advantage of the EBL over other forms of nanometer-scale lithography (such as nano-imprint lithography for instance): the side of the pattern is shaded during the metallic deposition by the resist edge itself, allowing a good access for the solvent and an efficient lift-off.

The other reason we use EBL in our case is the following. Even-though the lithography itself is relatively time (and therefore cost) demanding, the creation of the mask in the case EBL is made by myself on a computer, i.e. costless, quick and above all adjustable (potentially for each sample). In our case, the fabrication

of sample is long, expensive and difficult due to epitaxy and substrate transfer. EBL is very convenient to test rapidly a lot of different structures on a limited amount of samples. The technique itself also allows a good adaptability in terms of aspect ratios and amplitude of sizes for the patterns by contrast with nano-imprint lithography, holographic lithography and colloidal lithography.

Note that once a suitable geometry is found, nano-imprint lithography is available at LPN for large and quick patterning in these GaAs samples in the optic of process optimization and up-scalling. This technique is presented for the CIGS case in Chapter 7.

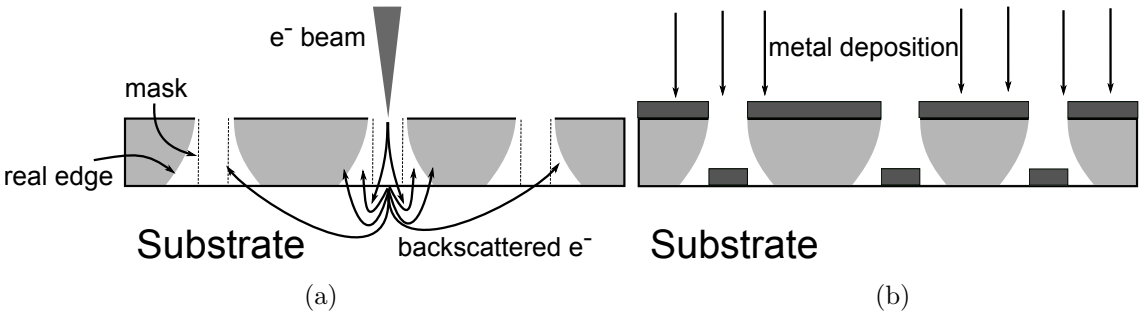

Figure 5.2.4: (a) Proximity effect: back-scattered electrons increase the exposition dose and modify the flanks of the resist. (b) Anisotropic metal deposition in the case of EBL.

5.2.3.4 Metal deposition and lift-off

The properties of metallic nanoparticles are often different from the bulk crystalline material. The geometry and deposition techniques are some of the factors that can affect their optical response. Metal films deposited by evaporation are inherently rough due to polycrystallinity. Our goal is to fabricate a 2D metallic array with a thickness of 20 nm-thick. The EBL has a largely sufficient resolution to realize squares of 100 nm x 100 nm. However, this is not the only condition for a satisfactory realization.

Fig. 5.2.5 represents the same 2D metallic array of period 200 nm and particle width 100 nm realized on a GaAs layer with the deposition of (a) a 20 nm-thick titanium layer (Ti) (b) a 20 nm-thick silver layer and (c) a 20 nm-thick silver layer with a 0.5 nm-thick germanium (Ge) nucleation layer. Ti allows to realize square nanoparticles unlike Ag, although with the same process. This is due to the tendency of silver to nucleate with large grains, resulting in deformed nanoparticles and rough surfaces. The nucleation of silver and the difficulty to fabricate continuous ultra-thin silver films have been addressed in the paper of Logeeswaran *et al.*

[195]. They proposed an ultra-thin (0.5-1 nm-thick) Ge layer to improve the nucleation of silver on a SiO_2 substrate. In our case, the same technique has allowed to achieved the array of Fig. 5.2.5c that is much more uniform with well-defined square nanoparticles. However, the 0.5 nm-thick Ge nucleation layer itself risks to degrade the performances of the structure. It probably causes more parasitical absorption being placed where the EM field is often the more intense. Similar detrimental effects have been observed on Ti/Au (5/27 nm) MIM arrays in the paper of Collin *et al.* [196]. In our case, the numerical analysis of this nucleation layer is yet to be done.

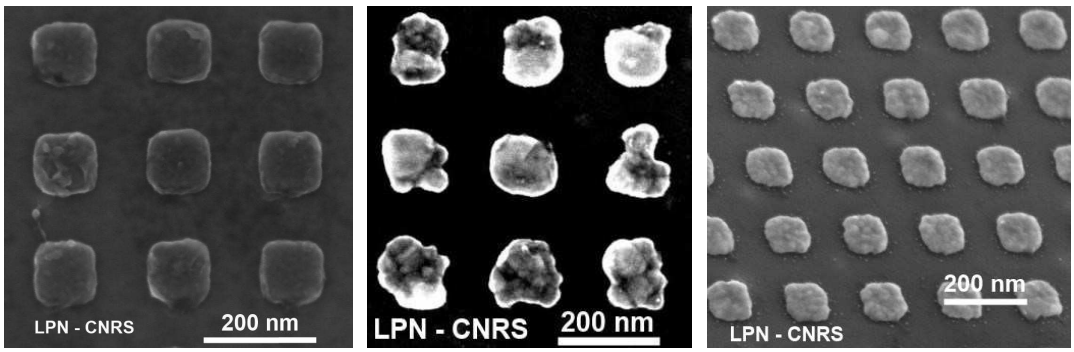

(a) (b) (c)

Figure 5.2.5: SEM images of the 2D metallic arrays realized by EBL and lift-off on a GaAs layer with the deposition of (a) a 20 nm-thick titanium layer (Ti) (b) a 20 nm-thick silver layer and (c) a 20 nm-thick silver layer with a 0.5 nm-thick germanium (Ge) nucleation layer

5.2.3.5 ZnO:Al deposition

The properties of ZnO:Al are very dependent of deposition parameters, in particular of the pressure, the temperature and the content of aluminum. For an ideal TCO, there is a trade-off between a high conductivity and transparency. Another factor is important in our case: the crystallinity of the layer. Fig. 5.2.6 represents the SEM pictures of two types of ZnO:Al layers deposited by sputtering playing the role of encapsulation for the silver array: (a) deposited at IRDEP (400 nm-thick) and (b) deposited at LPN (55 nm-thick). In the case of Fig. 5.2.6a, the ZnO:Al from IRDEP is optimized for CIGS solar cells. In the case of Fig. 5.2.6b, the ZnO:Al has much smaller grains, which is probably better for an efficient encapsulation. For these reasons, this ZnO:Al (55 nm-thick) is chosen for our samples.

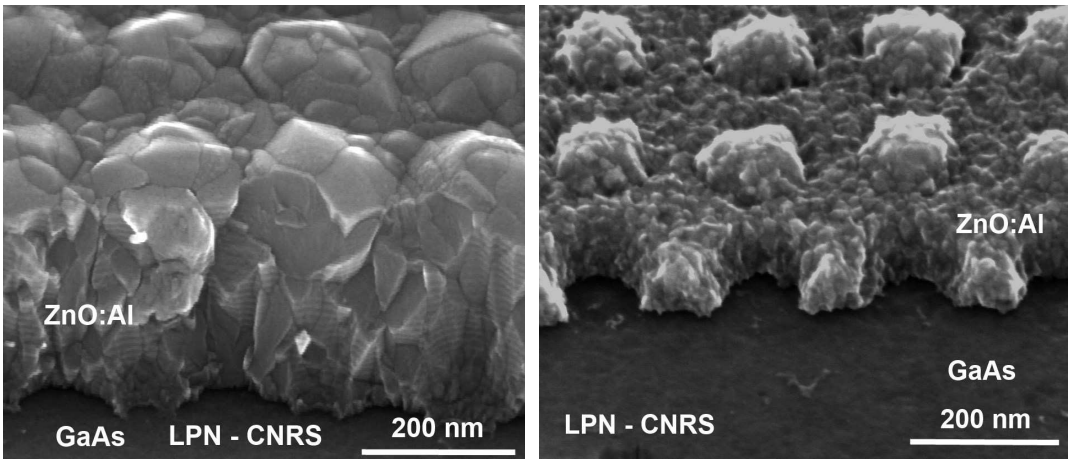

(a) (b)

Figure 5.2.6: SEM pictures of two types of ZnO:Al layers playing the role of encapsulation for the silver array: (a) deposited at IRDEP (400 nm-thick) and (b) deposited at LPN (55 nm-thick)

5.3 Optical characterization setups

In this section, we describe the optical setups used to measure the reflection (or transmission) of the samples fabricated following the process of the previous section on a broad range of wavelengths, incident angles and for different light polarizations.

First a Sentech reflectometer is used for the fast clean-room measurement of specular reflection of the sample at normal incidence with unpolarized light with respect to a reference sample. The wavelength range is 0.2-0.950 µm.

In depth measurements are performed with a Fourier Transform Infra Red (FTIR) spectrometer (Brüker Equinox 70) with a homemade goniometer setup. Fig. 5.3.1 represents the schematic of the GonioVISIR setup for angle-resolved reflection and transmission measurement. It is designed to measure transmission and reflection spectra under polarized light as a function of the angle of incidence. It was first developed by Cyrille Billaudeau during his PhD thesis [197]. The setup is composed of three distinct parts: the FTIR (source and spectrometer) (A), the achromatic focusing system (B) and the measurement and detection platform (C).

The principle of the FTIR spectrometer is based on a broadband light source passing through a Michelson interferometer before imaging the sample. The interferogram obtained contains the intensity measured. A Fourier Transform is then performed by the software to obtain the final spectrum. FTIR spectrometers allow to achieve a much higher spectral resolution than standard dispersive spec-

trometers. In our case, the highest spectral resolution possible is $\delta\sigma = 0.5\,\mathrm{cm}^{-1}$. The diameter of the probe is $\phi = 1.7$ mm in our configuration. The measure can be done on a wide spectral range. Several sources and detectors are available to cover the 0.4-17 µm range. The detection platform is composed of two mobile rotation stages and the excitation and detection angles can be varied independently. The angular resolution of the system is 0.5 °. For our samples, we approximate the total reflection as the specular reflection (planar surface exclude diffusion and sub-wavelength arrays exclude non-specular diffracted order).

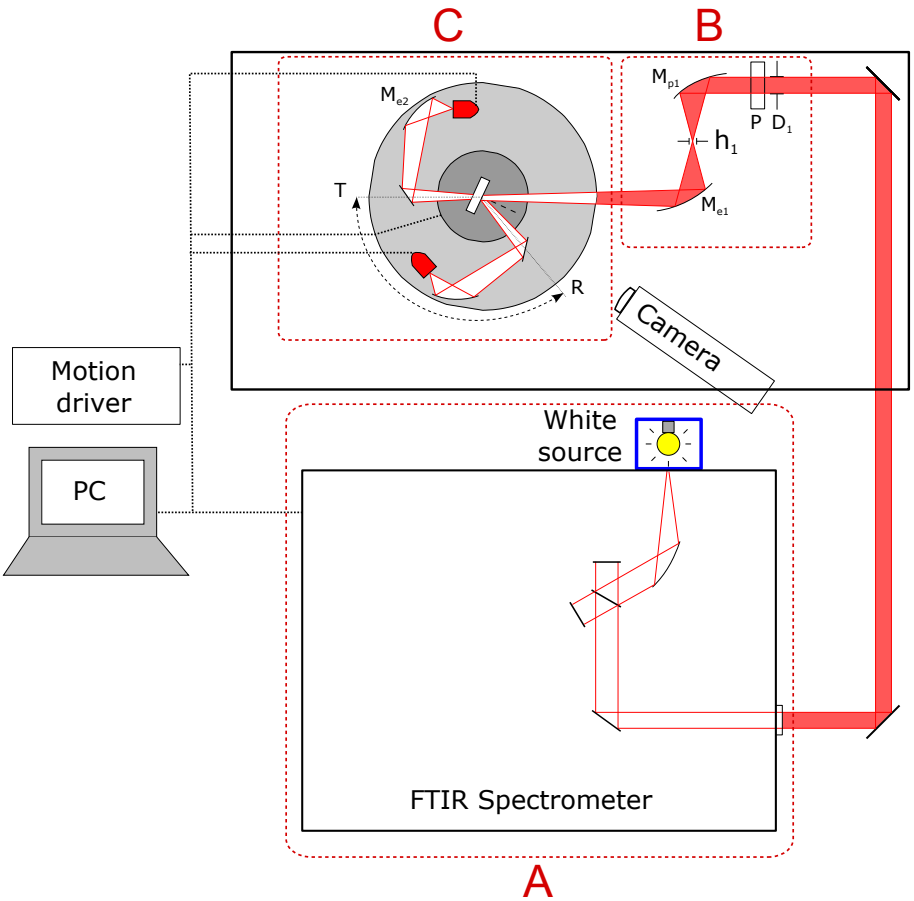

Figure 5.3.1: Schematic of the GonioVISIR setup for angle-resolved reflection and transmission measurements; A: FTIR; B: Achromatic focusing system; C: Measurement and detection platform.

5.4 Optical characterization of Ag/GaAs/Au nano-cavity array demonstrators

The goal of this section is to highlight experimentally the broadband multi-resonant absorption spectrum of Ag/GaAs/Au nano-cavity array demonstrators sketched in Fig. 5.2.1 without ZnO:Al layer. The sample presented is realized with process described at the beginning of this chapter without a Ge nucleation layer. The 2D array has a geometry close to the simulated 2D structure of Chapter 4. The nominal dimensions of the array, fabricated on a 2*2 mm² area, are: period p =200 nm, thickness $t = 20$ nm and width $w = 120$ nm. Practically, the particles are deformed because of the nucleation of silver (see Fig. 5.2.5b). The smaller the particles the more deformed the shape is because of the fixed size of the grain. The effective width of the particles is therefore slightly lower than the nominal value, with an important dispersion in size.

We have performed reflectivity measurements on the fabricated samples 1) after the 25 nm-thick GaAs layer transfer and 2) after the fabrication of the 2D dimensional array. The results are presented successively in the following sections. The measured spectra are compared to numerical simulations in order to explain the optical responses based on the observation and characterization of the samples. Numerical calculations are performed with the same indices as before for the different materials. For Au, a comparison between Palik [69] and Johnson and Christie [175] is made for the metallic mirror.

5.4.1 Optical response of planar GaAs/Au samples

We first measured the reflectivity (R) spectrum of the GaAs/Au stack at normal incidence. The results are shown in Fig. 5.4.1 (blue line). The total absorption (1-R) is compared to numerical calculation with different parameters. As explained in Chapter 4, the main resonance peak at at $\lambda = 680$ nm is due to a Fabry-Perot resonance in the GaAs layer.

First, the numerical calculation of Fig. 5.4.1a are carried out for different GaAs layer thicknesses and for a permittivity of gold taken from Johnson and Christie [175]. As expected, the resonance wavelength is in agreement with experiments for $h = 25$ nm. A slight discrepancy is found for the absorption efficiency close to the resonance maximum.

Second, the numerical results obtained with two different permittivity data for gold are compared in Fig. 5.4.1b. The permittivity from Johnson and Christie [175] gives a better agreement than data from Palik [69]. These results confirm the very good optical quality of our samples made of 25 nm-thick GaAs samples transferred on gold mirror.

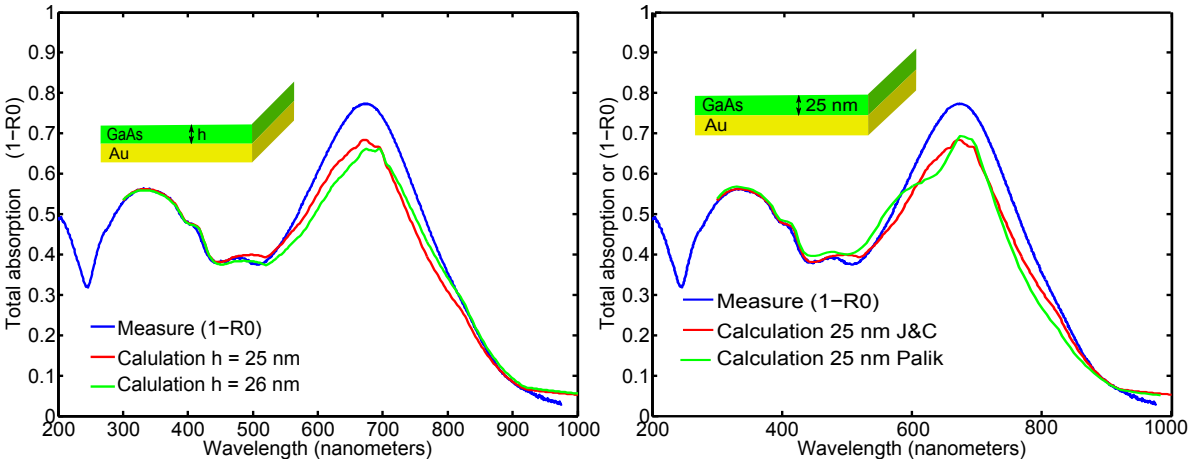

(a) (b)

Figure 5.4.1: The 1-R spectrum measured on the 25 nm-thick GaAs layer on gold mirror at normal incidence and under unpolarized light (in blue in both figures) is compared to: (a) simulated 1-R spectra for a thickness of 25 nm (red curve) and 26 nm (green curve) for the GaAs layer (gold data: Johnson and Christie [175]); (b) simulated 1-R spectra for a thickness of 25 nm for the GaAs layer and either Johnson and Christie [175] (red curve) or Palik [69] (green curve) optical data for gold.

5.4.1.1 Measure of the multi-resonant absorption spectrum in ultra-thin Ag/GaAs/Au nano-cavity array demonstrators

In Fig. 5.4.2a are plotted the measured 1-R (total absorption) spectrum at normal incidence and under unpolarized light of the fabricated structure along to the spectrum of the unstructured stack (same as Fig. 5.4.1). In the simulation of Fig. 5.4.2b , the array is considered as ideal (perfectly square) and the particles is equal to 120 nm.

The addition of the silver array has several impacts of the total absorption spectrum. First, below $\lambda = 300$ nm, the total absorption is 20 % higher with the array, probably due to parasitic absorption in silver. Then, the unique absorption peak (identified as a Fabry-Pérot) at $\lambda = 620$ nm is now divided into two peaks (A and B). This effect is expected and can be seen as well in the simulated spectra. The peaks seem to have a similar full width at half maximum (FWHM) compared to numerical results. At $\lambda = 680$ nm, the absorption is almost total (97 %). However, the two peaks do not have the same amplitude and are not as separated compared to simulation. A third absorption peak appears around $\lambda = 980$ nm, in accordance with simulations. Experimentally this resonance peak, identified as the C_3 reso-

nance, is larger and higher than expected numerically. This is beneficial as the absorption spectrum is broadened. Unfortunately, it resonates also well above the value expected by the calculation ($\lambda = 980$ nm instead of $\lambda = 850$ nm), and above the band gap of GaAs.

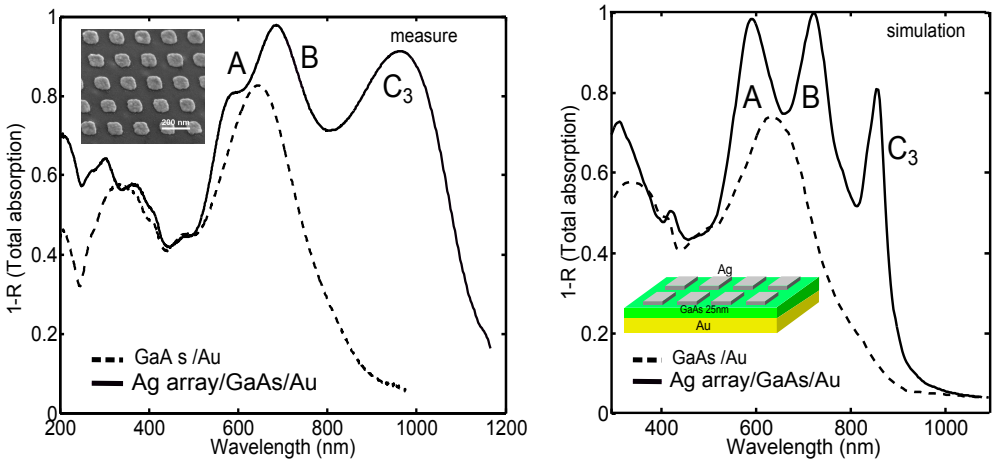

(a) (b)

Figure 5.4.2: (a) Measured and (b) calculated 1-R spectrum of the structured 25nm-thick GaAs layer in inset (black line) compared to the 1-R spectrum (measured and simulated, respectively) of unstructured 25nm-thick GaAs layer on gold. The simulation is made with the following geometrical parameters: period = 200 nm, width of the particle = 120 nm, thickness of metal = 20 nm, thickness of GaAs = 25 nm.

Two effects can explain these disagreements. First, the dispersion in size of the particles due to nucleation probably has an impact, especially in the widening of the MSM resonance. This defect can not be simulated easily but one can imagine that if each MSM resonator has a size scattered around a mean value, each resonator has its own resonance wavelength, resulting in a broader peak.

Second, a strong uncertainty remains on the optical data of the silver array. A difference in these values would affect resonances A and C_3, but not resonance B in first approximation according to the model of Chapter 4. The silver array has been exposed to the atmosphere (tarnished). The silver sulfur Ag_2S forms rapidly a layer of 1-3nm when silver is exposed to air. Bennett *et al.* [198] and other studies [199, 200] have measured the dielectric constants of the data Ag_2S in the visible. The real part for instance is completely different from the one of silver (superior to 2.8 between $\lambda = 300-1000$ nm). According to Eq. 4.5.1, a higher effective index (itself function of the index of the particle) would contribute to a red shift of the resonance. Moreover, the silver film is very thin (20 nm, amorphous or

nano-crystalline) and its dielectric constant of the nano-particle array is probably different from the bulk material. The dielectric constant is however complex to determine by ellipsometry and for now, this remains just a hypothesis.

In conclusion, the measurement displays a broadband, multi-resonant (3 peaks) and polarization independent absorption spectrum, accordingly to the simulation. The behavior of each peak can be explained and foreseen by the comparison with the calculated absorption spectra. A few disagreements (potentially beneficial) subsist however due to fabrication difficulties. Further studies are needed to characterize the silver array in order to control perfectly the optical response of the structure.

5.5 Study of the influence of an aluminum-doped zinc oxyde (ZnO:Al) encapsulation layer on the absorption spectrum

5.5.1 Role of the extra ZnO:Al layer

The results of the previous section are really important for the comprehension of the nano-cavity array structure. However, the degradation of silver is a serious candidate to explain one of the disagreements between simulation and experiment. To solve this problem in the future, a 55 nm-thick aluminum-doped zinc oxyde (ZnO:Al) layer is deposited on the samples characterized in the previous section. ZnO:Al is a transparent conducting oxyde (TCO). There is a trade-off to find between good transparency (absorption of light by the free carriers) and proper conduction of the charge by adjusting the doping level. The role of this layer is to act as a:

Protection layer: We have considered each material has ideal, i.e. non-oxidized or non-sulfured. But GaAs and especially silver are subject to a quick chemical reaction at the contact of air. The role of the ZnO:Al layer is to encapsulate the silver array.

Front contact: If sufficiently conductor, ZnO:Al could play the role of a front contact allow the carrier collection via a grid. This is why we are using a doped window layer. Of course, for a proper transport, the TCO layer has to be conductive and thick enough to display a low sheet-resistance. This is however not the first selection criteria in our case

ARC: For our GaAs nano-cavity structure, about 50 % of the light is lost due to reflection below $\lambda = 450\,\text{nm}$ (see the absorption spectra in Fig. 4.4.2). To

reduce this effect, the extra ZnO:Al can be usefull as an ARC in this spectral region.

The anti-reflection effect can be adjusted by a simple quarter wavelength anti-reflection coating model. In this model, the thickness t_{ARC} of the anti-reflection coating is chosen so that the thickness in the dielectric material is one quarter the wavelength of the incoming wave. Therefore:

$$t_{ARC} = \frac{\lambda}{4n_{ARC}} \tag{5.5.1}$$

where λ is the wavelength of the incoming wave and n_{ARC} the real part of the refractive index of the ARC (here ZnO:Al). We therefore have an additional degree of freedom in our optimization process of the nano-cavity array design. The thickness of this layer allows to place a minimum of reflectivity (which can be seen as a fourth resonance peak even though its nature is different) where needed with a single geometrical parameter. This is extremely convenient for the simplicity of our optimization process. Finally, for a cavity that thin, we have seen previously in section 4.6.4 that the spectral shift of this peak is also very limited with the variation of the incident angle.

5.5.2 Optical response of planar ZnO:Al/GaAs/Au samples

The aim of this section is to evaluate the effect of an extra ZnO:layer on the structure. According to Eq. 5.5.1 for a quarter wavelength anti-reflection coating efficient at $\lambda = 400\,\text{nm}$, the thickness of the ZnO:Al layer should be $t_{ZnO:Al} = \frac{\lambda}{4n_{ZnO:Al}} = 52\,\text{nm}$. Experimentally, a 55 nm-thick ZnO:Al layer has been sputtered in the sample of the previous section. First, we study the influence of this layer on the planar stack.

Fig. 5.5.1 represents a comparison between the measured (plain) and simulated (dashed) 1-R spectra for a ZnO:Al/GaAs/Au stack at normal incidence and under unpolarized light. The simulation is made for a 25 nm-thick GaAs layer on a gold mirror and covered by a 55 nm-thick ZnO:Al layer (see inset). The optical data of aluminum-doped zinc oxyde (ZnO:Al) from Ehrmann and Reineke-Koch (Ehrmann2010) in the "bulk ZnO:Al" case. These spectra display both a reflection minimum around $\lambda = 400\,\text{nm}$ that is absent in the case without the ZnO:Al layer (see Fig. 5.4.1): this is the ARC effect. The agreement between simulation and experiment is good around $\lambda = 400\,\text{nm}$ and legitimates the optical data chosen for ZnO:Al.

The Fabry-Pérot resonance in the GaAs still present but resonates at $\lambda = 750\,\text{nm}$ experimentally (instead of$\lambda = 680\,\text{nm}$ in the case without ZnO:Al). Hypothetically, this red shift appears because the upper boundary of the resonator has changed from air to ZnO:Al, increasing the phase of the reflection coefficient.

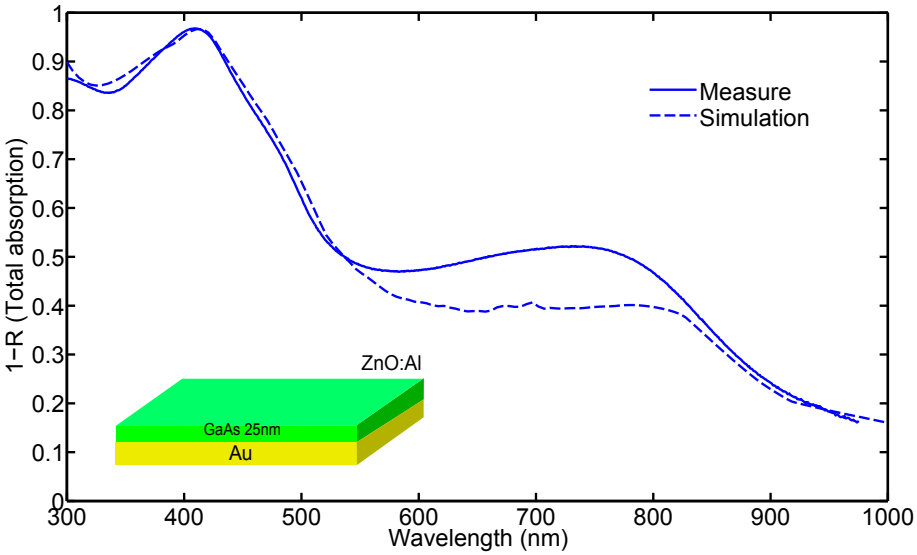

Figure 5.5.1: Comparison between the measured (plain) and simulated (dashed) 1-R spectra for a ZnO:Al/GaAs/Au (55 nm/25 nm/substrate) stack (see inset) at normal incidence and under unpolarized light.

5.5.3 Multi-resonant and broadband total absorption measurement on the encapsulated nano-cavity array demonstrators

We are now analyzing the measurements of the structure, sketched in Fig. 5.2.1 and pictured in Fig. 5.2.6b with the 55 nm-thick ZnO:Al structure. Note that for the samples characterized in this section, the silver array has not been encapsulated directly after lift-off and the silver is already tarnished. The dynamic of this tarnishing is also hard to control, especially in the succession of steps in clean room (metal deposition, lift-off, dielectric deposition).

Fig. 5.5.1 represents in red the (a) measured and (b) calculated 1-R spectrum of the final structure under normal incidence and unpolarized light. This spectrum is compared to the structure without encapsulation (plain black) and to the structure without array and encapsulation (dashed black).

In Fig. 5.5.1, 4 distinct absorption peaks appear clearly on the red curve. Experimentally, this spectrum is independent of the polarization and has mean absorption value of 85 % over the range 200-1200 nm. This is a very interesting value. Nevertheless, as before the 4th absorption peak at $\lambda = 1050$ nm resonates clearly above the band gap of GaAs and need to be re-positioned.

The modification of the spectra with the addition of the ZnO:Al layer in the experimental data is in accordance to the simulation. First, in both figures there is

a decrease of reflectivity around $\lambda = 400\,\text{nm}$ in both spectra. Second, resonance A at $\lambda = 600\,\text{nm}$ stays still while the two other absorption peaks (B and C_3) red shift with the ZnO:Al layer. In the case a the vertical resonances, the Ag/GaAs/Au resonator (resonance A) is not affected by the ZnO:Al and does not shift. For resonance B (vacuum/GaAs/Au), the addition of ZnO:Al modify the condition of resonance and the peak shift like in the previous section. For the MIM resonance, the EM field is extremely strong at the edge of the particle. This is why modifying the environment cause such a difference in the resonance condition.

Resonance C_3 is still experimentally larger than in calculations and resonates about 100 nm red shifted compared to the expected value, probably due to the tarnishing of silver. The quickest solution is therefore to downsize the size of the particle. Another solution is to conceive the same design for another material for a larger gap in wavelength (see for instance GaSb in Chapter 6).

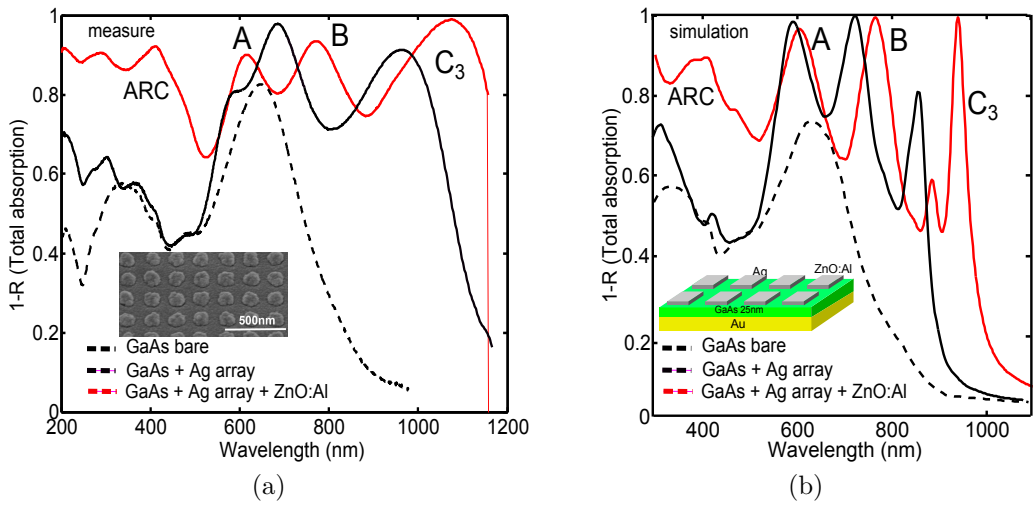

(a) (b)

Figure 5.5.2: Comparison of the (a) measured and (b) calculated 1-R spectrum of the final structure (red) under normal incidence and unpolarized light to the structure without encapsulation (plain black) and to the structure without array and encapsulation (dashed black).

5.5.4 Influence of the width of the particle on the total absorption spectrum and discussion about fabrication tolerance

One of the conclusions in Chapter 4 was that the width of the particle is the key parameter to position the MSM resonance C_3. The goal of this section is to

evaluate experimentally the influence of this parameter.

Fig. 5.5.3 displays the comparison of the experimental 1-R absorption spectrum realized on the 25 nm-thick patterned GaAs sample with an encapsulation layer and different nominal width of the particle: $w = 100$ nm, $w = 120$ nm and $w = 140$ nm

The first thing to see is that obviously the ARC peak and resonances A and B do not shift with the variation of the width of the particle (we can assume that for the $w = 100$ nm case, resonance B is included in resonance C_3). On the contrary, the MSM resonance C_3 shifts towards higher wavelength with increasing width of the particle, confirming both the Fabry-Pérot model and simulations of Chapter 4.

As hinted, a smaller width of the particle of $w = 100$ nm allows to brought the C_3 resonance at $\lambda = 820$ nm, below the gap of the GaAs. Unfortunately, in this case the benefit of resonance B is lost and the absorption intensity a resonance A is decreased. This results in an average absorption in the 200-870 nm range of 84 % for $w = 120$ nm and only 81 % for $w = 100$ nm. The difficulty of optimization is sensible here. A better uniformity of the square particles would be a good idea for comparison to simulation (with a Ge nucleation layer) on to increase our control on the optical response.

The precise statistic of the size of the particle is difficult to obtain. However, if we consider the nominal sizes, the change from $w = 100$ nm to $w = 120$ nm induces a shift of resonance C_3 of $\delta\lambda = 250$ nm in Fig. 5.5.3. This value is smaller in simulation ($\delta\lambda = 125$ nm), hypothetically due to silver tarnishing and the particle homogeneity. We have an order of magnitude of the degree of tolerance for our design ($\tau = 12.5$ nm/nm). Fortunately, this tolerance is smaller than the FWHM of our resonance peak. Moreover, a resolution of 1 nm is easily reachable for a decently optimized EBL/lift off process, past the nucleation of silver problem.

5.5.5 Influence of the incident light angle on the total absorption spectrum

With our setup, measuring the 1-R spectrum as a function of the incident light angle is possible. Angle-independence is a important criteria for an efficient light trapping structure. Fig. 5.5.4 displays the measured 1-R (total absorption) spectra on the 25 nm-thick GaAs sample with $w = 120$ nm as a function of the incident light angle. Remarkably, the absorption spectra is almost perfectly angle independent up to 45 °, regardless of the polarization and in accordance with simulation. Above this value, the size of the spot becomes too important compared to the size of the array to have a correct measurement.

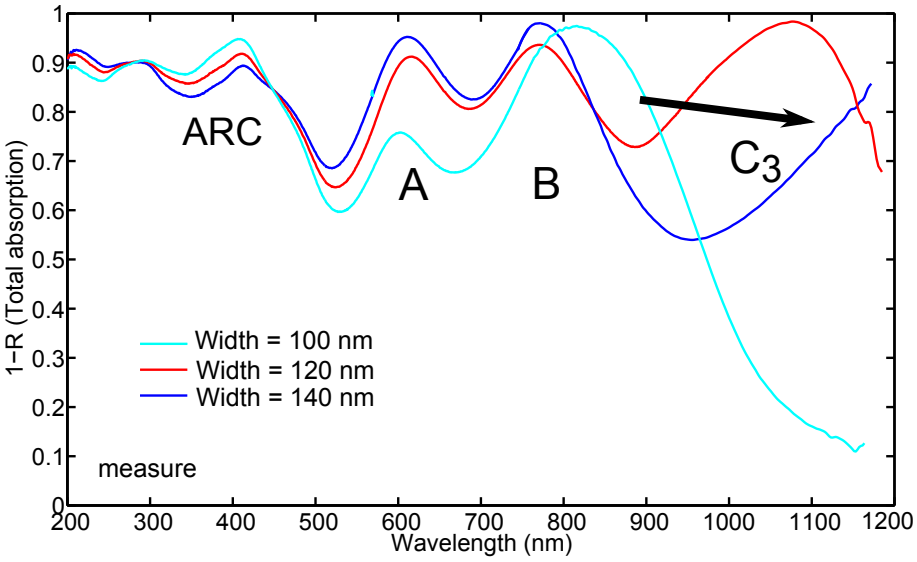

Figure 5.5.3: Comparison of the measured 1-R absorption spectrum realized on the 25 nm-thick patterned GaAs samples with an encapsulation layer and different nominal width of the particle: $w = 100$ nm (cyan), $w = 120$ nm (red) and $w = 140$ nm (blue).

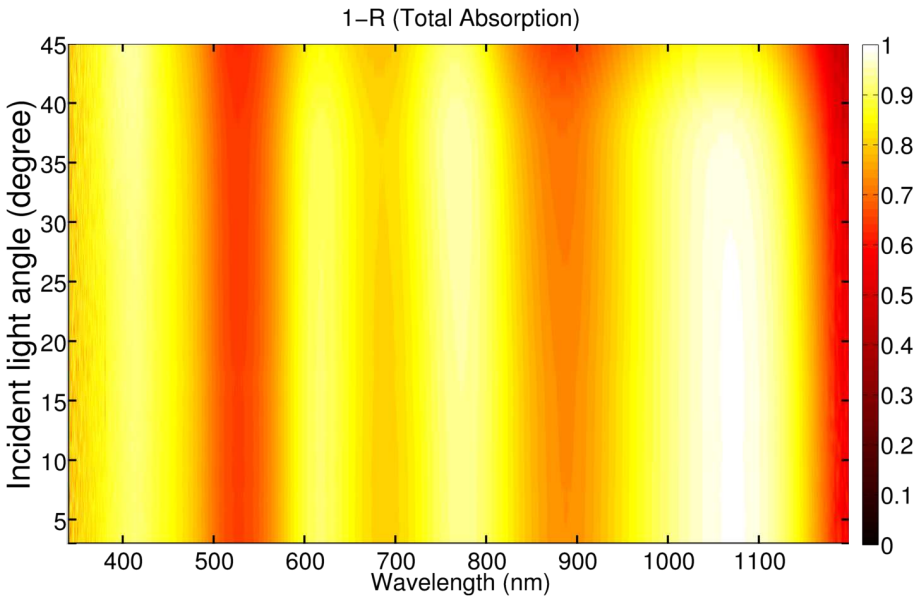

Figure 5.5.4: Measured 1-R (total absorption) spectra on the 25-nm thick GaAs sample with $w = 120$ nm as a function of the incident angle under unpolarized light.

5.5.6 Comparison to literature

For now, we have enlightened the faculty of our structure to absorb light on a large spectrum in the visible region. The discrimination between total absorption and absorption in GaAs is not done experimentally. In this section, we compare the performance of our structure to papers of the literature.

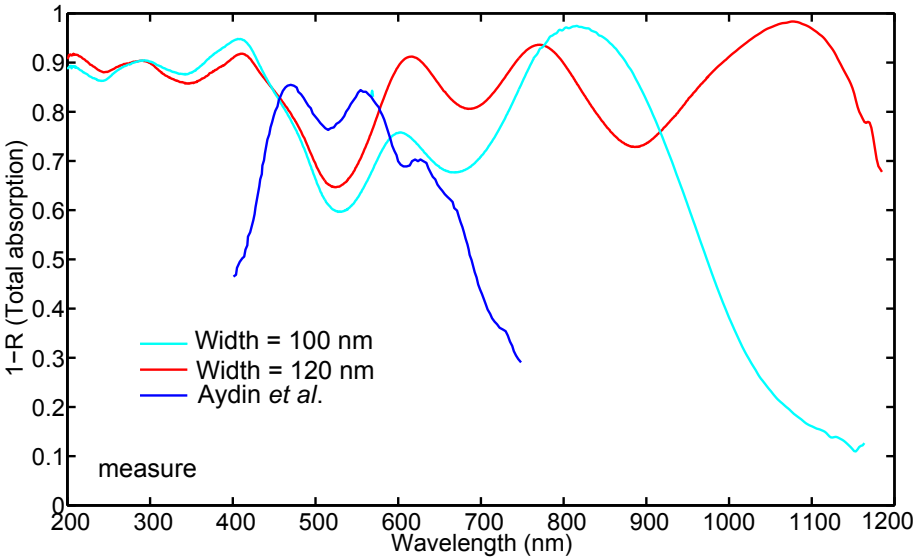

Figure 5.5.5: Comparison of the measured 1-R absorption spectra of Aydin and Atwater [174] at normal incidence (blue) compared to the previous spectra plotted in Fig. 5.5.3 (25 nm-thick patterned GaAs samples with an encapsulation layer and different nominal width of the particle: $w = 100$ nm (cyan) and $w = 120$ nm (red).

As stated in Chapter 3, one of the paper closest in structure and principle to our nano-cavity array design is the proposition of Aydin and Atwater [174] represented in Fig. 3.2.3c. In their case, the structure is a silver array (100 nm-thick) / SiO_2(60 nm-thick) / silver mirror stacking. The structure is similar to our own, except for the type of patterning (and therefore the type of nanophotonic mechanisms) and for the fact that the absorption takes place exclusively in metal. After fabrication and measurement, they have achieved a state-of-the-art average measured total absorption between 400 and 700 nm of 71 %.

Fig. 5.5.5 represents comparison of the 1-R spectra of Aydin and Atwater at normal incidence compared to the previous spectra plotted in Fig. 5.5.3 ($w = 100$ nm and $w = 120$ nm). In the 400-700 nm, our sample ($w = 120$ nm) displays an average absorption of 80 %, (i.e. 9 % more than the state-of-the-art value). The absorption is however locally lower around $\lambda = 500$ nm. On the other hand, our

sample displays a 85 % average absorption in the $\lambda = 200 - 1200$ nm range, that is to say thrice the range of the measurement of Aydin and Atwater.

Our measurement also brought a new element as the structure already contains (experimentally and theoretically) a semi-conductor that absorb light for potential charge separation (although the amount of light absorbed in GaAs cannot be determined by other means than simulation).

5.6 Conclusion

In conclusion, optical proofs of concept of the 25 nm-thick GaAs design have been fabricated and characterized. Several process steps have been specially developed and are now well mastered (transfer of a 25 nm-thick crystalline GaAs layer on gold miror). Yet, the fabrication process is delicate and would probably need more optimization for a cleaner comprehension of the structure through confrontation with simulation. In particular, the optical data of silver remains an uncertainty, either because our sample is tarnished and need a quicker encapsulation or because the properties of the nanoparticles are different from bulk Ag, or both. Second, a Ge nucleation layer should be included in future runs. However, its effect (the degradation, more likely) on the absorption spectrum needs to be carefully evaluated numerically.

Still, the $w = 120$ nm sample displays impressive results in terms of broadband multi-resonant, angle and polarization independent total absorption spectrum. The average absorption is of 85 % in the 200-1200 nm range for incident angle up to 50 ° in both polarization, a performance well above the state-of-the-art in this domain. Moreover, the experimental behavior of the spectrum is in quantitative agreement with the simulation, confirming the models and hypothesis developed in Chapter 4. This optical proof a concept is extremely encouraging in terms of novel solution light management for ultra-thin devices. The results achieved in terms of comprehension and performances meet the needs and the objectives of ultra-thin solar cells.

One could say that the absorption spectrum is in the end not extremely well adapted to GaAs as one absorption peak resonates above the band gap of the material. The structure could indeed benefit of a re-run and a slight re-optimization of the geometrical parameters and an amelioration of some of the process steps. However, these imperfections have led to beneficial effects such as the broadening of the absorption peaks. In conclusion of Chapter 4, we have make the hypothesis that the symmetry breaking of the structure and to have randomly shaped particles would be an improvement in terms of performances (see for instance the work of Aydin *et al.* Aydin et al. [174] and trapezoidal particles).

Finally, GaAs was our ideal test material. In the present state of the GaAs PV

technology, it is unlikely to conceive such ultra-thin devices that would sacrifice to much the efficiencies. Nevertheless, this really broad absorption spectrum and the possibilities it brings can be adapted to materials that have a larger gap such as CIGS and GaSb (hot carrier solar cells) that have specific needs. This is the subject of Chapter 6. The very promising performances of this structure in terms of broadband absorption is also an additional motivation towards a more fundamental study of truly ultra-thin devices, (new junctions for PV, photodetectors or thin-film thermal emitters).

Still, many challenges remain to go further toward ultra-thin solar cells. First, some technological aspects are to be optimized or developed: the simplest and most robust layer transfer of each materials on a silver substrate if possible and the control of the degradation and diffusion of silver for instance. However, the main challenge lies now in the fact to have actual working devices and optoelectronic characterizations of nanophotonic enhanced ultra-thin crystalline solar cells. From the beginning of this manuscript, the ultra-thin structure was designed first for its optical performances. The optimization have led to a geometry (thickness = 25 nm) not compatible with a correct functioning of a junction as we control it today.

The tasks remaining to be done are a matter of compromise. What is the minimal thickness for a working junction? Should we select a p-i-n junction or a new, thinner design of charge separation? Is silver a viable option in a solar cell structure from an electronic point of view? Many questions need to be answered. Once the electronic structure is fixed, a re-optimization of the light-management is necessary. A coupled optical and transport simulation would be a good start to select the structure that is the best compromise between optical and electronic properties (see for instance the work of Deceglie *et al.* [185] on the design of nano-structured solar cells using coupled optical and electrical modeling).

We have attempted to go further on the understatement of this structure with several optoelctronic characterizations. Amongst other, we have realized photoluminescence excitation measurement in order to evaluate the absorption in the GaAs layer. However, no clear conclusion has emerged from these characterizations, probably because of the ultra-thin nature of our device. Yet, the study of nano-structured improved ultra-thin GaAs devices continues at LPN. This study now represents the most part of the Ph.D of Nicolas Vandamme, arrived 1 year and half after the beginning of my own thesis.

In our case, in the dynamic of the ANR ULTRACIS, we have focused on ultra-thin CIGS devices. In the next chapter, we propose an application of these light management concepts to CIGS solar cells along with GaSb. In Chapter 7, we are interested in the fabrication and characterization of working CIGS devices improved by nanophotonic light management in the 100-200 nm thickness range.

Chapter 6

Light-trapping in ultra-thin crystalline solar cells: application to GaSb and CIGS

Outline

6.1 Introduction 124
6.2 Application to GaSb and hot carrier solar cells 126
6.2.1 Motivation: opportunities and challenges in hot carrier solar cells 126
6.2.2 Efficient light confinement in a 25 nm-thick GaSb structure 127
6.2.2.1 Optimized simulated structure 127
6.2.2.2 Absorption spectrum simulation 128
6.2.2.3 Absorption peaks analysis 129
6.2.2.4 Study of the angular dependence 131
6.2.3 Performances as a hot carrier solar cell and conclusion . . . 132
6.3 Application to CIGS and low-cost, efficient thin-film solar cells . . . 134
6.3.1 Introduction 134
6.3.2 Generalities about numerical calculations on CIGS 134
6.3.3 Reference planar CIGS solar cell 135
6.3.4 Nearly perfect absorption in a 45 nm-thick CIGS layer with a nano-cavity array design 137
6.3.4.1 Simulated absorption spectrum 138
6.3.4.2 Electromagnetic field intensity maps analysis . . . 140
6.3.5 Geometrical parametric study 141
6.3.5.1 Study of the angular and polarization dependence . 143
6.3.5.2 Performances and conclusion 144

6.4 Toward a complete CIGS solar cell: 100 nm-thick CIGS nano-cavity array solar cell . . . 145
6.4.1 Presentation and discussion about the ultra-thin CIGS solar cell . . . 146
6.4.2 Broadband absorption enhancement in the 100 nm-thick CIGS structure . . . 147
6.4.3 Study of the angular dependence . . . 149
6.4.4 Replacing the buffer layer: from CdS to ZnS . . . 149
6.4.5 Conclusion . . . 150
6.5 Back nano-structured CIGS solar cells . . . 151
6.5.1 Introduction . . . 151
6.5.2 150 nm-thick Back nano-structured CIGS solar cell . . . 152
6.5.2.1 Simulated structure . . . 152
6.5.2.2 Simulated absorption spectrum . . . 153
6.5.2.3 Balance of the optical losses in the cell . . . 154
6.5.2.4 Magnetic intensity maps . . . 155
6.5.2.5 Influence of the period . . . 156
6.5.2.6 Influence of the angle of incidence . . . 156
6.5.3 Optimization of the short circuit current for different thickness of CIGS . . . 157
6.5.3.1 Conclusion on the back structure . . . 158
6.6 Conclusion and perspectives . . . 159

6.1 Introduction

With the knowledge about the nano-cavity array design developed in the case of GaAs, a next step is to apply this idea to other materials of the PV technology. The aim is to prove the versatility of the structure and to potentially solve dedicated issues on specific solar cell technologies or concepts. To make use of the full potential of the nano-cavity design, the thickness of the absorber should be ultra-thin (< 100 nm) as seen before. Therefore, we investigate in this manuscript materials of thin-films technology that displays absorption coefficient in the same order of magnitude as GaAs. Here, we are interested in two different materials: crystalline GaSb semiconductor for hot-carrier solar cell applications, and CIGS poly-crystalline chalcopyrite for thin-film photovoltaic applications.

Fig. 6.1.1 compares the real part of the refractive index of GaAs, CIGS and GaSb and Fig. 6.1.2 compares their absorption depth $d = 1/\alpha = \frac{\lambda}{4\pi k}$. We use here the optical data of Palik for cubic GaAs and cubic GaSb [69] and Orgassa (x=0.23)

for CIGS [201]. The refractive indices range from 3 to 5. The absorption depths $d = 1/\alpha = \frac{\lambda}{4\pi k}$ of the three materials are equal ($d \approx 50\,\text{nm}$) around $\lambda = 450\,\text{nm}$.

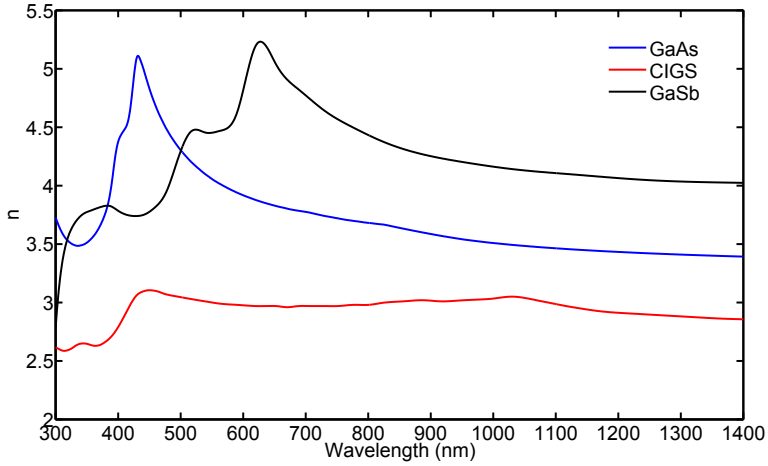

Figure 6.1.1: Comparison of the real part of the refractive index of GaAs (blue), CIGS (red) and GaSb (black).

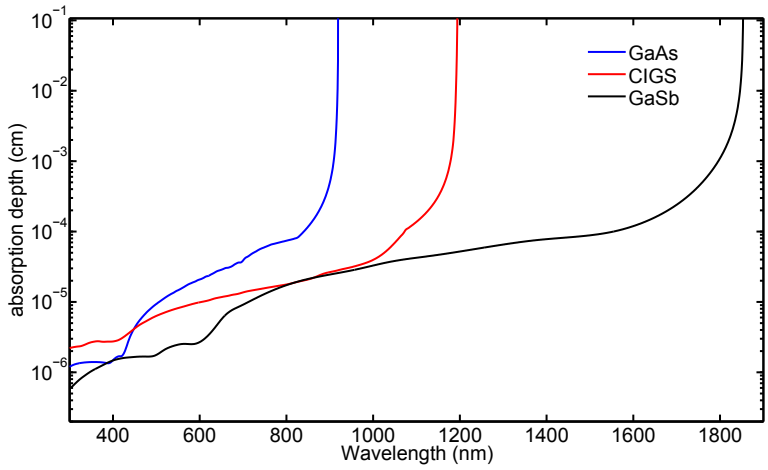

Figure 6.1.2: Comparison of the absorption depth of GaAs (blue), CIGS (red) and GaSb (black).

This chapter first presents a structure designed for broadband absorption in ultra-thin GaSb layer in the frame of hot carrier solar cell. The second part of this chapter provides solutions for CIGS solar cells, a thin-film solar cell technology displaying very high efficiencies. In the case of CIGS, the MSM nano-cavity structure is first studied for a sole CIGS layer and then for a more complete solar cell. Eventually, considering the difficulty to conceive a CIGS solar cell thinner

than 100 nm-thick, an alternative light management solution included in the back contact is proposed for thicker and effective CIGS solar cell in the 200-400 nm range: a back mirror nano-structure.

6.2 Application to GaSb and hot carrier solar cells

The aim of this section is to apply the nano-cavity design to gallium antimonide (GaSb) solar cells that are a serious candidate for hot carrier solar cells (relatively low band gap in energy) [64].

6.2.1 Motivation: opportunities and challenges in hot carrier solar cells

In most efficient photovoltaic devices, at least 40 % of the incident power is lost as heat dissipation. The hot carrier solar cell was proposed as a promising concept to limit such losses by converting most of the residual heat into electricity. This concept enables notably a conversion efficiency exceeding the Shockley-Queisser limit [18]. Upon solar photon absorption, photo-generated electron-hole pairs gain an excess kinetic energy over their thermal average. The efficiency enhancement results from the conversion of this excess kinetic energy, normally lost as heat because of carrier thermalization, into electrical work. In this case, the collected energy per extracted electron-hole pair is larger than the band-gap energy, and the conversion efficiency is increased. The dominant carrier energy loss mechanism in polar semiconductors is the emission of longitudinal optical (LO) phonons that occurs at a subpicosecond time scale. A reduction of the carrier cooling rate is necessary to allow the formation of an out of equilibrium steady state carrier distribution. It has been demonstrated experimentally that the carrier cooling rate could be reduced in high injection regime [202, 203], thanks to a LO phonon bottleneck phenomenon [204]. Thus, an increased carrier density can lead to a higher carrier temperature population and therefore to a higher cell efficiency. A small material thickness would also be beneficial to allow very fast extraction of carriers from the absorber before they interact with lattice vibrations. The importance of an efficient light concentration in an ultra-thin GaSb layer is therefore extremely important.

We present here the results on a hot carrier solar cell study with an architecture with semi selective contacts (see Fig. 6.2.1) studied by Arthur Le Bris and Jean-François Guillemoles [64, 65]. This manuscript focuses on the light-trapping part of this study. This collaboration has been done is the frame of the THRIPV ANR. We demonstrate here a mandatory milestone toward a feasible GaSb hot carrier

solar cell: efficient absorption of light in an ultra-thin (25 nm-thick) GaSb layer to reach a high injection regime.

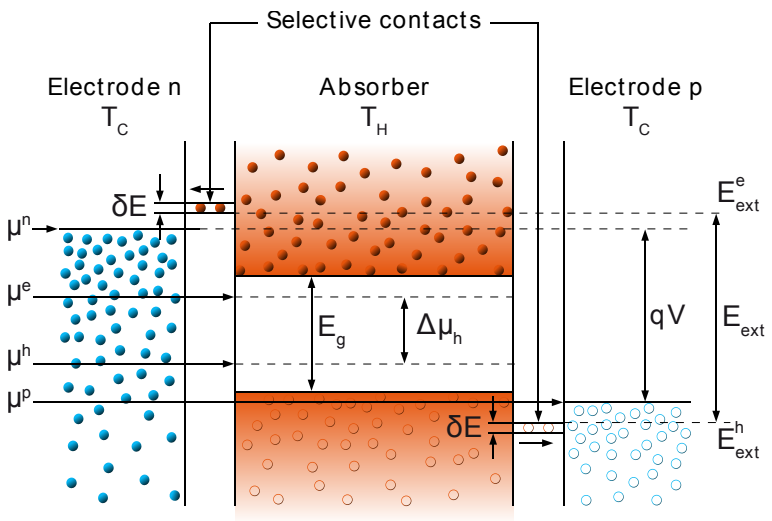

Figure 6.2.1: Schematic band diagram of a hot carrier solar cell. The non-equilibrium photo-generated electron and hole populations at a hot temperature T_H in the absorber are extracted through energy selective contacts, having a transmission range δE, towards electrodes at a cold temperature T_C. The energy collected per extracted electron-hole pair is E_{ext}. The quasi Fermi level splitting in the absorber is $\Delta\mu_H$, and the output voltage is V. qV is limited by E_{ext} and can be larger than the absorber band gap E_G. Figure from Le Bris *et al.* [65]

6.2.2 Efficient light confinement in a 25 nm-thick GaSb structure

6.2.2.1 Optimized simulated structure

We consider a design similar to the 2D GaAs structure. It consists in a 25 nm-thick GaSb layer on a silver mirror, covered by a two-dimensional array of silver square nanoparticles (thickness $t_{array} = 26$ nm, width $w = 170$ nm, period $p = 300$ nm) and a 50 nm-thick n-type ZnO:Al window layer (i.e a 76 nm-thick ZnO:Al in total), as described in Fig. 6.2.2. The selective contacts of the hot carrier solar cell are not included in this optical simulation, but we can assume that they can be optically decoupled from the sub-wavelength arrays.

For the upcoming simulations, we use the following refractive indices:

- silver (Ag) from Johnson and Christy [183].
- Cubic gallium antimonide (c-GaSb) from Palik [69].
- Aluminum-doped zinc oxyde (ZnO:Al) from Ehrmann and Reineke-Koch [205] in the "bulk ZnO:Al" case.

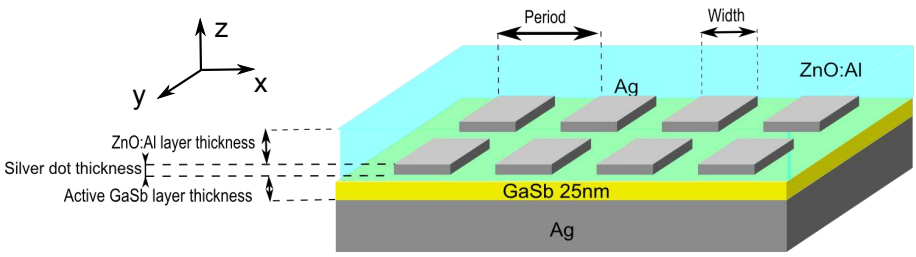

Figure 6.2.2: Schematic of the 25 nm-thick GaSb solar cell. It consists in a 25 nm-thick GaSb layer on a silver mirror, covered by a two-dimensional array of silver square nanoparticles (thickness $t_{array} = 26$ nm, width $w = 170$ nm, period $p = 300$ nm) and a 50 nm-thick n-type ZnO:Al window layer.

6.2.2.2 Absorption spectrum simulation

The absorption spectrum of the 2D 25 nm-thick GaSb structure is plotted in Fig. 6.2.3. The blue and red curves represent the total absorption and the absorption in GaSb, respectively. The difference between these two curves represents the absorption in the metal or in the ZnO:Al layer (mostly below $\lambda = 400$ nm here). The gray curve represents the normalized spectral density of AM1.5G solar spectrum. The black curve represents absorption in the a 25 nm-thick GaSb layer with no silver array.

The absorption spectrum is similar to the experimental 25 nm-thick GaAs structure: there are four clear absorption peaks ($\lambda = 550$ nm, $\lambda = 740$ nm, $\lambda = 900$ nm and $\lambda = 1090$ nm) that spread over the 400nm-1100 nm range. In this region, the absorption is very high, above 70 %, and the absorption spectrum fit closely to the maximum of the solar spectrum density. There is a very low absorption in the metal in the whole wavelength range (< 15 %). The window layer absorbs almost all the incident light below $\lambda = 450$ nm.

Compared to the black curve, the red curve displays a sensibly higher absorption above $\lambda = 600$ nm due to the array. The theoretical short-circuit current is increased from $J_{th} = 27.8$ mA/cm^2 to $J_{th} = 36.7$ mA/cm^2 with the array at normal incidence, representing a 30 % enhancement.

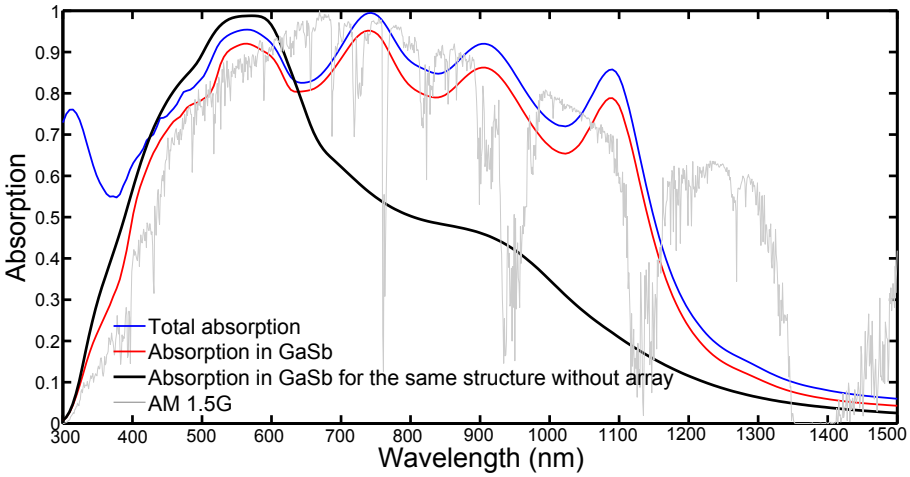

Figure 6.2.3: Simulated absorption spectra of the 25nm-thick GaSb solar cell. The blue and red curves represent the total absorption and the absorption in GaSb, respectively. The black curve represents the absorption in the same structure without the array. The gray curve represents the normalized spectral density of AM1.5G solar spectrum.

6.2.2.3 Absorption peaks analysis

In this paragraph, we study the magnetic field intensity maps of the four peaks of the 25 nm-thick GaSb absorption spectrum. In Fig. 6.2.4 is represented the magnetic field intensity maps of the four peaks of the GaSb design:

- Resonance at $\lambda_1 = 550\,\text{nm}$ displays a localized field in the ZnO:Al layer. It corresponds to the ARC effect with a thickness of the ZnO:Al layer of $t_{ARC} = 72\,\text{nm}$ according to Eq. 5.5.1. This in accordance with our structure.

- Resonance at $\lambda_2 = 740\,\text{nm}$ displays a map a bit more complicated. We can see the same feature than resonance 1 above the particle and than resonance 3 with the maximum of the magnetic field localized between (and not under) the particle. If we remove the contribution of these two resonances, the signature of this map is a maximum of the magnetic field localized below the metallic particle. This is similar to resonance A of the 25 nm-thick GaAs structure with a single horizontal lobe in the GaSb layer. The resonance is tunable with the GaSb thickness and is attributed to a vertical Fabry-Perot resonator in the GaSb layer.

- Resonance at $\lambda_3 = 900\,\text{nm}$ displays a map that is very similar to resonance B of the 25 nm-thick GaAs structure with a single horizontal lobe in the GaSb

layer. The resonance is tunable with the GaSb thickness and is attributed to a vertical Fabry-Perot resonator in the GaSb layer.

- Resonance at $\lambda_4 = 1090\,\text{nm}$ displays a map with three vertical lobes below the silver particle. It is spectrally tunable with the width of the particle and matches the characteristic of the MSM resonance.

The maps and mechanisms display strong similitude with the corresponding peaks (sorted in wavelength) in the 25 nm-thick GaAs design. Based on these observations, we assume that the mechanisms are similar. It remains a small uncertainty for resonance 2. However, the global behavior is very similar to the GaAs structure and for further details about these resonances, refer to the 25 nm-thick GaAs design. Additional electromagnetic field intensity maps are provided in the appendix.

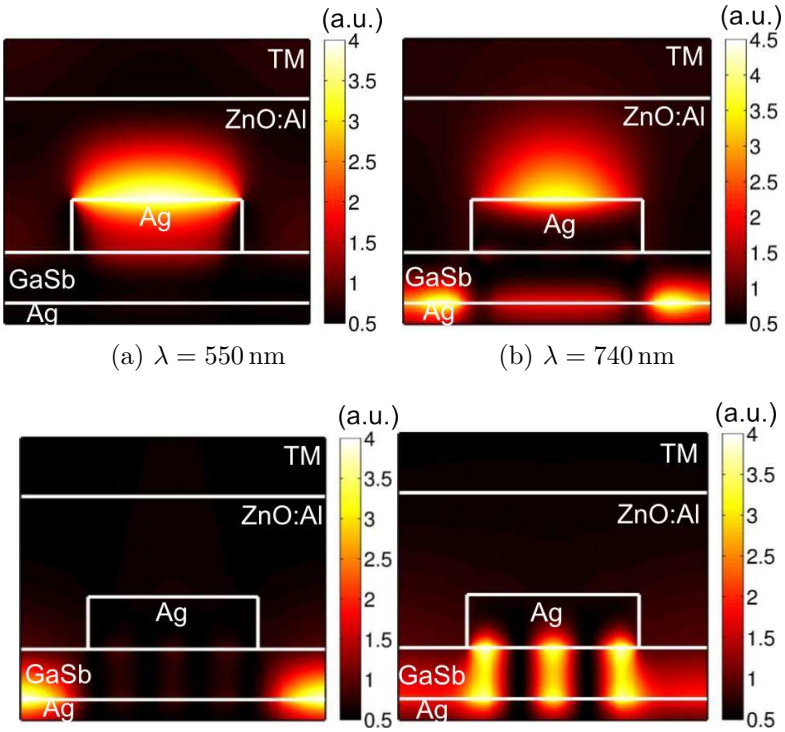

(a) $\lambda = 550\,\text{nm}$ (b) $\lambda = 740\,\text{nm}$

(c) $\lambda = 900\,\text{nm}$ (d) $\lambda = 1090\,\text{nm}$

Figure 6.2.4: Magnetic field $|\text{H}|^2$ intensity maps plotted in the plane perpendicular to the magnetic field (TM polar) at (a) 540 nm (b) 720 nm (c) 900 nm and (d) 1090 nm, calculated at normal incidence for the figure depicted in Fig. 6.2.2.

6.2.2.4 Study of the angular dependence

Fig. 6.2.5 represents the GaSb absorption of the GaSb structure as the function of the incident angle and the wavelength in TM polarization. Up to an incident light angle of 45 °, the absorption spectrum is independent of the incident angle. The only notable change is the expected apparition of the second-order of the MSM resonator for non-normal incidence that now resonates under the gap of the GaSb at $\lambda = 1450$ nm. This contributes to an additional increase of the short-circuit current. This figure is once again very similar to the GaAs case (Fig. 4.6.7). However, we know from the GaAs structure that the second order of the MSM resonance does not appear in TE resonance. Nevertheless, the TE absorption spectrum is also independent of the angle of incidence.

Fig. 6.2.6 represents the angular diagram of the theoretical short circuit current (in mA/cm²) for the 2D 25nm-thick GaSb structure as a function of the incident light angle (in degree), averaged over both TE and TM polarization. We can see that when moving away from the normal incidence, the theoretical short-circuit current increases a little (we have a short circuit current of $J_{th} = 36.7\,\mathrm{mA/cm^2}$ at $\theta = 0\,°$ and a short circuit current of $J_{th} = 37.7\,\mathrm{mA/cm^2}$ at $\theta = 45\,°$). The theoretical short-circuit current is in average conserved up to a 60 ° angle.

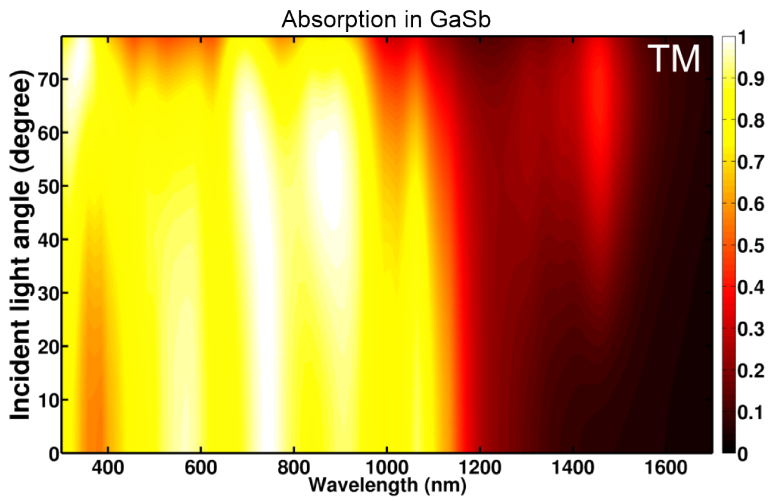

Figure 6.2.5: GaSb absorption of the GaSb structure as the function of the incident angle and the wavelength in TM polarization.

Hot carrier structures are to function under concentration. Determining the highest angle of incidence conceivable without a drop in short-circuit current allows to determine the highest possible concentration. The concentration is given by $(NA/\sin(\theta_0))^2$, where NA is the numerical aperture of the lens, and $\theta_0 = 0.26\,°$ is the half angle of the cone under which the sun is viewed from Earth without

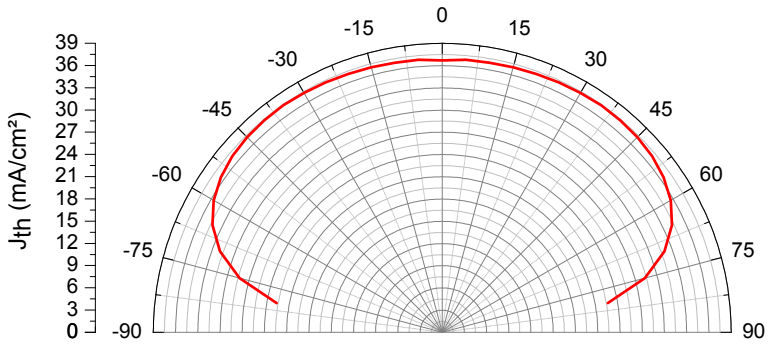

Figure 6.2.6: Angular display of the theoretical short circuit current (in mA/cm²) for the 2D 25nm-thick GaSb structure in function of the incident light angle (in degree) averaged over both TE and TM polarization.

concentration. We also express our results in terms of fraction of absorbed power compared to the power available from the spectrum AM1.5D (Direct for concentration) under the gap of GaSb. Fig. 6.2.7 represents the fraction of absorbed power as a function of the concentration. Our structure leads to an average absorption of 68 % of the power up to a concentration factor of 35000 suns.

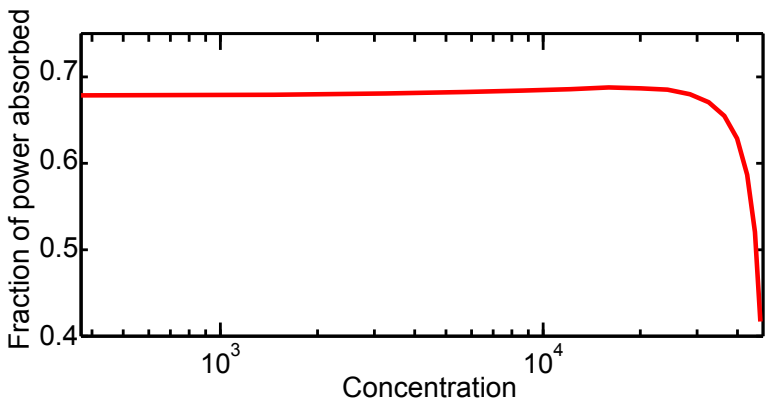

Figure 6.2.7: Fraction of the concentrated AM1.5G spectrum power fluxes that is absorbed with the nano-cavity array design 25 nm-thick GaSb structure, as a function of the concentration in number of suns. Values are given for an unpolarized light.

6.2.3 Performances as a hot carrier solar cell and conclusion

We have seen that a large amount of photons is absorbed over the solar spectrum and that regardless of the angle of incidence. As a result of design optimization, about 60 % of the incident photons available above the gap of GaSb in energy are

absorbed. It leads to an absorption of 68 % of the power available in the gap of GaSb up to a concentration factor of 35.000 sun. The metallic array improves therefore significantly (about 50%) the absorption compared to a simple 25 nm-thick GaSb layer on a silver back mirror.

Le Bris *et al.* [65] have shown that, with the absorption calculated above for the considered structure, one can simulate the potential efficiency of theoretical hot carrier solar cells. For this particular solution of light trapping, the efficiency could reach up to 38 % efficiency (the details of the calculations are given in ref. [65]). This high value is obtained thanks to a very high absorption in a very small volume (better extraction of the hot carriers before thermalization).

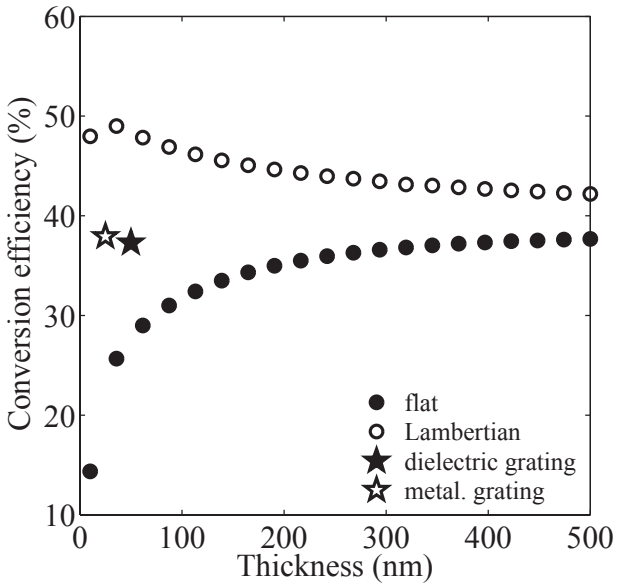

Figure 6.2.8: Conversion efficiency as a function of the absorber thickness for a flat absorber (filled circles) and in the Lambertian limit (empty circles). The efficiency is found to monotonously decrease with the absorber thickness in the case of a flat absorber, but an optimal thickness of about 50 nm is absorbed, giving a maximal efficiency of 55%, in the Lambertian limit. The efficiencies obtained with the dielectric grating (filled star, from Esteban *et al.*[123]) and with the nano-cavity array design («metallic grating», empty star) are also reported. This figure is taken from Le Bris *et al.* [65].

Fig. 6.2.8, taken from the paper of Le Bris *et al.* [65], displays the comparison of different light-trapping solution and the impact in conversion efficiency for a hot carrier solar cell with semi-selective contact. Our 25 nm-thick GaSb design with nano-cavities array design is compared in particular to a 50 nm-thick GaSb

with dielectric grating (from Esteban *et al.*[123], see chapter 2) and to the perfect lambertian limit. Our design displays a higher efficiency than for the dielectric design despite similar optical average absorption: this is due to the twice thinner GaSb layer. Moreover, our design has the advantage to be more practical from a technological point of view (an even relatively simple) over the dielectric design and the perfect lambertian limit. This is therefore a good choice to pursue the study of ultra-thin hot carrier solar cells in GaSb and derivatives.

In conclusion, we have applied successfully the nano-cavity array design to a 25 nm-thick GaSb layer. The absorption spectrum behaves similarly to the GaAs design. The excellent optical performances of this structure (68 % of the power available absorbed) allow to conceive further experimental study of hot carrier structures.

6.3 Application to CIGS and low-cost, efficient thin-film solar cells

6.3.1 Introduction

Among potential candidates, CIGS is one of the most promising material in the thin-film PV technology with the high achieved efficiency and relative low cost compared to crystalline technologies. It is also a technology that needs a thickness reduction due to the indium issue. However, novel light management research is just beginning for CIGS as the priority is still given to material and device studies. Nevertheless, the CIGS community is eager for new approaches considering the stakes.

The study of structure of the complete CIGS solar cell is more complex to replace the active material from GaAs to CIGS for instance. The hetero-junction (classically CIGS/CdS/i-ZnO/ZnO:Al) is mandatory for the band alignment and a correct extraction of the charges. However, it complicates our optical study compared to the previous cases. In a (nano-)photonic point of view, having several contrasts of optical indices in the same stack will complicate the understanding of the electromagnetic modes. This is why, to have a progressive approach, we are studying first in this part the potential of periodic nano-structures to confine light absorption in a unique thin-film of CIGS. A similar study of a more complete CIGS solar cell will be made later in Part 6.4.

6.3.2 Generalities about numerical calculations on CIGS

There is few available optical data for $CuIn_{1-x}Ga_xSe_2$. They are incomplete/imprecise since the CIGS is hard to characterize (roughness complicating ellipsometry) and

since there are several deposition conditions and methods. Here we are using the following refractive indices: glass will be taken as a homogenous medium with n = 1.5; CIGSe from Paulson *et al.* [206] in the case $x = 0.31$ below the gap in wavelength and linear interpolation of the data of Orgassa *and al.* *[201]* in the case $x = 0.23$ otherwise (therefore, we consider an optical gap for our CIGS lying around $\lambda = 1200$ nm); ZnO:Al from Ehrmann and Reineke-Koch [205] in the "bulk ZnO:Al" case; i-ZnO is taken as an homogeneous medium with n = 2; CdS is taken from Khawaja *et al.* [207] in the case "thin evaporated films of cadmium sulphide"; Mo mirror (measured with the MoSe2 interface by ellipsometry) is taken from Erfurth *et al.*[86]; gold and silver from Johnson and Christy [175]. We have chosen this particular range of gallium content in our simulation as it is close to the effective gallium content of our samples (see Chapter 7). A justification about the optical indices and the calculation method can be found in the appendix.

The aim of this part is to simulate optically ideal ultra-thin CIGS structure (< 100 nm). Therefore, we are assuming two strong approximations: we consider here no gallium grading in the CIGS layer and assume that all interface are perfectly flat. This is imposed by the nature of the structure (no roughness greater than the effective thickness of the CIGS layer for a continuous film). This lead for instance to interference effects in the absorption spectra that are absent from measurements and calculation assuming that the phase coherence of light is lost in the structure. Further discussions on the technological feasibility are given in Chapter 7.

6.3.3 Reference planar CIGS solar cell

We study here reference planar CIGS solar cells. The cell is modeled with a glass encapsulation (upper medium), a 400 nm-thick ZnO:Al layer, a 70 nm i-ZnO layer, a 50 nm-thick CdS buffer layer, a CIGS absorber layer with variable thickness and a back contact. This simulated structure is depicted in Fig. 6.3.1. We first study numerically the impact of the CIGS layer thickness and alternative back contacts (from Mo to Au and Ag) on the performances of CIGS solar cells.

The absorption spectra of the planar reference solar cell with Mo back contact are shown in Fig. 6.3.3a. The absorption spectrum in the CIGS layer (active absorption) is plotted for CIGS thicknesses varying from 2 µm to 0.045 µm. The Table 6.1 gives the value of the theoretical short-circuit current of each of these spectra. When the thickness of the absorber decreases below 500 nm, the absorption and therefore the theoretical short-circuit current density (J_{th}) drop significantly from $J_{th} = 39\,\mathrm{mA/cm^2}$ for 2 µm of CIGS to $J_{th} = 12.5\,\mathrm{mA/cm^2}$ for 45 nm of CIGS (meaning a drop of 210 %; see also Jehl *et al.*[81]). This is easily explained as the light path diminishes and the non-absorption losses rise.

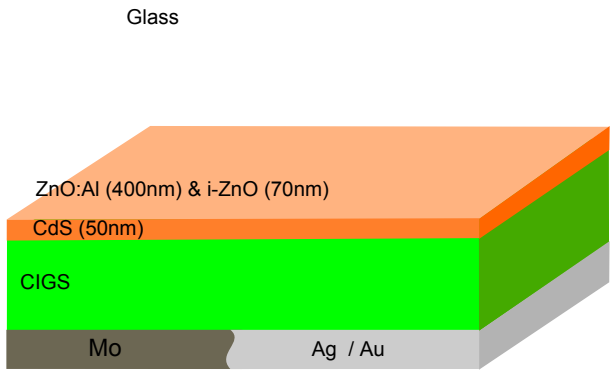

Figure 6.3.1: Schematic of the reference planar CIGS solar cell. The simulated solar cell is composed of a glass encapsulation, a 400 nm-thick ZnO:Al layer, a 70 nm i-ZnO layer, a 50 nm-thick CdS buffer layer, a CIGS layer with variable thickness and either a Mo, Ag or Au back contact.

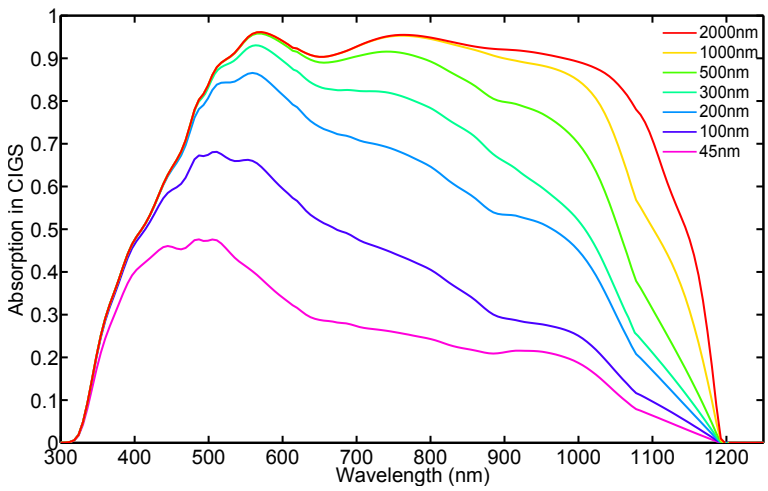

Figure 6.3.2

Figure 6.3.3: (a) CIGS absorption spectrum for conventional CIGS solar cells with decreasing thickness of the CIGS layer and Mo back contact (as depicted in Fig. 6.3.1).

Molybdenum is a bad reflector for the visible wavelengths. Part of the light is not reflected but absorbed in the metallic layer. To illustrate this, we calculate the Fresnel coefficient for reflection (Eq. 2.2.1) for a CIGS/Mo interface with our indices at $\lambda = 800\,\text{nm}$ (a wavelength where the absorption depth becomes important: $d = 1.8\,\mu\text{m}$): $R_{CIGS/Mo} \approx 14\,\%$. This means, if the CIGSe thickness is inferior to $2\,\mu\text{m}$, that 86 % of the light reaching the back contact is lost, absorbed

at the Mo interface.

This value stresses the importance to change the back mirror for applications to ultra-thin solar cells. However, it is interesting to point out that the absorption of a 1 µm-thick CIGS solar cell remains relatively high, giving a short-circuit current of $J_{th} = 37.7\,\mathrm{mA/cm^2}$.

Fig. 6.3.4a shows the absorption spectra of the planar reference solar cell with (a) silver back contact and (b) with gold back contact. Silver and gold are two of the most reflective metal for CIGS in the visible range ($R_{CIGS/Ag} \approx 80\,\%$ and $R_{CIGS/Au} \approx 76\,\%$ at $\lambda = 800\,\mathrm{nm}$ respectively). Table 6.1 shows the calculated theoretical short-circuit current for the spectra of these reference solar cells.

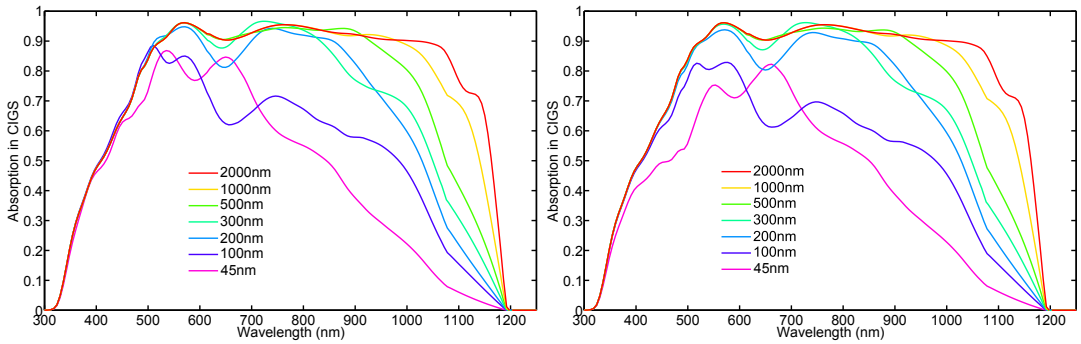

(a) Silver (b) Gold

Figure 6.3.4: CIGS absorption spectra for conventional CIGS solar cells with decreasing thicknesses for (a) Ag back contact and (b) Au back contacts (as depicted in Fig. 6.3.1).

In that case, the absorption spectra for the 200 nm-thick CIGS solar cell is for instance higher for silver than for molybdenum ($J_{th} = 34.5\,\mathrm{mA/cm^2}$ vs. $J_{th} = 27.5\,\mathrm{mA/cm^2}$) . Nevertheless, for the 45 nm-thick CIGS layers, the J_{th} still drops of about 70 % for gold and about 60% for silver compared to 2 µm ot CIGS. If a good reflector is a critical aspect for the light trapping in ultra-thin CIGS solar cells, it is insufficient for thicknesses below 500 nm. The optical path is doubled in CIGS with a good reflector. However, the absorption length in CIGS at λ =1 µm for instance is about 400 nm (see Fig. 6.1.2). As for GaAs with ultra-thin thicknesses, new solutions for light-trapping are needed.

6.3.4 Nearly perfect absorption in a 45 nm-thick CIGS layer with a nano-cavity array design

We present here the nano-cavity array design in the case of CIGS. This new structure is composed of a 45 nm-thick CIGS layer on a silver back mirror. The

Thickness (nm)	J_{th}(mA/cm^2) for Mo	J_{th}(mA/cm^2) for Ag	J_{th}(mA/cm^2) for Au
2000	38.9	39.4	39.4
1000	37.7	38.7	38.6
500	35	37.2	37.6
300	30.8	34.7	34.5
200	27.5	34.9	33.7
100	19.2	27.4	26.6
45	12.5	24.3	22.9

Table 6.1: Table of the theoretical short-circuit current calculated from each absorption spectrum for the reference solar cell for Mo, Ag and Au mirror, respectively.

CIGS layer is covered with a 2D silver nano-array (thickness $t = 20$ nm, width $w = 290$ nm, period $p = 530$ nm) and embedded in a 50 nm-thick ZnO:Al window layer (50+20 = 70 nm in total, see Fig. 6.3.5). Again, these geometrical parameters were obtained after optimization of the theoretical short-circuit current.

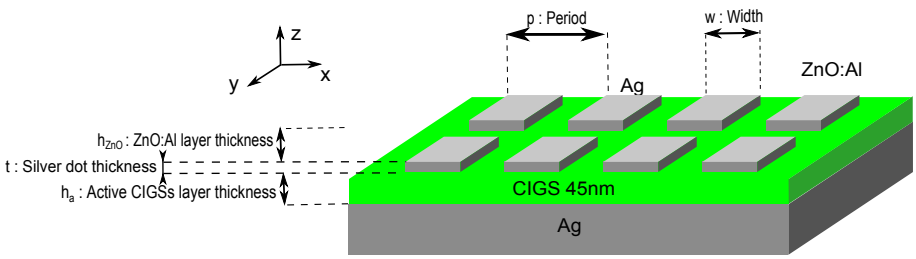

Figure 6.3.5: Schematic of the 45 nm-thick CIGS structure: a 50 nm-thick ZnO:Al window layer, a 2D silver nano-particles array, a 45 nm-thick absorbing CIGS layer and a silver back mirror. The parameters of the array are: thickness $t = 20$ nm, width $w = 290$ nm, period $p = 530$ nm.

6.3.4.1 Simulated absorption spectrum

The absorption spectrum of the 45nm-thick CIGS layer structure (depicted in Fig. 6.3.5) is shown in Fig. 6.3.6. The blue and red curves represent the total absorption and the absorption in CIGS, respectively. The plain and the dashed black curve represent the absorption of the reference 45 nm-thick CIGS planar solar cell with Mo and Ag back, respectively. The gray curve represents the normalized spectral density of AM1.5G solar spectrum.

The absorption in CIGS is multi-resonant (red-curve) and on average superior to 80 % on a very large spectral range (400 nm-1100 nm). The loss in the metal, which is the difference between the total absorption (blue) and the absorption in the CIGS (red), remains extremely low (10 %). A very high short-circuit current of $J_{th} = 38\,\mathrm{mA/cm^2}$ can be calculated, assuming a perfect collection of the photo-carriers. This is a strong enhancement compared both to the absorption of the reference planar 45 nm-thick CIGS solar cell on molybdenum and on silver. It also corresponds to the theoretical short-circuit current of the 1 µm-thick reference solar cell on Mo and Ag.

We can distinguish clearly the apparition of four different absorption peaks that are under the maximum of the solar illumination spectrum and below the gap of the material (in wavelength) at $\lambda_1 = 490\,\mathrm{nm}$, $\lambda_2 = 840\,\mathrm{nm}$, $\lambda_3 = 999\,\mathrm{nm}$ and $\lambda_4 = 1100\,\mathrm{nm}$, similarly to the GaAs and GaSb case. The absorption enhancement in the $\lambda = 300 - 400\,\mathrm{nm}$ range compared to the reference cell is due to the fact that we use here a significantly thinner layer of ZnO:Al and no CdS layer at all.

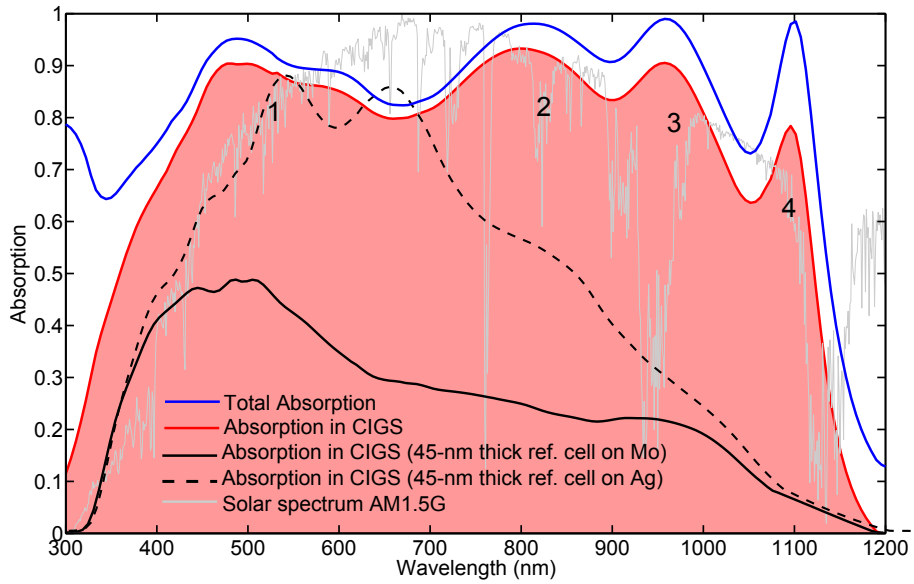

Figure 6.3.6: Simulated absorption spectra of the 45 nm-thick CIGS structure. The blue and red curves represent the total absorption and the absorption in CIGS (see Fig. 6.3.5) respectively. The plain and the dashed black curve represents the absorption of the reference 45 nm-thick CIGS planar solar cell with Mo and Ag back contacts depicted in Fig. 6.3.1, respectively. The gray curve represents the normalized spectral density of AM1.5G solar spectrum. We have labeled resonances $\lambda_1 = 490\,\mathrm{nm}$, $\lambda_2 = 800\,\mathrm{nm}$, $\lambda_3 = 960\,\mathrm{nm}$ and $\lambda_4 = 1090\,\mathrm{nm}$.

6.3.4.2 Electromagnetic field intensity maps analysis

Even though the detailed analysis of the nano-cavity array design has been made in the case of GaAs, we have studied the magnetic field intensity maps at the wavelengths of the different absorption peaks for the CIGS structure at normal incidence and TM polarization. These maps can be consulted in Fig. 6.3.7.

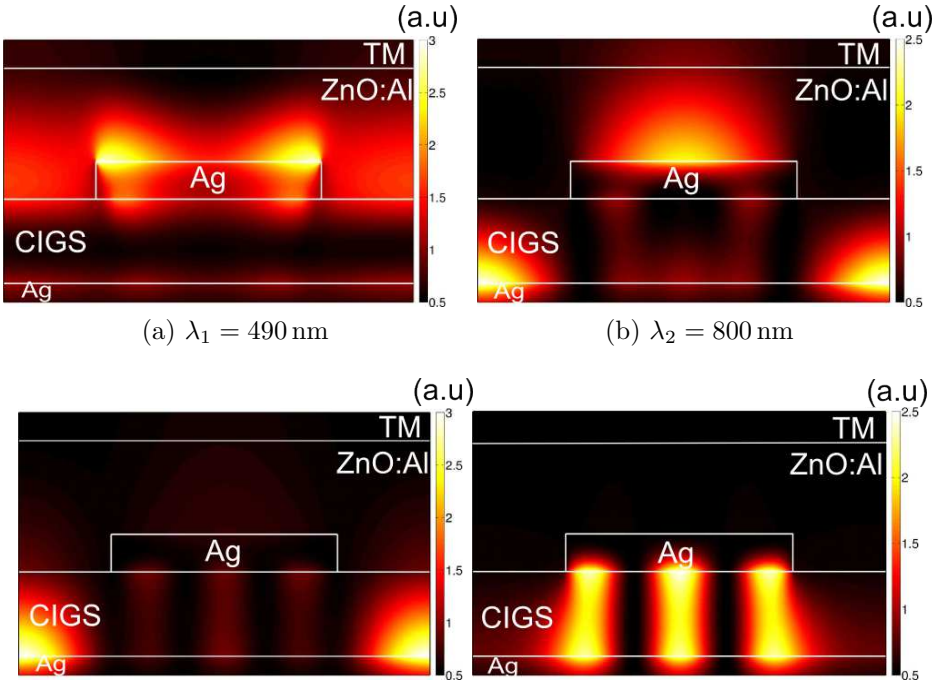

(a) $\lambda_1 = 490\,\text{nm}$

(b) $\lambda_2 = 800\,\text{nm}$

(c) $\lambda_3 = 960\,\text{nm}$

(d) $\lambda_4 = 1090\,\text{nm}$

Figure 6.3.7: Magnetic field (Hy) intensity maps with the direction perpendicular to the plane (xz) of the figure at (a) $\lambda_1 = 490\,\text{nm}$ (b)$\lambda_2 = 800\,\text{nm}$ (c) $\lambda_3 = 960\,\text{nm}$ and (d) $\lambda_4 = 1090\,\text{nm}$ calculated at normal incidence and TM polarization for the figure depicted in Fig. 6.3.5.

- For the first absorption peak at $\lambda_1 = 490\,\text{nm}$ (Fig. 6.3.7a), the mode is localized in the upper ZnO:Al layer and almost homogeneous horizontally. It indicates the classical an single interference effect in this layer that can be understood with the quarter wavelength ARC model. To obtain a minimum of reflection at $\lambda = 500\,\text{nm}$, the thickness of the ARC must be according to Eq. 5.5.1 $t_{ARC} = 68\,\text{nm}$. We assume that the effect of the array is here negligible (the area fill factor is only about 25 %). This is how the thickness of the ZnO:Al has been optimized in our case.

- For the absorption peak at $\lambda_2 = 800\,\text{nm}$ (Fig. 6.3.7b), the situation is not clear (and similar to the GaSb case). At this wavelength, the magnetic field seems to be partly a superposition of the component of resonance 1 and 3 (with a reserve on the shape of the field above the nano-particle). Without, these two components, we effectively observe a weak localization of the field in the CIGS layer at the lower interface like for resonance A for GaAs (we also observe the component of the MSM resonance). Past this observation, it is hard to conclude clearly on the nature of this resonance without more arguments.

- For the absorption peak at $\lambda_3 = 960\,\text{nm}$ (Fig. 6.3.7c), the magnetic field is strongly localized in CIGS, outside the region of the nano-particle. This seems to be similar to the vertical resonator B behavior in the case of GaAs.

- The last absorption mechanism at $\lambda_4 = 1090\,\text{nm}$ (Fig. 6.3.7d) is very similar to the MSM resonance C_3 of the GaAs case. Here, we observe the three maxima in the magnetic field intensity map indicating the 3rd order of a horizontal Fabry-Pérot resonance.

It seems that the behavior of the structure share some similarity with the GaAs case. The situation is however a bit different than the previous case, in particular for the second resonance. A parametric study is needed to confirm the identification and the behavior of the absorption peaks.

6.3.5 Geometrical parametric study

The aim of this section is to verify if, like for the GaAs case, each resonance peak seems to be tunable with a single geometrical factor depending on the nano-photonic mechanism of the resonance.

- Fig. 6.3.8a represents the spectral position of the maximum of the four absorption peaks as a function of the thickness of CIGS. Resonances 2 and 3 seem to respond similarly to the variation of the CIGS thickness. They display also the strongest shift, confirming the hypothesis that these resonances can be modeled as a vertical Fabry-Perot resonator in the CIGS layer. Resonances 1 and 4 are less impacted (the average value of the slope is more than twice lower), accordingly to our description.

- Fig. 6.3.8b represents the spectral position of the maximum of the four absorption peaks as a function of the width of the metallic dots (fixed period at 530 nm). Resonance 4 is shifting over 200 nm for a variation of the metallic dots of 100 nm. This was expected with the MSM model. The other

resonances stay still as expected by our modeling except for resonance 2, indicating that the geometry of the particle as indeed an impact on this resonance (see Fig. 6.3.7b). This particular phenomenon is unexpected in our analysis of this structure. This resonance 2 seems to be effectively slightly different from resonance A.

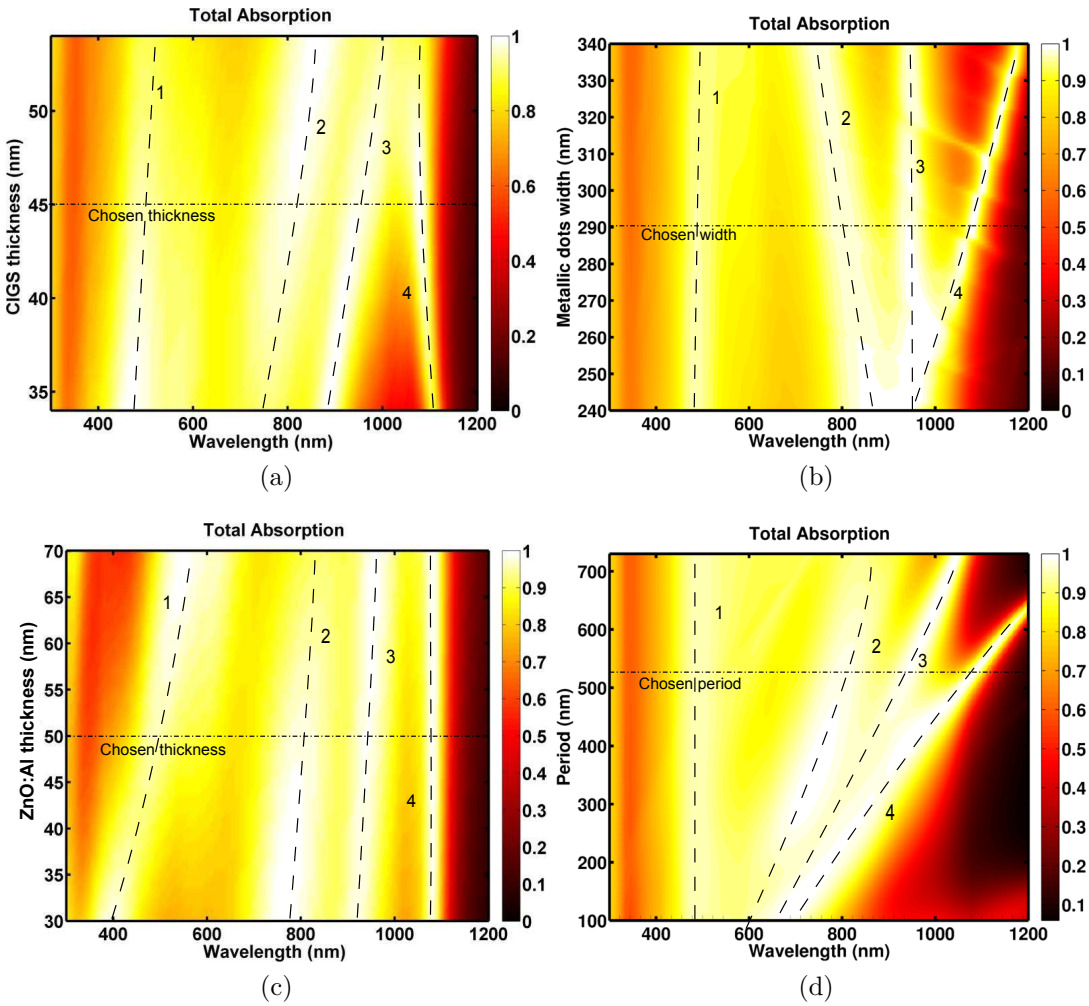

Figure 6.3.8: Parametric study: total absorption calculated for the 45 nm-thick CIGS structure as a function of the wavelength and either of (a) the thickness of the CIGS layer, (b) the width of the dots (at a given period of 530 nm), (c) the thickness of the ZnO:Al window layer and (d) the period of the silver array and the wavelength for a fixed fill factor of value $ff = 0.55$ in TM polarization

- Fig. 6.3.8c represents the spectral position of the maximum of the four ab-

sorption peaks as a function of the thickness of the window layer. The main consequence is seen on resonance 1 as expected: the thickness of the ARC determine the spectral position of the reflection minimum. The thickness of the ARC also affects resonance 2 and 3 but not resonance 4, in accordance with our description.

- Finally, Fig. 6.3.8d represents the CIGS absorption for the structure depicted in Fig.6.3.5 as a function of the period and the wavelength for a fixed fill factor of value $ff = 0.55$. In this figure, resonance 1 does not shift. This peak is attributed to the ARC effect and has no reason to shift at a fixed fill factor. Resonance 4 shifts linearly. This is in accordance with the MSM behavior. However, resonances 2 and 3 are clearly dependent of the period of the array. This is unexpected by our model and suggest potentially a diffraction of light, coupled to the CIGS waveguide. However, the period remains a degree of freedom for us as it allows to spread the different peak across the visible range. As a matter of fact, each absorption mechanism seems to have a different dependency (slope) regarding the period.

6.3.5.1 Study of the angular and polarization dependence

Having detailed the mechanisms of absorption, we test if this structure meets the basic requirements of a solar cell. We have chosen a 2D structure in order to be polarization independent at normal incidence. However, we investigate here if the angle independence is preserved from the GaAs design.

The total absorption spectrum as a function of the angle of incidence is plotted in Fig. 6.3.9a in TM polarization. We note θ the angle of incidence. In this plot, resonances 1, 2 and 4 are angle independent. However, resonance 3 shifts with the increase of the angle of incidence. This is potentially an evidence of a diffraction mechanism. I did not manage however to fit this shift with a diffraction model. A calculation of the exact effective index of the mode might help us in this task.

On the other hand, a diagonal perturbation line crosses the plot, starting at $\lambda = 500$ nm at $\theta = 0\,°$ incident light angle. This perturbation is well described with the dispersion relation of the first order of light diffracted into air by the metallic grating (plotted as the the dashed line in the figure with $\Re\left(k_x^{(p)}\right) = k_0 sin\theta + p\frac{2\pi}{d}$ with $p = 1$ and $n_{eff} = \frac{k_x}{k_0} = 1$ for diffraction into air/vacuum). Below this dashed line, the array is sub-wavelength and no diffraction order is permitted back into the air. Nevertheless, the diffraction mechanism has nearly no effect on the absorption efficiency. Remarkably, the metallic array is responsible for efficient light confinement in the CIGS layer with 4 different resonances in the 400-1100 nm range, but it has a very weak effect on light diffraction in free space.

The shift of resonance 3 causes a hollow in the absorption spectrum near $\lambda =$

1 µm for angle of incidence above $\theta = 30\,°$ and therefore a diminution of the short-circuit current. On the contrary, resonance 1 and 2 seems to collide around $\theta = 40\,°$, party counterbalancing this drawback. The general shape of the spectrum is preserved up to $\theta = 60\,°$, except for resonance 3.

Fig. 6.3.9b represents the total absorption spectrum as a function of the angle of incidence in TE polarization. In this case, the spectrum is independent to the angle of incidence.

The theoretical short-circuit current is preserved up to 60 °. Fig. 6.3.10 represents the angular diagram of the theoretical short circuit current (in mA/cm^2) for the 2D 45 nm-thick CIGS structure (even if there is no actual junction in this design) averaged over both polarizations. We see that the value of the short-circuit current is practically angle-independent. It starts at $J_{th} = 38\,\mathrm{mA/cm^2}$ at normal incidence and is decreased by only 6% at $\theta = 30\,°$. At $\theta = 60\,°$, the short-circuit current has lowered of 15 %.

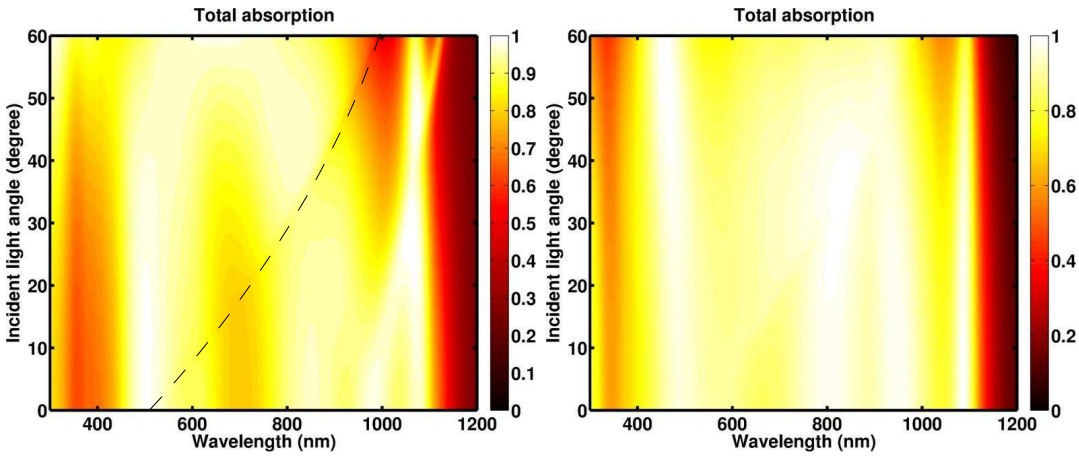

(a) TM (b) TE

Figure 6.3.9: Simulated total absorption as a function of the angle of incidence and the wavelength for 2D 45nm-thick CIGS structure in (a) TM polarization and (b) TE polarization. The dashed line in TM polarization represents the dispersion relation of the first diffracted order in air.

6.3.5.2 Performances and conclusion

We have shown here that it is possible to build a remarkably broad absorption spectrum for the case of a 45 nm-thick layer of CIGS. With the nano-cavity array design, we are able to confine light efficiently in the CIGS layer with 4 distinct absorption peaks. The structure is built and behaves much like the ultra-thin GaAs

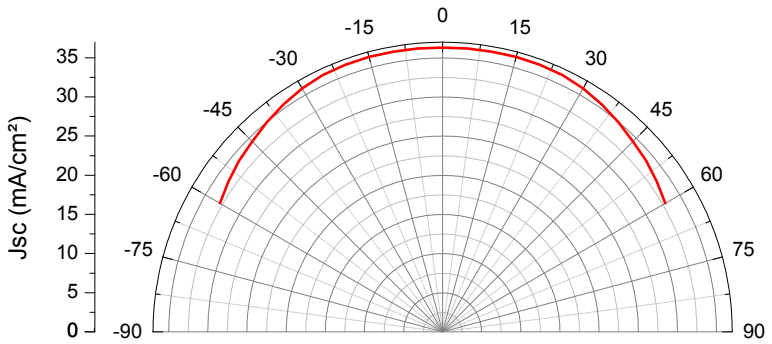

Figure 6.3.10: Angular diagram of the theoretical short-circuit current (in mA/cm²) for the 2D 45nm-thick CIGS structure as a function of the incident light angle (in degree) averaged over both TM and TE polarizations.

structure. Several points in the analysis of this structure are not as clear as for the GaAs structure. However, the optimization process in both cases is very similar. A deeper study is necessary to understand everything perfectly, yet our knowledge in the nano-cavity array is sufficient to submit an efficient light-management for ultra-thin CIGS structures.

In terms of performance, the increase is very important compared to an unstructured 45 nm-thick CIGS solar cell (see Fig. 6.3.6). If we could speak of collection of the carriers, from an optical point of view this structure would lead to a very high short-circuit current value (J_{th} = 38 mA/cm²) for only 45nm of the CIGS. This is a 180 % increase compared to the reference 45 nm-thick CIGS solar cell on Mo and almost of 50 % increase to the reference cell on Ag. It also correspond the same short-circuit current calculated for a 1 µm-thick CIGS solar cell.

This first numerical step has allowed highlighting very promising results and is important toward the application to complete solar cells. In the next section, we go further by applying this design to a more complete solar cell structure.

6.4 Toward a complete CIGS solar cell: 100 nm-thick CIGS nano-cavity array solar cell

The previous sections have demonstrated the potential of the nano-cavity array design in the case of a sole CIGS layer. The aim of this section is to consider a more complete solar cell and to give a first overview of the nano-cavity array design in this case. We propose a potential structure for a 100 nm-thick CIGS solar cell including a buffer layer to form the hetero-junction and a diffusion barrier at the back contact. We investigate if the nano-cavity array design can still enhance the

absorption in this more complex structure.

6.4.1 Presentation and discussion about the ultra-thin CIGS solar cell

We study in this section the solar cell design described in Fig. 6.4.1. It is similar to the 45 nm-thick CIGS structure but it incorporates two new layers that are important for the electronic behavior of the device: a CdS buffer layer (50 nm) on the front and a 50 nm-thick TCO layer (here ZnO:Al) between CIGS and the back mirror to play the role of diffusion barrier.

Concerning the front contact, we have chosen the conventional CdS layer that is widely used for the charge separation and the electronic transport in CIGS solar cells. A different option using ZnS instead of CdS is considered later in this chapter. We assume here that the silver does not diffuse through cadmium sulfide but we could think of a design where the metallic array would be embedded in an intrinsic window layer. Besides, there is no i-ZnO layer in this design. The real part of the refractive index of i-ZnO is close to ZnO:Al, which is an advantage. However, the thickness of the i-ZnO would change the ARC condition and a deeper study is necessary to submit a proper structure.

Concerning the back contact, Matson *et al.* [208] have presented results about the characterization of the interface between $CuInSe_2$ and different metals. Highly reflective metals such as silver (Ag) and copper (Cu) performed poorly whatever the deposition method due to interdiffusion of the metal throughout the CIGSe layer even at room temperature. Some teams have started to study transparent back contacts (TCOs) between CIGSe and a metal that would block the diffusion of metallic particles and allows benefiting from the high reflectivity of silver for instance. The good optical properties of a hybrid ZnO:Al/Ag mirror was reported in the paper of Campa *et al.* [209]. However, using a n-ZnO:Al contact at the p-CIGSe extremity leads to rectifying behavior. However, interesting experimental results were obtained in the team of Prof. Nakada [210, 211] using either $SnO_2 : F$ (FTO) or $SnO_2 : In$ (ITO) as a back contact for bifacial CIGS solar cells. In this dynamic, Rostan *et al.* [212] have reported the ohmic behavior of a CIGSe/MoSe2 (20 nm-thick)/ZnO:Al contacts. As an ideal candidate for efficient transparent back contact has not emerged yet from literature, we select for now a ZnO:Al (50 nm) layer. This study can be (and should be) start again with another TCO.

The structure is not complete from a electronic point of view but it is already more complex optically speaking. We use here the same parameters of the metallic array as for the 45 nm-thick CIGS structure: thickness $t = 20$ nm, width $w = 290$ nm, period $p = 530$ nm to see its effect on the absorption spectrum.

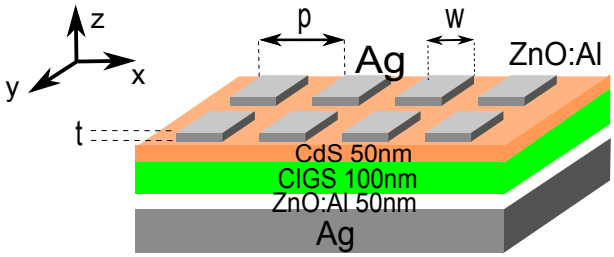

Figure 6.4.1: Schematic of the 100 nm-thick CIGS solar cell: a 50 nm-thick ZnO:Al window layer, a 2D silver nano-particles array, a 50nm-thick CdS layer, a 100 nm-thick absorbing CIGS layer, a 50 nm-thick ZnO:Al to prevent diffusion layer and a silver back mirror. The parameters the array are: thickness $t = 20\,\text{nm}$, width $w = 290\,\text{nm}$, period $p = 530\,\text{nm}$.

6.4.2 Broadband absorption enhancement in the 100 nm-thick CIGS structure

The absorption spectrum of the 100 nm-thick CIGS structure is shown in Fig. 6.4.2a. The total absorption is plotted in blue and the absorption in the CIGS is plotted in red. These spectra are compared to the CIGS absorption of the 100 nm-thick reference CIGS solar cell on Mo (black curve) and the solar irradiance spectrum (gray).

The difference between the blue and the red curve represents the light lost in the other layers. Above $\lambda = 500\,\text{nm}$, this difference is never superior to 15 %. Below $\lambda = 500\,\text{nm}$, a large fraction of the light is absorbed both in the window and buffer layer: at $\lambda = 300\,\text{nm}$, the totality of the light is parasitically absorbed.

The red curve displays resonant absorption peaks and reaches perfect absorption two times at $\lambda = 540\,\text{nm}$ and $\lambda = 720\,\text{nm}$. At $\lambda = 1050\,\text{nm}$, The red curve represents a strong enhancement in absorption over the absorption of the reference solar cell (at $\lambda = 750\,\text{nm}$ the absorption in doubled). It results in a 80 % increase in photo-current from $J_{sc} = 19.4\,\text{mA/cm}^2$ to $J_{sc} = 29\,\text{mA/cm}^2$.

It is harder to differentiate clearly the different contribution of each element of the structure on the red curve compared to the 45 nm-thick CIGS structure. The electromagnetic field intensity maps (see the appendix) are very hard to interpret. We are not showing here an analysis of the absorption mechanism as it would need more study. The «visual» optimization of the absorption spectrum (positioning of the peaks) is not really possible anymore. Here, only a simple, blind optimization of the geometric parameters of the array have been realized in order to max the calculated theoretical short-circuit current

Fig. 6.4.2b represents the comparison between the absorption spectra with two

more adequate references. The CIGS absorption spectrum of the structure is plotted in red. It is compared to the absorption spectrum of the same structure with no metallic array (dotted red) and to the absorption spectrum of the 100 nm-thick reference CIGS solar cell on silver. With this figure, we can identify the contribution of the array on the absorption enhancement.

The main effect of the array is to increase the absorption at $\lambda = 750\,\text{nm}$ and at $\lambda = 1100\,\text{nm}$ over the two references. It also reduces the absorption at $\lambda = 950\,\text{nm}$, but partly in one of the atmosphere absorption band in the solar irradiance spectrum. The peak at $\lambda = 1100\,\text{nm}$ is clearly a product of the array but is not very efficient and would need to be optimized as it resonates in an interesting region of the solar spectrum.

The absorption enhancement is not as spectacular as for the 45 nm-thick CIGS structure for instance. Yet, the theoretical short circuit current calculated from the red curve represents an increase of $+3.5\,\text{mA/cm}^2$ over the dotted red curve and of $+3.4\,\text{mA/cm}^2$ over the dotted black curve. This increase is understandable as the array leads to an increase in absorption in spectral regions where more photons are available.

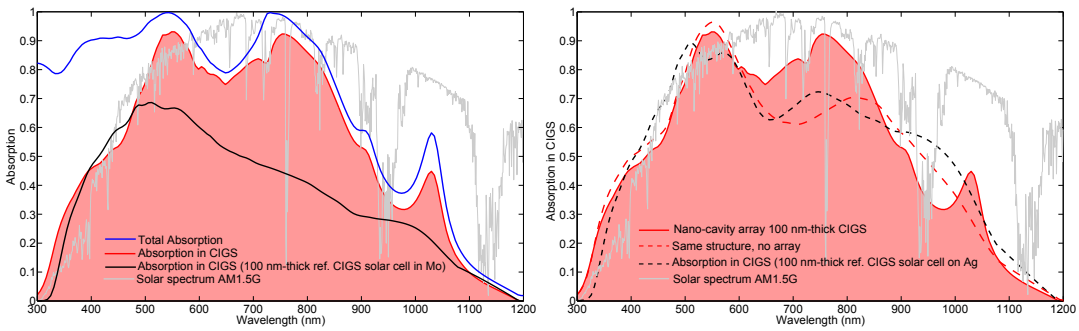

(a) (b)

Figure 6.4.2: (a) Simulated absorption spectra of the 100 nm-thick CIGS solar cell. The blue and red curves represent the total absorption and the absorption in CIGS of the structure depicted in Fig. 6.4.1 respectively. The black curve represents the absorption in CIGS for the reference planar 100nm-thick CIGS solar cell with Mo back contact depicted in Fig. 6.3.1. The gray curve represents the normalized spectral density of AM1.5G solar spectrum. (b) Comparison of the simulated absorption spectra of the 100 nm-thick CIGS solar cell to the absorption spectrum of the same structure without array and to the absorption spectrum of the reference planar 100 nm-thick CIGS solar cell on Ag.

6.4.3 Study of the angular dependence

Fig. 6.4.3 shows the absorption in CIGS of the 100 nm-thick CIGS structure as a function of the incident light angle and the wavelength. The absorption spectrum remains stable in the $\lambda = 300 - 800$ nm range up to an angle of incidence of 50 °. Above $\lambda = 800$ nm, one can note the apparition of angle dependent mechanisms that limit the absorption for angles superior to 35 °. This hints the presence of diffraction induced modes that need to be properly discussed in a future study.

Nevertheless, Fig. 6.4.4 represents the angular diagram of the theoretical short-circuit current (in mA/cm^2) for the 2D 100nm-thick CIGS structure as a function of the incident angle (in degree) averaged over both TE and TM polarization. The theoretical short-circuit current is stable up to an angle of at least 60° for a value of $J_{sc} = 29$ mA/cm^2 at normal incidence to a value of $J_{sc} = 28$ mA/cm^2 at $\theta = 45$ °. This is compatible for standard PV applications.

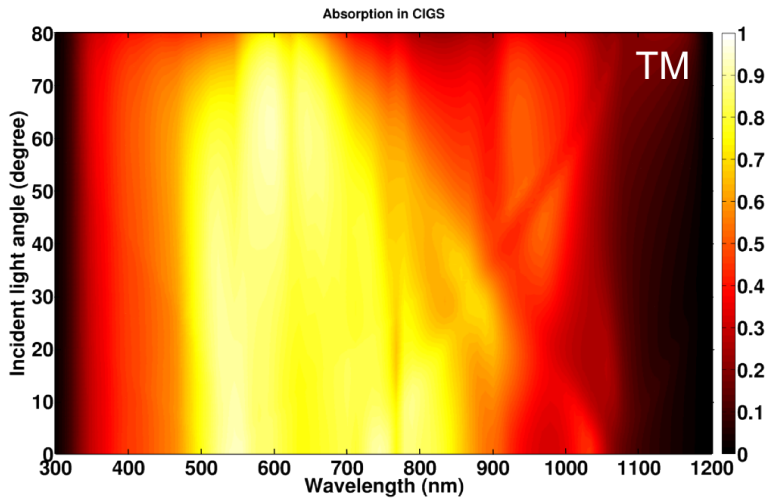

Figure 6.4.3: Simulated absorption in CIGS of the 2D 100 nm-thick CIGS structure as a function of the incident angle and the wavelength in TM polarization.

6.4.4 Replacing the buffer layer: from CdS to ZnS

Zinc sulphide and by products are the most promising candidates to replace the cadmium sulfide as the buffer layer in CIGS solar cells [213, 214]. It would allow to get rid from cadmium and its high bandgap (3.6 eV), associated to a surface passivation due to the incorporation of sulfur and short deposition times (<10 min) makes it an excellent alternative to CdS for carrier extraction.

From an optical point of view, ZnS has a much lower extinction coefficient than CdS (below 0.1 in the $\lambda = 300 - 500$ nm range using the data of Siqueiros *et*

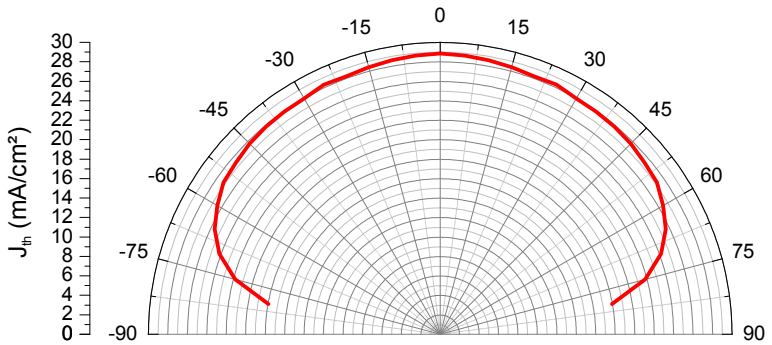

Figure 6.4.4: Angular diagram of the theoretical short-circuit current (in mA/cm²) for the 2D 100 nm-thick CIGS structure as a function of the incident light angle (in degree) averaged over both TE and TM polarization.

al. [215] compared to 0.4-0.7 for CdS). It leads to less parasitic absorption in the buffer layer (and minority carrier recombination). The two materials have however roughly the same value for n (around 2 in the visible spectrum).

We replace CdS by ZnS in the 100 nm-thick CIGS structure of Fig. 6.4.1 with the same thickness (50 nm) and keep the same geometrical parameters. Fig. 6.4.5 represents the comparison of the absorption spectra with either a CdS (red) or ZnS (black) buffer layer of 50 nm. As expected, the absorption in CIGS is increased in the 350-450 nm range. For longer wavelengths, the absorption spectra stay almost the same. The theoretical short-circuit current is enhanced from $J_{th} = 29\,\mathrm{mA/cm^2}$ to $J_{th} = 30.2\,\mathrm{mA/cm^2}$. Despite the absorption enhancement, the increase of short circuit current is limited due to the small amount of photons received from the sun between $\lambda = 350\,\mathrm{nm}$ and $\lambda = 450\,\mathrm{nm}$.

6.4.5 Conclusion

We have adapted the nano-cavity array structure to a CIGS solar cell and have proposed a set of parameters that allow an enhancement of the absorption in the active layer and of the theoretical short-circuit current compared to unstructured references. To our knowledge, this is one of the first numerical propositions of a light trapping involving nano-photonic concepts and metallic array for CIGS solar cells.

In the case of the 100nm-thick CIGS solar cell with the ZnS buffer layer, we have calculated a theoretical short-circuit current of $J_{th} = 30.2\,\mathrm{mA/cm^2}$. This is a 85 % enhancement over the value of the reference planar 100nm-thick CIGS solar cell on Mo. However, this represents only a $+5\,\mathrm{mA/cm^2}$ absolute increase compared the 100 nm-thick CIGS solar cell on Ag. The problems of indium and deposition time make CIGS one of the most eager technology to reduce the thickness of the absorber. We have proposed an optical solution that paves the way to future study

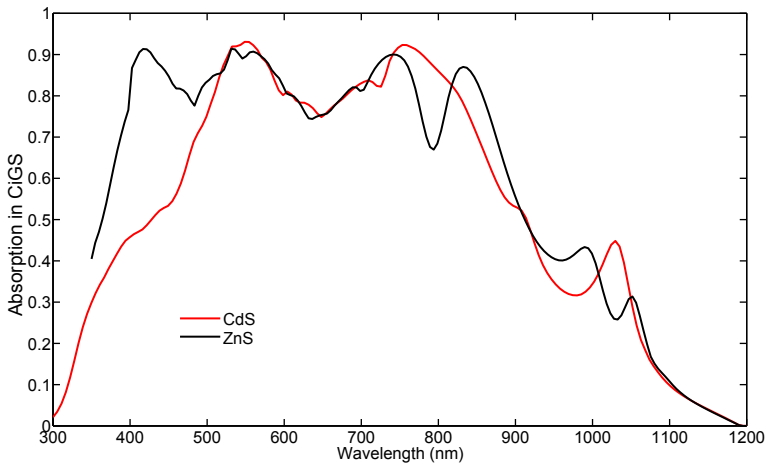

Figure 6.4.5: Comparison of the absorption spectra in CIGS of the 100nm-thick structure of Fig. 6.4.1 with either a CdS (red) or ZnS (black) buffer layer of 50 nm. The theoretical short-circuit current is enhanced from $J_{th} = 29\,\mathrm{mA/cm^2}$ to $J_{th} = 30.2\,\mathrm{mA/cm^2}$.

on ultra-thin CIGS solar cells. There is however several mandatory steps required for a complete solar cell such as the integration of a i-ZnO layer and the passivation of the silver grating. However, right now, the focus should be on producing high quality ultra-thin, ultra-flat CIGS layers on alternative substrate. This process is described in Chapter 7; along with the patterning process of CIGS structures.

Moreover, we see in this particular case the limitations of the nano-cavity array structure. It is excellent to increase absorption in confined space but the drawback is that, for increased thickness of the active absorber (100-300 nm), we are losing the beneficial coupling of the array and the back mirror (in the case of the MSM resonance). Moreover, the optimization and the comprehension of the resonance are more complex due to the high number of layers. In the following of this chapter, we are presenting an alternative way to enhance the absorption in solar cells in the 100-400 nm thickness.

6.5 Back nano-structured CIGS solar cells

6.5.1 Introduction

Our first idea was to fabricate and characterize the nano-cavity array design simulated for ultra-thin CIGS layers. However, the conclusion of the previous section was that the nano-cavity array design is truly optically interesting for thicknesses inferior or equal to 100 nm and that further studies are required for its integration

in working devices. For devices in the 100-400 nm range, we propose here an alternative light management design: placing a nano-structured mirror at the back of a solar cell. The solution has two main advantages: to excite wave-guided modes in the CIGS layer with the use of a metallic grating and to be integrated in the back contact. The potential of this solution has been already demonstrated for amorphous silicon solar cells [2, 3, 159] (see Chapter 2). Optically, the advantage of this structure is to have no metallic particles on the front and thus to reduce the parasitic losses compared to the previous structure in the spectral range where the light is absorbed through in single pass in the CIGS layer. Therefore, we expect an enhancement of the absorption only in the red part of the spectrum. In this section, we evaluate the potential of this structure for CIGS solar cells in the 100-400 nm thickness range. We start by studying in detail a 150 nm-thick CIGS structure.

At the point in the manuscript, we pursue the change in our approach engaged in the previous section: now, we focus on structures that can be applied to solar cells in a short term range.

6.5.2 150 nm-thick Back nano-structured CIGS solar cell

6.5.2.1 Simulated structure

In the following section, we consider first the structure of Fig. 7.3.6. It is a 150 nm-thick CIGS solar cell (the hetero-junction is formed with a stack similar to the reference solar cell) with a patterned Au back mirror.

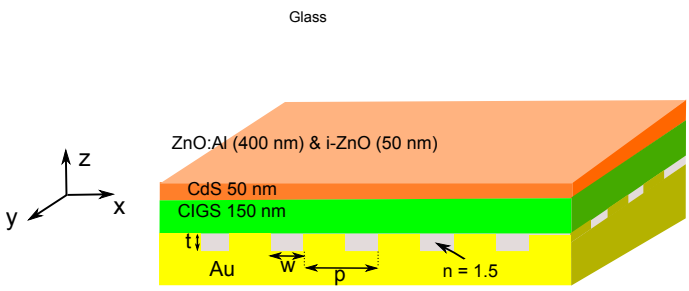

Figure 6.5.1: Simulated 150 nm-thick CIGS structure with a patterned Au back mirror. The parameters the back mirror are t the thickness of the structure, w the width of the structuration and p the period of the structure ($p = 600$ nm, $w = 300$ nm and $t = 100$ nm). The medium between the Au structure is considered as a homogeneous material with a refractive index of $n = 1.5$. The incident medium is considered also as a homogeneous material with a refractive index of $n = 1.5$ (glass).

The parameters of the back mirror are t the thickness of the structure, w the width of the structure and p the period of the structure. The medium between the Au structure is considered as a homogeneous material with a refractive index of $n = 1.5$. To take into account a glass encapsulation, the incident medium is considered also as a homogeneous material with a refractive index of $n = 1.5$.

The originality of this design is to create a structure while keeping a flat active material, integrated in a hybrid back contact. Fabrication considerations and potential advantages are discussed in Chapter 7. First, the design is simulated with the Reticolo code in order to evaluate the absorption increase. To optimize the short-circuit current, the optimal parameters of the array are $p = 600\,\text{nm}$, $w = 300\,\text{nm}$ and $t = 100\,\text{nm}$.

6.5.2.2 Simulated absorption spectrum

Fig. 6.5.2 represents the simulated absorption spectrum for the 150 nm-thick CIGS solar with a patterned Au back mirror of period 600 nm. This absorption spectrum is compared to the absorption spectra of the reference solar cells (on Au and on Mo). This absorption spectrum is independent of the polarization at normal incidence.

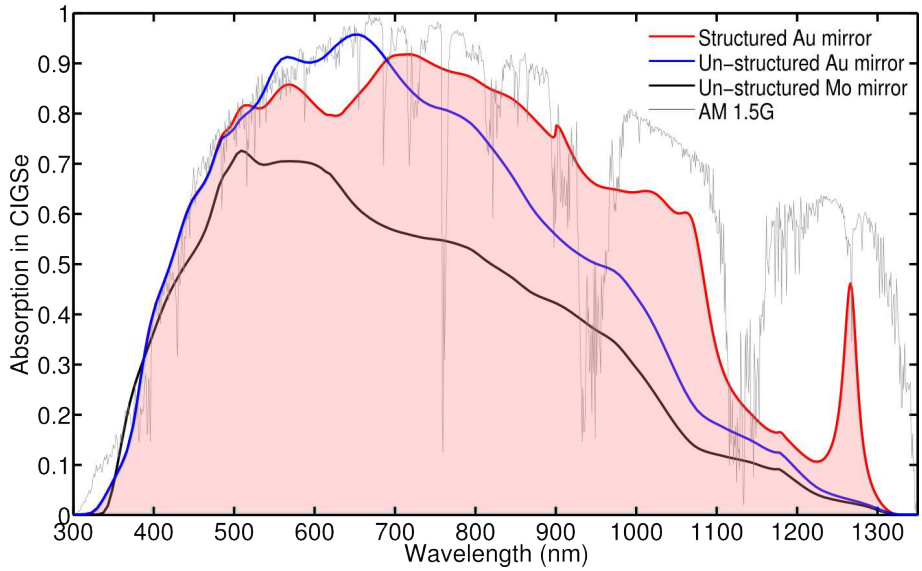

Figure 6.5.2: Simulated absorption spectrum in CIGS (in red) for the 150 nm-thick CIGS solar with a patterned Au back mirror of period 600 nm. This absorption spectrum is compared to the absorption spectra of the reference solar cells: Au (blue) and Mo (black). The AM1.5g normalized spectral density is represented by the gray curve.

The maximum absorption enhancement takes place in the red part of the spectrum (in the 700-1200 nm range). In particular, we can note specific absorption peaks at $\lambda = 1060$ nm and $\lambda = 1260$ nm. The red absorption is expected for this structure, as noticed in literature for a-Si:H solar cells. It only affects weakly the blue photons as they are absorbed in CIGS through a single path. A notable exception is present around $\lambda = 600$ nm where the flat reference is superior to the structured stack.

6.5.2.3 Balance of the optical losses in the cell

Fig. 6.5.3 represents the simulated absorption spectrum for the 150 nm-thick CIGS solar in each layer, i.e. the balance of the optical losses in the cell. The main source of optical loss in this system is the window layers, absorbing strongly below $\lambda = 450$ nm and over $\lambda = 1110$ nm (absorption by the free carriers). The CdS accounts for loss up to 30 % in the 300-500 nm wavelength range.

Interestingly, less than 10 % of the light is lost as absorption in the metal with the back structure, except for the resonance peak at $\lambda = 1260$ nm. The absorption in the metal is here not a limitation. In fact, the parasitic losses in the metal are globally inferior to the absorption enhancement compared to reference solar cell on flat Au mirror (an average of 4 % of the light is already lost in the back mirror for the planar solar cell).

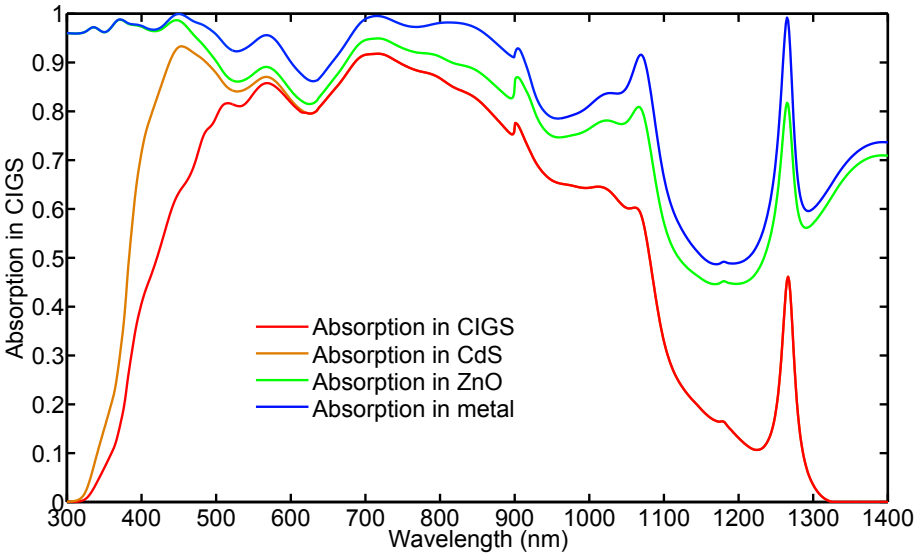

Figure 6.5.3: Simulated absorption spectrum in CIGS (in red) for the 150 nm-thick CIGS solar with a patterned Au back mirror of period 600 nm. This absorption spectrum is compared to the absorption spectra of the reference solar cells: Au (blue) and Mo (black).

6.5.2.4 Magnetic intensity maps

To understand better the behavior the absorption spectrum, we have plotted in Fig. 6.5.4 the intensity of magnetic field along the y direction at normal incidence and in TM polarization at (a) 560 nm (b) 710 nm (c) 1060 nm and (d) 1260 nm.

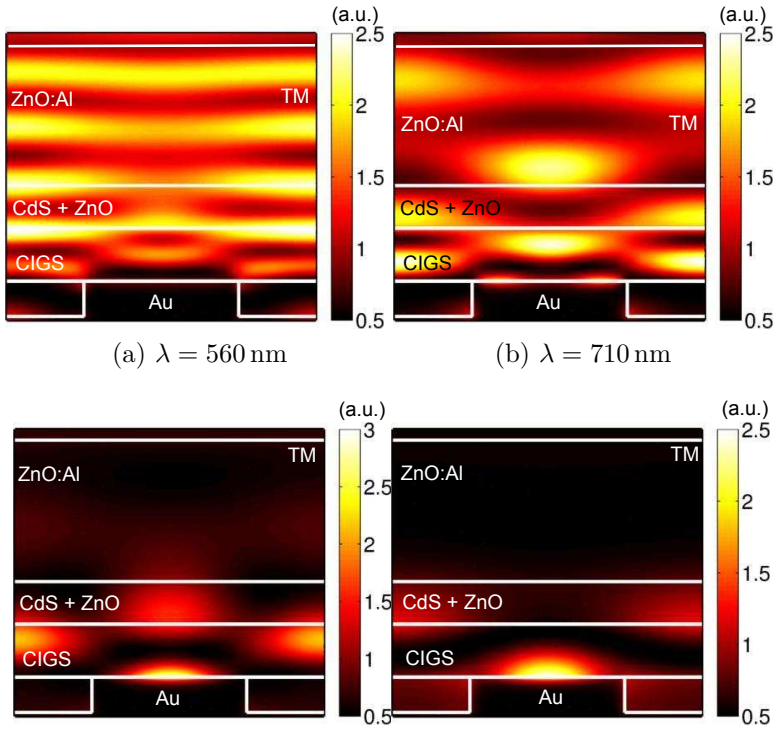

(a) $\lambda = 560\,\text{nm}$ (b) $\lambda = 710\,\text{nm}$

(c) $\lambda = 1060\,\text{nm}$ (d) $\lambda = 1260\,\text{nm}$

Figure 6.5.4: Magnetic field (Hy) intensity maps with the direction perpendicular to the plane (xz) of the figure at (a) 560 nm (b) 710 nm (c) 1060 nm and (d) 1260 nm; calculated at normal incidence and TM polarization for the figure depicted in Fig. 6.3.5.

At $\lambda = 560\,\text{nm}$, as expected, we witness the presence of interference effects in all the layers leading the high absorption in CIGS. In this interference effect, the structure has an effect of the shape of the field, resulting at this wavelength in a diminution of the absorption in CIGS. The effect of the structure is even more sensible at $\lambda = 710\,\text{nm}$. Around $\lambda = 1060\,\text{nm}$ and $\lambda = 1260\,\text{nm}$, the interaction between the the structure and the CIGS layer seems strong, with maxima of the magnetic field localized.

6.5.2.5 Influence of the period

Fig. 6.5.4 represents absorption in CIGS as a function of the period of the back structure and the wavelength in normal incidence. The variation of the period of the structure creates straight dispersive lines in the 900-1200 nm range.

This linear behavior is coherent with the expected dependency of diffracted orders in the CIGS layer according to Eq. 2.5.10. However, to fit properly these dispersive lines and to go further in the comprehension of the light-trapping mechanism, we would need to compute the effective index of the wave-guided mode propagating in the CdS/CIGS/Au slab.

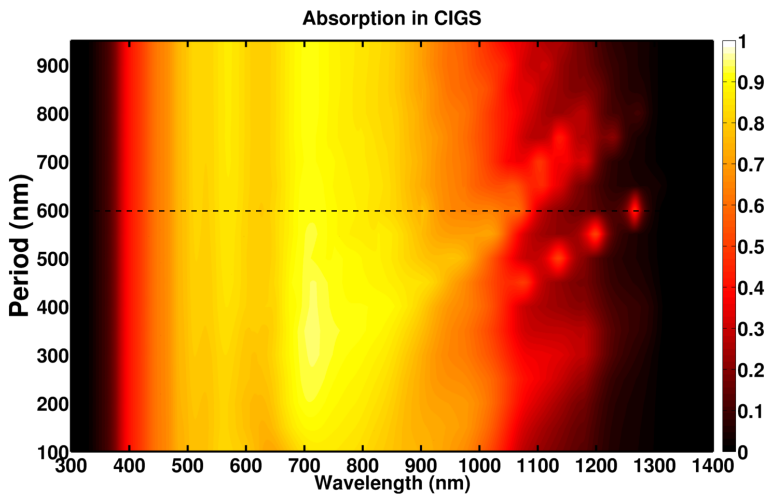

Figure 6.5.5: Simulated absorption in CIGS as a function of the period of the back structure and the wavelength and normal incidence. The black horizontal line represents the optimal period in terms of theoretical short-circuit current.

6.5.2.6 Influence of the angle of incidence

Fig. 6.5.4a represents total absorption of the structure as a function of the angle and the wavelength in TM polarization for a period of $p = 600$ nm. Below $\lambda = 1000$ nm, there is a small blue shift of the absorption peaks, in accordance with the facts that the mechanisms in this spectral region are vertical cavities. However, with the variation of the angle, the resonance at $\lambda = 1060$ nm (at normal incidence) red shifts linearly. This is typical with the dispersion of mode coupled to the grating.

Fig. 6.5.4b represents the same figure in TE polarization. Below $\lambda = 1000$ nm, the plot is similar to TM polarization. Above, dispersive lines still appears but the resonance at $\lambda = 1060$ nm is no longer present, indicating that may be a plasmon assisted resonance that does exists off normal incidence in TE polarization.

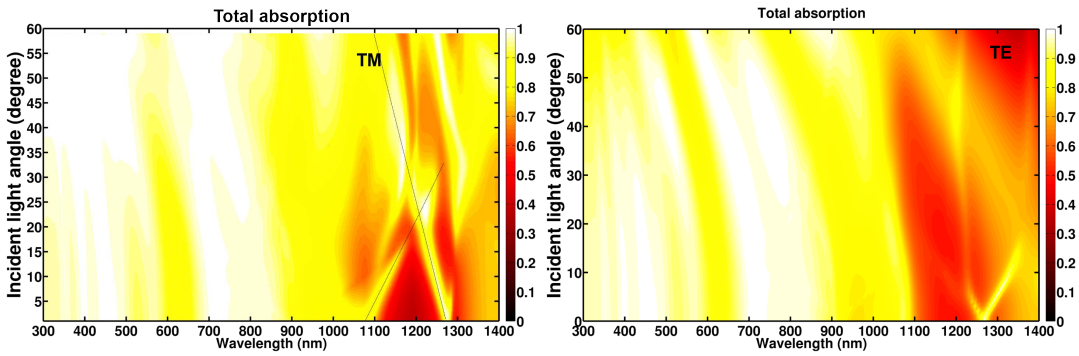

(a) (b)

Figure 6.5.6: Total absorption of the structure as a function of the angle and the wavelength in TM and TE polarization for a period of $p = 600\,\text{nm}$.

Fig. 6.5.7 represents the angular diagram of the theoretical short-circuit current (in mA/cm²) for the 150nm-thick CIGS solar cell with a back nano-structure as a function of the incident angle (in degree), averaged over both TE and TM polarization. The theoretical short-circuit current is stable up to an angle of at least 60° for a value of $J_{sc} = 34.1\,\text{mA/cm}^2$ at normal incidence to a value of $J_{sc} = 33.8\,\text{mA/cm}^2$ at $\theta = 45\,°$. This is compatible for standard PV applications.

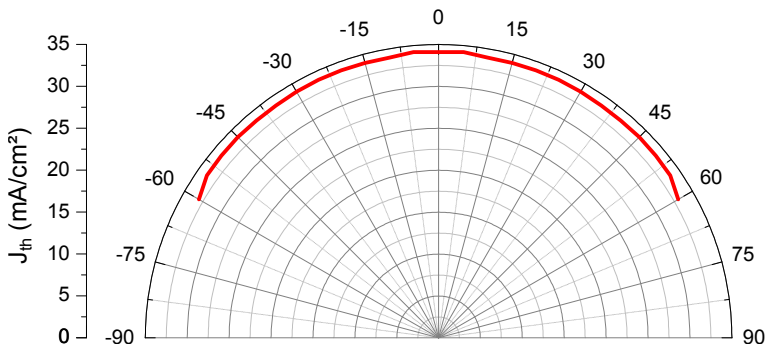

Figure 6.5.7: Angular diagram of the theoretical short-circuit current (in mA/cm²) for the 2D 100 nm-thick CIGS structure as a function of the incident light angle (in degree) averaged over both TE and TM polarization.

6.5.3 Optimization of the short circuit current for different thickness of CIGS

In this section, we submit the results of the optimization of the geometrical parameters for CIGS thickness varying from 100 nm to 400 nm. In this design, the

main parameter we need to choose is the period of the grating. The thickness of the grating does not have much influence on the optical response at the first order (tested in our simulations). Moreover, we have a constraint concerning the aspect ratio of the pattern in fabrication (see Chapter 7). The thickness is therefore taken a constant at a value of 100 nm.

Several configurations have been tested for CIGS thickness varying from 100 nm to 400 nm. For each thickness, the period p (from $p = 100$ nm to $p = 1000$ nm) and the width of the structure are varied in order to achieve the highest theoretical short-circuit current. Table 6.2 lists the best J_{th} results for each thickness, obtained each time for a width value that is half of the period, compared to the J_{th} calculated for the reference CIGS solar cell of Fig. 6.3.1.

Interestingly, regardless of the CIGS thickness (in the 150-300 nm range at least) the best period seems to be around 500/600 nm. Moreover, if the enhancement compared to the reference solar cell on Mo decreases with the increase of the thickness (as expected), the enhancement compared to the reference solar cell on a plane Au mirror is constant, equal to 11-12 %. This is a modest value compared to the nano-cavity array design but is objectively interesting and original for CIGS solar cell. This universal solution is well adapted, regardless of the thickness of the CIGS thickness.

CIGS thickness (nm)	Best period (nm)	J_{th} (mA/cm^2)	J_{th}(mA/cm^2) of ref. cell on Mo	Enhance-ment	J_{th}(mA/cm^2) of ref. cell on Au	Enhance-ment
100	300	29.9	19.2	55 %	26.7	12 %
150	600	34.1	23.8	44 %	30.4	12 %
200	500	36.5	27.5	32 %	33.7	11 %
300	500	37.4	30.8	22 %	34.5	11 %

Table 6.2: Best J_{th} results obtain for the simulation of the structure depicted in Fig. 7.3.6a for different CIGS thickness. For each thickness, the period is mentioned and the J_{th} is compared to the theoretical short-circuit current calculated for the reference solar cell depicted in 6.3.1 with the same CIGS thickness and either Mo or Au as a back mirror.

6.5.3.1 Conclusion on the back structure

In this section, we have evaluated the potential of a back metallic structure to CIGS solar cells in the 100-400 nm range. The originality of this structure is to conserve a flat absorber compared to literature [2–4]. As expected, the main absorption enhancement can be seen in the red part of the spectrum. We have demonstrated

that this solution can enhance the short-circuit current of a constant value of 11 % regardless of the thickness of the CIGS layer in the 150-400 nm thickness range. Besides, This enhancement is rather independent of the angle of incidence. Moreover, in each case, the best period seems to be be around 500/600 nm. This is a real advantage for the fabrication of demonstrators: this solution is universal for the thin CIGS solar cell study we are interested in. More work is needed to fully understand the mechanisms at stake in the coupling of the incident light to wave-guide mode, however. The performances of this structure are less spectacular than the nano-cavity array structure but seems more adapted for the 100-400 nm range CIGS range. Fabrication consideration of this structure are tackled in the next chapter.

6.6 Conclusion and perspectives

In this chapter, we have first transposed the nano-cavity array design from GaAs to ultra-thin GaSb and CIGS layers. With the addition of an ARC, the absorption spectrum is even broader than the GaAs case with 4 distinct absorption peaks in both cases. This allows taking advantage of higher band gap in wavelength of the materials. Moreover, the absorption spectra are still polarization and angle independent on average.

From a performance point of view, the GaSb design is a interesting alternative to the dielectric grating design of Esteban *et al.* [123] that practically the same optical performances, but has the advantage to be more feasible experimentally and to use a twice thinner GaSb layer. This lead to a higher potential as a hot carrier solar cell, as calculated by the Arthur Le Bris et Jean-François Guillemoles [65]. The same conclusion can be said about the 45 nm-thick CIGS structure: we can achieve over 80 % average absorption in the CIGS layer of the 400-1100 nm range. This a very promising results that could lead, if conceivable from an electronic point of view, to theoretical short-circuit current densities comparable to a 1 µm-thick CIGS solar cell on Mo. This is, in absolute terms, a 50 % enhancement in theoretical short-circuit current compared to the same structure without the metallic array.

In the second part, we have adapted the nano-cavity design to a more complete CIGS solar cell structure, taking into account buffer and diffusion barrier layers. We have seen for the 100 nm-thick CIGS design that the addition of the array is certainly beneficial for absorption, but not in the same spectacular way as for the 45 nm-thick CIGS structure for instance. Nevertheless, this design leads numerically to a +5 mA/cm² absolute increase compared the 100 nm-thick CIGS solar cell on Ag. Yet, increasing the thickness cause to progressively loose the benefit of the high confinement of light. It would need a lot more study (numerically

and experimentally) to conclude on this design. For instance, one would need to take into account more the electronic properties of CIGS solar cells (buffer layers, passivation, recombination due to the metallic array). Then we should re-optimize this light-trapping design to conclude on its worth in terms of fabrication cost and complexity.

Considering the immediate complexity of this study, we have proposed a alternative design CIGS solar cells in the 100-400 nm range: a back metallic structure included in the back contact, yet applied for a flat CIGS absorber layers. This structure is found to be optimal for a period of 500/600 nm, enhancing the short-circuit current of a constant value of 11 % regardless of the thickness of the CIGS layer. This solution is original, provides a constant short-circuit enhancement and seems more adapted to CIGS solar cells in the 100-400 nm range.

In this chapter, we have proposed two structures able to enhance the short-circuit current for CIGS solar cells: one for ultra-thin structures in the 25-100 nm range (nano-cavity array) and one for thin structures in the 100-400 nm (flat back mirror structure). The next chapter deals with the technological development and the fabrication of the experimental nano-structured CIGS solar cells demonstrators for both designs.

Chapter 7

Fabrication process of ultra-thin nano-structured CIGS solar cells

Outline

7.1 Previous results of the ULTRACIS project and context of this work . 162
7.2 Fabrication of flat ultra-thin CIGS layer on alternative substrate . 163
7.2.1 Goal and context 163
7.2.2 Substrate transfer process 164
7.2.3 Etching and polishing 165
7.3 Patterning CIGS layers 167
7.3.1 Goal and problematic 167
7.3.2 Degassed-assisted patterning soft-UV nano-imprint lithography (DAP NIL) 168
7.3.3 Lift-off process on a flat CIGS surface 173
7.3.4 Back nano-structured mirror 174
7.3.5 Conclusion 176
7.4 Optical characterization of back nano-structured CIGS solar cells . 177
7.5 Conclusion and perspectives on optoelectronic characterization of ultra-thin nano-structured CIGS solar cells 178
A.1 Optical constants of CIGS 189
A.2 Optical constants of CdS 192
A.3 Optical constants of Mo 193
A.4 Optical constants of GaAs 194
A.5 Optical constants of GaSb 194
A.6 Optical constants of silver 194
A.7 Optical constants of gold 195
A.8 Optical constants of i-ZnO 195

A.9 Optical constants of ZnO:Al 196
A.10 Optical constants of MgF_2 196
A.11 Optical constants of ZnS 196
B.1 25 nm-thick GaAs nano-cavity array structure of Chapter 4 199
B.2 25 nm-thick GaSb nano-cavity array structure of Chapter 6 201
B.3 45 nm-thick CIGS nano-cavity array structure of Chapter 6 202
B.4 100 nm-thick CIGS nano-cavity array solar cell of Chapter 6 204
B.5 Back nano-structured 150 nm-thick CIGS solar cell of Chapter 6 . . 206

7.1 Previous results of the ULTRACIS project and context of this work

As stated in Chapter 1, one of the main achievements of the early ULTRACIS project was the development of a layer transfer of chemically etched CIGS absorber on alternative substrate [81, 87]. This has led to a 10.2 % efficient 400 nm-thick CIGS solar cell on a gold back substrate [85], the most efficient CIGS solar cell for this thickness range so far (see Fig. 1.4.1). In this manuscript, we want to go further lying on the knowledge accumulated at IRDEP. The aim is to apply experimentally the light-management structures of Chapter 6 to enhance even more the short-circuit current density in solar cells of comparable thickness or thinner. CIGS, due to its poly-crystalline rough nature, is very difficult to process and to manipulate in a clean room. In order to achieve this ambitious objective, a heavy technological development is needed to manipulate and pattern CIGS samples properly in clean-room.

The two first problematics tackled in this chapter are on a technological point of view: (1) how to produce a flat ultra-thin (< 400 nm) CIGS layers on an alternative substrate and (2) how to pattern at the sub-micron resolution a CIGS surface? The collaboration of knowledge between IRDEP and LPN has led to the fabrication of ultra-thin nano-structured CIGS solar cells. Preliminary characterizations are presented and discussed at the end in this chapter.

7.2 Fabrication of flat ultra-thin CIGS layer on alternative substrate

7.2.1 Goal and context

To conceive geometries close to our simulated structures of Chapter 6, the CIGS layer should be as thin, as flat and as continuous as possible. The two possible solutions to produce such samples, as seen in Chapter 1, are either to grow directly ultra-thin CIGS layers [72–74, 77] or to etch thick CIGS layers [81, 83, 84, 87]. Because roughness and shunt issues are becoming critical below thickness of 400 nm [72, 73], our samples are produced with the second solution that gives for now better results. The amount of material lost in the process is obviously to be taken into account precisely for further development. Further details about etching and polishing of CIGS layers are given later in this chapter.

Concerning the alternative substrate, studies have showed that the high temperature deposition process (co-evaporation) of the CIGS on Mo leads to a reproducible ohmic contact formation [216, 217] via the formation of an intermediate $MoSe_2$ layer at the metal/semiconductor interface [218]. Over the progress of the research on CIS/CIGS based solar cells, Mo has become the reference back contact metal for CIGS, meeting both the low cost requirements and the electrical compatibility with CIGS. The high temperature substrate based process complicates the use of alternative materials (interdiffusion) [216], and the different studies could not take advantage of the best candidates materials for light-trapping purpose (such as Au and Ag). As a consequence, we use in this study high-quality Mo grown CIGS layers that we have to transfer on another back contact.

Among the studies dealing with a variety of different back contact metals applied specifically to thin CIGS solar cells ($< 1\,\mu m$), we can cite the work of Orgassa *et al.* [216] (W, Mo, Cr, Ta, Nb, V, Ti, Mn) and Malmström *et al.* [219] (ZrN). In particular, silver does not form a ohmic contact with CIS and tend to diffuse in CIS at room temperature [208]. On the contrary, in a publication from 1988, Moons *et al.* showed that the best ohmic contact on CIGS can be achieved using Au [220], thanks to the high work function and chemical compatibility of CIGS with Au. We have seen previously that gold is one of the most reflective metal for CIGS in the visible range (see also Jehl *et al.* [81]).

The «lift-off» process that has been used for flexible solar cells by Minemoto and Anegawa [221, 222] in order to separate the CIGS layer from its Mo growth substrate. We use in this manuscript this interesting idea to process the alternative back contact at room temperature (and therefore to prevent diffusion). We refer to this process as a «substrate transfer» process in order not to confuse with the lift-off clean room process seen in Chapter 5.

In our case, the CIGS samples were supplied by ZSW as a soda lime glass / Mo / $MoSe_2$/ CIGS (≈ 2.5 µm-thick, no gallium grading) stack. The samples were deposited on their pre-production line [223] and we had practically no inputs on the process parameters. In the following, we present the different steps of the substrate transfer process.

7.2.2 Substrate transfer process

The substrate transfer process for CIGS solar cells have been mainly developed at IRDEP by Zacharie Jehl Li-Kao [81, 85, 224] and optimized by Benoît Fleutot. Fig. 7.2.1 represents the simplified steps of the substrate transfer process and the fabrication of ultra-thin CIGS solar cells used. For additional details please refer to the references linked above.

- 7.2.1a: Co-evaporated CIGS sample as received from ZSW (≈ 2.5 µm-thick, no gallium grading). The roughness of the samples are variable, though in average around 200 nm RMS.
- 7.2.1b: Front CIGS wet etching and polishing down to a CIGS thickness of about 500 nm. We use a etch solution of the bromine family [84, 87].
- 7.2.1c: Cyanide solution (KCN) etch that cleans the surface from elemental Se and eventual Cu_xSe binaries [84, 225] and window layer deposition (CdS 50 nm via chemical bath deposition; i-ZnO 70 nm and ZnO:Al 400 nm via sputtering). After this step, a 110 nm-thick Ni grid is sputtered with a physical mask on the window layers in order to contact the front of the cell (not shown).
- 7.2.1d: Substrate transfer: the sample is bounded on a soda lime glass (SLG) superstrate with a transparent epoxy (Araldite 2020) and is separated from the old substrate by a mechanical cleaving (at the weak $MoSe_2$ interface).
- 7.2.1e: Back CIGS wet etching down to the a few hundredth of nanometers. The purpose of this step is also to get rid of the old interface impurities and defects (Mo/$MoSe_2$ residuals, cracks, holes). The atomic force microscope AFM measured roughness of this interface is rather low (about 20 nm RMS) but not perfect as the bromine solution tends to roughened flat CIGS surface (different kinetics at the grain boundaries).
- 7.2.1f: Deposition of the alternative mirror/substrate (gold by evaporation at LPN for instance).

The substrate transfer process can be realized on rather large surface (2*2 cm²), enough to perform standard solar cell tests. The process of our samples reported below was made at IRDEP except for the CIGS etching (made at ILV). I have fabricated the samples of this manuscript following this previous process and putting additional efforts to obtain thinner and flatter CIGS layers. Precision about these specific points are developed in the next section.

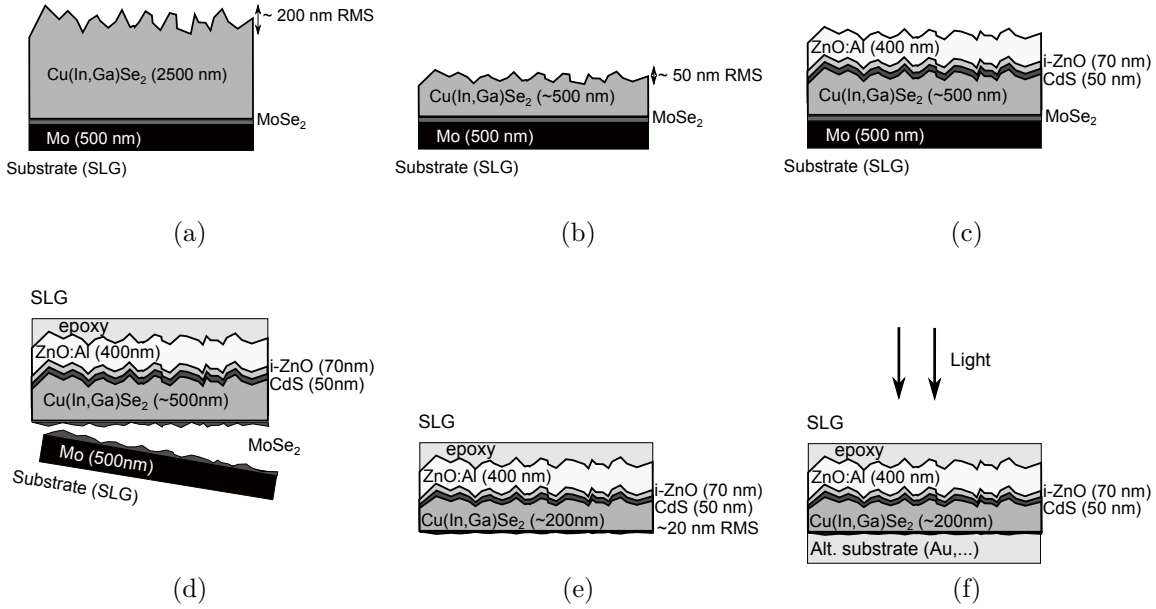

Figure 7.2.1: Overview of the CIGS substrate transfer process: (a) Co-evaporated CIGS sample as received from ZSW; (b) Front CIGS etching and polishing; (c) KCN treatment and window layers deposition; (d) Substrate transfer: the sample is stuck on a SLG superstrate with a transparent epoxy (Araldite 2020) and is separated from the old substrate by a mechanical cleaving (at the weak$MoSe_2$ interface); (e) Back CIGS etching; (f) Alternative mirror/substrate deposition.

7.2.3 Etching and polishing

In this manuscript, the CIGS is etched by a HBr/Br_2 solution thanks to the knowledge of IRDEP and the Institut Lavoisier de Versailles on Br_2 based etching process (described in Refs. [84, 87]). The etching rate of this solution depends of the temperature, the $[HBr]/[Br_2]$ concentration ratio and the spin speed of the vertical rotating-disk system used to homogenize the etching over the sample (typically 40 rpm in our case).

HBr is preferred to KBr as a stabilizing additive for Br_2: previous experiments

in our collaboration [226] have shown that although the dissolution rate and the asymptotic roughness remain the same between the two solutions, the surface roughness decreased significantly faster when using HBr instead of KBr. Moreover, some In and Ga oxides on the etched CIGS surface have been observed when using a KBr/Br_2 solution; using HBr instead of KBr allows the dissolution of these oxide and leaves the CIGS surface almost unchanged compared to a non-etched surface. However, HBr based solutions have an acid pH that can dissolve both CdS and ZnO window layers if exposed. This can be an issue during the back etching of ultra-thin CIGS layers where pin holes can appear. KBr based solution can be buffered with KOH to achieve a neutral pH if needed.

In order to conserve a high control on thickness, the etching rate is kept as low as possible (temperature close to zero degree Celsius) in order to be able to react and stop the etching process. The $[HBr]/[Br_2]$ concentration ratio is maintained constant to a value of 125 to adjust the average etching rate, determined by titration using graphite furnace atomic absorption spectrometry (GF-AAS) for the quantification of the Ga, In and Cu dissolved during the etching treatment. This etching rate is accurate for a bulk material and for a given sample area. However, the determination of the front etch rate is more difficult when the sample displays a high roughness (different etch kinetic, impossibility to determine precisely the amount of material etched). Moreover, native CIGS samples from ZSW displays an average roughness greater to 200 nm RMS and an average peak-to-valley of about 500 nm (AFM measurement, LPN) in our case. It is therefore impossible to determine precisely (i.e. at the 10 nm or less) the thickness of the sample. The uncertainties about the roughness, the CIGS thickness and the etching rate lead to a global uncertainty on the CIGS thickness layer of about 100 nm after the front etch. To measure the CIGS thickness, a destructive solution is to cleave the sample to realize a SEM cross section measurement afterward. However, the consequence is that it is very difficult to aim to 100 nm thick CIGS layers during the back etch without shunting the device or worse, piercing the CIGS layer and dissolving the front contact. Today, the success rate to obtain 200/300nm-thick CIGS solar cells on alternative substrate is correct. However, this process is not reproducible enough to conceive 100 nm-thick or thinner CIGS devices.

The second problematic is the roughness of the CIGS layer, critical for the future patterning of the layer. The bromine etching solution can decrease the surface roughness of the ZSW samples down from 200 nm RMS to an average plateau value of 50 nm RMS during the front etch [87, 226]. On the contrary, during the back etch, the solution tends to increase the roughness of the flat CIGS surface up to this same plateau of 50 nm RMS [224]. In our case, we want to go beyond this value in order to ease the patterning of CIGS layers. The constraints concerning this specific problem are addressed in the next section. A mechanical/chemical

etching was developed at LPN to reduce further the roughness. The principle is to rub homogeneously and softly a HBr/Br_2 soaked cleanroom wipe on the CIGS surface. This homemade technique has allowed to reach record RMS values for CIGS down to 6 nm RMS (10*10 µm² AFM measurements). Fig. 7.2.2 represents the SEM image of a polished CIGS surface. One can note the different grains constitutive of the layer. This is interesting for our purpose and for advanced surface characterizations. Anyhow, achieving such a low roughness is not very reproducible and depends strongly on the initial sample parameters co-evaporated at ZSW. Moreover, we can not control precisely the etching rate of this process so we are limiting this step to a minimum. We estimate the roughness of our samples to be 30 nm RMS in average.

Eventually, we have to take another difficulty into account in our process. Both with chemical etching and chemical-mechanical etching, the resulting thickness of the CIGS layer is not homogeneous on the whole sample: the sides of the sample are etch preferentially. This has a consequence on the patterning of CIGS layers.

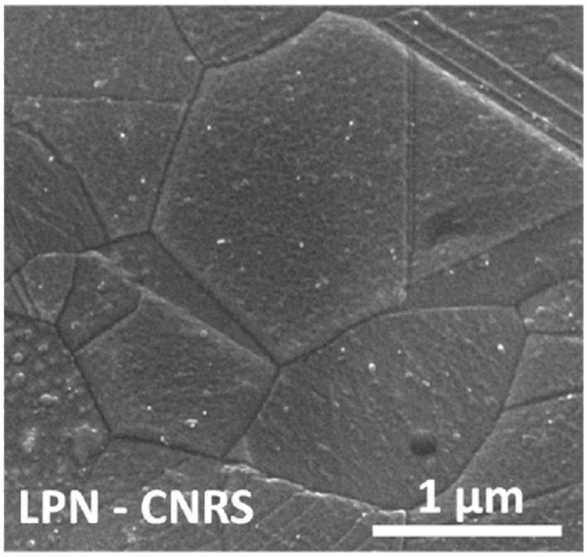

Figure 7.2.2: SEM image of a chemically polished CIGS surface with a measured roughness of 20 nm RMS.

7.3 Patterning CIGS layers

7.3.1 Goal and problematic

The original goal of this chapter is to fabricate the ultra-thin CIGS solar cell numerically studied in Chapter 6. Two designs were proposed for CIGS:

1. The nano-cavity array design for a 100 nm-thick CIGS layer of Fig. 6.4.1. This design requires to pattern a metallic array at the front of the cell, either directly on CIGS or CdS, or even embeded in i-ZnO. This point has to be determined from an electronic point of view. To produce the metallic grating, we have here to have recourse to a lift-off process, similar to the process of Chapter 5. This step adds an additional difficulty compared to a classic patterning and impose a constraint on the lithography technique used (shape of the resist).

2. A back mirror structure for CIGS solar cells in the 100-400 nm thickness range (sketched in Fig. 6.5.1). The fabrication process of this structure is potentially simpler than the previous case. At the state of Fig. 7.2.1f, before the metallic mirror deposition, we just need to pattern a resist layer.

The question is now the following: which kind of lithography technique is compatible with the inhomogeneities of CIGS samples? The issue is to pattern at a sub-micron scale a surface that is rough and inhomogeneous both at the local scale (grains, defects) and at the global scale (defects, uneven sample surface).

The control of the resist thickness is a critical point during sub-micrometer lithography. Both local and global inhomogeneities of the CIGS layer are typically likely to cause inhomogeneity of the resist thickness during a spin-coating. This may cause definitive problems depending on the lithography technique. This is the first motivation to have the flattest and perfect surface possible.

Moreover, large scale inhomogeneities of our CIGS samples (inhomogeneity in thickness over the sample, planarity of the transfer) are typically the type of constraints incompatible with EBL because of the limited focus dynamic of the electron beam. This was our motivation to use anodic bonding for GaAs samples in Chapter 5. This limitation forces us to focus on alternative lithography techniques. At LPN, nano-imprint lithography (NIL) is a resource developed over the last decade and we naturally have decided to use this adaptable and attractive technique for uneven substrates. Holographic lithography could also been considered.

7.3.2 Degassed-assisted patterning soft-UV nano-imprint lithography (DAP NIL)

The principle of nano-imprint lithography (NIL) has been introduced by Chou in 1995 [227, 228]. The original principle is to fabricate a hard mold and to press it into a thin film of polymer at a controlled pressure thereby creating a thickness contrast in the polymer. The pattering is usually realized in a NIL equipment to control the pressure and the temperature. The advantages of this technique

are the rapidity of the process (a couple of minutes) and the possibility to re-use several times the same mold for several samples (the number of re-use depends on the nature of the mold). This process has rapidly become an excellent alternative to achieve fast and relatively cheap sub-100 nm scale lithography on large surface in the semi-conductor industry. The several points below retrace the different historical types of NIL and the principal changes (nature of the mold, reticulation of the resist):

- T-NIL for temperature assisted NIL [227, 228]. The mold is made of Si that is pressed at high temperature and high pressure on a thin-film polymer.
- UV-NIL for ultra-violet assisted NIL [229]. The mold replaced by a transparent mold (glass, quartz...) and pressed on a liquid precursor, cured by UV light through the mold. The process has replaced T-NIL because it can be achieved at room temperature and at comparatively low pressures. It shares however a problem with T-NIL: the removal of the hard mold is delicate and often leads to the breakage of the mold, limiting the re-use potential of the technique. This is particularly problematic when using costly quartz mold.
- Soft-UV-NIL for soft mold, ultra violet assisted NIL [230, 231]. The hard mold is here replaced by a soft transparent stamp made of poly(dimethylsiloxane) (PDMS) that is simply casted or spin-coated on a master hard mold. Soft UV-NIL has thus several advantages among which: (i) dozens of cheap PDMS stamps can be easily prepared from one expensive EBL silicon master mold, (ii) the flexible stamp ensures a conformal contact without applying high external pressure even on non-planar substrates, and finally, (iii) the mold can be easily peeled off without cracking contrary to a rigid mold. However, due to its low Young's modulus, soft PDMS leads to resolution losses cannot be used for replication at the sub-100 nm scale.
- Degassed assisted patterning (DAP) Soft-UV-NIL: to improve this resolution problem, we use at LPN composite bi-layer mold of hard-PDMS/PDMS in order to extend soft UV-NIL for resolution down to 20 nm. The soft PDMS low Young's modulus confers flexibility to the stamps while the hard PDMS high Young's modulus (less deformation) allows a better resolution. Moreover, Andrea Cattoni has developed new method call degassed assisted patterning. This technique can be realized without any NIL specific equipment and is particularly adapted for non-conformal substrates.

Fig. 7.3.1 represents the simplified steps of the DAP Soft-UV-NIL. This technique, inspired by Luo *et al.*[232], has been developed by Andrea Cattoni (LPN). Further details can be found in Cattoni *et al.* [233, 234], especially on the fabrication of the

HSQ master and on the replication of the composite bi-layer mold (or stamp) made of hard-PDMS/PDMS. We have tested at LPN sizes of the stamp (and therefore the patterned area) up to tens of cm^2 areas.

- Fig. 7.3.1a: Before the process, the surface is cleaned and deoxydized according to the nature of the material. For the NIL process especially, it is important to remove any organic elements from the surface that could prevent the correct removal of the stamp in step (g) and if possible to make the surface as hydrophilic as possible in order to achieve a perfect spin coating of the amonil liquid precursor (step b - For CIGS, the process that is closer to a deoxidization is a KCN treatment that is unfortunately not available at LPN. A 2' oxygen plasma is applied on the surface in order to remove organic pollutant). Simultaneously, a trichloromethylsilane (TMCS) anti-sticking treatment is applied to the stamp in order to ease the removal of the mold.

- Fig. 7.3.1b: The porous PDMS stamp is degassed for at least 10' in a dessicator. Amonil (M4) is spin coated in the surface to reach a thickness of about 150 nm in a UV-free room.

- Fig. 7.3.1c: Immediately after the spin-coating, the stamp taken from the dessicator is applied progressively on the amonil in order to avoid bubbles. The sample is kept for 1' in a UV free room.

- Fig. 7.3.1d: Potential trapped micro-bubbles are sucked by the porous and degassed PDMS stamp.

- Fig. 7.3.1e: The holes of the stamp are filled with liquid amonil thanks to the depression induced by the porous PDMS stamp. Here, no external pressure controlled by a specific equipment is needed, simplifying extremely the NIL process.

- Fig. 7.3.1f: The sample is exposed to a UV lamp for 20' for the reticulation of the amonil layer.

- Fig. 7.3.1g: The mold is removed carefully from the sample and stocked to be re-used. A residual layer remains after the imprint.

- Fig. 7.3.1h: The residual layer is removed by reactive ion etching (RIE: CHF_3,O_2). The duration of the etching depends on the thickness of the residual layer.

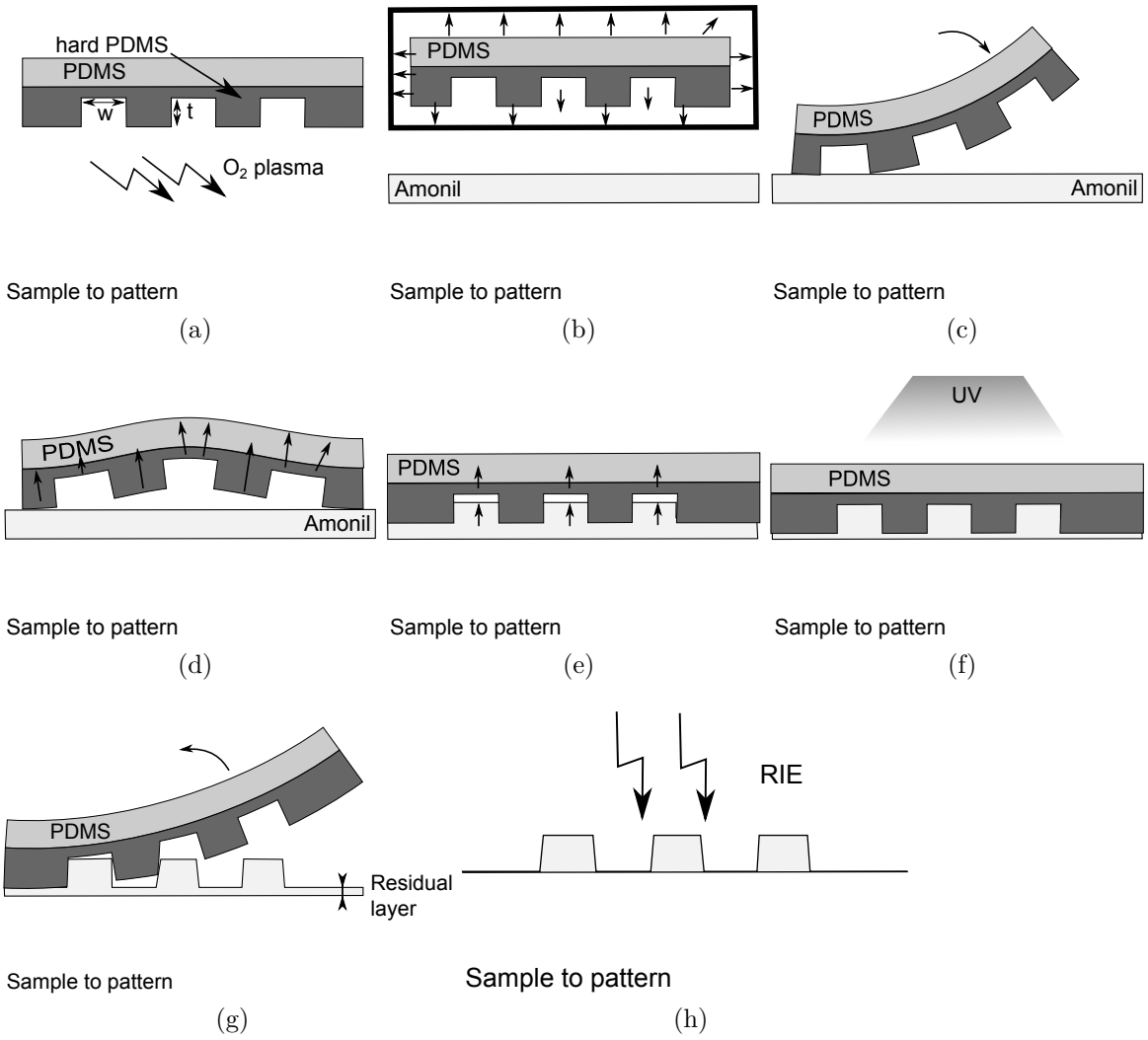

Figure 7.3.1: Overview of the DAP soft-UV NIL process: (a) The surface to pattern is cleaned by a plasma oxygen; (b) The stamp is degassed and a thin-film polymer (Amonil) is spin-coated on the surface; (c) The stamp is applied progressively and carefully ; (d) Degassed assisted patterning: micro-bubbles are sucked by the PDMS; (e) Degassed assisted patterning: holes are filled with amonil without any applied pressure ; (f) Amonil is cured by UV exposition; (g) The PDMS stamp is peeled off the sample; (h) The amonil residual layer is etched by reactive ion etching (RIE: CHF_3,O_2).

The removal of the mold is the stamp critical step of the process. To prevent the sticking and the damaging of the mold, the pattern and the sample, the process

is made if possible at the same room temperature and at the lowest air humidity possible for higher success rate (in addition of the TMCS treatment). Moreover, the aspect ratio of the stamp pattern is usually limited to values $w/t \geq 1$ to limit the PDMS deformation (even more so for $w \leq 150\,\text{nm}$).

Fig. 7.3.2 represents the cross section SEM image of a DAP NIL processed with a amonil resist on a silicon substrate with a square pattern of period 400 nm. For a flat substrate, the residual layer thickness is constant at a value of about 20/30 nm (measured on the SEM image). A successful etching of the residual layer relies on its constant thickness.

We sense here the difficulty of the NIL on uneven samples like CIGS layers. If the residual layer is not homogeneous, it is difficult to converge toward the optimal etching time in order to remove this layer on the whole sample. A solution is to over etch the residual layer but this it comes with a degradation of the shape of the patterns and therefore, a degradation of the resolution.

For the samples presented in this chapter, I have adapted this DAP NIL process to CIGS samples, taking advantage of both the flexibility of the mold and the DAP process. As we have seen in the previous paragraph, the application to uneven samples remains tricky because of the thickness of the resist. To have a homogeneous spin-coating, we select the flatter and less damaged CIGS surfaces available after polishing. We have also chosen the liquid precursor with the lowest viscosity possible.

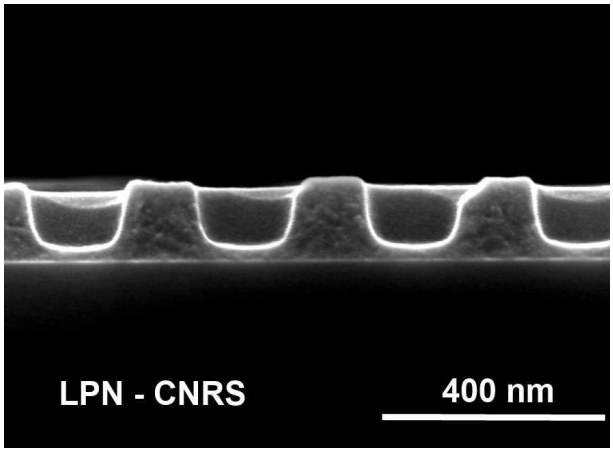

Figure 7.3.2: Cross section SEM image of a degassed assisted patterning NIL processed on a amonil layer on a silicon substrate with a square pattern of period 400 nm. For a flat substrate, the residual layer thickness is constant at a value of about 20/30 nm.

7.3.3 Lift-off process on a flat CIGS surface

The first goal of this approach is to produce 2D-metallic nano-particle array on a CIGS surface, similarly to what have been done on GaAs in Chapter 5. Nano-imprint patterning is not compatible immediately with a classic lift-off technique. The first reason is that amonil can not be efficiently selectively wet etched or dissolved. Second and more fundamentally, on Fig. 7.3.2, we can see that the flanks of the patterns are exposed to a metal deposition, contrary to the EBL case. This configuration leads to a continuous metallic thin film during anisotropic metal evaporation (see Fig. 7.3.3a) that makes the lift-off impossible.

To enable the lift-off, a bi-layer configuration is used (see Fig. 7.3.3b). An additional PMMA layer that can be dissolved in thrichlorethylen and that can be selectively etched in RIE (O_2) in relation to the amonil layer is deposited on the substrate before the amonil layer. After the NIL, the residual amonil layer is removed (RIE: CHF_3,O_2) and then the PMMA is etched by isotropic RIE (O_2) in order to create an undercut. This way, the lift-off of the PMMA is possible. The O_2 RIE etching rate of CIGS is pretty low, ensuring a good selectivity of the bi-layer etch.

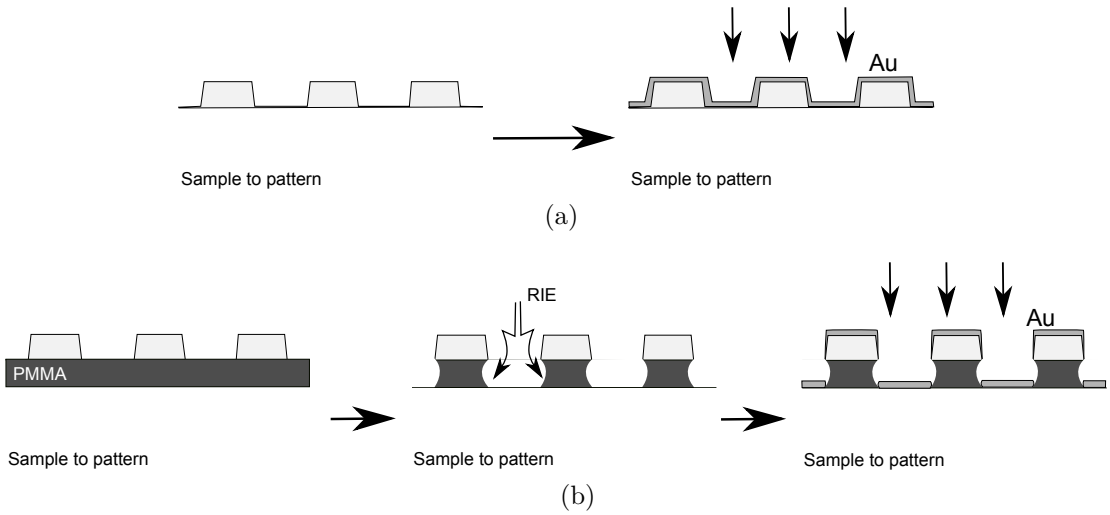

Figure 7.3.3: (a) Simple layer soft UV-NIL: impossible lift-off. (b) Bi-layer soft UV-NIL: the lift-off of PMMA is possible after isotropic reactive ion etching.

Fig. 7.3.4 represents the 45 ° tilted SEM images of the nano-structured metallic (Au) array processed on a CIGS surface. The period of the array is 400 nm, the width of the particles is 200 nm and the thickness is 20 nm. We see that the particles are well defined and that the resolution is sufficient for our application

(and similar to the GaAs demonstrator fabrication). Moreover, we can see that the process is very robust: a few squares are missing but the Au nano-squares can even be deposited at the junction between two grains. The process is successful on a relatively large area even on rough substrate (roughness about 50 nm RMS in this case, patterning over 0.25 cm^2 for now, limited by the available CIGS surface and not by the NIL technique). Each defect on the CIGS surface leads to a defect on the gold array. However, this perturbation is very localized and does not extend over large surfaces ($< 1\,\mu m^2$).

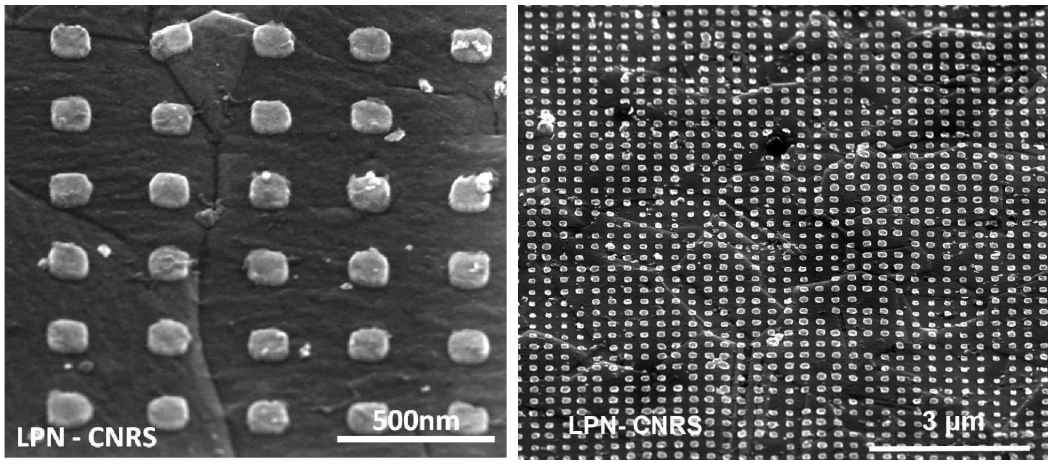

(a) (b)

Figure 7.3.4: 45 ° tilted SEM images of gold array (period = 400 nm, width = 200 nm and thickness = 20 nm) realized on CIGS surfaces by nano-imprint lithography.

7.3.4 Back nano-structured mirror

The second goal is to produce a back nano-structured mirror sketched in Fig. 6.5.1. In order to realize this, we have developed a process taking advantage of the superstrate configuration of the sample after the layer transfer. The idea is to replace the process step of Fig. 7.2.1f by only a few additional steps: directly on the CIGS layer, we pattern an amonil layer with DAP NIL and remove the residual layer. Fig. 7.3.5 represents the SEM cross-section image of the 300 nm-thick of the structure amonil layer on a CIGS surface after the DAP-NIL process and the removal of the residual layer. After that, a thick (> 200 nm) gold back contact/mirror is deposited on the pattern. If the residual layer is correctly removed, then the gold particles are in contact with the CIGS layers.

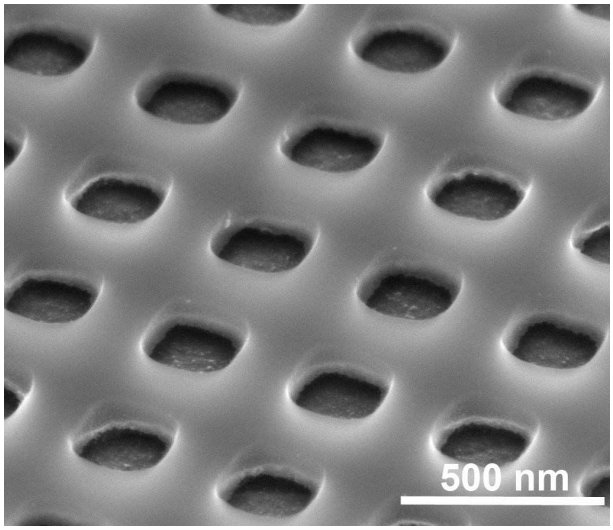

Figure 7.3.5: SEM cross-section image of the 300 nm-thick of the structure amonil layer on a CIGS surface after the DAP-NIL process and the removal of the residual layer.

Fig. 7.3.6 represents the SEM cross-section image of the fabricated structure for a 400 nm-thick CIGS layer. The period of the array is 400 nm in this case. In this picture, the ZnO:Al/i-ZnO/CdS/CIGS stack is flat. The thickness of the structure is about 100 nm. The CIGS seems to lay directly on the gold nano-structure although the gaps are filled by amonil (insulator, electrically inert). Note that the amonil can be replaced by TiO_2 sol-gel in the NIL process if needed. This is also the first realization of ultra-thin (400 nm-thick on the picture) CIGS solar cell with nano-structured back contact.

This structure is extremely interesting from two aspects. First, from an optical point of view, the light sees the back contact as a 2D nano-structured diffraction grating. According to the simulation of Chapter 6, this geometry should lead to an increase in short-circuit current of at least 10 % for a CIGS thickness between 100-400 nm. It is important to note that the CIGS layer is kept flat in the process and that the back surface is not degraded by uncontrolled etching or roughening that may lead to increased surface recombination. From a collection point of view, the contacts between the CIGS and the back contact are now localized (200*200 nm^2 in the picture). We have decreased the contact area of a factor 4, therefore decreasing the surface recombination, while conserving a high density of contacts (no increase of the parallel resistance). Potentially, we have here a structure that may increase both the short-circuit current and the open-circuit voltage compared to an unstructured cell of the same thickness.

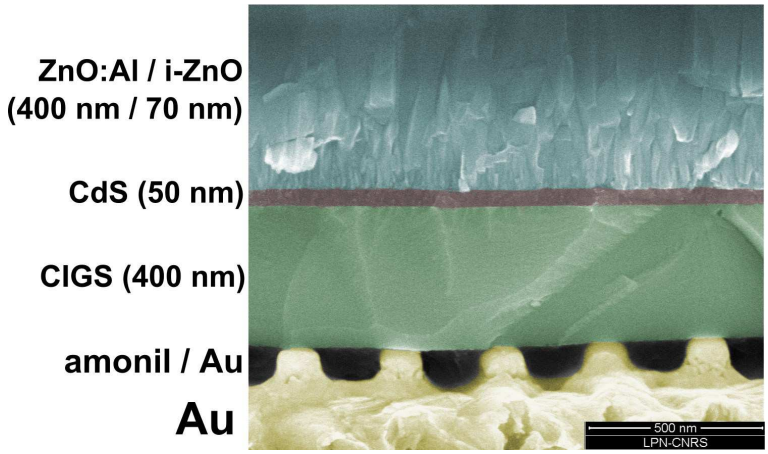

Figure 7.3.6: SEM cross-section image of the 300 nm-thick CIGS solar cell with nano-structured gold back contact by nano-imprint lithography and punctual contacts.

7.3.5 Conclusion

In this section, we have demonstrated the possibility to pattern CIGS layers at the sub-micron scale with an original DAP soft-UV nano-imprint lithography with a good resolution. In our range of thickness, the difficulty to produce reproducible samples adds challenge to the task. This to our knowledge the first realization of this kind for CIGS solar cells. Both patterning (followed by a etch for grooves for instance) and lift-off processes have been validated for moderately rough (50 nm RMS) surfaces with a relatively high numbers of defects. The technique is relatively robust and can pave the way to other studies requiring the fabrication of nano-structures on CIGS devices (or any moderately rough samples).

Validating the lift-off process on a CIGS surface is a key step toward the fabrication of nano-cavity arrays demonstrators for ultra-thin CIGS layers. However, due to the difficulty to produce homogeneous < 100 nm-thick CIGS layers, we have not pushed the development is this design too far. The efficiency of the nano-cavity array design is arguable for CIGS thicknesses superior to 100 nm. Either way, the CIGS thickness should be controlled precisely as it is a critical parameter of the optimization, which is not the case actually for our process. Moreover, the integration of nano-particles embedded in the front contact and its potential influence on the increased recombination need to be studied precisely.

The aim of our application CIGS was really to focus on actually working devices. That is why we have developed an original process to fabricate a back mirror nano-structure for CIGS solar cells that takes advantage of the superstrate configuration of the sample after the layer transfer. The advantage of this design is to integrate

the light-trapping scheme at the back contact (no need for passivation and less parasitic absorption in metal compared to the front structure approach). According to simulation and literature, this back grating should raise the short-circuit current by 10 % by trapping red-photons in waveguide modes inside the CIGS layer, regardless of the CIGS thickness. This is a good point as the uncertainty of the CIGS thickness is at stake in our process. First optical characterizations are presented in the next section.

Moreover, the point contacts formed with this back structure also allow to reduce the contact area by a factor 4 while conserving a high density of contacts. This could lead potentially to enhanced open-circuit voltage. The property of this hybrid contact is to be studied theoretically, numerically and experimentally in order to validate its potential, however.

This design can be adapted to any crystalline solar cell design as all the layers are kept flat. The universality of this method is a very good point as for similar experimental nano-photonic schemes has been proposed for crystalline solar cells technologies yet.

7.4 Optical characterization of back nano-structured CIGS solar cells

To verify the simulations of Chapter 6 , reflection measurements were carried out on the samples fabricated through the substrate transfer process and the NIL back mirror structure (see for instance Fig. 7.3.6). The optical setup used for the measurements is the same as for Chapter 5: a Sentech reflectometer and the Gognio-VISIR FTIR setup. The measure is made on a CIGS sample of estimated thickness 300 nm and for a back structure of optimal period (period $p = 500$ nm, width $w = 250$ nm, thickness $t = 100$ nm) processed on several samples with different thicknesses.

For comparison purposes, the measured reflection spectra are compared with numerically simulated reflection spectra obtained for the corresponding 300 nm ideal structure (refer to Chapter 6).

Fig. 7.4.1 represents the specular reflectivity spectra measured at normal incidence on a 300 nm-thick (estimated) CIGS solar cell with (red) and without (blue) back nano-structure. The simulated R spectra of the structure with and without nano-structure are plotted in black for comparison (see Chapter 6).

As expected by the simulation, the back mirror structure decreases the reflectivity in λ =700-1200 nm range of the whole samples as it enhances the absorption in CIGS. The simulated R spectra seem to be in a qualitative accordance with the measure although it displays interference effects absent in the measure because of

the residual roughness of the sample.

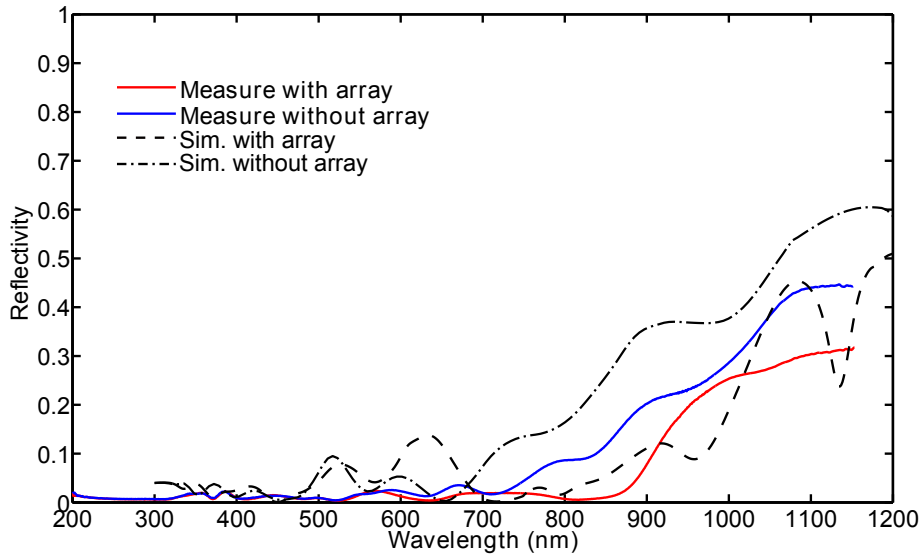

Figure 7.4.1: Measured specular reflection spectrum measured at normal incidence on a 150 nm (estimated) CIGS solar cell with (red) and without (blue) structure. These spectra are compared to the simulated R spectra of the corresponding stack with and without nano-structure.

7.5 Conclusion and perspectives on optoelectronic characterization of ultra-thin nano-structured CIGS solar cells

In this chapter, we have first presented technological developments centered around two key points: achievement of ultra-thin CIGS solar cells and pattering of CIGS surfaces. Our objective was first to fabricate and experimentally validate the potential of the metallic nano-structures studied in Chapter 6. Yet, the encouraging results obtained go beyond the scope of this manuscript and pave the way to further studies on ultra-thin CIGS solar cells such as advanced CIGS surface characterizations and novel light management by patterning CIGS solar cells (or inhomogeneous devices).

In our case, we have proposed an original way to pattern robustly the back surface of an ultra-thin CIGS solar cell on a large area and minimal equipment through DAP soft-UV nano-imprint lithography. This process allows to fabricate an optical back nano-structured metallic mirror that enhances the absorption in the structure (validated experimentally) with all the more reason an increase in

short-circuit current (see simulations of Chapter 6). On an electrical point of view, this hybrid back contact is also interesting: reducing the contact area by a factor 4 while conserving a high density of contacts, leading potentially to enhanced open-circuit voltage.

The first optoelectronic characterizations of approximately 300 nm-thin CIGS samples fabricated from thick ZSW layers unfortunately to heavily degraded devices (0.5 cm^2 patterned area with for instance: $J_{sc} = 7.6\,mA/cm^2$, $V_{oc} = 350\,mV$, $FF = 25\,\%$ and a conversion efficiency of 1 %), due to shunt issues.

Currently, we are re-runing the process on new samples with more a higher density of smaller diodes to prevent shunts and to enable a statistical study of the device. Moreover, the samples are now fabricated from 300 nm CIGS layers grown by co-evaporation at IRDEP. The increased control over the CIGS growth leads to a better success rate in the sample fabrication. For now, encouraging rectifying dark IV measurements have been obtained with a satisfying dark current density.

The perspectives at short-terms are obviously to perform further characterizations of these new devices (EQE, 1 sun IV) after a few setup developments. Then, the potential of the back structure with point contacts has to be evaluated properly from an optical (EQE measurement) and a electronic point (IV curves) point of view, compared to an unstructured solar cell.

Conclusion and perspectives

General conclusion

In the frame of this thesis, we have proposed original light-management schemes for crystalline ultra-thin solar cells through numerical and experimental studies. We have seen in Chapter 1 that a strong reduction of the solar cell thicknesses is a promising way to lift constraints on the large scale development of the photovoltaic technology. One of the main challenges is to be able to confine and absorb efficiently light in very small volumes. The literature overview of Chapter 2 demonstrates the actual ferment in the research field of nano-photonics applied for solar cells. Our goal was to offer new solutions for ultra-thin crystalline solar cells in particular.

First, we have followed an uncommon approach by proposing an ultra-thin structure, motivated more by the optical performances than the device property. In particular, we have drawn our inspiration from plasmonics and metallic gratings and their unique ability to control light at the nano-scale. In Chapter 3, I have introduced the metal/insulator/metal structure for omni-directionnal absorption in very small volumes along with the numerical code used in this manuscript.

Nano-cavity array design for broadband multi-resonant absorption in ultra-thin GaAs layer

The first important result of this manuscript is the proposition of the nano-cavity array design to enhance the absorption in ultra-thin semiconductor layers. This is especially adaptable to crystalline materials as it keeps the stack flat. In a first step, this structure has been demonstrated in the case of GaAs. In Chapter 4, we have proposed an in-depth numerical analysis of this design, inducing a broadband multi-resonant absorption spectrum in 25 nm-thick layer GaAs layer. This spectrum is obtained with the combination of Fabry-Pérot resonances (classic and plasmonic). In the 2D-design, the average total absorption value on the range $\lambda = 550 - 800$ nm is 81 %, with a 100 % absorption peak at $\lambda = 670$ nm. According to our simulation, 85 % of the light which is absorbed by the stack is absorbed in the semiconductor area. Beyond performances, we have highlighted

several important properties: 1) its insensitivity to incident polarization and angle; 2) the limited absorption losses in the metal (<15 %) despite the presence of the grating on the front surface of the cell; 3) the multi-resonant behavior in very small volumes; 4) the total absorption at resonant wavelength. We have proposed a detailed analysis of the mechanisms at stake and provided guidelines for the optimization of its performances.

We have reported the fabrication of first ultra-thin GaAs demonstrators in Chapter 5. First, the optical characterizations of the samples have shown a good agreement with the numerical analysis of the absorption mechanism. Absorption enhancement due to Fabry-Perot resonances has been evidenced. Second, the addition an extra ZnO:Al coating for encapsulation, front contact, and anti-reflection coating purpose has allowed to broaden even more the absorption spectrum. An average total absorption of 85 % in the $\lambda = 200 - 1200$ nm range has been measured on a $\theta = 0 - 50\,^\circ$ range, a performance well above the state-of-the-art in this domain. However, the experimental devices have shown several differences with the numerical structure, such as the spectral position of the MSM resonance.

Application to GaSb and CIGS structures

After validating experimentally the nano-array cavity design for GaAs, an additional proof of its versatility was to adapt this design for other materials.

In the frame of ANR THRIPV, the high-injection of carriers in very small volumes has been identified has a key point to achieve the extraction of un-thermalized carriers. We have therefore proposed a design for a 25 nm-thick GaSb idealized layer in the context of hot carrier solar cells. It results in a very broad, multi-resonant absorption spectrum harvesting 68 % of the power available regardless of the numerical aperture. The metallic array improves therefore significantly (about 50 %) the absorption compared to a simple 25 nm-thick GaSb layer on a silver back mirror. The result has been used in theoretical simulation of hot carrier solar cell conversion efficiency, resulting in an evaluation as high a 38 % [65]. Moreover, our design turns out to be technologically feasible and motivates future prospects and developments in the field of GaSb hot carrier solar cells at IRDEP.

Alternatively, CIGS solar cells are a technology that displays amongst the highest efficiencies of the second generation but has to face the shortage of one of its constitutive element: indium. This has motivated several projects such as the french ANR project ULTRACIS whose objective is to reduce drastically the thickness of CIGS solar cells from 1 µm down to 100 nm. In this manuscript, we have demonstrated the potential of the nano-cavity array design for a 45 nm-thick CIGS layer by achieving a very promising absorption in CIGS above 80 % on the $\lambda = 400 - 1100$ nm range. We have also successfully implemented this solution to a more complete idealized 100 nm-thick CIGS solar cell with +5 mA/cm^2 absolute increase in theoretical photo-current compared to the flat 100 nm-thick CIGS

solar cell on Ag. Although ambitious, the nano-cavity array structure display impressive results in term of absorption enhancement in ultra-thin semi-conductor layers. These results paves the way to the future study of ultra-thin to GaAs, GaSb and CIGS solar cells allowing a strong reduction of the absorber thickness while keeping a high short-circuit current density.

Alternatively, we have demonstrated numerically the potential of a back nano-structured mirror design to enhance absorption in flat solar cells in the 100-400 nm thickness range. For the CIGS case, the short-circuit current enhancement is constant at a value of 11 %, regardless of the thickness of CIGS and for a constant period of 500-600 nm.

Fabrication and characterization of ultra-thin CIGS solar cells in the frame of ANR project ULTRACIS

Although presented briefly in this manuscript, the experimental results on ultra-thin nano-structured CIGS solar cells of Chapter 7 has represented a large amount of work for me and the collaboration. The first result of this chapter was the development of a robust, large area patterning for CIGS systems through polishing and nano-imprint lithography. This result represents a promising opportunity for further prospects in either front or back nano-structured CIGS solar cells.

The ULTRACIS collaboration is today able to produce routinely working 300 nm-thick CIGS solar cells transferred on alternative mirrors/contacts. However, with this technique or with direct growth of the absorber, it seems for now impossible to produce consistently un-shunted devices thinner than this value. Although all technological steps have been developed, the nano-cavity array design is not applicable until at least 100 nm-thick devices are produced.

However, in this manuscript, an innovative fabrication process of thin back nano-structured CIGS solar cells is presented. From an optical point of view, simulations and first characterization have confirmed absorption enhancement at long wavelengths. However, in literature, this solution was limited until now to amorphous solar cells. The originality of our approach is to process a back nano-structure to a planar solar cell, taking advantage in our case of the superstrate configuration of our CIGS samples after the layer transfer. From an electronic point of view, the point contacts also allow to reduce the contact area by a factor 4 while conserving a high density of contacts, leading potentially to enhanced open-circuit voltage.

Perspectives

From broadband absorbers to ultra-thin crystalline solar cells with nano-cavity array design

Our results on ultra-thin metal/GaAs/metal absorbers are very promising. Nevertheless, some points in the numerical and experimental studies still remain to be

clarified. First, the numerical results of Chapter 4 have shown that the absorption mechanism is complex and some of its properties are not fully understood yet. In particular, the absorption in the metal is very low and this remains a surprising, yet beneficial, property. Moreover, a deeper analysis of the effect of the geometrical parameters on the critical coupling condition would be interesting to pursue to go further in the optimization of our structure. We can also think of other refinements to optimize further the performances of our structure. For instance, a more efficient anti-reflection coating should allow to maximize even more the absorption in the semiconductor layer. In the same way, the symmetry breaking and the trapezoidal shape of the particles are undoubtedly an interesting track to pursue to broaden the MSM resonance. Moreover, this same resonance is already broaden in our experiment compared to simulation. This aspect should be investigated further to take advantage of it. This would require a better control during fabrication and further studies. From a fabrication aspect also, a few points are to be improved, such as the control of the properties and the tarnishing of our silver grating. An interesting short-term idea is also to replace the gold mirror by a silver mirror. According to simulation, this should allow to reduce the optical parasitic losses in our structure.

However, the most limiting factor in this study is the impossibility to realize further optoelectronic characterizations. Indeed, the very next step is the integration of this design to a working device. In this perspective, 25 nm of GaAs for instance is pretty ambitious for our current knowledge and we are investigating devices around 100 nm-thick. The optimization of the optical and electronic properties of this ultra-thin structure should be led in parallel as the thickness of the junction directly impose the spectral position of at least one Fabry-Pérot resonance inside the structure. Amongst other issues, the use of silver is to be carefully studied (best for optical performances but hard to process, diffusive at low temperature and unstable). Considering the amount of work and depending on the objective, coupling optical and electronic simulation [185] is a promising solution to converge faster to a breakthrough device, regardless of the nanophotonic light-management scheme.

Concerning GaAs solar cells, one would not obviously aim to ultra-thin junctions because conversion efficiency is more important than cost in this particular case (although the conclusion might be different for CIGS solar cells because of the indium issue). Anyway, our approach opens novel perspectives towards ultra-thin crystalline solar cells with a thickness of 50-200 nm. The very promising performances of this structure in terms of broadband light confinement are an additional motivation to pursue further studies of both ultra-thin junctions (an maybe ballistic approaches) and new concepts that require ultra-small volumes (hot carrier solar cells). It can also be applied to other systems such as photodetectors or

thin-film thermal emitters.

Ultra-thin CIGS nano-structured solar cells: *perspectives of the ANR project ULTRACIS-M*

Recently, new ultra-thin nanostructured CIGS solar cells have been fabricated following the back mirror nanostructure process of Chapter 7 with CIGS co-evaporated at IRDEP. To be able to control each step of the process and to reduce the process time has led to the fabrication of proper and cleaner samples. The early characterizations of these samples have led to promising optical and dark IV measurement. The short-term perspectives of the ANR ULTRACIS-M are obviously to characterize further these new demonstrators to evidence both the expected increase in short-circuit current and open-circuit voltage. Amongst the potential improvements, we can think of a better treatment and protection of the CIGS surface, a more rigorous control of the sample thickness and roughness and, of course, the multiplication of samples in order to do statistical measurements.

Mid-terms perspectives include the direct growth of ultra-thin CIGS layers on alternative patterned substrate with the IRDEP and the Institut des Matériaux Jean Rouxel of Nantes. This would allow to remove the substrate transfer and the etching/polishing step and therefore to ease the general process, leading to a larger amount of samples available for further studies.

In a last note, this thesis has been the result of the encounter between nanophotonics and photovoltaics. This peculiar research field is nowadays in full expansion, aiming toward the ultimate low-cost high-efficiency solar cell. The competition between different technologies is strong. The common thread of this thesis has been to propose light-trapping schemes that can be applied regardless of the system. The nature of our study was therefore very exploratory. We have focused our research on metallic nano-structures and crystalline technologies. Eventually, we were able to propose two structures adapted for different solar cell thicknesses: one for ultra-thin structures in the 25-100 nm range (nano-cavity array) and one for thin structures in the 100-400 nm (flat back mirror structure).

The first structure is born from our desire to propose something new and ambitious, with a voluntary strong reduction in thickness and a will to design first a structure from an optical point of view. The nano-cavity array design is an original design, both from a photovoltaic and a nano-photonic point of view, that allows an impressive absorption enhancement for ultra-thin structures. Moreover, it fulfills all the requirements for a PV light trapping structure: angle and polarization independence and low parasitic losses. This work really motivates further studies on ultra-thin structures: new junctions and new concepts for PV (ballistic trans-

port, hot carriers solar cells, up-conversion concepts from Andriamiadamanana *et al.*[66]) or other area (photodetectors).

The second structure completes our work on light-trapping structures by dealing with solar cells in the 100-400 nm range. Our goal with the back nano-structure design was to propose a design immediately applicable to devices that can not be thinner than 100 nm for now, either from a fabrication or an electronic point of view. We have proposed a structure and a process that is original for CIGS solar cells. This structure is potentially promising to increase both the short-circuit current and the open-circuit voltage, regardless of the thickness and the technology.

In this manuscript, promising results have been obtained for GaAs, GaSb and CIGS structures. However, this concept could be extended further to other thin film materials such as CdTe or thin-film silicon (see for example the results of our team and collaborations on a-Si:H from Massiot *et al.* [162, 163] and up-conversion concepts from Andriamiadamanana *et al.* [66]).

Along with novel light trapping schemes, we have developed key technological steps for the fabrication of ultra-thin GaAs and CIGS nano-structured solar cells. Whatever the considered technology, this thesis has shown that the efficient implementation of advanced light-trapping structures requires a synergy between numerical design, material science and nanofabrication techniques.

Appendix

Appendix A

Optical constants used in the numerical calculations

In this appendix, we give the optical constants used in the numerical simulations presented in this thesis. For each material, the reference is given as well as a plot of the real and imaginary parts of the refractive index.

A.1 Optical constants of CIGS

There are very little data on poly-crystalline $CuIn_{1-x}Ga_xSe_2$ thin films with varying Ga contents. Moreover, taking a closer look at the different available optical data obtained through either ellipsometry or transmittance measurements shows sensible difference in the absorption coefficient, even at the same Ga content. The determination of optical properties is more difficult than for the other layers in the structure because of the following complications:

- **High surface roughness**: Device-quality CIGS films have a relatively high surface roughness. The roughness depends on the specifics of the deposition process. For our baseline process, the root-mean-square (RMS) value of the surface roughness (σ_{RMS}) is typically 5% of the film thickness. The surface roughness distorts the spectrophotometric as well as the ellipsometric response of the film relative to the case of smooth surfaces, in a way that is not trivial to take into account. For example, effective medium theories for the roughness layer are not applicable when σ_{RMS} is comparable with ($>$ 10% of) the wavelength of the light.

- **Surface overlayers**. An unprotected CIGS surface is known to react with the atmosphere. The surface overlayers formed, essentially indium oxides, have lower refractive index than the CIGS material, which affects the optical

response. In particular, the reflectance is lowered since the surface overlayers act as index-matching anti-reflective coatings.

- **High absorption coefficient**. The high absorption coefficient of Cu(In,Ga)Se2 implies that a non-vanishing transmittance throughout the spectral region of interest is obtained only for very thin films. Thus, methods for determination the optical properties relying on the transmittance cannot be applied for films of standard thickness. This is a potential problem, since thinner films may have different optical properties (due to different crystal quality) than standard-thick films. Note that high absorption coefficient is not a problem for ellipsometry.

- **Density of the material**. In addition to the influence of the surface properties already discussed, differences in bulk properties might contribute to discrepancies between data. In particular, the density of the films can differ between samples. Lower density is expected for thin films relative to bulk material, which could contribute to the decrease in k-values. This implies that the density is lower for the films on glass than for the films on Mo, an effect that is probably related to a difference in substrate temperature.

Three interesting optical data for CIGS are the following:

- Alonso et *al.* determined by spectroscopic ellipsometry the optical properties of bulk samples of polycrystalline $CuIn_{1-x}Ga_xSe_2$ with $x = 0.2$, 0.4, 0.6, and 0.75 [235]. The surface roughness and surface overlayers were addressed by careful mechanical and chemical polishing.

- Paulson *et al.* *[206]* solved the surface roughness issue of thick co-evaporated $CuIn_{1-x}Ga_xSe_2$ films in an elegant way: the films were peeled off from the Mo substrate (a technique similar will be used in Chapter 3.), and the optical properties could then be measured by spectroscopic ellipsometry on the smooth back surface side. The influence of oxidation was reduced by characterizing the films immediately after peeling. Results were reported for x=0.00, 0.31 0.45, 0.66 and 1.00.

- Orgassa et *al.* determined n and k from R- and T-measurements at normal incidence of co-evaporated $CuIn_{1-x}Ga_xSe_2$ thin films with Ga content $x =$ 0.00, 0.23, 0.51, 0.73 and 1.00 [71, 201]. By using thin samples (210 nm – 270 nm), smooth surfaces (σ_{RMS} measured to a few nanometers by atomic force microscopy, AFM) and high enough transmittance was obtained.

The different sets of extinction coefficient data are plotted on Fig.A.1.1. We have plotted sets of data with Ga contents close to the material we use in Chapter 7. We

can see that there is not much of a problem for n values for there are quite similar between the studies. For k values however, we can start be seeing that all data from Alonso et *al.* are overestimated on the whole visible range, probably due to the fact that that her data are for bulk single crystals, while the other data are for poly-crystalline thin-film. It can be noted that Alonso did not include results for $k < 0.1$, since they were judged inaccurate. The ellipsometry data of Paulson also states that $k > 0$ is obtained also for subbandgap (long) wavelengths, in disagreement with k-values by Orgassa, obtained from RT-measurements, which decrease sharply to $k = 0$ at the band-edge. The determination of k by ellipsometry is know to be difficult for wavelengths close to the bandgap whereas this region is critical for the photocurrent generation. Therefore, for this region we will favorise the R-T measurements done by Orgassa. On the other hand, for photon energies well above the bandgap, the data from Paulson *et al.* are the most accurate available, since the smooth back surfaces of standard-thick films were characterized.

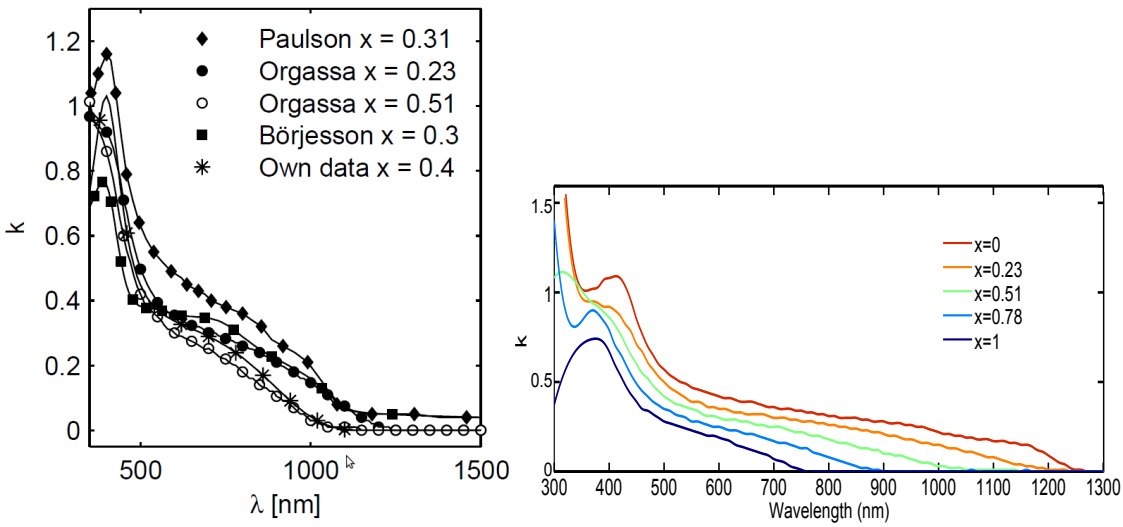

(a) (b)

Figure A.1.1: (a) CIGS extinction coefficient data plotted from Alonso et *al.* [235], Paulson *et al.* *[206]*, Orgassa et *al.* [71, 201] and Malmstrom *et al.* [78] for different Ga content. From Malmstrom *et al.* [78]. (b) Imaginary part of the refractive index of CIGS measured by Orgassa et al. [71] for several gallium contents.

More than for mono-crystalline materials, due to its nature and its relative youth, CIGS is hard to manipulate in laboratories. Considerable efforts are cur-

rently made to understand the materials and better ways to process it in order to characterize it properly.

On conclusion, we use the data plotted on Fig.A.1.2. The n values are the Paulson *et al.* for a Ga content of $x = 0.31$. For the k-values, we will use the k-values of Paulson *et al.* in the for a Ga content of x=0.31 for wavelengths below the bandgap (determine with the empirical approximation of Dullweber *et al.*[40]: $E_g(x)[\text{eV}] = 1.02 + 0.67x + 0.11x(x-1)$). For wavelengths above the band-gap, we will use an linear interpolation with the same «coefficient» than the Orgassa's data for a Ga content of $x = 0.23$. This approximation is not perfect but is satisfying for our purpose.

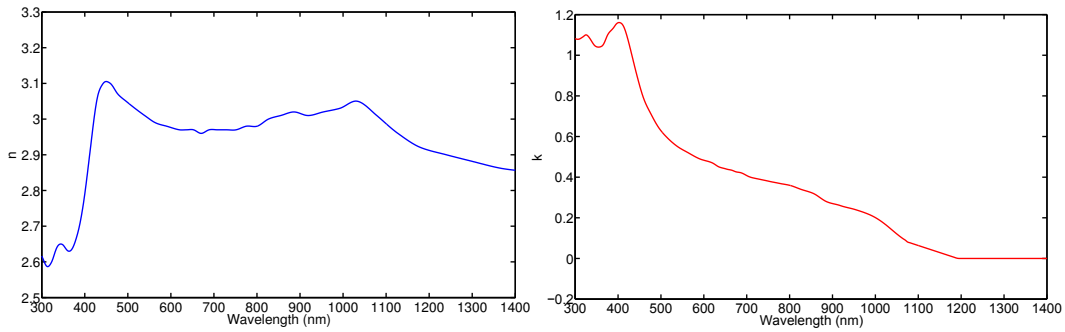

(a) (b)

Figure A.1.2: Real (a) and imaginary (b) parts of the refractive index of CIGS

A.2 Optical constants of CdS

Cadmium sulphide is a semiconductor with an optical band-gap around 2.4 eV (515 nm). It crystallizes both in hexagonal closed-packed (wurtzite) structure and cubic fcc (zinc-blende) structure; the hexagonal structure is slightly more stable. In thin films of CdS prepared by CBD, both structures are normally present. The optical properties of bulk CdS have been measured many times. A good reference source is the CdS chapter in Handbook of optical constants of solids (II) [69], but there are also many newer publications available, for instance by [236]. However, the refractive indexes for thin film CdS is known to be significantly lower than bulk materials.

Moreover, it would be more interesting to determine the optical properties of CdS grown on device quality Cu(In,Ga)Se2 film because the material properties of CdS strongly depend the growth technique and the substrate used. However, due to the high roughness and uncertainties about the optical data of CIGS, there are to date no such satisfactory data and most of the studies focused on CdS

on glass substrate. We could cite ref. [207] for evaporated CdS thin films. They determined the optical properties of evaporated thin films of CdS (and ZnS) in the range 250-2500 nm from reflectance and transmittance measurements, including the effect of surface roughness into their model. On the other hand, the best data so far available for CBD-CdS on glass is probably found in the thesis of ref. [201]. He determined the refractive index of samples prepared using the a recipe for high performance CIGS cells on glass (about 80 nm).

In the following calculation, we will take the refractive indexes from ref. [207] for evaporated CdS thin films plotted in Fig. A.2.1.

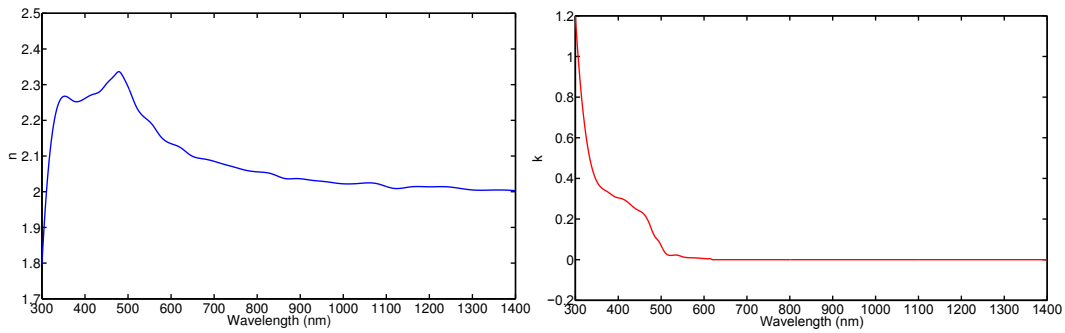

Figure A.2.1: Real (a) and imaginary (b) parts of the refractive index of CdS.

A.3 Optical constants of Mo

The optical constants of molybdenum used in the numerical calculations and displayed in Fig. A.3.1 are taken from Erfurth *et al.* [86] in the case of a real Mo/$MoSe_2$ interface.

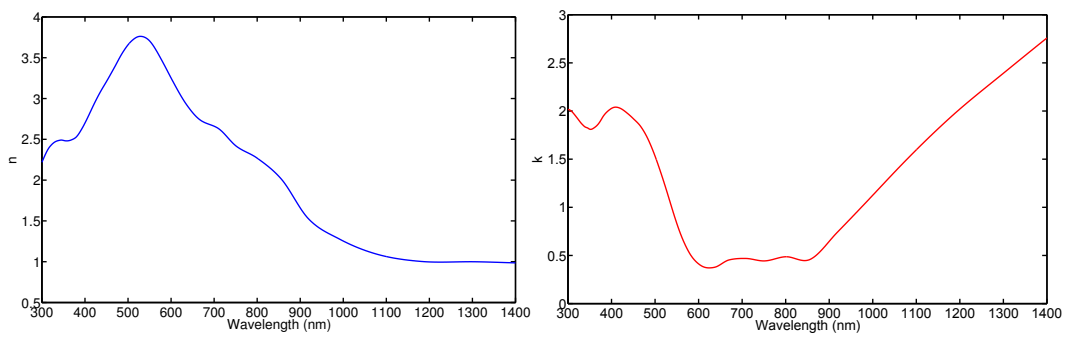

Figure A.3.1: Real (a) and imaginary (b) parts of the refractive index of GaAs.

A.4 Optical constants of GaAs

The optical constants of c-GaAs used in the numerical calculations and displayed in Fig. A.4.1 are taken from Palik [69], p. 429-443.

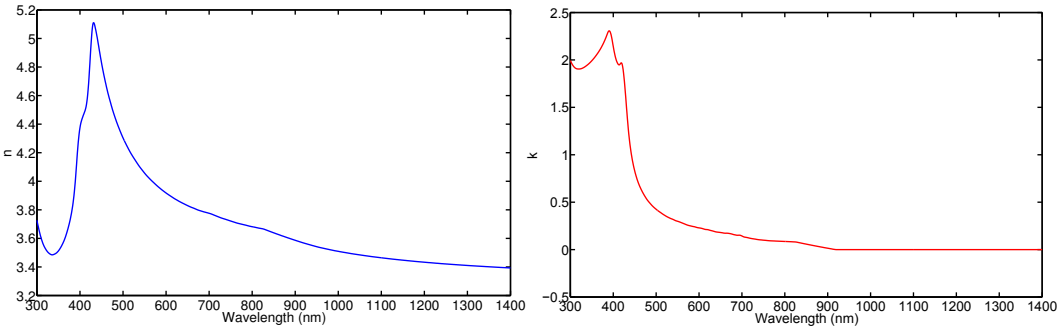

Figure A.4.1: Real (a) and imaginary (b) parts of the refractive index of GaAs.

A.5 Optical constants of GaSb

The optical constants of c-GaSb used in the numerical calculations and displayed in Fig. A.5.1 are taken from Palik [69].

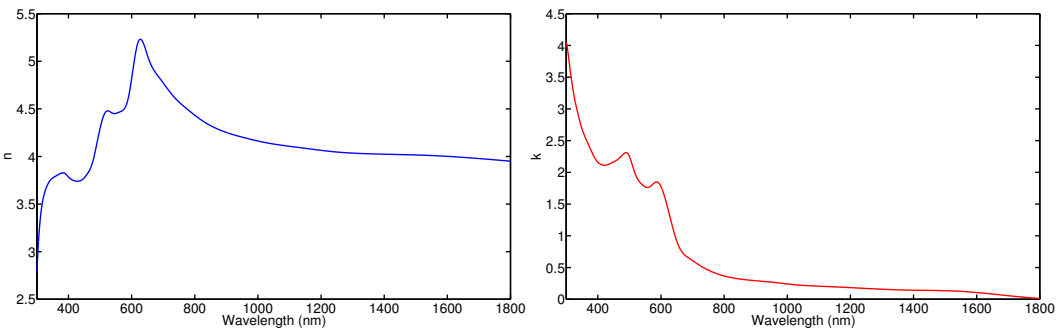

Figure A.5.1: Real (a) and imaginary (b) parts of the refractive index of GaSb.

A.6 Optical constants of silver

In this thesis, we have used two sources for the optical constants of silver: Palik [69] p. 350-357 and Johnson and Christy **(author?)** [183]. Both data are shown in Fig. A.6.1

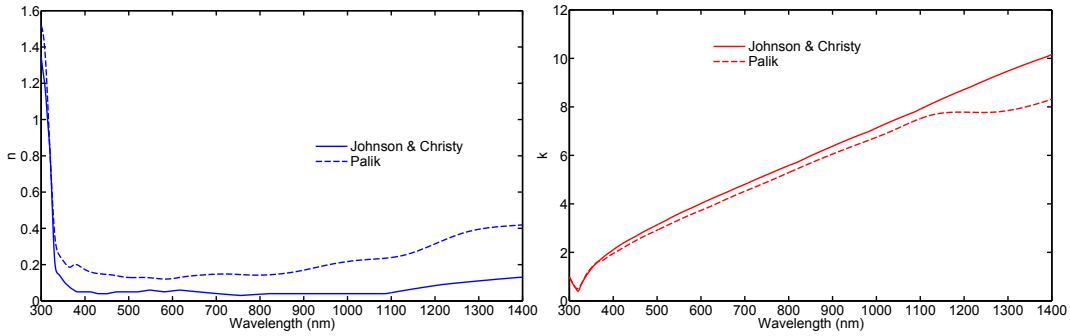

Figure A.6.1: Real (a) and imaginary (b) parts of the refractive index of Ag.

A.7 Optical constants of gold

In this thesis, we have used two sources for the optical constants of gold: Palik [69] p. 286-295 and Johnson and Christy **(author?)** [183]. Both data are shown in Fig. A.7.1.

In chapter 5, we have used both references to fit our experimental measurements. We have shown that data from Johnson and Christy seemed to adjust better our experimental results.

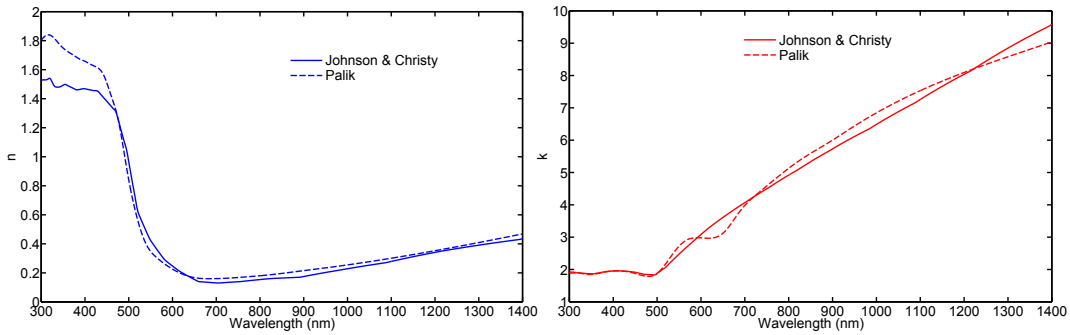

Figure A.7.1: Real (a) and imaginary (b) parts of the refractive index of Au.

A.8 Optical constants of i-ZnO

In this manuscript, i-ZnO is taken as a homogenous medium with n=2. The model is very basic yet sufficient for this study.

A.9 Optical constants of ZnO:Al

The data for aluminum-doped zinc oxyde (ZnO:Al) are taken from Ehrmann and Reineke-Koch [205] in the "bulk ZnO:Al" case (see Fig. A.9.1).

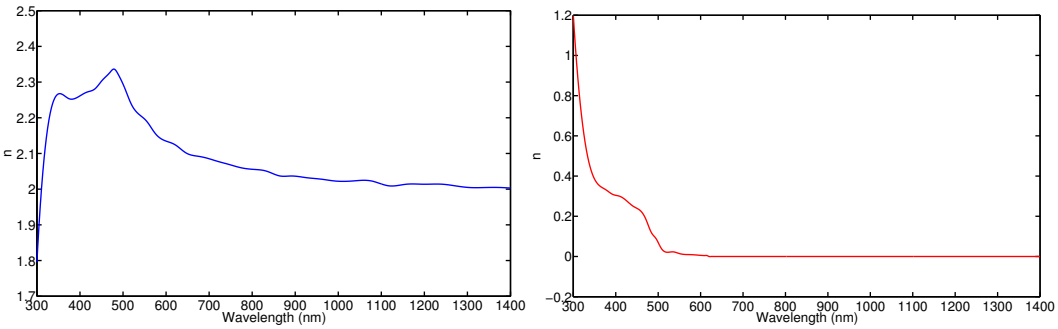

Figure A.9.1: Real (a) and imaginary (b) parts of the refractive index of ZnO:Al.

A.10 Optical constants of MgF_2

The data for magnesium fluoride (MgF_2 - tetragonal, ordinary index) are taken from are taken from Palik [69] (see Fig. A.10.1).

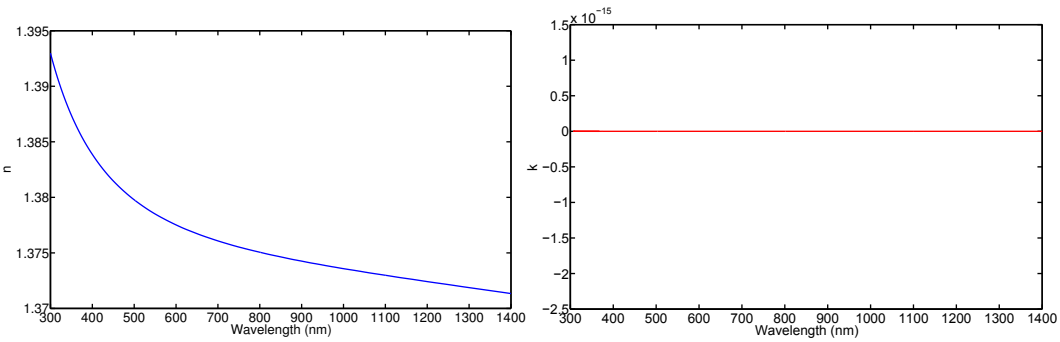

Figure A.10.1: Real (a) and imaginary (b) parts of the refractive index of MgF_2.

A.11 Optical constants of ZnS

The data for cubic zinc sulfide are taken from are taken from Palik [69] (see Fig. A.11.1).

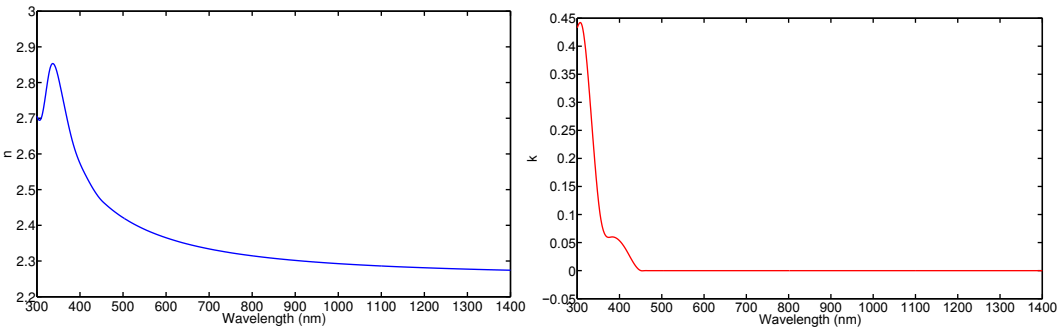

Figure A.11.1: Real (a) and imaginary (b) parts of the refractive index of ZnS.

Appendix B

Electromagnetic field intensity maps

The purpose of this appendix is to list the full electromagnetic field intensity maps (ϵ". $|E|^2$, E_x, E_z and H_y) calculated at normal incidence, TM polarization and 30 Fourier orders for the wavelengths of interest of the structure simulated in this manuscript (arbitrary units). ϵ". $|E|^2$ is proportional to the absorption, where ϵ" is the imaginary part of the dielectric constant.

B.1 25 nm-thick GaAs nano-cavity array structure of Chapter 4

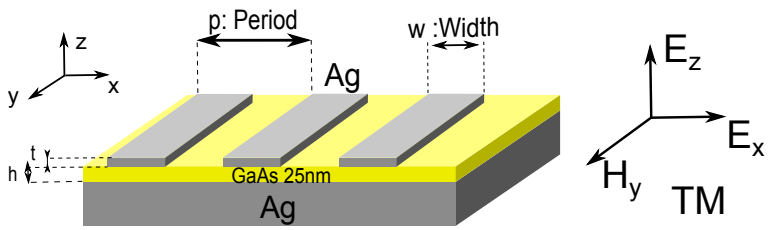

Figure B.1.1: 1D MSM nano-cavity array structure of Chapter 4. It is composed of a 25 nm-thick GaAs layer, a silver mirror and a metallic array of one dimensional (i.e. infinite along their length and the y axis) silver wires array. The definition of transverse magnetic (TM) mode is displayed.

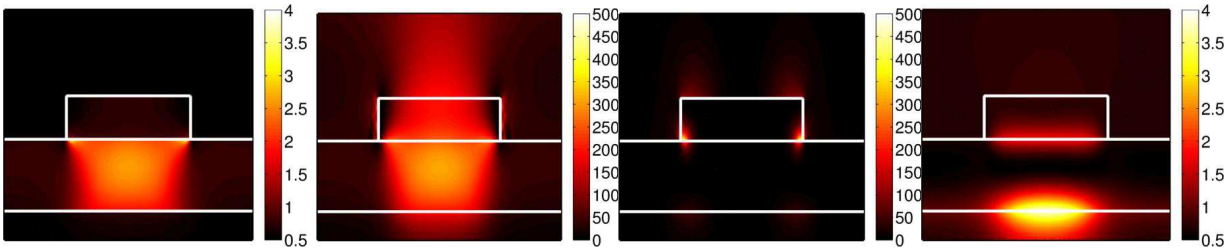

(a) $\epsilon''.|E|^2$ (b) E_x (c) E_z (d) H_y

Figure B.1.2: GaAs 25 nm $\lambda = 560$ nm

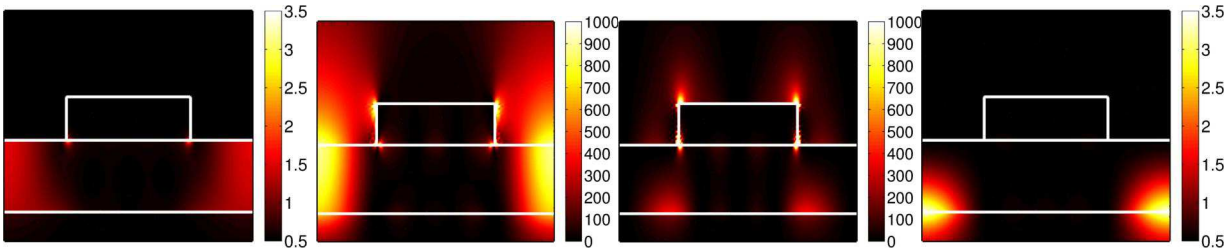

(a) $\epsilon''.|E|^2$ (b) E_x (c) E_z (d) H_y

Figure B.1.3: GaAs 25 nm $\lambda = 675$ nm

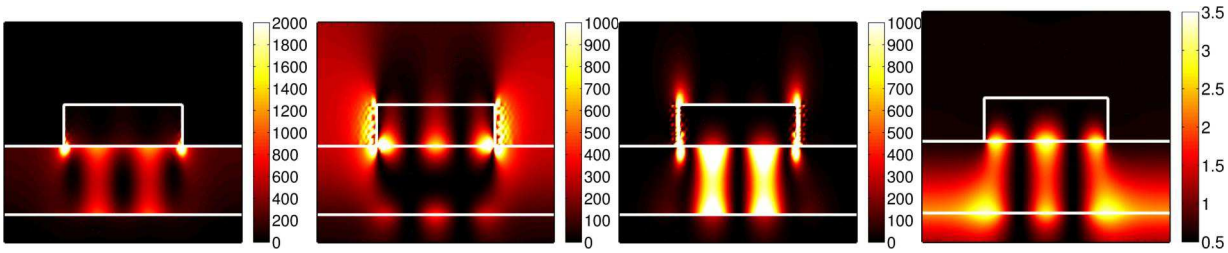

(a) $\epsilon''.|E|^2$ (b) E_x (c) E_z (d) H_y

Figure B.1.4: GaAs 25 nm $\lambda = 760$ nm

B.2 25 nm-thick GaSb nano-cavity array structure of Chapter 6

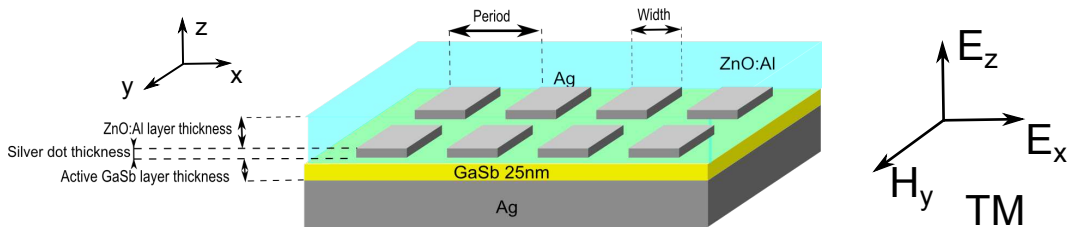

Figure B.2.1: Schematic of the 25 nm-thick GaSb solar cell of Chapter 6. It consists in a 25 nm-thick GaSb layer on a silver mirror, covered by a two-dimensional array of silver square nanoparticles (thickness t_{array} = 26 nm, width w = 170 nm, period p = 300 nm) and a 50 nm-thick n-type ZnO:Al window layer. The definition of transverse magnetic (TM) mode is displayed.

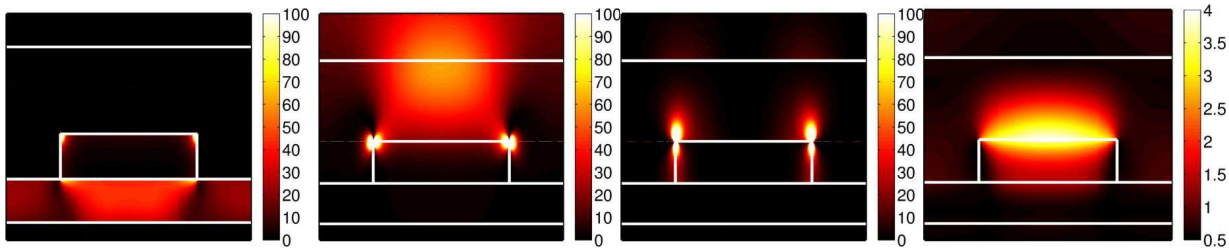

(a) $\epsilon''.|E|^2$ (b) E_x (c) E_z (d) H_y

Figure B.2.2: GaSb 25 nm $\lambda = 550$ nm

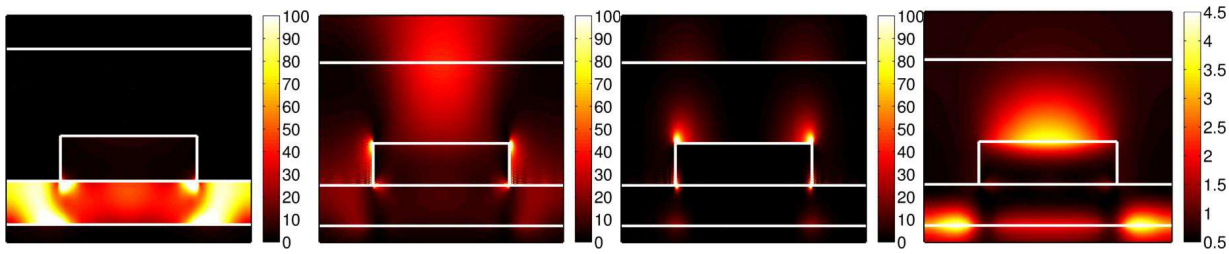

(a) $\epsilon''.|E|^2$ (b) E_x (c) E_z (d) H_y

Figure B.2.3: GaSb 25 nm $\lambda = 740$ nm

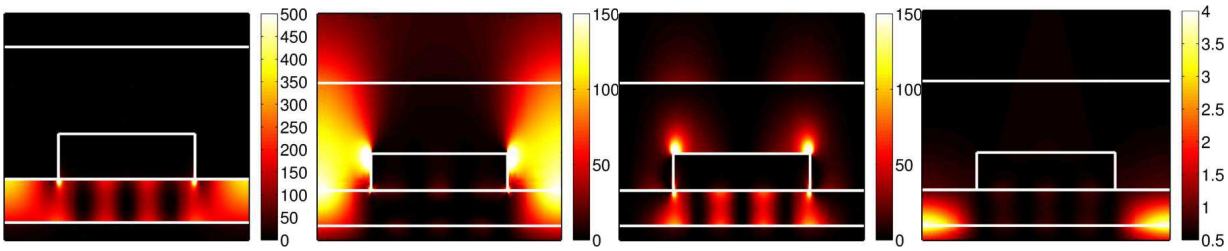

(a) $\epsilon''.|E|^2$ (b) E_x (c) E_z (d) H_y

Figure B.2.4: GaSb 25 nm $\lambda = 900$ nm

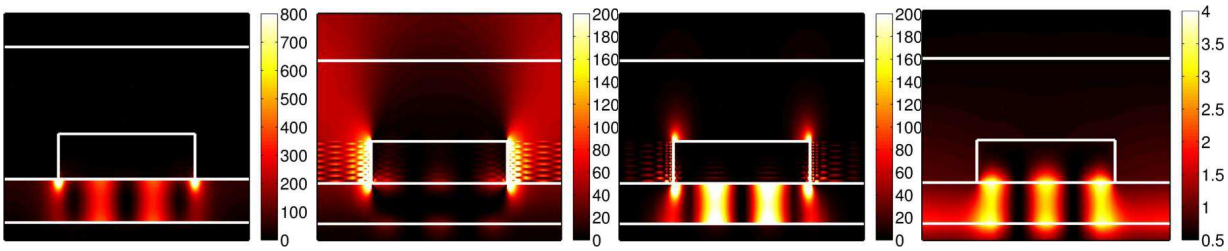

(a) $\epsilon''.|E|^2$ (b) E_x (c) E_z (d) H_y

Figure B.2.5: GaSb 25 nm $\lambda = 1090$ nm

B.3 45 nm-thick CIGS nano-cavity array structure of Chapter 6

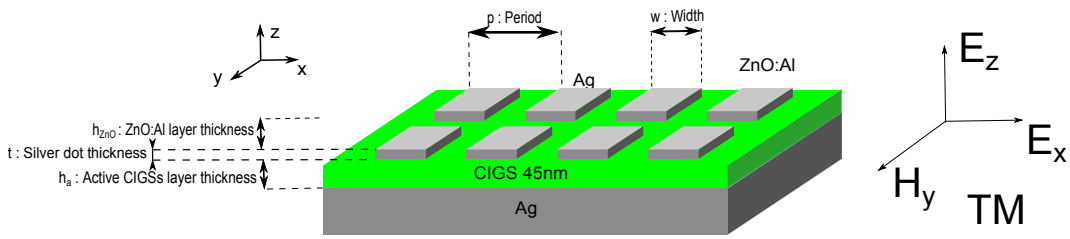

Figure B.3.1: Schematic of the 45 nm-thick CIGS structure of Chapter 6: a 50 nm-thick ZnO:Al window layer, a 2D silver nano-particles array, a 45 nm-thick absorbing CIGS layer and a silver back mirror. The parameters of the array are: thickness $t = 20$ nm, width $w = 290$ nm, period $p = 530$ nm. The definition of transverse magnetic (TM) mode is displayed.

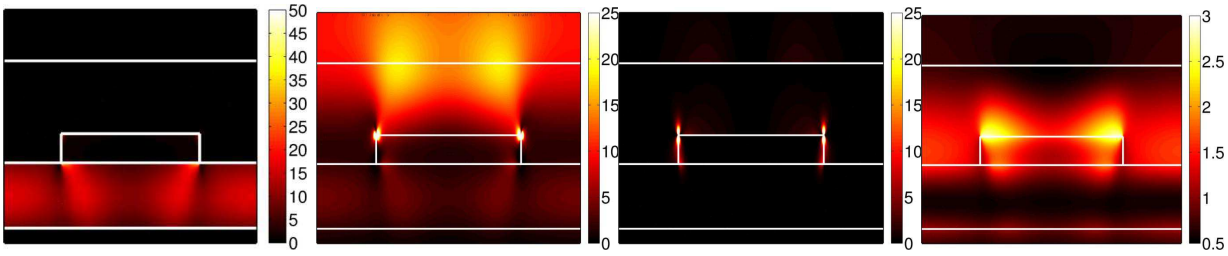

(a) $\epsilon''.|E|^2$ (b) E_x (c) E_z (d) H_y

Figure B.3.2: CIGS 45 nm $\lambda = 490$ nm

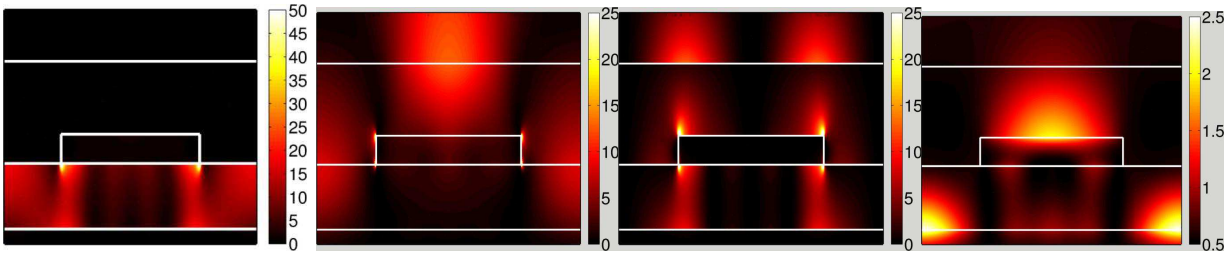

(a) $\epsilon''.|E|^2$ (b) E_x (c) E_z (d) H_y

Figure B.3.3: CIGS 45 nm $\lambda = 840$ nm

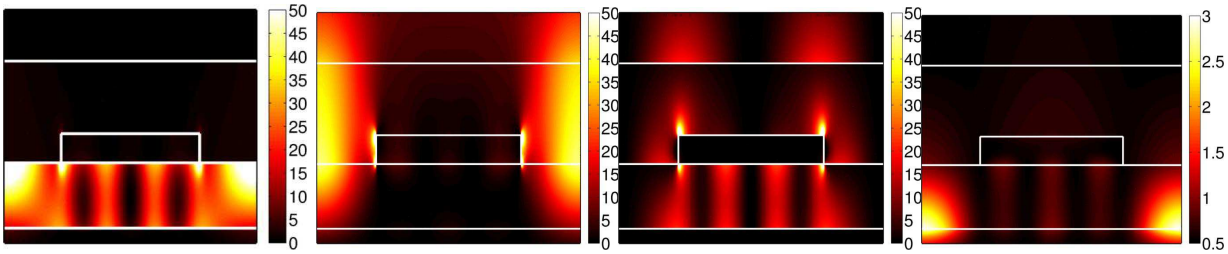

(a) $\epsilon''.|E|^2$ (b) E_x (c) E_z (d) H_y

Figure B.3.4: CIGS 45 nm $\lambda = 999$ nm

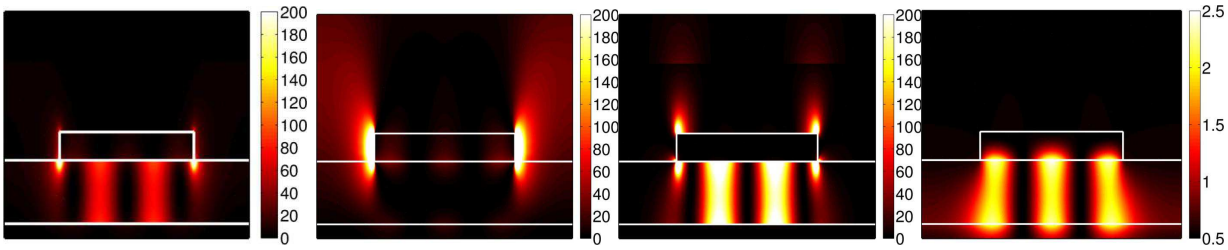

(a) $\epsilon''.|E|^2$ (b) E_x (c) E_z (d) H_y

Figure B.3.5: CIGS 45 nm $\lambda = 1100$ nm

B.4 100 nm-thick CIGS nano-cavity array solar cell of Chapter 6

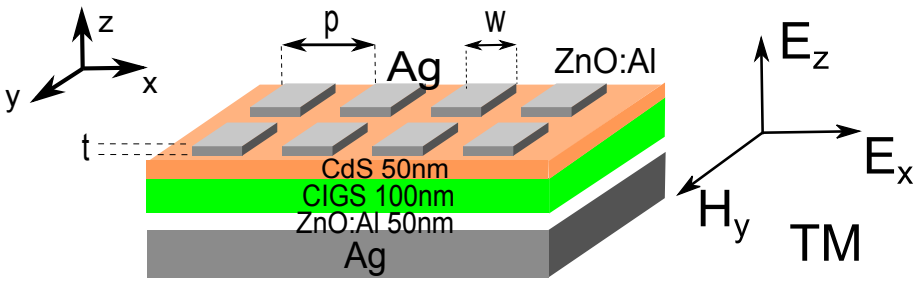

Figure B.4.1: Schematic of the 100 nm-thick CIGS solar cell of Chapter 6: a 50 nm-thick ZnO:Al window layer, a 2D silver nano-particles array, a 50nm-thick CdS layer, a 100 nm-thick absorbing CIGS layer, a 50 nm-thick ZnO:Al to prevent diffusion layer and a silver back mirror. The parameters the array are: thickness $t = 20$ nm, width $w = 290$ nm, period $p = 530$ nm. The definition of transverse magnetic (TM) mode is displayed.

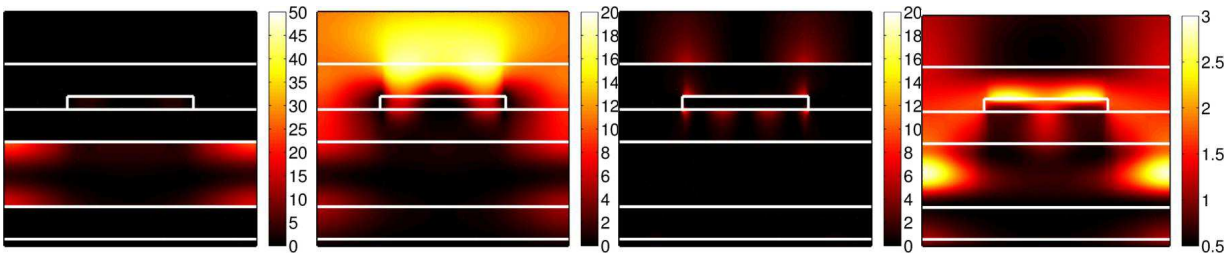

(a) $\epsilon''.|E|^2$ (b) E_x (c) E_z (d) H_y

Figure B.4.2: CIGS 100 nm $\lambda = 550$ nm

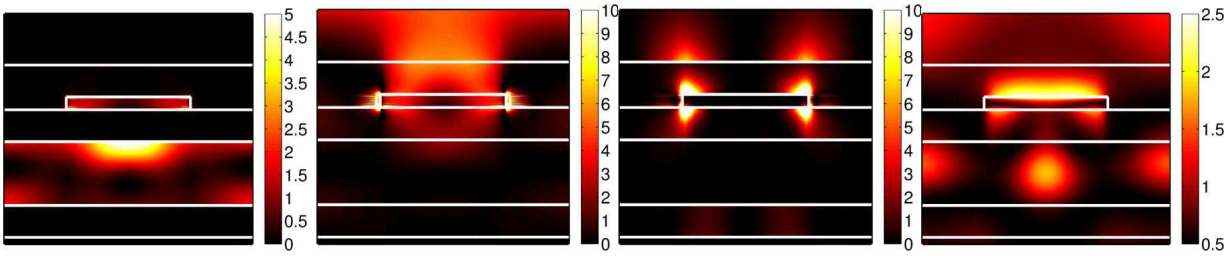

(a) ϵ". $|E|^2$ (b) E_x (c) E_z (d) H_y

Figure B.4.3: CIGS 100 nm $\lambda = 760$ nm

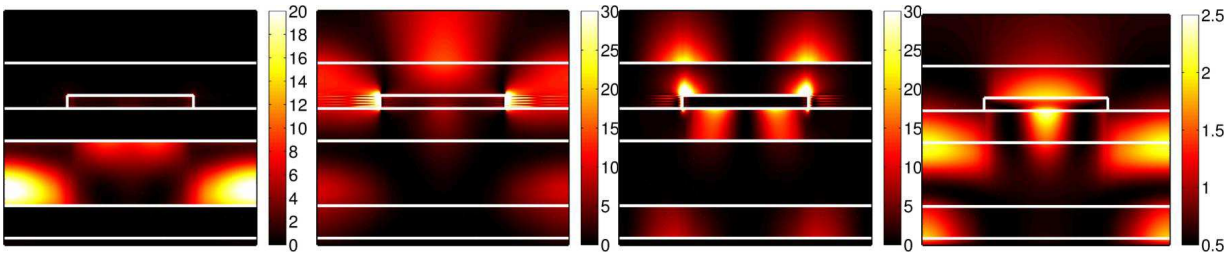

(a) ϵ". $|E|^2$ (b) E_x (c) E_z (d) H_y

Figure B.4.4: CIGS 100 nm $\lambda = 760$ nm

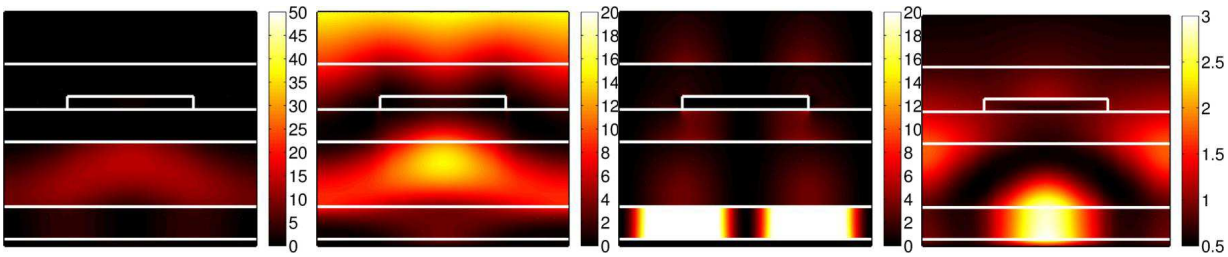

(a) ϵ". $|E|^2$ (b) E_x (c) E_z (d) H_y

Figure B.4.5: CIGS 100 nm $\lambda = 1020$ nm

B.5 Back nano-structured 150 nm-thick CIGS solar cell of Chapter 6

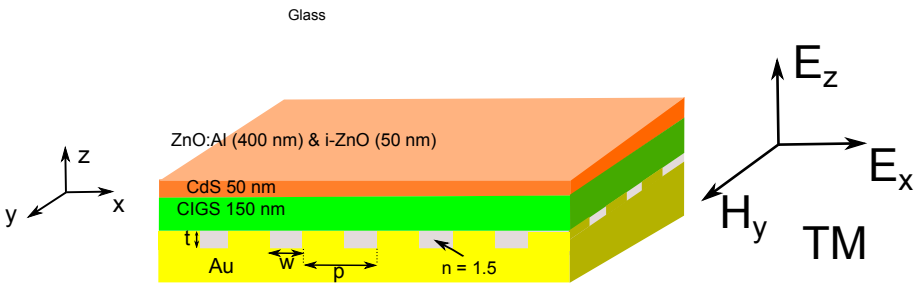

Figure B.5.1: Simulated 150 nm-thick CIGS structure with a patterned Au back mirror of Chapter 6. The parameters the back mirror are t the thickness of the structure, w the width of the structuration and p the period of the structure ($p = 600$ nm, $w = 300$ nm and $t = 100$ nm). The definition of transverse magnetic (TM) mode is displayed.

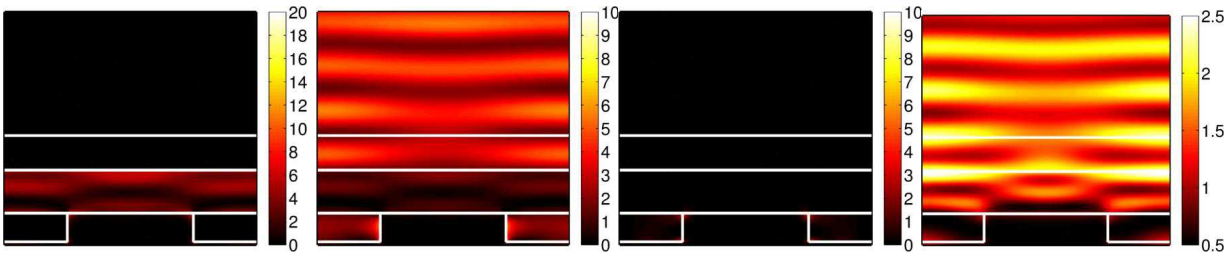

(a) ϵ". $|E|^2$ (b) E_x (c) E_z (d) H_y

Figure B.5.2: Back nano-structured CIGS 150 nm $\lambda = 560$ nm

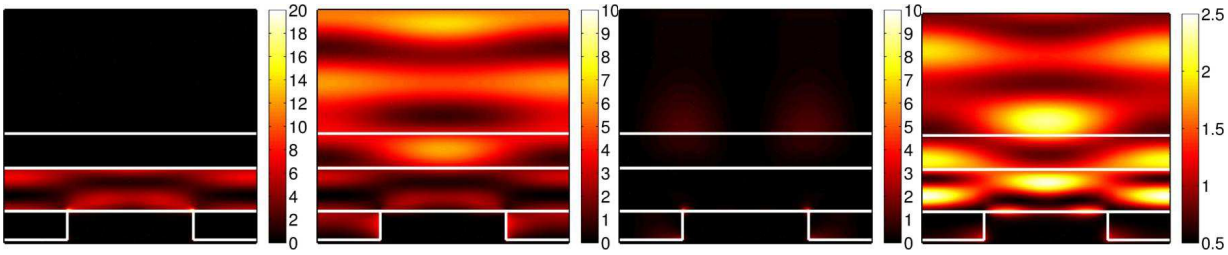

(a) $\epsilon''.|E|^2$ (b) E_x (c) E_z (d) H_y

Figure B.5.3: Back nano-structured CIGS 150 nm $\lambda = 710$ nm

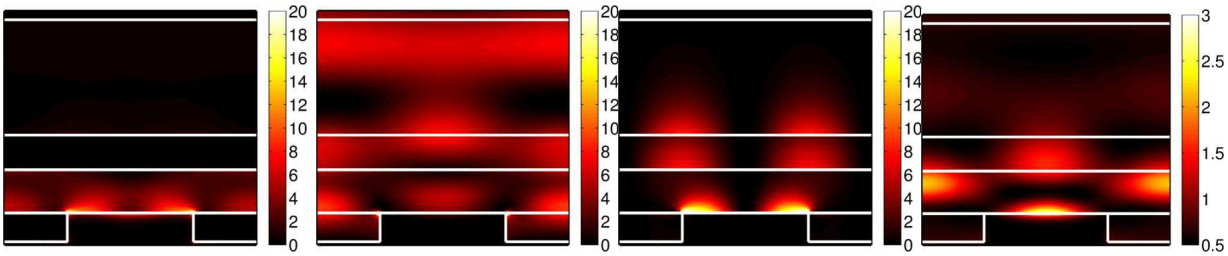

(a) $\epsilon''.|E|^2$ (b) E_x (c) E_z (d) H_y

Figure B.5.4: Back nano-structured CIGS 150 nm $\lambda = 1060$ nm

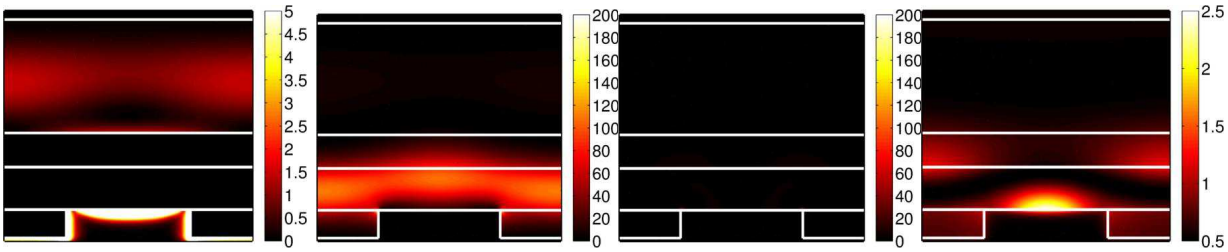

(a) $\epsilon''.|E|^2$ (b) E_x (c) E_z (d) H_y

Figure B.5.5: Back nano-structured CIGS 150 nm $\lambda = 1260$ nm

Annexe C

Résumé

Introduction

Le management optique pour les cellules solaires connait une demande croissante. Ces dernières années, la communauté photovoltaïque a pris conscience de l'importance de cette problématique (voir, par exemple, les présentations d'ouverture de l'EU-PVSEC 2012 et 2013). Parmi d'autres axes de la recherche, la forte réduction (d'un facteur de 10) de l'épaisseur des cellules solaires a été identifiée comme une solution prometteuse pour résoudre les challenges en matière de fabrication, de réduction des coûts et du développement au niveau du terra watt (TW) de la technologie photovoltaique (PV). Le défi consiste désormais à proposer un piégeage de la lumière approprié pour faire face à cet objectif ambitieux. Le contrôle efficace de la lumière est l'un des facteurs limitants actuels vers des cellules solaires plus efficaces et moins coûteuses et est la clé vers de nouveaux concepts en PV. En réponse, les communautés de nano-photoniques et plasmoniques ont proposé de nouvelles solutions permettant de contrôler la lumière à l'échelle nanométrique. La tâche est conséquente en raison de la diversité des technologies, des matériaux et des dispositifs existants. Certaines structures ont déjà montré leur capacité à confiner la lumière dans des couches très minces (épaisseur = 100-200 nm) avec des cristaux photoniques [1] ou des miroirs arrières nano-structurés [2–4]. Dans les deux cas, la couche active est structurée et ces géométries sont donc réservées aux matériaux non cristallins. Cette remarque est valable pour l'essentiel des exemples présents dans la littérature. Il reste encore beaucoup de travail (et donc de possibilités) pour concevoir des cellules cristallines ultra-fines.

Le Laboratoire de Photonique et Nanostructures (LPN) développe depuis des années des solutions nano-photoniques et des compétences de salle blanche dans le domaine des dispositifs photo-détecteurs proche et moyen infrarouge. En 2006, l'Institut de Recherche et Développement sur l'Energie Photovoltaïque (IRDEP), spécialiste de la technologie PV et CIGS, a approché le LPN dans le cadre du projet français ANR THRIPV (Très Hauts Rendements et Innovation Photovoltaïque)

pour fournir des nouvelles solutions afin d'augmenter l'absorption dans des couches ultra-fines d'arsenures de gallium (GaSb) cristallines pour des applications aux cellules solaires à porteur chaud. La collaboration se poursuit en 2009 suivant les mêmes lignes directrices avec l'application aux cellules solaires CIGS ultra-minces dans le cadre des projets français ULTRACIS (ANR HABISOL) et ULTRACIS-M (depuis 2013).

Cette thèse de doctorat, effectuée entre le LPN et l'IRDEP, a commencé dans la dynamique de ces projets. L'objectif était de développer une ou plusieurs structures novatrices pour le contrôle de la lumière pouvant être universellement appliquées à des cellules solaires fines ou ultra-fines ($< 100\,\mathrm{nm}$) quelle que soit la technologie envisagée. La première structure envisagée est une structure type métal/isolant/métal adaptée à de cellules solaires. Nous étudions trois matériaux dans ce manuscrit : l'arsenure de gallium (GaAs - record de conversion pour des cellules solaires simple jonction), l'antimonure de gallium (GaSb - application aux cellules solaires à porteurs chaud - ANR THRIPV) et diséléniure de cuivre, d'indium et de gallium (CIGS - cellule solaire bas coût, haute efficacité - ANR ULTRACIS). L'objectif de notre étude est de réduire l'épaisseur de l'absorbeur de ces dispositifs pour ouvrir la voie vers des cellules solaires ultra-minces (épaisseur de 25 à 250 nm).

Ce manuscrit est structuré est de trois parties :

- La partie 1, comprenant trois chapitres, propose une introduction à l'étude. Le Chapitre 1 est une introduction générale sur le photovoltaïque dressée afin de motiver notre étude. En particulier, nous montrons que les cellules solaires ultra-minces sont une solution prometteuse pour réduire les coûts, pour améliorer la production et pour permettre le développement du PV à l'échelle mondiale. Le Chapitre 2 donne un aperçu des stratégies proposées dans la littérature pour piéger la lumière dans les cellules solaires et en particulier dans les cellules solaires ultra-minces. Dans le Chapitre 3, nous présentons les outils nanophotoniques et les concepts utilisés dans ce manuscrit. En particulier, nous présentons la structure métal/isolant/métal (MIM) ainsi que le code numérique utilisé dans le reste du manuscrit.

- Dans la partie 2, nous présentons une structure de piégeage de la lumière originale, appelée réseau de nano-cavité, appliqué à une couche ultra-mince (25 nm) de GaAs. Le Chapitre 4 s'intéresse à l'analyse numérique ainsi qu'aux règles de conception et d'optimisation de la structure pour obtenir une absorption large bande et multi-résonante à l'intérieur de la couche de semiconducteur. Le Chapitre 5 est consacré à la fabrication et la caractérisation optique d'échantillons preuve-de-concept en GaAs.

- Dans la partie 3, nous proposons d'étendre cette étude pour des structures ultra-minces en GaSb et en CIGS. Le Chapitre 6 présente l'adaptation et l'optimisation de la conception de réseau de nano-cavité pour ces deux matériaux avec des résultats obtenus dans le cadre des ANR THIRPV et ULTRACIS respectivement. Pour le CIGS en particulier, deux cas sont étudiés dans un premier temps : une couche ultra-mince de 45 nm de CIGS et une étude d'une structure de cellule solaire plus complète de 100 nm. Ensuite, nous soumettons une nouvelle structure alternative adaptée pour des cellules CIGS dans la gamme d'épaisseur de 100 à 400 nm basée sur un miroir arrière métallique nano-structuré. La fabrication de cellules solaires ultra-minces nano-structurées en CIGS est présentée dans le Chapitre 7.

L'objet de ce résumé est de rassembler les résultats majeurs de cette étude. L'intégralité du travail de thèse peut être trouvée dans la version en anglais.

Introduction au photovoltaïque et motivation de l'étude

Le premier défi à relever par le marché de l'énergie actuel est la croissance de la demande énergétique pour répondre au développement économique et social. Ainsi, l'Agence Internationale de l'Energie (IEA) a rapporté une valeur de 150 000 TWh (TWh= térawatts-heures) pour la consommation mondiale d'énergie pour l'année 2010 et une valeur de 175 000 TWh est prévue à l'horizon 2020. Comment allons-nous répondre à cette demande croissante en énergie ? Le marché énergétique actuel, basé à 80 % sur les énergies fossiles, est remis en question par la nécessité de limiter l'augmentation de température due au réchauffement climatique. Le dernier rapport de l'IEA [5] montre que la baisse des émissions liées à l'énergie ne peut se faire qu'à la condition que les sources d'énergie renouvelables (énergie éolienne, énergie solaire, biomasse, géothermie, hydroélectricité, énergie océanique) occupent une part plus importante dans le mix énergétique mondial (27 % en 2020). La production renouvelable d'électricité est un secteur très dynamique qui, en dépit du contexte économique difficile, a montré une croissance remarquable de 8 % en 2012, pour atteindre une production d'énergie renouvelable totale de 4 860 TWh [5]. Les énergies renouvelables ont un bel avenir devant elles, mais des politiques à long terme et des mesures incitatives sont nécessaires afin de permettre un développement à large échelle.

En 2012, le secteur de l'énergie solaire a représenté plus de la moitié des investissements mondiaux. L'énergie solaire a un très fort potentiel comme source d'électricité. En effet, elle est la plus grande ressource d'énergie sur Terre. La puissance lumineuse frappant la Terre en 90 min est suffisante pour subvenir aux besoins énergétiques de la planète pendant une année entière [6]. L'énergie solaire est exploitée sous deux formes : le solaire photovoltaïque (PV) et l'énergie solaire

à concentration. Dans cette thèse, nous nous focaliserons sur le solaire photovoltaïque, c'est-à-dire la conversion directe de l'énergie solaire en électricité. Le marché du photovoltaïque a connu une croissance très impressionnante depuis 2003 avec un taux de croissance moyen de 40 % jusqu'en 2009 [5]. Une capacité de production de plus de 40 GW a été atteinte en 2010 avec un déploiement dans plusieurs pays, l'Allemagne étant le premier marché du photovoltaïque depuis 2001.

Le prix du photovoltaïque, bien que relativement plus élevé que les autres sources d'énergies renouvelables et non renouvelables, n'est pas le premier défi à relever. En effet, la parité réseau a déjà été atteinte dans certaines régions et pourrait être atteint dans le monde d'ici 2020 grâce à des effets d'échelles dans les développements industriels [7]. En résumé, les facteurs importants sont les suivants pour le développement de technologies photovoltaïques : un taux de production élevé est essentiel pour le développement à grande échelle ; la consommation de matériaux devrait être abaissée pour éviter les pénuries et réduire les coûts ; l'efficacité doit être élevée pour garantir des prix bas pour l'ensemble du système.

Le marché du photovoltaïque repose sur plusieurs filières technologiques qui s'organisent en deux groupes : la filière silicium cristallin et les filières couches minces. À l'heure actuelle, 80 % de l'industrie photovoltaïque est encore basée sur la technologie silicium cristallin (monocristallin ou polycristallin). Le silicium est un matériau abondant et non toxique qui a une énergie de bande interdite presque optimale (1.1 eV) pour les cellules solaires. Les cellules solaires en silicium actuelles utilisent des wafers avec une épaisseur de 100 à 200 µm. La technologie de silicium cristallin est limitée par son coût : autour de 50 % du coût du module est dû au coût du matériau et à la purification nécessaire pour obtenir une qualité suffisante pour les cellules solaires. En outre, le silicium cristallin a un coefficient d'absorption faible du fait de son gap indirect. Par conséquent, une deuxième génération de cellules solaires à base de matériaux à gap direct (GaAs, a-Si :H, CdTe, CIGS) a été développée avec des cellules solaires d'une épaisseur de quelques microns. Les technologies couches minces se sont considérablement développées jusqu'à atteindre des efficacités talonnant les 20 % pour les filières CdTe et CIGS ou dépassant même le silicium cristallin comme la filière GaAs (28.8 % par Alta Devices [15]). Malgré son faible coût de production, le développement de la filière silicium amorphe est limité par les faibles efficacités de conversion : le record actuel dépasse à peine les 10 %. Au contraire, la filière CIGS est en pleine expansion grâce à son coût réduit (croissance cellule et panneau intégrée) et ses très hautes efficacités (record 20.4 % sur substrat flexible [33]). Cependant, l'avenir de cette filière est très fortement dépendant du cours de l'un de ces éléments constitutifs : l'indium. Ce problème est aujourd'hui au coeur de nombreuses études qui cherchent soit à limiter l'usage de l'indium, soit à le remplacer définitivement.

Les technologies couches minces ont été la première étape vers des dispositifs

photovoltaïques plus efficaces et moins coûteux. Le point de départ de cette thèse est de concevoir des cellules solaires efficaces à partir d'absorbeurs ultra-fins. Pour les matériaux en couches minces, notre objectif est de descendre en dessous de 100 nm pour l'épaisseur de la couche absorbante. Quels seraient les avantages d'aller plus loin dans la réduction de l'épaisseur des cellules vers des cellules solaires ultra-fines ? Cela permettrait de réduire les coûts et d'augmenter la vitesse de production tout en augmentant le rendement de conversion grâce à une meilleure efficacité de collection. Cela permettrait également de relâcher les contraintes pesant sur les matériaux rares comme l'indium ou toxiques comme le tellure [59]). Cependant, la conception des cellules solaires ultra-minces n'a d'intérêt que si l'on parvient à générer un photo-courant élevé à partir de couches de semiconducteur ultra-fines. La recherche de techniques avancées de piégeage de la lumière pour les cellules solaires ultra-fines a connu un véritable essor au cours des dernières années. Parmi les stratégies proposées, les nanostructures métalliques montrent un fort potentiel pour améliorer l'absorption de la lumière dans les couches d'absorption très fines. Dans cette thèse, nous avons donc choisi de nous focaliser dans un premier temps sur les nanostructures plasmoniques intégrées en face avant de la cellule solaire. Cette approche offre l'avantage de conserver une couche active plane.

En particulier, notre approche est motivée par les résultats obtenus par notre équipe sur les structure métal/isolant/métal (MIM) [165]. Les principaux résultats de cette étude sont présentés sur la figure C.1. Cette structure est composée d'un miroir métallique semi-infini fait d'or, d'une couche de diéletrique non-absorbant d'épaisseur $t_l = 20$ nm et d'un réseau uni-dimensionnel de nano-particules d'or d'épaisseur $t_M = 20$ nm et de largeur $w = 200$ nm. Cet élément unique est répété avec une période $p = 400$ nm. Sur la figure, nous pouvons trouver les cartes de simulations montrant l'intensité du champ magnétique sous le métal pour le mode fondamental (m = 1, $\theta = 0$ °) et le mode du second ordre ($m = 2$, $\theta = 30$ °), sous l'illumination d'une onde plane de deux résonances. (une, en bas) : spectres d'absorption des résonateurs MIM mesurés sous une polarisation TM (champ magnétique parallèle aux fils) à différents angles d'incidence. (b, c) Détermination de la décroissance γ_r des pertes radiatives et non radiatives γ_{nr} à plusieurs angles pour m = 1 (b) et m = 2 (c). (d) Diagramme angulaire de l'absorption maximale des deux modes entre 3° et 60°. Les principales propriétés de ce spectre d'absorption sont la présence de deux résonances distinctes dont le mode fondamental résonne indépendamment de l'angle d'incidence avec une absorption presque totale dans un très petit volume. Le mécanisme de résonance est le suivant : la lumière incidente se couple à un mode électromagnétique se propageant le long de la couche de diélectrique composé de deux plasmons couplés. Ce mode plasmonique résonne aux extrémités de la cavité formée par la particule d'or, conformément au modèle

de Fabry-Pérot.

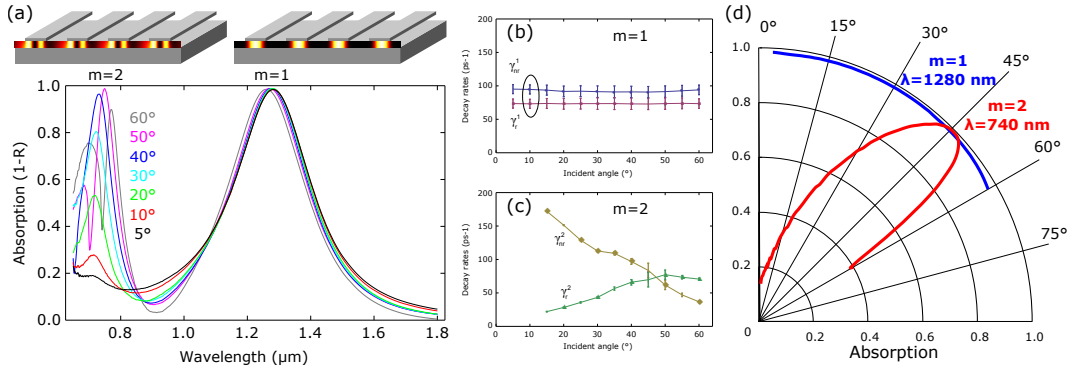

Figure C.1: Schéma de la simulation effectuée pour la structure MIM superposée aux cartes de simulations montrant l'intensité du champ magnétique sous le métal pour le mode fondamental (m = 1, θ=0 °) et le mode du second ordre (m = 2, θ = 30 °), sous l'illumination d'une onde plane. (une, en bas): spectres d'absorption des résonateurs MIM mesurés sous une polarisation TM (champ magnétique parallèle aux fils) à différents angles d'incidence. (b, c) Détermination de la décroissance γ_r des pertes radiatives et non radiatives γ_{nr} à plusieurs angles pour m = 1 (b) et m = 2 (c). (d) Diagramme angulaire de l'absorption maximale des deux modes entre 3° et 60°. Tiré de Cattoni *et al.* [165].

Expérimentalement, cette structure en deux dimensions a validé une absorption totale, indépendante de l'angle et de la polarisation. Ces résultats très importants démontrent la capacité de la structure à confiner la lumière efficacement dans des volumes très inférieurs à la longueur d'onde. Pour l'instant, l'intégralité de l'absorption a lieu dans le métal. Notre objectif est d'appliquer ce concept aux cellules solaires. Des contraintes supplémentaires apparaissent néanmoins : la nécessité de limiter fortement l'absorption dans le métal et de produire un spectre d'absorption large bande afin d'absorber le maximum de photons disponibles sous le gap du matériau envisagé.

Réseaux de nano-cavité métal/semi-conducteur/métal pour absorption multi-résonante et large spectre dans des couches ultra-fines de GaAs

Dans cette partie, nous nous intéressons à l'étude numérique de l'application du concept de réseaux de nano-cavité pour la conception de cellules solaires ultrafines en GaAs. Nous considérons ainsi le cas d'une couche de GaAs ultra-mince avec une épaisseur de 25 nm. La réponse optique de cette structure est étudiée par des calculs numériques avec le code Reticolo développé par Philippe Lalanne et ses

collègues à IOGS. Il est basé sur une méthode Rigorous Coupled Wave Analysis (RCWA) et permet de déterminer la réponse optique d'empilements de structures lamellaires. Les paramètres d'entrée des calculs sont les suivants :

- les épaisseurs des différentes couches de l'empilement
- les paramètres géométriques du réseau (w, p)
- les constantes optiques (n, k) de chaque matériau (ici, GaAs et Ag).

Nous proposons ainsi une structure avec un réseau métallique unidimensionnel pour obtenir un spectre d'absorption multi-résonant et large spectre. Notre approche est décrite dans la figure C.2a. Elle est composée d'une couche de GaAs 25nm d'épaisseur, un miroir en argent et d'un réseau métallique unidimensionnel (c.-à-d. infini sur la longueur et l'axe des y) de fils d'argent. Nous avons calculé numériquement l'absorption intégrée dans la couche de GaAs entre 300 et 1000 nm en fonction des différents paramètres de la structure variable. Le meilleur résultat est obtenu pour les paramètres du réseau suivant: période $p = 200\,\mathrm{nm}$; largeur $w = 100\,\mathrm{nm}$; épaisseur $t = 15\,\mathrm{nm}$. Nous avons représenté le spectre d'absorption correspondant à la structure optimale sur la figure C.2c. Nous obtenons trois pics distincts d'absorption quasiment totale. Un spectre d'absorption très large est obtenu grâce à ces multiples résonances comparé aux structures de références. On peut remarquer tout de suite que l'absorption dans le métal, représentée par la différence entre la courbe d'absorption totale et d'absorption dans le GaAs, reste inférieure à 15 % sur tout le spectre.

Dans la partie rouge du spectre, l'amélioration de l'absorption est due aux effets de piégeage de la lumière. De façon plus précise, nous avons analysé le mécanisme d'absorption en étudiant l'influence des différents paramètres de la structure. Le résumé de cette analyse est présenté dans le tableau C.1. Nous avons mis en exergue des lignes directrices simples pour l'optimisation visuelle du spectre d'absorption de cette structure grâce à des modèles simplifiés de Fabry-Pérot. Nous avons réalisé une étude poussée des mécanismes de résonances et du phénomène d'absorption totale grâce à la théorie des modes-couplés temporelle.

Par la suite, nous avons montré que la version bidimensionnelle de la structure donnait des résultats et des performances similaires et ce selon les deux polarisations (TE et TM). Nous avons aussi étudié la dépendance en angle des performances de la structure comme montré sur la figure C.3. Pour les deux polarisations (TE et TM), la dépendance angulaire du spectre d'absorption est faible. Au final, nous pouvons calculer, pour cette structure 2D, un courant de court-circuit théorique de $18\,\mathrm{mA/cm^2}$ indépendamment de l'angle d'incidence. Cela représente une amélioration très prometteuse de 92 % par rapport à une cellule solaire de référence de 25 nm en GaAs. C'est également une amélioration notable par rapport aux structures similaires disponibles dans la littérature [164].

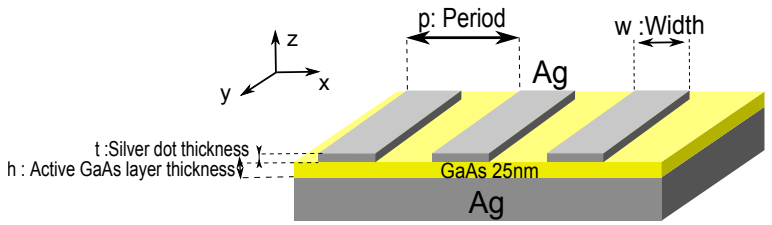

(a)

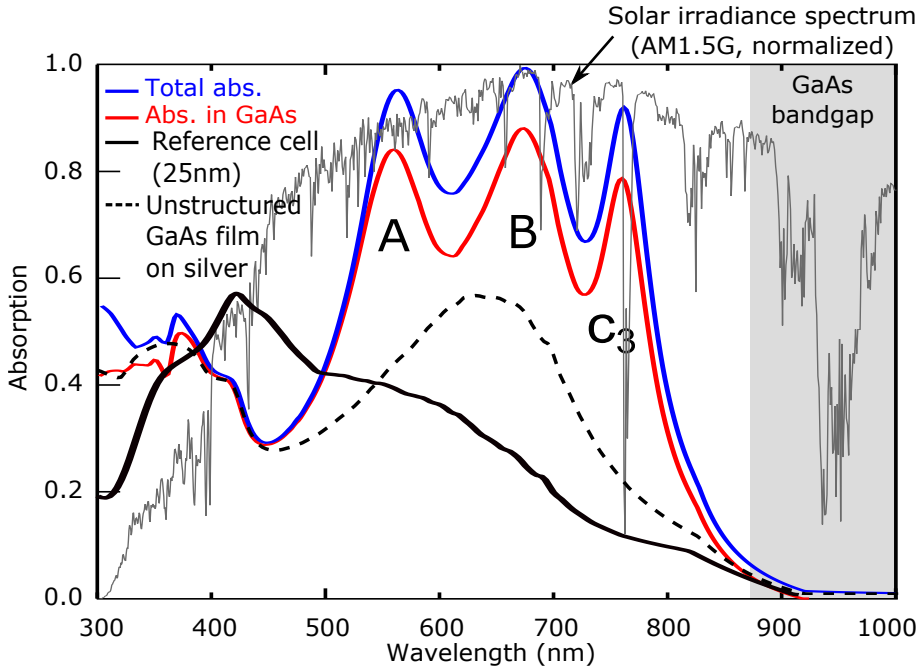

(b)

Figure C.2: (a) Structure du réseau nano-cavité MSM de 1D. Elle est composée d'une couche de GaAs 25nm d'épaisseur, un miroir en argent et d'un réseau métallique unidimensionnel (c.-à-d. infini sur la longueur et l'axe des y) de fils d'argent. Les paramètres du réseau sont: période $p = 200\,\text{nm}$; largeur $w = 100\,\text{nm}$; épaisseur $t = 15\,\text{nm}$. (b) Simulation du spectre d'absorption dans les 25 nm d'épaisseur GaAs en polarisation TM et à incidence normale. Les courbes bleues et rouges représentent l'absorption totale et l'absorption en GaAs respectivement. La différence entre ces deux courbes représente l'absorption dans les autres couches, c'est-à-dire dans le métal. Elle est comparée à l'absorption dans le GaAs d'une cellule solaire de régérence en GaAs de 25 nm (en noir) et à l'absorption dans un film de la GaAs 25 nm d'épaisseur sur un miroir argenté avec aucune structure (ligne pointillée). Le spectre du rayonnement solaire est tracé en gris. Le gap du GaAs est représenté en gris à \lambda\geqslant870 nm.

Paramètre géométrique	Type de résonance	Label
Epaisseur de GaAs	Rés. F-P dans la couche de GaAs sous les plots du réseau	Résonance A : $\lambda = 560\,\text{nm}$
Epaisseur de GaAs	Rés. F-P dans la couche de GaAs entre les plots du réseau	Résonance B : $\lambda = 675\,\text{nm}$
Largeur des particules d'Ag	Résonance type metal/semi-conducteur/métal plasmonique d'ordre 3	Résonance C_3 : $\lambda = 560\,\text{nm}$

TABLE C.1: Résumé de l'analyse du mécanisme d'absorption. "Rés. F-P" signifie "Résonance de Fabry-Pérot".

Au travers cette étude numérique, nous avons montré que la combinaison de résonances de Fabry-Pérot verticales et horizontales (résonance MSM) conduit à un spectre d'absorption large bande avec une faible dépendance par rapport à la polarisation et l'angle d'incidence. Nous avons ainsi montré que notre structure vérifiait les critères indispensables propres aux cellules solaires. Cette approche versatile peut être appliquée à différents matériaux et géométries de cellules solaires. Elle ouvre de nouvelles possibilités vers l'étude de dispositifs ultra-fins dans le visible.

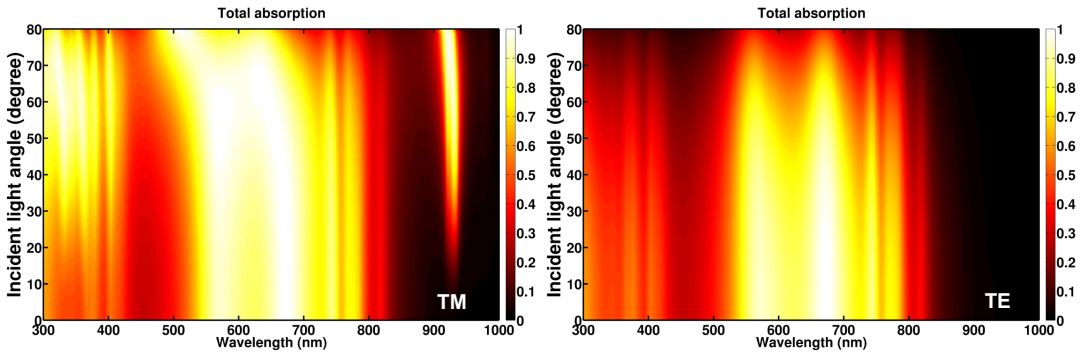

(a) (b)

Figure C.3: Total absorption spectrum of the 2D GaAs structure as a function of the incident light angle (rotating around the y axis) with either (a) the magnetic field H parallel to the y axis (TM polarization) or (b) the electric field E parallel to the y axis (TE polarization).

Mise en évidence expérimentale d'une absorption multi-résonante et large spectre dans des couches ultra-fines de GaAs

Pour valider les simulations numériques du chapitre précédent, nous avons développé un procédé de fabrication afin de réaliser des absorbeurs large spectre à base de couches ultra-fines (épaisseur nominale de 25 nm) de GaAs. Nous utilisons du GaAs cristallin obtenu par croissance épitaxiale sur un substrat de GaAs. La fabrication de démonstrateurs nécessite d'abord un transfert de la couche de GaAs épitaxiée depuis le substrat initial de GaAs sur un miroir d'or. Un réseau bidimensionnel d'argent est ensuite structurée par lithographie électronique sur la couche de GaAs. Enfin, la grille métallique est encapsulée dans une couche d'oxyde de zinc dopé aluminium (ZnO :Al) de 55 nm d'épaisseur.

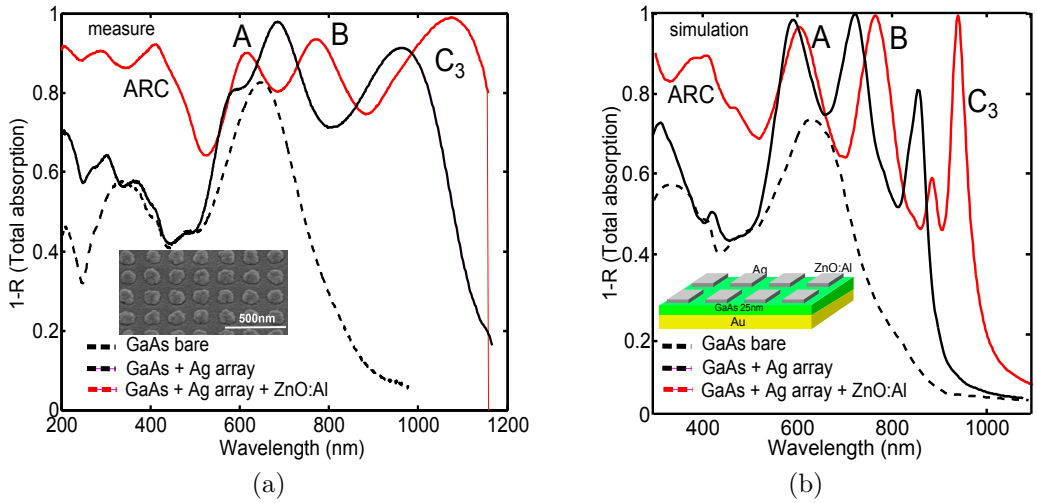

Figure C.4: Absorption totale mesurée (a) et calculée (b) pour une couche de GaAs de 25 nm transférée sur un miroir d'or avec un réseau bidimensionnelle d'argent (épaisseur= 20 nm, période= 200 nm, largeur des plots= 120 nm) encapsulée dans une couche e oxyde de zinc dopé aluminium (ZnO :Al) de 55 nm d'épaisseur. En médaillon sont disponible respectivement l'image MEB d'un réseau bidimensionnel d'argent après dépôt de la couche de ZnO :Al et le schéma de la structure modélisée dans les simulations.

La figure C.4a montre une image MEB d'un réseau à la fin du procédé de fabrication. Nous avons mesuré la réflectivité à incidence normale de ces structures et déduit l'absorption totale comme montré sur la figure. Le spectre noir représente le spectre d'absorption de la structure sans couche de ZnO :Al. Ce spectre présente

effectivement trois pics d'absorption, en bon accord avec les calculs numériques (figure C.4b). Le spectre rouge représente le spectre d'absorption de la structure encapsulée. Il présente une large bande d'absorption (A_{tot}> 80 % e, moyenne entre 200 et 1200 nm) encore plus large que celle du chapitre précédent avec un pic d'absorption supplémentaire autour de 400 nm.

Ce dernier pic d'absorption est dû à l'effet anti-reflet de la couche d'encapsulation (l'épaisseur de cette dernière étant choisie en conséquence). En plus de cet effet anti-reflet, la couche d'encapsulation sert à éviter la sulfuration du réseau d'argent et également de jouer le rôle de contact avant. Le rajout de cette couche d'encapsulation permet donc d'élargir encore plus le spectre d'absorption. Son effet optique est prévu de manière quantitative par les simulations optiques, validant le modèle développé dans le chapitre précédent.

Dans la figure C.5, nous avons vérifié expérimentalement que la structure fabriquée présentait effectivement un spectre d'absorption d'une indépendance remarquable par rapport à l'angle d'incidence et ce en lumière non polarisée jusqu'à un angle de 45 ° au moins.

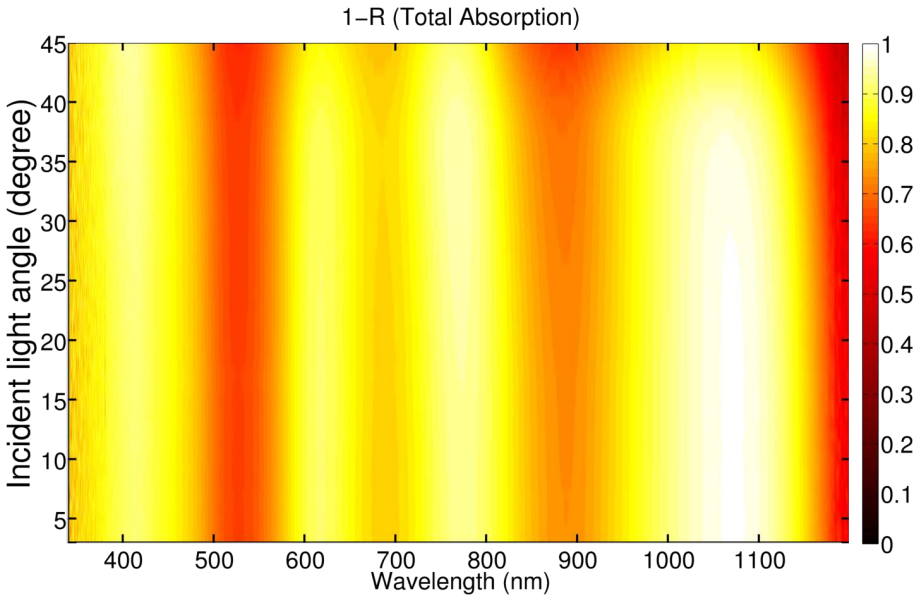

Figure C.5: Spectres mesurés 1-R (absorption totale) sur l'échantillon de GaAs d'épaisseur 25 nm avec w = 120 nm en fonction de l'angle d'incidence pour une lumière non polarisée.

Les performances de cette structure en termes d'absorption dans de petits volumes sont supérieures aux performances des autres « super-absorbeurs » de la littérature [174]. De plus, il est important de noter que dans la plupart des approches de type plasmonique existantes pour réaliser des absorbeurs larges bandes, la lu-

mière est absorbée entièrement dans le métal. Afin d'intégrer les structures plasmoniques dans des dispositifs photovoltaïques efficaces, la lumière doit être absorbée principalement dans la couche de semi-conducteur active. Dans le cadre de notre étude, nos calculs montrent des valeurs de densité de courant de court-circuit importantes, comme mentionné plus haut. Cette étude expérimentale confirme donc le potentiel de réseau de nano-cavités 2D non seulement pour obtenir une absorption totale importante mais surtout pour confiner la lumière dans une couche semi-conductrice dans un volume sub-longueur d'onde tout en conservant de bonnes performances. Nous capitalisons ces très bons résultats en adaptant cette structure à deux autres matériaux cristallins et poly-cristallins que sont le GaSb (application aux cellules à porteurs chauds) et le CIGS (cellules bas coût et haute efficacité).

Piégeage optique dans de cellules solaires cristalline ultra-fines : application au GaSb et au CIGS

Dans un premier temps, une adaptation directe de la structure de réseau de nano-cavités a été proposée pour une couche simple de GaSb de 25 nm (cf. figure C.6a). Le GaSb un l'un des candidats les plus prometteurs dans l'étude des cellules à porteurs chauds grâce à son petit gap en énergie comparé aux matériaux standards du PV et de ses bonnes propriétés électroniques. L'enjeu de ce genre de concept est d'obtenir une population de porteurs très chauds, ce qui peut être obtenu grâce à un fort confinement de la lumière dans de très petits volumes. Après optimisation des paramètres géométriques ($t_{réseau}$ =26 nm, largeur $w = 170$ nm, période $p = 300$ nm), le spectre d'absorption tracé sur la figure C.6b est obtenu. Les courbes bleues et rouges représentent respectivement l'absorption totale et l'absorption dans GaSb de la structure. La courbe noire représente l'absorption dans la même structure sans le réseau. La courbe grise représente la densité spectrale normalisée du spectre solaire AM1.5G. La courbe rouge présente quatre pics d'absorption comme dans le cas du GaAs et s'étend sur la gamme 400nm-1100 nm avec une valeur toujours supérieure à 70 % (avec toujours moins de 15% d'absorption dans le métal). Le spectre d'absorption est encore une fois indépendant de l'angle d'incidence et de la polarisation.

Dans le cadre de l'ANR TRHIPV, ces résultats ont servi à estimer les performances de cellules à porteur chaud dans le cadre du projet de recherche d'Arthur Le Bris et de Jean-François Guillemoles. Cette structure permet d'atteindre des courants de court-circuit de l'ordre de 37.7 mA/cm^2 jusqu'à des angles d'incidence de 60°, soit jusqu'à une concentration de 40 000 soleils. Cela représente une amélioration de la densité de courant de court-circuit de l'ordre de 50% par rapport à la même structure sans réseau. Avec ces hypothèses et dans le modèle des cellules à porteurs chauds à contacts semi-sélectifs [64, 65], une efficacité de 38 % est envisagée pour une telle structure. Ces résultats sont encourageants et pour le

moment supérieurs aux autres propositions de la littérature [123] (couche de GaSb plus fine) ainsi plus facilement réalisable expérimentalement.

Dans la dynamique de l'ANR ULTRACIS, nous avons ensuite appliqué la structure de réseau de nano-cavités pour des cellules solaires en CIGS. Dans un premier temps, nous avons vérifié que la structure s'appliquait a une couche simple de CIGS de 45 nm d'épaisseur (cf. figure C.7a) composée d'une couche de fenêtre de 50 nm d'épaisseur ZnO :Al, un réseau 2D de nano-particules d'argent, une couche de 45 nm d'épaisseur absorbante de CIGS et un miroir arrière en argent. Les paramètres du réseau donnant le meilleur courant de court-circuit sont : épaisseur $t = 20\,\text{nm}$, largeur $w = 290\,\text{nm}$, période $p = 530\,\text{nm}$. Les spectres d'absorption simulés de la structure CIGS 45 nm d'épaisseur sont présentés sur la figure C.7b. Les courbes bleues et rouges représentent respectivement l'absorption totale et l'absorption dans le CIGS. La courbe noire pleine et pointillée représente l'absorption d'une cellule solaire CIGS plane de référence référence de 45 nm d'épaisseur plane avec un contact arrière respectivement en Mo ou en Ag. La courbe grise représente la densité spectrale normalisée du spectre solaire AM1.5G. Nous avons marqué quatre résonances $\lambda_1 = 490\,\text{nm}$, $\lambda_2 = 840\,\text{nm}$, $\lambda_3 = 999\,\text{nm}$ et $\lambda_4 = 1100\,\text{nm}$. Le spectre d'absorption multi-résonant et large spectre présente les mêmes caractéristiques que pour le cas GaAs et GaSb (indépendance par rapport à l'angle d'incidence et à la polarisation). Le courant de court-circuit théorique calculé à partir de cette structure est comparable à celui d'une cellule solaire CIGS non structurée de 1 micron d'épaisseur sur un contact en Mo (38 mA/cm^2). Cette structure de piégeage optique permettrait donc une très forte réduction de l'épaisseur de CIGS, permettant de relâcher les contraintes sur l'approvisionnement en indium.

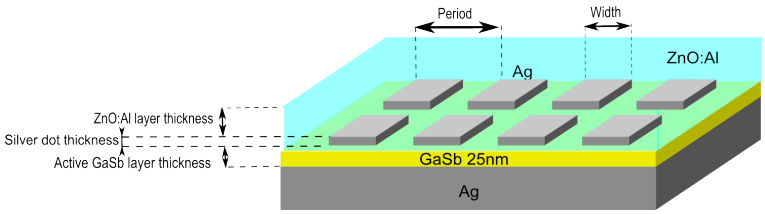

(a)

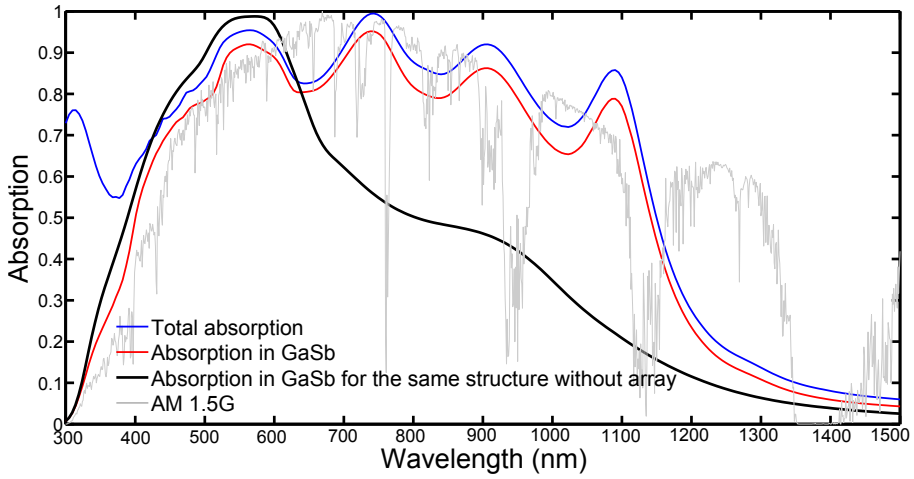

(b)

Figure C.6: (a) Schéma de la structure de GaSb de 25 nm d'épaisseur. Elle se compose d'une couche de GaSb 25 nm d'épaisseur sur un miroir argent, couvert par un réseau à deux dimensions des nanoparticules d'argent carrées (épaisseur $t_{réseau}$ =26 nm, largeur $w = 170$ nm, période $p = 300$ nm) et une couche de fenêtre de 50 nm d'épaisseur en ZnO :Al. (b) Spectres d'absorption simulés de la cellule solaire de 25 nm d'épaisseur GaSb. Les courbes bleues et rouges représentent l'absorption totale et l'absorption dans GaSb de la structure, respectivement. La courbe noire représente l'absorption dans la même structure sans le réseau. La courbe grise représente la densité spectrale normalisée du spectre solaire AM1.5G.

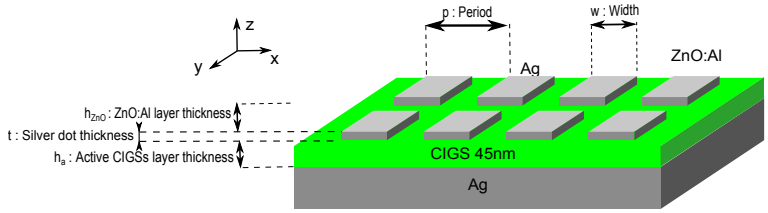

(a)

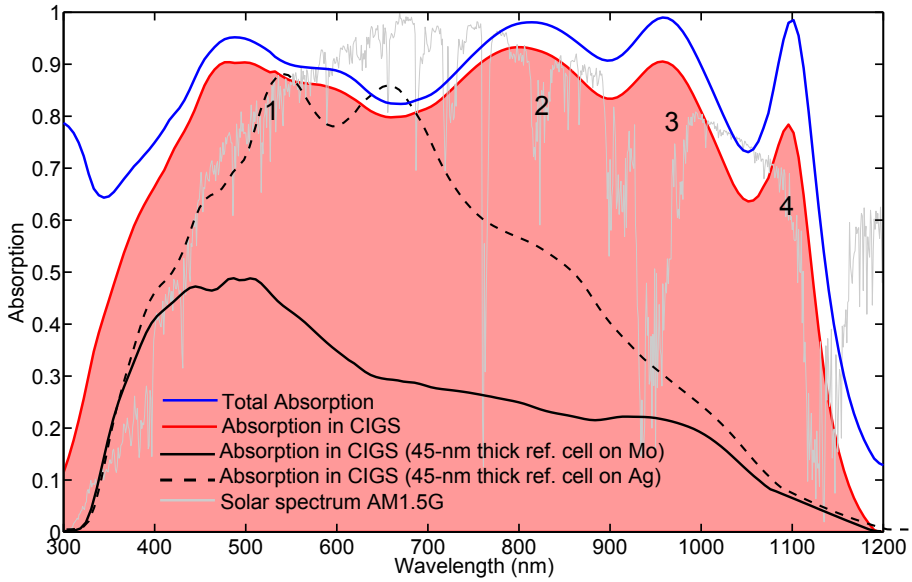

(b)

FIGURE C.7: (a) Schéma de la structure CIGS de 45 nm d'épaisseur : une couche de fenêtre de 50 nm d'épaisseur ZnO :Al, un réseau 2D de nanoparticules d'argent, une couche de 45 nm d'épaisseur absorbante de CIGS et un miroir arrière en argent. Les paramètres du réseau sont : épaisseur $t = 20\,\text{nm}$, largeur $w = 290\,\text{nm}$, période $p = 530\,\text{nm}$. (b) Spectre d'absorption simulé de la structure CIGS 45 nm d'épaisseur. Les courbes bleues et rouges représentent l'absorption totale et l'absorption dans le CIGS respectivement. La courbe noire pleine et pointillée représente l'absorption d'une cellule solaire CIGS plane de référence référence de 45 nm d'épaisseur plane avec un contact arrière en Mo ou en Ag respectivement. La courbe grise représente la densité spectrale normalisée du spectre solaire AM1.5G. Nous avons marqué les résonances $\lambda_1 = 490\,\text{nm}$, $\lambda_2 = 840\,\text{nm}$, $\lambda_3 = 999\,\text{nm}$ et $\lambda_4 = 1100\,\text{nm}$

Pour aller plus loin, nous avons évalué le potentiel de cette structure sur une cellule solaire CIGS plus complète, schématisée sur le figure C.8a. Elle est com-

posée d'une couche de fenêtre de 50 nm d'épaisseur en ZnO :Al, un réseau 2D de nano-particules d'argent, une couche de sulfure de cadmium de 50 nm d'épaisseur, une couche absorbante en CIGS d'épaisseur 100 nm, une couche de ZnO :Al de 50 nm d'épaisseur pour empêcher la diffusion du miroir arrière en argent. Les paramètres du réseau optimisé sont : épaisseur $t = 20$ nm, largeur $w = 290$ nm, période $p = 530$ nm. Les spectres d'absorption simulés sont présentés sur la figure C.8b. Les courbes bleues et rouges représentent l'absorption totale et l'absorption dans le CIGS de la structure représentée en (a) respectivement. La courbe noire représente l'absorption dans le CIGS pour la cellule planaire de CIGS de référence de 100 nm d'épaisseur avec contact en Mo. La structure nano-structurée permet une amélioration de l'ordre de 80 % de la densité de courant de court-circuit théorique par rapport à une cellule de référence de même épaisseur sur molybdène et ce, indépendamment de l'angle d'incidence et de la polarisation. C'est un résultat prometteur, motivant une étude plus complète sur les cellules CIGS ultra-fines. Cependant, de nombreux problèmes sont à résoudre et de différents éléments à prendre en compte pour imaginer un jour un dispositif complet.

L'étude de la structure précédente nous a confirmé une chose : les réseaux de nano-cavités sont efficaces pour absorber la lumière dans des couches ultra-fines mais ne sont peut être pas les plus adaptés pour des épaisseurs supérieures à 100 nm. De plus, il est pour l'instant difficile de concevoir des cellules solaires de cette épaisseur en CIGS avec les moyens technologiques à notre disposition. C'est pour cela que nous avons proposé en dernier lieu une structure alternative pour confiner la lumière dans des cellules CIGS d'épaisseur comprise entre 100 et 400 nm. Le principe est de remplacer le miroir arrière plan par une miroir arrière métallique nano-structuré. Cette solution, ayant déjà prouvé son potentiel dans la littérature [2, 3, 159] pour le silicium amorphe, permet de coupler les photons non absorbés par un simple passage dans la couche à un mode guidé dans le guide d'onde constitué de la couche active. La structure est présentée sur la figure C.9a. L'originalité de cette structure est de conserver une couche active plane grâce à un procédé innovant présenté dans le chapitre suivant et donc de pouvoir appliquer cette structure aux matériaux cristallins ou polycristallins. Suite à une optimisation des paramètres géométriques de la structure (synthétisés dans le figure C.9b), nous avons montré numériquement que cette dernière permettait d'augmenter le courant de court-circuit théorique (J_{th}) d'une valeur moyenne de 12% quelque soit l'épaisseur de la couche de CIGS (dans la gamme 100-400 nm). De plus, cette augmentation est maximale pour une période constante d'environ 600 nm. L'universalité de cette structure est donc un très bon point pour la future fabrication de démonstrateurs.

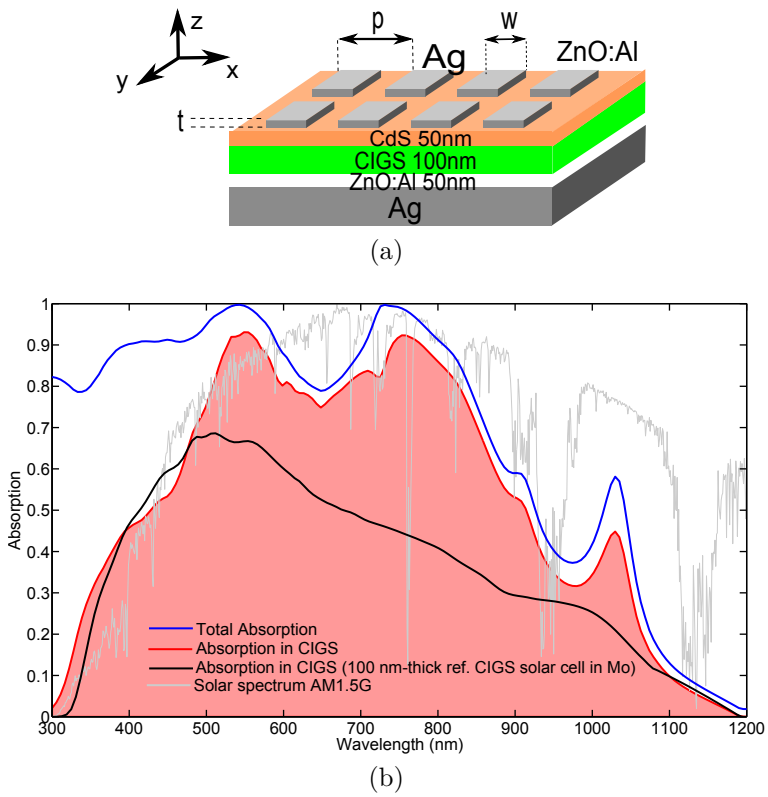

Figure C.8: (a) Schéma de la cellule solaire CIGS de 100 nm d'épaisseur nanostructurée : une couche de fenêtre de 50 nm d'épaisseur en ZnO :Al, un réseau 2D de nano-particules d'argent, une couche de sulfure de cadmium de 50 nm d'épaisseur une couche absorbante en CIGS d'épaisseur 100 nm, une couche de ZnO :Al de 50 nm d'épaisseur pour empêcher la diffusion du miroir arrière en argent. Les paramètres du réseau sont : épaisseur $t = 20\,\text{nm}$, largeur $w = 290\,\text{nm}$, période $p = 530\,\text{nm}$. (b) Spectres d'absorption simulés. Les courbes bleues et rouges représentent l'absorption totale et l'absorption dans le CIGS de la structure représentée en (a) respectivement. La courbe noire représente l'absorption dans le CIGS pour la cellule planaire de CIGS de référence de 100 nm d'épaisseur avec contact en Mo. La courbe grise représente la densité spectrale normalisée du spectre solaire AM1.5G.

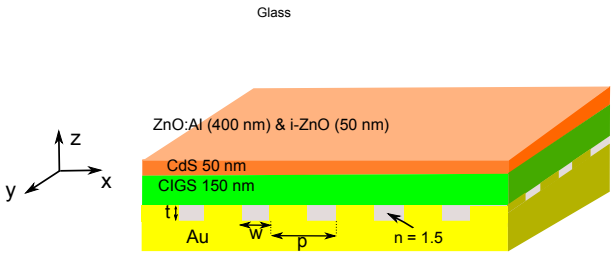

(a)

Epaisseur de CIGS (nm)	Meilleure période (nm)	J_{th} (mA/cm^2)	J_{th}(mA/cm^2) de la cell. de ref. cell on Mo	Amélioration	J_{th}(mA/cm^2) de la cell. de ref. sur Au	Amélioration
100	300	29.9	19.2	55 %	26.7	12 %
150	600	34.1	23.8	44 %	30.4	12 %
200	500	36.5	27.5	32 %	33.7	11 %
300	500	37.4	30.8	22 %	34.5	11 %

(b)

Figure C.9: (a) Structure CIGS de 150 nm d'épaisseur avec un miroir arrière nanostructuré en Au. Les paramètres de la structuration du miroir arrière sont t l'épaisseur de la structure, w la largeur de la structuration et p la période de la structure. Le milieu entre la structure et le CIGS est considéré comme un matériau homogène avec un indice de réfraction n = 1, 5. Le milieu incident considéré également comme un matériau homogène avec un indice de réfraction n = 1,5 (verre). (b) Meilleurs résultats J_{th} obtenus avec la simulation de la nano-structure face arrière pour différentes épaisseurs CIGS. Pour chaque épaisseur est mentionnée la meilleure période et le J_{th} est comparé au courants calculés pour les cellules solaires de référence en CIGS de même épaisseur sur des mirroirs en Mo ou Au.

Procédé de fabrication de cellules solaires CIGS ultra-fines nanostructurées

Pour terminer ce manuscrit, nous avons souhaiter apporter des solutions technologiques pour la problématique de fabrication de cellules solaires CIGS ultra-fines nanostructurées. Pour cela nous avons repris et amélioré un procédé existant à l'IRDEP pour transférer des couches épaisses de CIGS co-evaporé sur Mo sur des substrats alternatifs. Nous avons fourni un effort particulier pour amincir et polir les couches de CIGS au maximum pour tester les structures simulées dans le chapitre précédent.

Cependant, le résultat le plus marquant est le développement d'un procédé de nano-structuration pour des couches de CIGS rugueuses, non planes et présentant des défauts. Nous avons mis en place un procédé de lithographie par nano-impression avec un moule mou de PDMS assisté par dégazage. Ce procédé a permis d'obtenir des résultats inédits concernant les cellules solaires en CIGS, dépassant le cadre de ce manuscrit. Par exemple, nous avons mené à bien la fabrication d'un réseau de nano-particules d'Au (cf. figureC.10a) ainsi que d'une structuration face arrière d'une cellule solaire CIGS de 300 nm d'épaisseur (cf. figure C.10b) avec contacts ponctuels.

Ce dernier procédé innovant permet d'intégrer simplement une nano-structuration améliorant le piégeage de lumière au contact arrière. De plus, le contact arrière présente désormais des contacts ponctuels très denses. Cette géométrie permet potentiellement de réduire d'un facteur 4 la surface de contact arrière et ainsi que le courant de saturation à l'obscurité et donc d'améliorer la tension de circuit ouvert de la cellule. Les échantillons fabriqués avec ce procédé font l'objet de caractérisations poussés et présentent des premiers résultats optiques et électroniques prometteurs qui restent à renforcer.

Conclusion et perspectives de l'étude

En conclusion générale, cette thèse s'est présentée comme le fruit de la rencontre entre la nanophotonique et le domaine du photovoltaïque. En effet, la réduction de l'épaisseur de l'absorbeur vers des couches ultra-minces pourrait ouvrir la voie vers des dispositifs photovoltaïques plus efficaces et moins coûteux et soulager la contrainte pesant sur les matériaux rares. Cependant, cette avancée technologique n'a lieu d'être que s'il est possible de générer un photocourant élevé dans de très petits volumes de semi-conducteurs. Dans ce but, nous avons proposé une nouvelle structure avec une très fine couche métallique nanostructurée pour concentrer la lumière dans la cellule solaire ultra-mince. Dans cette thèse, nous avons montré des résultats prometteurs pour l'application de ce concept à des matériaux que sont l'arsenure de gallium, l'antimoniure de gallium et le CIGS. Actuellement, les perspectives à court terme sont de caractériser complètement des cellules solaires

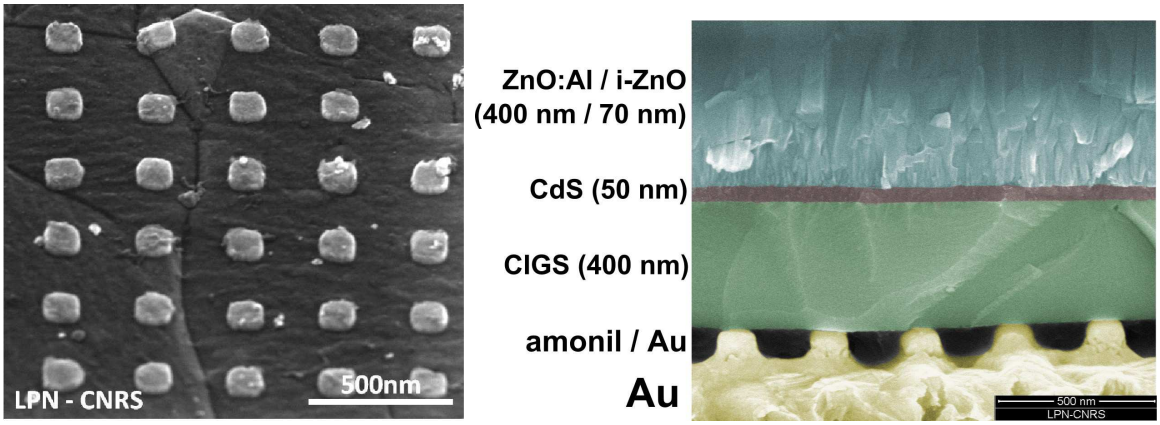

(a) (b)

Figure C.10: (a) Image au microscope électronique (MEB) d'un réseau d'or tableau (période = 400 nm, largeur = 200 nm et épaisseur = 20 nm) réalisées sur des surfaces CIGS par nano-impression. (b) image en coupe transversale (MEB) de la cellule de solaire CIGS de 300 nm d'épaisseur nano-structurée face arrière par par nano-impression et ses contacts ponctuels.

ultra-fines et nanostructurées en CIGS, ce qui représente une première mondiale.

Pourquoi ne pas étendre cette approche dans un premier temps à d'autres matériaux couches minces tels que CdTe ou et le silicium amorphe et dans un deuxième temps aux cellules ultra-fines en silicium cristallin ainsi qu'au nouveaux concepts ? De fait, la recherche des cellules photovoltaïques ultimes à faible coût et à haut rendement brouille les frontières entre les différentes filières technologiques. Par exemple, dans cette thèse, nous avons déjà étudié l'application de techniques de nanofabrication classiquement associées aux technologies couches minces à la structuration du silicium monocristallin. Plus globalement, quelle que soit la technologie considérée, cette thèse a montré que la mise en œuvre efficace de structures avancées de piégeage optique nécessite une forte synergie entre la conception numérique, la science des matériaux et les techniques de nanofabrication.

Appendix D

List of publications

Journal contributions

1. Massiot, I., **Colin, C**., Sauvan, C., Lalanne, P., Cabarrocas, P.R. i, Pelouard, J.-L., and Collin, S., *Multi-resonant absorption in ultra-thin silicon solar cells with metallic nanowires,* Optics Express 21(S3), A372 (2013).

2. Massiot, I., **Colin, C**., Péré-Laperne, N., Roca i Cabarrocas, P., Sauvan, C., Lalanne, P., Pelouard, J.-L., and Collin, S., "Nanopatterned front contact for broadband absorption in ultra-thin amorphous silicon solar cells," *Applied Physics Letters* 101(16), 163901 (2012).

3. Le Bris, A., Rodiere, J., **Colin, C**., Collin, S., Pelouard, J.-L., Esteban, R., Laroche, M., Greffet, J.-J., and Guillemoles, J.-F., "Hot Carrier Solar Cells: Controlling Thermalization in Ultrathin Devices," *IEEE Journal of Photovoltaics* 2(4), 506–511 (2012).

Conference proceedings as first author

1. **C. Colin,** I. Massiot, A. Cattoni, N. Vandamme, C. Dupuis, N. Bardou, I. Gerard, N. Naghavi, J.-F. Guillemoles, J.-L. Pelouard, S. Collin, *Broadband light-trapping in ultra-thin nano-structured solar cells*, in SPIE Photonics West OPTO Conference Proceedings, p. 86200C–86200C–12 (San Francisco, Feburary 2013) [doi:10.1117/12.2004269]**.**

2. **C. Colin,** A. Cattoni, I. Massiot, J.F. Guillemoles, N. Bardou, C. Dupuis, J.-L. Pelouard, D. Mercier, I. Gérard, A. Etcheberry, Z. Jehl, D. Lincot, N. Naghavi, S. Collin, *Broadband Light Trapping in Ultra-Thin Nano-Structured Cu(In,Ga)Se2 Solar Cells,* EU-PVSEC 2012 proceedings, page 2244 - 2248)

3. **C. Colin**, S. Collin, N. Péré-Laperne, I. Massiot, G. Dagher, N. Quach-Vu, N. Bardou, C. Dupuis, J.-F. Guillemoles, J.-L. Pelouard, *Ultrathin CIGS*

Solar Cells with Metallic Nanoparticles, EU-PVSEC 2011 proceedings, page 2863 - 2866)

Conference proceedings as co-author

1. I. Massiot, **C. Colin**, N. Vandamme, N. Bardou, P. Roca i Cabarrocas, C. Sauvan, P. Lalanne, J-L. Pelouard and S. Collin, *Towards high-efficiency ultra-thin solar cells with nanopatterned metallic front contact*, In Proceedings of the 39th IEEE Photovoltaic Specialists Conference, Tampa, United States (2013).

2. I. Massiot, **C. Colin**, P. Roca i Cabarrocas, N. Bardou, C. Dupuis, C. Sauvan, P. Lalanne, J-L. Pelouard and S. Collin, *Nanopatterned front contact for multiresonant absorption in ultra-thin amorphous silicon solar cells*, In Proceedings of the 27th European Photovoltaic Solar Energy Conference, 3 AO.6.5, p. 2132-2136, Frankfurt, Germany (2012).

3. I. Massiot, S. Collin, **C. Colin**, N. Péré-Laperne, N. Bardou, C. Dupuis, P. Roca i Cabarrocas and J-L. Pelouard, *Conception of ultra-thin amorphous silicon solar cells*, In Proceedings of the 26th European Photovoltaic Solar Energy Conference, 1DV.1.28, p. 398-401, Hamburg, Germany (2011).

4. S. Collin, C. Sauvan, **C. Colin**, I. Massiot, F. Pardo, N. Bardou, P. Lalanne and J-L. Pelouard, *High-efficient ultra-thin solar cells*, In Proceedings of the 25th European Photovoltaic Solar Energy Conference, 1CO.8.4, p. 265-268, Valencia, Spain (2010).

Bibliography

[1] X. Meng, *Conception et réalisation de cristaux photoniques et de réseaux de diffraction pour les cellules photovoltaïques silicium en couches ultra-minces.* PhD thesis, Oct. 2012.

[2] K. Soderstrom, F.-J. Haug, J. Escarre, O. Cubero, and C. Ballif, "Photocurrent increase in n-i-p thin film silicon solar cells by guided mode excitation via grating coupler," *Applied Physics Letters* **96**(21), p. 213508, 2010.

[3] J. Zhu, C.-M. Hsu, Z. Yu, S. Fan, Y. Cui, and Z. Y. S. F. Jia Zhu Ching-Mei Hsu, "Nanodome Solar Cells with Efficient Light Management and Self-Cleaning," *Nano Letters* **10**, pp. —-, 2009.

[4] V. E. Ferry, M. A. Verschuuren, H. B. T. Li, R. E. I. Schropp, H. A. Atwater, and A. Polman, "Improved red-response in thin film a-Si:H solar cells with soft-imprinted plasmonic back reflectors," *Applied Physics Letters* **95**(18), p. 183503, 2009.

[5] IEA, "Renewable energy technologies, Solar Energy Perspectives," tech. rep., 2012.

[6] IEA, "Key world energy statistics," tech. rep., 2009.

[7] EPIA, "Solar photovoltaics competing the energy sector, on the road to competitiveness," tech. rep., 2011.

[8] E. Becquerel, "Mémoire sur les effets électriques produits sous l'influence des rayons solaires," *Comptes Rendus* **9**, pp. 561–567, 1839.

[9] D. Chapin, G. Pearson, and C. Fuller, "Energy converting apparatus (OCR)," 1957.

[10] C. Gueymard, D. Myers, and K. Emery, "Proposed reference irradiance spectra for solar energy systems testing," *Solar Energy* **73**, pp. 443–467, Dec. 2002.

[11] I. E. Commission, "IEC 60904-3: Photovoltaic devices – Part 3: Measurement principles for terrestrial photovoltaic (PV) solar devices with reference spectral irradiance data," 1989.

[12] A. S. f. T. (ASTM) and Materials, "Solar Spectral Irradiance: Air Mass 1.5."

[13] P. Wurfel, *Physics of Solar Cells: From Basic Principles to Advanced Concepts (Physics Textbook)*, Wiley-VCH, 2009.

[14] J. Nelson, *The Physics of Solar Cells (Properties of Semiconductor Materials)*, Imperial College Press, 2003.

[15] M. A. Green, K. Emery, Y. Hishikawa, W. Warta, and E. D. Dunlop, "Solar cell efficiency tables (version 42)," *Progress in Photovoltaics: Research and Applications* **21**, pp. 827–837, Aug. 2013.

[16] A. Luque and S. Hegedus, eds., *Handbook of Photovoltaic Science and Engineering*, John Wiley & Sons, Ltd, Chichester, UK, Dec. 2010.

[17] M. Brozel and G. Stillman, *Properties of Gallium Arsenide (3rd Edition)*, Institution of Engineering and Technology, 1996.

[18] W. Shockley and H. J. Queisser, "Detailed Balance Limit of Efficiency of p-n Junction Solar Cells," *Journal of Applied Physics* **32**(3), pp. 510–519, 1961.

[19] M. A. Green, *Solar cells: operating principles, technology, and system applications*, Prentice-Hall series in solid state physical electronics, Prentice-Hall, 1982.

[20] M. A. Green, K. Emery, Y. Hishikawa, W. Warta, and E. D. Dunlop, "Solar cell efficiency tables (version 41)," *Progress in Photovoltaics: Research and Applications* **21**, pp. 1–11, Jan. 2013.

[21] B. M. Kayes, H. Nie, R. Twist, S. G. Spruytte, F. Reinhardt, I. C. Kizilyalli, and G. S. Higashi, "27.6% Conversion efficiency, a new record for single-junction solar cells under 1 sun illumination," in *2011 37th IEEE Photovoltaic Specialists Conference*, pp. 000004–000008, IEEE, June 2011.

[22] C.-W. Cheng, K.-T. Shiu, N. Li, S.-J. Han, L. Shi, and D. K. Sadana, "Epitaxial lift-off process for gallium arsenide substrate reuse and flexible electronics," *Nature Communications* **4**, p. 1577, Mar. 2013.

[23] G. Bauhuis, P. Mulder, E. Haverkamp, J. Huijben, and J. Schermer, "26.1% thin-film GaAs solar cell using epitaxial lift-off," *Solar Energy Materials and Solar Cells* **93**, pp. 1488–1491, Sept. 2009.

[24] D. Shahrjerdi, S. W. Bedell, C. Ebert, C. Bayram, B. Hekmatshoar, K. Fogel, P. Lauro, M. Gaynes, T. Gokmen, J. A. Ott, and D. K. Sadana, "High-efficiency thin-film InGaP/InGaAs/Ge tandem solar cells enabled by controlled spalling technology," *Applied Physics Letters* **100**(5), p. 053901, 2012.

[25] S. W. Bedell, D. Shahrjerdi, B. Hekmatshoar, K. Fogel, P. A. Lauro, J. A. Ott, N. Sosa, and D. Sadana, "Kerf-Less Removal of Si, Ge, and III–V Layers by Controlled Spalling to Enable Low-Cost PV Technologies," *IEEE Journal of Photovoltaics* **2**, pp. 141–147, Apr. 2012.

[26] A. Yoshida, T. Agui, N. Katsuya, K. Murasawa, H. Juso, K. Sasaki, and T. Takamoto, "Development of InGaP/GaAs/ InGaAs inverted triple junction solar cells for concentrator application," in *21st International Photovoltaic Science and Engineering Conference (PVSEC-21)*, (Fukuoka, Japan), 2011.

[27] J. Schmidtke, "Commercial status of thin-film photovoltaic devices and materials.," *Optics express* **18 Suppl 3**, pp. A477–86, Sept. 2010.

[28] "Solar Frontier press releases," (http://investor.firstsolar.com/releases.cfm), 2013.

[29] M. J. Shiao, "Thin Film 2012 – 2016 : Technologies , Markets and Strategies for survival," tech. rep., GreenTech Media (GTM) Research, 2012.

[30] S. Wagner, "CuInSe2/CdS heterojunction photovoltaic detectors," *Applied Physics Letters* **25**(8), p. 434, 1974.

[31] R. A. Mickelsen and W. S. Chen, "High photocurrent polycrystalline thin-film CdS/CuInSe2 solar cella," *Applied Physics Letters* **36**, p. 371, Mar. 1980.

[32] Z. für Sonnenenergie, U. Wasserstoff-Forschung, and B.-W. (ZSW), "Press release : ZSW produces world record solar cell - Thin-film photovoltaics achieves 20.8% efficiency and overtakes multicrystalline silicon technology," (http://www.zsw-bw.de/uploads/media/pi18-2013-ZSW-WorldrecordCIGS.pdf).

[33] A. N. Tiwari, "EMPA Media release : A new world record for solar cell efficiency," (http://www.empa.ch/plugin/template/empa/*/131441), 2013.

[34] "Solar Frontier Manufactures 14.6% Efficiency CIS Module," (http://www.solar-frontier.com/eng/news/2013/C020760.html), 2013.

[35] Harnergy, "Hanergy Solar media release : Achievement of thin film efficiency of 18.7% with Solibro's CIGS thin film technology," (http://www.hanergysolargroup.com/pdf/LTN20131007017_E.pdf), 2013.

[36] A. Chirila, S. Buecheler, F. Pianezzi, P. Bloesch, C. Gretener, A. R. Uhl, C. Fella, L. Kranz, J. Perrenoud, S. Seyrling, R. Verma, S. Nishiwaki, Y. E. Romanyuk, G. Bilger, and A. N. Tiwari, "Highly efficient Cu(In,Ga)Se2 solar cells grown on flexible polymer films.," *Nature materials* **10**, pp. 857–61, Nov. 2011.

[37] P. Bommersbach, L. Arzel, M. Tomassini, E. Gautron, C. Leyder, M. Urien, D. Dupuy, and N. Barreau, "Influence of Mo back contact porosity on co-evaporated Cu(In,Ga)Se 2 thin film properties and related solar cell," *Progress in Photovoltaics: Research and Applications* **21**, pp. 332–343, May 2013.

[38] X. Zhu, Z. Zhou, Y. Wang, L. Zhang, A. Li, and F. Huang, "Determining factor of MoSe2 formation in Cu(In,Ga)Se2 solar Cells," *Solar Energy Materials and Solar Cells* **101**, pp. 57–61, June 2012.

[39] R. Scheer, *Chalcogenide Photovoltaics: Physics, Technologies, and Thin Film Devices*, Wiley-VCH.

[40] T. Dullweber, U. Rau, M. A. Contreras, R. Noufi, and H.-w. Schock, "Photogeneration and Carrier Recombination in Graded Gap Cu (In , Ga) Se 2 Solar Cells," **47**(12), pp. 2249–2254, 2000.

[41] A. M. Gabor, J. R. Tuttle, D. S. Albin, M. A. Contreras, R. Noufi, and A. M. Hermann, "High-efficiency CuInGaSe2 solar cells made from InGa2Se3 precursor films," *Applied Physics Letters* **65**(2), p. 198, 1994.

[42] G. Voorwinden, R. Kniese, and M. Powalla, "In-line Cu(In,Ga)Se2 co-evaporation processes with graded band gaps on large substrates," *Thin Solid Films* **431-432**, pp. 538–542, May 2003.

[43] J. A. Thornton, "Reactive sputtered copper indium diselenide films for photovoltaic applications," *Journal of Vacuum Science & Technology A: Vacuum, Surfaces, and Films* **2**(2), p. 307, 1984.

[44] T. Nakada, K. Migita, and S. Niki, "Microstructural Characterization for Sputter-Deposited CuInSe2 Films and Photovoltaic Devices," *Japanese Journal of Applied Physics* **34**, pp. 4715–4721, Sept. 1995.

[45] D. Lincot, J. Guillemoles, S. Taunier, D. Guimard, J. Sicx-Kurdi, A. Chaumont, O. Roussel, O. Ramdani, C. Hubert, J. Fauvarque, N. Bodereau, L. Parissi, P. Panheleux, P. Fanouillere, N. Naghavi, P. Grand, M. Benfarah, P. Mogensen, and O. Kerrec, "Chalcopyrite thin film solar cells by electrodeposition," *Solar Energy* **77**, pp. 725–737, Dec. 2004.

[46] S. Taunier, J. Sicx-Kurdi, P. Grand, A. Chomont, O. Ramdani, L. Parissi, P. Panheleux, N. Naghavi, C. Hubert, M. Ben-Farah, J. Fauvarque, J. Connolly, O. Roussel, P. Mogensen, E. Mahé, J. Guillemoles, D. Lincot, and O. Kerrec, "Cu(In,Ga)(S,Se)2 solar cells and modules by electrodeposition," *Thin Solid Films* **480-481**, pp. 526–531, June 2005.

[47] P. Jackson, D. Hariskos, E. Lotter, S. Paetel, R. Wuerz, R. Menner, W. Wischmann, and M. Powalla, "New world record efficiency for Cu(In,Ga)Se2 thin-film solar cells beyond 20%," *Progress in Photovoltaics: Research and Applications* **19**, pp. 894–897, Nov. 2011.

[48] I. Repins, M. A. Contreras, B. Egaas, C. DeHart, J. Scharf, C. L. Perkins, B. To, and R. Noufi, "19 · 9%-efficient ZnO/CdS/CuInGaSe 2 solar cell with 81 · 2% fill factor," *Progress in Photovoltaics: Research and Applications* **16**, pp. 235–239, May 2008.

[49] K. Orgassa, U. Rau, Q. Nguyen, H. Werner Schock, and J. H. Werner, "Role of the CdS buffer layer as an active optical element in Cu(In,Ga)Se2 thin-film solar cells," *Progress in Photovoltaics: Research and Applications* **10**, pp. 457–463, Nov. 2002.

[50] D. Lincot, "Chemical Bath Deposition of Cadmium Sulfide Thin Films. In Situ Growth and Structural Studies by Combined Quartz Crystal Microbalance and Electrochemical Impedance Techniques," *Journal of The Electrochemical Society* **139**(7), p. 1880, 1992.

[51] R. Ortega-Borges, "Mechanism of Chemical Bath Deposition of Cadmium Sulfide Thin Films in the Ammonia-Thiourea System," *Journal of The Electrochemical Society* **140**(12), p. 3464, 1993.

[52] N. Naghavi, D. Abou-Ras, N. Allsop, N. Barreau, S. Bücheler, A. Ennaoui, C.-H. Fischer, C. Guillen, D. Hariskos, J. Herrero, R. Klenk, K. Kushiya, D. Lincot, R. Menner, T. Nakada, C. Platzer-Björkman, S. Spiering, A. Tiwari, and T. Törndahl, "Buffer layers and transparent conducting oxides for chalcopyrite Cu(In,Ga)(S,Se)2 based thin film photovoltaics: present status and current developments," *Progress in Photovoltaics: Research and Applications* **18**, pp. 411–433, Sept. 2010.

[53] R. Anderson, "Experiments on Ge-GaAs heterojunctions," *Solid-State Electronics* **5**, pp. 341–351, Sept. 1962.

[54] M. Burgelman, J. Verschraegen, S. Degrave, and P. Nollet, "Modeling thin-film PV devices," *Progress in Photovoltaics: Research and Applications* **12**, pp. 143–153, Mar. 2004.

[55] J. Pettersson, C. Platzer-Bjorkman, U. Zimmermann, and M. Edoff, "Baseline model of graded-absorber Cu(In,Ga)Se2 solar cells applied to cells with ZnMgO buffer layers," *Thin Solid Films* **519**, pp. 7476–7480, Aug. 2011.

[56] SOLER (commission solaire du Syndicat des énergies renouvelables), "Repenser le développement de la filière photovoltaïque française," tech. rep., 2011.

[57] C. Wadia, A. P. Alivisatos, and D. M. Kammen, "Materials Availability Expands the Opportunity for Large-Scale Photovoltaics Deployment," *Environmental Science & Technology* **43**, pp. 2072–2077, Mar. 2009.

[58] B. A. Andersson, "Materials availability for large-scale thin-film photovoltaics," *Progress in Photovoltaics: Research and Applications* **8**, pp. 61–76, Feb. 2000.

[59] V. Fthenakis, "Sustainability of photovoltaics: The case for thin-film solar cells," *Renewable and Sustainable Energy Reviews* **13**, pp. 2746–2750, Dec. 2009.

[60] M. Paire, L. Lombez, J.-F. Guillemoles, and D. Lincot, "Toward microscale Cu(In,Ga)Se2 solar cells for efficient conversion and optimized material usage: Theoretical evaluation," *Journal of Applied Physics* **108**(3), p. 034907, 2010.

[61] P. Y. Yu and M. Cardona, *Fundamentals of Semiconductors: Physics and Materials Properties*, Springer, 2010.

[62] J. S. Blakemore, "Semiconducting and other major properties of gallium arsenide," *Journal of Applied Physics* **53**(10), p. R123, 1982.

[63] S. M. Sze, *Physics of Semiconductor Devices*, Wiley, New York, 1981.

[64] A. Le Bris, L. Lombez, S. Laribi, J.-F. Guillemoles, C. Colin, S. Collin, J.-L. Pelouard, M. Laroche, R. Esteban, J.-J. Greffet, G. Boissier, and P. Christol, "Hot carrier solar cells: Controlling thermalization in ultra thin devices," *2011 37th IEEE Photovoltaic Specialists Conference* , pp. 001913–001913, June 2011.

[65] A. Le Bris, J. Rodiere, C. Colin, S. Collin, J.-L. Pelouard, R. Esteban, M. Laroche, J.-J. Greffet, and J.-F. Guillemoles, "Hot Carrier Solar Cells: Controlling Thermalization in Ultrathin Devices," *IEEE Journal of Photovoltaics* **2**, pp. 506–511, Oct. 2012.

[66] C. Andriamiadamanana, A. Joudrier, L. Lombez, A. Ferrier, N. Naghavi, P. Ghenuche, N. Bardou, N. Vandamme, J.-L. Pelouard, S. Collin, F. Pellé, and J. Guillemoles, "Resonance Induced Enhancement of Up-Conversion in Ultrathin Layers," in *27th European Photovoltaic Solar Energy Conference and Exhibition*, pp. 61–62, WIP, Oct. 2012.

[67] M. Bernardi, M. Palummo, and J. C. Grossman, "Extraordinary sunlight absorption and one nanometer thick photovoltaics using two-dimensional monolayer materials.," *Nano letters* **13**, pp. 3664–70, Aug. 2013.

[68] R. Brendel and H. Queisser, "On the thickness dependence of open circuit voltages of p-n junction solar cells," *Solar Energy Materials and Solar Cells* **29**, pp. 397–401, May 1993.

[69] E. D. Palik, *Handbook of Optical Constants of Solids*, Academic Press, 1998.

[70] "SOPRA N&K Database."

[71] K. Orgassa and J. Rau, U. ; Schock, H.-W. ; Werner, "Optical constants of Cu(ln,Ga)Se/sub 2/ thin films from normal incidence transmittance and reflectance," *Proceedings of 3rd World Conference on Photovoltaic Energy Conversion* **1**, pp. 372–375, 2003.

[72] W. Shafarman, R. Birkmire, S. Marsillac, M. Marudachalam, N. Orbey, and T. Russell, "Effect of reduced deposition temperature, time, and thickness on Cu(InGa)Se/sub 2/ films and devices," in *Conference Record of the Twenty Sixth IEEE Photovoltaic Specialists Conference - 1997*, pp. 331–334, IEEE.

[73] T. Negami, S. Nishiwaki, Y. Hashimoto, N. Kohara, and T. Wada, "Effect of the absorber thickness on performance of Cu(In,Ga)Se2 solar cells," in *Proceedings of the 2nd WCPEC*, pp. 1181–1184, (Vienna), 1998.

[74] K. Ramanathan, R. Noufi, B. To, D. Young, R. Bhattacharya, M. Contreras, R. Dhere, and G. Teeter, "Processing and Properties of Sub-Micron CIGS Solar Cells," in *2006 IEEE 4th World Conference on Photovoltaic Energy Conference*, pp. 380–383, IEEE, 2006.

[75] B. S. Delahoy A.E. , L. Chen, "Subcontractor report NREL," **SR-520-401**, 2006.

[76] N. G. Dhere, A. A. Kadam, S. S. Kulkarni, J. S. Shirolikar, and S. A. Pethe, "Low Toxic Processing of Thin and Ultra-thin CIGSS Absorber Solar Cells," **2**(Fig 5), pp. 2–4.

[77] O. Lundberg, M. Bodegard, J. Malmstrom, and L. Stolt, "Influence of the Cu(In,Ga)Se2 thickness and Ga grading on solar cell performance," *Progress in Photovoltaics: Research and Applications* **11**(2), pp. 77–88, 2003.

[78] J. Malmström, *On Generation and Recombination in Cu(In,Ga)Se2 Thin-Film Solar Cells.* PhD thesis, 2005.

[79] K. Ramanathan, R. Noufi, B. To, D. Young, R. Bhattacharya, M. Contreras, R. Dhere, and G. Teeter, "Processing and Properties of Sub-Micron CIGS Solar Cells," in *2006 IEEE 4th World Conference on Photovoltaic Energy Conference*, pp. 380–383, IEEE, 2006.

[80] W. Shafarman, R. Huang, and S. Stephens, "Characterization of Cu(InGa)Se2 Solar Cells using Etched Absorber Layers," in *2006 IEEE 4th World Conference on Photovoltaic Energy Conference*, pp. 420–423, IEEE, 2006.

[81] Z. Jehl, L. Kao, N. Naghavi, F. Erfurth, J. F. Guillemoles, I. Gérard, A. Etcheberry, J. L. Pelouard, S. Collin, G. Voorwinden, D. Lincot, and Z. J. Li-Kao, "Towards ultrathin copper indium gallium diselenide solar cells: proof of concept study by chemical etching and gold back contact engineering," *Progress in Photovoltaics: Research and Applications* **20**, pp. 582–587, Aug. 2012.

[82] M. Gloeckler and J. R. Sites, "Potential of submicrometer thickness Cu(In,Ga)Se2 solar cells," *Journal of Applied Physics* **98**(10), p. 103703, 2005.

[83] R. W. Birkmire and B. E. McCandless, "Specular CuInSe2 films for solar cells," *Applied Physics Letters* **53**(2), p. 140, 1988.

[84] B. Canava, J. Guillemoles, J. Vigneron, D. Lincot, and A. Etcheberry, "Chemical elaboration of well defined Cu(In,Ga)Se2 surfaces after aqueous oxidation etching," *Journal of Physics and Chemistry of Solids* **64**, pp. 1791–1796, Sept. 2003.

[85] Z. Jehl, F. Erfurth, N. Naghavi, L. Lombez, I. Gerard, M. Bouttemy, P. Tran-Van, A. Etcheberry, G. Voorwinden, B. Dimmler, W. Wischmann, M. Powalla, J. Guillemoles, and D. Lincot, "Thinning of CIGS solar cells:

Part II: Cell characterizations," *Thin Solid Films* **519**, pp. 7212–7215, Aug. 2011.

[86] F. Erfurth, Z. Jehl, M. Bouttemy, N. Dahan, P. Tran-Van, I. Gerard, A. Etcheberry, J.-J. Greffet, M. Powalla, G. Voorwinden, D. Lincot, J. Guillemoles, and N. Naghavi, "Mo/Cu(In, Ga)Se2 back interface chemical and optical properties for ultrathin CIGSe solar cells," *Applied Surface Science* **258**, pp. 3058–3061, Jan. 2012.

[87] M. Bouttemy, P. Tran-Van, I. Gerard, T. Hildebrandt, A. Causier, J. Pelouard, G. Dagher, Z. Jehl, N. Naghavi, G. Voorwinden, B. Dimmler, M. Powalla, J. Guillemoles, D. Lincot, and A. Etcheberry, "Thinning of CIGS solar cells: Part I: Chemical processing in acidic bromine solutions," *Thin Solid Films* **519**, pp. 7207–7211, Aug. 2011.

[88] N. Dahan, Z. Jehl, T. Hildebrandt, J.-J. Greffet, J.-F. Guillemoles, D. Lincot, and N. Naghavi, "Optical approaches to improve the photocurrent generation in Cu(In,Ga)Se2 solar cells with absorber thicknesses down to 0.5 μm," *Journal of Applied Physics* **112**(9), p. 094902, 2012.

[89] J. Moghal, J. Kobler, J. Sauer, J. Best, M. Gardener, A. A. R. Watt, and G. Wakefield, "High-performance, single-layer antireflective optical coatings comprising mesoporous silica nanoparticles.," *ACS applied materials & interfaces* **4**, pp. 854–9, Feb. 2012.

[90] A. Yoshikawa, "Optimum design for window layer thickness of GaAlAs-GaAs heteroface solar cell regarding the effect of reflection loss," *Journal of Applied Physics* **52**(6), p. 4345, 1981.

[91] K. A. Bertness, S. R. Kurtz, D. J. Friedman, A. E. Kibbler, C. Kramer, and J. M. Olson, "29.5%-efficient GaInP/GaAs tandem solar cells," *Applied Physics Letters* **65**(8), p. 989, 1994.

[92] I. Rey-Stolle and C. Algora, "Optimum antireflection coatings for heteroface AlGaAs/GaAs solar cells—Part II: The influence of uncertainties in the parameters of window and antireflection coatings," *Journal of Electronic Materials* **29**, pp. 992–999, July 2000.

[93] C. G. Bernhard, "Structural and functional adaptation in a visual system," *Endeavour* **26**, pp. 76–84, 1967.

[94] E. Yablonovitch, "Statistical ray optics," *J. Opt. Soc. Am.* **72**(7), pp. 899–907, 1982.

[95] P. Campbell and M. A. Green, "Light trapping properties of pyramidally textured surfaces," *Journal of Applied Physics* **62**(1), pp. 243–249, 1987.

[96] J. Müller, B. Rech, J. Springer, and M. Vanecek, "TCO and light trapping in silicon thin film solar cells," *Solar Energy* **77**, pp. 917–930, Dec. 2004.

[97] K. Söderström, J. Escarré, O. Cubero, F.-J. Haug, S. Perregaux, and C. Ballif, "UV-nano-imprint lithography technique for the replication of back reflectors for n-i-p thin film silicon solar cells," *Progress in Photovoltaics: Research and Applications* **19**, pp. 202–210, Mar. 2011.

[98] C. Battaglia, J. Escarré, K. Söderström, M. Charrière, M. Despeisse, F.-J. Haug, and C. Ballif, "Nanomoulding of transparent zinc oxide electrodes for efficient light trapping in solar cells," *Nature Photonics* **5**, pp. 535–538, Aug. 2011.

[99] C. Battaglia, C.-M. Hsu, K. Söderström, J. Escarré, F.-J. Haug, M. Charrière, M. Boccard, M. Despeisse, D. T. L. Alexander, M. Cantoni, Y. Cui, and C. Ballif, "Light trapping in solar cells: can periodic beat random?," *ACS nano* **6**, pp. 2790–7, Mar. 2012.

[100] D. Abou-Ras, R. Caballero, C. A. Kaufmann, M. Nichterwitz, K. Sakurai, S. Schorr, T. Unold, and H. W. Schock, "Impact of the Ga concentration on the microstructure of CuIn1–xGaxSe2," *physica status solidi (RRL) – Rapid Research Letters* **2**, pp. 135–137, June 2008.

[101] N. Dahan, Z. Jehl, J. F. Guillemoles, D. Lincot, N. Naghavi, and J.-J. Greffet, "Using radiative transfer equation to model absorption by thin Cu(In,Ga)Se2 solar cells with Lambertian back reflector.," *Optics express* **21**, pp. 2563–80, Feb. 2013.

[102] Z. Yu, A. Raman, and S. Fan, "Fundamental limit of nanophotonic light trapping in solar cells.," *Proceedings of the National Academy of Sciences of the United States of America* **107**, pp. 17491–6, Oct. 2010.

[103] Z. Yu, A. Raman, and S. Fan, "Fundamental limit of light trapping in grating structures.," *Optics express* **18 Suppl 3**, pp. A366–80, Sept. 2010.

[104] P. N. Saeta, V. E. Ferry, D. Pacifici, J. N. Munday, and H. A. Atwater, "How much can guided modes enhance absorption in thin solar cells?," *Optics Express* **17**(23), pp. 20975–20990, 2009.

[105] V. E. Ferry, J. N. Munday, and H. A. Atwater, "Design considerations for plasmonic photovoltaics.," *Advanced materials* **22**, pp. 4794–808, Nov. 2010.

[106] V. E. Ferry, L. A. Sweatlock, D. Pacifici, and H. A. Atwater, "Plasmonic nanostructure design for efficient light coupling into solar cells.," *Nano letters* **8**, pp. 4391–7, Dec. 2008.

[107] S. Mokkapati and K. R. Catchpole, "Nanophotonic light trapping in solar cells," *Journal of Applied Physics* **112**(10), p. 101101, 2012.

[108] C. Heine and R. H. Morf, "Submicrometer gratings for solar energy applications," *Appl. Opt.* **34**(14), pp. 2476–2482, 1995.

[109] D. Zhou and R. Biswas, "Photonic crystal enhanced light-trapping in thin film solar cells," *Journal of Applied Physics* **103**(9), p. 93102, 2008.

[110] X. Meng, G. Gomard, O. El Daif, E. Drouard, R. Orobtchouk, A. Kaminski, A. Fave, M. Lemiti, A. Abramov, P. Roca i Cabarrocas, and C. Seassal, "Absorbing photonic crystals for silicon thin-film solar cells: Design, fabrication and experimental investigation," *Solar Energy Materials and Solar Cells* **95**, pp. S32–S38, May 2011.

[111] O. El Daif, E. Drouard, G. Gomard, A. Kaminski, A. Fave, M. Lemiti, S. Ahn, S. Kim, P. Roca I Cabarrocas, H. Jeon, and C. Seassal, "Absorbing one-dimensional planar photonic crystal for amorphous silicon solar cell.," *Optics express* **18 Suppl 3**, pp. A293–9, Sept. 2010.

[112] G. Gomard, E. Drouard, X. Letartre, X. Meng, A. Kaminski, A. Fave, M. Lemiti, E. Garcia-Caurel, and C. Seassal, "Two-dimensional photonic crystal for absorption enhancement in hydrogenated amorphous silicon thin film solar cells," *Journal of Applied Physics* **108**(12), p. 123102, 2010.

[113] G. Gomard, X. Meng, E. Drouard, K. E. Hajjam, E. Gerelli, R. Peretti, A. Fave, R. Orobtchouk, M. Lemiti, and C. Seassal, "Light harvesting by planar photonic crystals in solar cells: the case of amorphous silicon," *Journal of Optics* **14**, p. 024011, Feb. 2012.

[114] Y. Park, E. Drouard, O. E. Daif, X. Letartre, P. Viktorovitch, A. Fave, A. Kaminski, M. Lemiti, and C. Seassal, "Absorption enhancement using photonic crystals for silicon thin film solar cells," *Opt. Express* **17**(16), pp. 14312–14321, 2009.

[115] X. Meng, E. Drouard, G. Gomard, R. Peretti, A. Fave, and C. Seassal, "Combined front and back diffraction gratings for broad band light trapping in thin film solar cell.," *Optics express* **20 Suppl 5**, pp. A560–71, Sept. 2012.

[116] M. Vanecek, O. Babchenko, A. Purkrt, J. Holovsky, N. Neykova, A. Poruba, Z. Remes, J. Meier, and U. Kroll, "Nanostructured three-dimensional thin film silicon solar cells with very high efficiency potential," *Applied Physics Letters* **98**(16), p. 163503, 2011.

[117] H. Sai, H. Fujiwara, and M. Kondo, "Back surface reflectors with periodic textures fabricated by self-ordering process for light trapping in thin-film microcrystalline silicon solar cells," *Solar Energy Materials and Solar Cells* **93**, pp. 1087–1090, June 2009.

[118] L. Zeng, P. Bermel, Y. Yi, B. A. Alamariu, K. A. Broderick, J. Liu, C. Hong, X. Duan, J. Joannopoulos, and L. C. Kimerling, "Demonstration of enhanced absorption in thin film Si solar cells with textured photonic crystal back reflector," *Applied Physics Letters* **93**(22), p. 221105, 2008.

[119] C. Granqvist and A. Hultå ker, "Transparent and conducting ITO films: new developments and applications," *Thin Solid Films* **411**, pp. 1–5, May 2002.

[120] J. G. Mutitu, S. Shi, C. Chen, T. Creazzo, A. Barnett, C. Honsberg, and D. W. Prather, "Thin film solar cell design based on photonic crystal and diffractive grating structures," *Opt. Express* **16**(19), pp. 15238–15248, 2008.

[121] L. C. Wang Yu and S. Fan, "Absorption Enhancement in Ultrathin Crystalline Silicon Solar Cells with Antireflection and Light-Trapping Nanocone Gratings," *NanoLetters* **12**, pp. 1616–1619, 2012.

[122] R. Dewan, M. Marinkovic, R. Noriega, S. Phadke, A. Salleo, and D. Knipp, "Light trapping in thin-film silicon solar cells with submicron surface texture.," *Optics express* **17**, pp. 23058–65, Dec. 2009.

[123] R. Esteban, M. Laroche, and J. J. Greffet, "Dielectric gratings for wide-angle, broadband absorption by thin film photovoltaic cells," *Applied Physics Letters* **97**(22), p. 221111, 2010.

[124] S. John, "Strong localization of photons in certain disordered dielectric superlattices," *Physical Review Letters* **58**, pp. 2486–2489, June 1987.

[125] E. Yablonovitch, "Inhibited Spontaneous Emission in Solid-State Physics and Electronics," *Physical Review Letters* **58**, pp. 2059–2062, May 1987.

[126] D. Duché, L. Escoubas, J.-J. Simon, P. Torchio, W. Vervisch, and F. Flory, "Slow Bloch modes for enhancing the absorption of light in thin films for photovoltaic cells," *Applied Physics Letters* **92**(19), p. 193310, 2008.

[127] D. Duché, *Structures photoniques pour le solaire organique : modélisations et expérimentations.* PhD thesis, Jan. 2010.

[128] A. Polman, "Applied physics. Plasmonics applied.," *Science (New York, N.Y.)* **322**, pp. 868–9, Nov. 2008.

[129] H. A. Atwater and A. Polman, "Plasmonics for improved photovoltaic devices," *Nat Mater* **9**(3), pp. 205–213, 2010.

[130] M. A. Green and S. Pillai, "Harnessing plasmonics for solar cells," *Nature Photonics* **6**, pp. 130–132, Feb. 2012.

[131] S. Pillai and M. Green, "Plasmonics for photovoltaic applications," *Solar Energy Materials and Solar Cells* **94**, pp. 1481–1486, Sept. 2010.

[132] S. A. Maier, *Plasmonics: Fundamentals and Applications*, Springer, 2007.

[133] C. F. Bohren and D. R. Huffman, eds., *Absorption and Scattering of Light by Small Particles*, Wiley-VCH Verlag GmbH, Weinheim, Germany, Apr. 1998.

[134] D. Derkacs, S. H. Lim, P. Matheu, W. Mar, and E. T. Yu, "Improved performance of amorphous silicon solar cells via scattering from surface plasmon polaritons in nearby metallic nanoparticles," *Applied Physics Letters* **89**(9), p. 93103, 2006.

[135] P. Matheu, S. H. Lim, D. Derkacs, C. McPheeters, and E. T. Yu, "Metal and dielectric nanoparticle scattering for improved optical absorption in photovoltaic devices," *Applied Physics Letters* **93**(11), p. 113108, 2008.

[136] M. van Lare, F. Lenzmann, M. A. Verschuuren, and A. Polman, "Mode coupling by plasmonic surface scatterers in thin-film silicon solar cells," *Applied Physics Letters* **101**(22), p. 221110, 2012.

[137] K. Nakayama, K. Tanabe, and H. A. Atwater, "Plasmonic nanoparticle enhanced light absorption in GaAs solar cells," *Applied Physics Letters* **93**(12), p. 121904, 2008.

[138] K. Nakayama, K. Tanabe, and H. A. Atwater, "Surface plasmon enhanced photocurrent in thin GaAs solar cells," in *Nanoscale Photonic and Cell Technologies for Photovoltaics*, L. Tsakalakos, ed., **7047**(1), p. 704708, SPIE, 2008.

[139] W. Liu, X. Wang, Y. Li, Z. Geng, F. Yang, and J. Li, "Surface plasmon enhanced GaAs thin film solar cells," *Solar Energy Materials and Solar Cells* **95**, pp. 693–698, Feb. 2011.

[140] D. Derkacs, W. V. Chen, P. M. Matheu, S. H. Lim, P. K. L. Yu, and E. T. Yu, "Nanoparticle-induced light scattering for improved performance of quantum-well solar cells," *Applied Physics Letters* **93**(9), p. 91107, 2008.

[141] G. Baraldi, R. Caballero, C. Kaufmann, and J. Gonzalo, "Application of PLD to the production of plasmonic structures containing Ag nanoparticles based on chalcopyrite solar cells," *Energy Procedia* **10**, pp. 38–42, Jan. 2011.

[142] K. R. Catchpole and A. Polman, "Design principles for particle plasmon enhanced solar cells," *Applied Physics Letters* **93**(19), p. 191113, 2008.

[143] J.-P. Barnes, A. K. Petford-Long, R. C. Doole, R. Serna, J. Gonzalo, A. Suárez-García, C. N. Afonso, and D. Hole, "Structural studies of Ag nanocrystals embedded in amorphous Al2O3 grown by pulsed laser deposition," *Nanotechnology* **13**, pp. 465–470, Aug. 2002.

[144] H. R. Stuart and D. G. Hall, "Absorption enhancement in silicon-on-insulator waveguides using metal island films," *Applied Physics Letters* **69**(16), p. 2327, 1996.

[145] H. R. Stuart and D. G. Hall, "Island size effects in nanoparticle-enhanced photodetectors," *Applied Physics Letters* **73**(26), pp. 3815–3817, 1998.

[146] H. Tan, R. Santbergen, A. H. M. Smets, and M. Zeman, "Plasmonic light trapping in thin-film silicon solar cells with improved self-assembled silver nanoparticles.," *Nano letters* **12**, pp. 4070–6, Aug. 2012.

[147] H. Fredriksson, Y. Alaverdyan, A. Dmitriev, C. Langhammer, D. S. Sutherland, M. Zäch, and B. Kasemo, "Hole–Mask Colloidal Lithography," *Advanced Materials* **19**, pp. 4297–4302, Dec. 2007.

[148] M. A. Vershuuren and H. A. van Sprang, "Large-area nanopatterns: improving LEDs, lasers, and photovoltaics," *SPIE Newsroom* , June 2012.

[149] F. J. Beck, A. Polman, and K. R. Catchpole, "Tunable light trapping for solar cells using localized surface plasmons," *Journal of Applied Physics* **105**(11), p. 114310, 2009.

[150] D. Duche, P. Torchio, L. Escoubas, F. Monestier, J.-J. Simon, F. Flory, and G. Mathian, "Improving light absorption in organic solar cells by plasmonic contribution," *Solar Energy Materials and Solar Cells* **93**, pp. 1377–1382, Aug. 2009.

[151] S. Vedraine, P. Torchio, D. Duché, F. Flory, J.-J. Simon, J. Le Rouzo, and L. Escoubas, "Intrinsic absorption of plasmonic structures for organic solar cells," *Solar Energy Materials and Solar Cells* **95**, pp. S57–S64, May 2011.

[152] S. Vedraine, "Intégration de nanostructures plasmoniques au sein de dispositifs photovoltaïques organiques : étude numérique et expérimentale," Oct. 2012.

[153] M. Python, O. Madani, D. Dominé, F. Meillaud, E. Vallat-Sauvain, and C. Ballif, "Influence of the substrate geometrical parameters on microcrystalline silicon growth for thin-film solar cells," *Solar Energy Materials and Solar Cells* **93**, pp. 1714–1720, Oct. 2009.

[154] A. Basch, F. Beck, T. Soderstrom, S. Varlamov, and K. R. Catchpole, "Enhanced light trapping in solar cells using snow globe coating," *Progress in Photovoltaics: Research and Applications* **20**, pp. 837–842, Nov. 2012.

[155] A. Basch, F. J. Beck, T. Soderstrom, S. Varlamov, and K. R. Catchpole, "Combined plasmonic and dielectric rear reflectors for enhanced photocurrent in solar cells," *Applied Physics Letters* **100**, p. 243903, June 2012.

[156] P. Spinelli, M. A. Verschuuren, and A. Polman, "Broadband omnidirectional antireflection coating based on subwavelength surface Mie resonators.," *Nature communications* **3**, p. 692, Jan. 2012.

[157] C. Hagglund, M. Zach, and B. Kasemo, "Enhanced charge carrier generation in dye sensitized solar cells by nanoparticle plasmons," *Applied Physics Letters* **92**(1), p. 013113, 2008.

[158] V. E. Ferry, M. A. Verschuuren, H. B. T. Li, E. Verhagen, R. J. Walters, R. E. I. Schropp, H. A. Atwater, and A. Polman, "Light trapping in ultrathin plasmonic solar cells," *Optics Express* **18**, p. A237, June 2010.

[159] V. E. Ferry, M. A. Verschuuren, H. B. T. Li, R. E. I. Schropp, H. A. Atwater, and A. Polman, "Improved red-response in thin film a-Si:H solar cells with soft-imprinted plasmonic back reflectors," *Applied Physics Letters* **95**(18), p. 183503, 2009.

[160] E. B. J. L. M. L. B. Pala Justin White, R. A. Pala, J. White, E. Barnard, J. Liu, and M. L. Brongersma, "Design of Plasmonic Thin-Film Solar Cells with Broadband Absorption Enhancements," *Advanced Materials* **21**, pp. 1–6, 2009.

[161] J. N. Munday and H. A. Atwater, "Large integrated absorption enhancement in plasmonic solar cells by combining metallic gratings and antireflection coatings.," *Nano letters* **11**, pp. 2195–201, June 2011.

[162] I. Massiot, C. Colin, N. Pere-Laperne, P. Roca i Cabarrocas, C. Sauvan, P. Lalanne, J.-L. Pelouard, and S. Collin, "Nanopatterned front contact for broadband absorption in ultra-thin amorphous silicon solar cells," *Applied Physics Letters* **101**, p. 163901, Oct. 2012.

[163] I. Massiot, C. Colin, C. Sauvan, P. Lalanne, P. R. i. Cabarrocas, J.-L. Pelouard, and S. Collin, "Multi-resonant absorption in ultra-thin silicon solar cells with metallic nanowires," *Optics Express* **21**, p. A372, Apr. 2013.

[164] J. Grandidier, D. M. Callahan, J. N. Munday, and H. A. Atwater, "Gallium Arsenide Solar Cell Absorption Enhancement Using Whispering Gallery Modes of Dielectric Nanospheres," *IEEE Journal of Photovoltaics* **2**, pp. 123–128, Apr. 2012.

[165] A. Cattoni, P. Ghenuche, A.-M. Haghiri-Gosnet, D. Decanini, J. Chen, J.-L. Pelouard, and S. Collin, "$\lambda^3/1000$ plasmonic nanocavities for biosensing fabricated by soft UV nanoimprint lithography.," *Nano letters* **11**, pp. 3557–63, Sept. 2011.

[166] J. P. Kottmann, O. J. F. Martin, D. R. Smith, and S. Schultz, "Plasmon resonances of silver nanowires with a nonregular cross section," *Physical Review B (Condensed Matter and Materials Physics)* **64**, p. 235402, 2001.

[167] N. Liu, M. Mesch, T. Weiss, M. Hentschel, and H. Giessen, "Infrared perfect absorber and its application as plasmonic sensor.," *Nano letters* **10**, pp. 2342–8, July 2010.

[168] H. Tao, C. M. Bingham, A. C. Strikwerda, D. Pilon, D. Shrekenhamer, N. I. Landy, K. Fan, X. Zhang, W. J. Padilla, and R. D. Averitt, "Highly flexible wide angle of incidence terahertz metamaterial absorber: Design, fabrication, and characterization," *Physical Review B (Condensed Matter and Materials Physics)* **78**(24), p. 241103, 2008.

[169] G. Lévêque and O. J. F. Martin, "Optical interactions in a plasmonic particle coupled to a metallic film," *Opt. Express* **14**(21), pp. 9971–9981, 2006.

[170] Y. Ekinci, A. Christ, M. Agio, O. J. F. Martin, H. H. Solak, and J. F. Löffler, "Electric and magnetic resonances in arrays of coupled gold nanoparticle in-tandem pairs," *Opt. Express* **16**(17), pp. 13287–13295, 2008.

[171] J. L. Perchec, Y. Desieres, and R. E. de Lamaestre, "Plasmon-based photosensors comprising a very thin semiconducting region," *Applied Physics Letters* **94**(18), p. 181104, 2009.

[172] H. A. Haus, *Waves and Fields in Optoelectronics (Prentice-Hall series in solid state physical electronics)*, Prentice Hall, 1983.

[173] S. Fan, W. Suh, and J. D. Joannopoulos, "Temporal coupled-mode theory for the {F}ano resonance in optical resonators," *J. Opt. Soc. Am. A* **20**(3), p. 569, 2003.

[174] K. Aydin, V. E. Ferry, R. M. Briggs, and H. A. Atwater, "Broadband polarization-independent resonant light absorption using ultrathin plasmonic super absorbers.," *Nature communications* **2**, p. 517, Jan. 2011.

[175] P. B. Johnson and R. W. Christy, "Optical Constants of Noble Metals," *Physical Review B (Condensed Matter and Materials Physics)* **6**(12), pp. 4370–4379, 1972.

[176] F. Pardo, J.-L. Pelouard, and S. Collin, "Waveguiding in nanoscale metallic apertures," *Opt. Express* **15**(7), pp. 4310–4320, 2007.

[177] M. G. Moharam and T. K. Gaylord, "Rigorous coupled-wave analysis of grating diffraction - E-mode polarization and losses," *J. Opt. Soc. Am.* **73**(4), pp. 451–455, 1983.

[178] M. G. Moharam, E. B. Grann, D. A. Pommet, and T. K. Gaylord, "Formulation for stable and efficient implementation of the rigorous coupled-wave analysis of binary gratings," *J. Opt. Soc. Am. A* **12**(5), pp. 1068–1076, 1995.

[179] P. Lalanne and G. M. Morris, "Highly improved convergence of the coupled-wave method for TM polarization," *J. Opt. Soc. Am. A* **13**(4), pp. 779–784, 1996.

[180] L. Li, "New formulation of the {F}ourier modal method for crossed surface-relief gratings," *J. Opt. Soc. Am. A* **14**(10), p. 2758, 1997.

[181] P. Lalanne and M. P. Jurek, "Computation of the near-field pattern with the coupled-wave method for transverse magnetic polarization," *Journal of Modern Optics* **45**(7), p. 1357, 1998.

[182] P. Lalanne, "Improved formulation of the coupled-wave method for two-dimensional gratings," *Journal of the Optical Society of America A* **14**, p. 1592, July 1997.

[183] P. B. Johnson and R. W. Christy, "Optical Constants of the Noble Metals," *Physical Review B* **6**, pp. 4370–4379, Dec. 1972.

[184] M. A. Green, K. Emery, Y. Hishikawa, W. Warta, and E. D. Dunlop, "Solar cell efficiency tables (version 40)," *Progress in Photovoltaics: Research and Applications* **20**, pp. 606–614, Aug. 2012.

[185] M. G. Deceglie, V. E. Ferry, A. P. Alivisatos, and H. A. Atwater, "Design of Nanostructured Solar Cells Using Coupled Optical and Electrical Modeling," *NanoLetters* **12**, pp. 2894–2900, 2012.

[186] X. Li, N. P. Hylton, V. Giannini, K.-H. Lee, N. J. Ekins-Daukes, and S. A. Maier, "Multi-dimensional modeling of solar cells with electromagnetic and carrier transport calculations," *Progress in Photovoltaics: Research and Applications* **21**, pp. 109–120, Jan. 2013.

[187] R. Wolffenbuttel and K. Wise, "Low-temperature silicon wafer-to-wafer bonding using gold at eutectic temperature," *Sensors and Actuators A: Physical* **43**, pp. 223–229, May 1994.

[188] Y. C. Lin, M. Baum, M. Haubold, J. Fromel, M. Wiemer, T. Gessner, and M. Esashi, "Development and evaluation of AuSi eutectic wafer bonding," in *TRANSDUCERS 2009 - 2009 International Solid-State Sensors, Actuators and Microsystems Conference*, pp. 244–247, IEEE, June 2009.

[189] D. Pomerantz, "Anodic bonding," 1966.

[190] G. Wallis, "Field Assisted Glass-Metal Sealing," *Journal of Applied Physics* **40**(10), p. 3946, 1969.

[191] V. G. Weizer and N. S. Fatemi, "The interaction of gold with gallium arsenide," *Journal of Applied Physics* **64**(9), p. 4618, 1988.

[192] H. Elfatimi, *Etude et réalisation de transistors bipolaires à hétérojonction InP/-GaAsSb/InP reportés sur substrat hôte pour application à la puissance.* PhD thesis, Université de Limoges, 2008.

[193] J. J. LePore, "An improved technique for selective etching of GaAs and GaAlAs," *Journal of Applied Physics* **51**(12), p. 6441, 1980.

[194] Z. Cui, *Nanofabrication: Principles, Capabilities and Limits*, Springer, 2008.

[195] V. Logeeswaran, N. P. Kobayashi, M. S. Islam, W. Wu, P. Chaturvedi, N. X. Fang, S. Y. Wang, and R. S. Williams, "Ultrasmooth silver thin films deposited with a germanium nucleation layer.," *Nano letters* **9**, pp. 178–82, Jan. 2009.

[196] S. Collin, F. Pardo, and J.-L. Pelouard, "Resonant-cavity-enhanced subwavelength metal-semiconductor-metal photodetector," *Applied Physics Letters* **83**(8), pp. 1521–1523, 2003.

[197] C. Billaudeau, *Guidage optique dans les cristaux plasmoniques 1D et 2D.* PhD thesis, UNIVERSITÉ PARIS-SUD 11, 2007.

[198] J. M. Bennett, J. L. Stanford, and E. J. Ashley, "Optical Constants of Silver Sulfide Tarnish Films," *Journal of the Optical Society of America* **60**, p. 224, Feb. 1970.

[199] H. Dlala, M. Amlouk, S. Belgacem, P. Girard, and D. Barjon, "Structural and optical properties of Ag 2 S thin films prepared by spray pyrolysis," *The European Physical Journal Applied Physics* **2**, pp. 13–16, Apr. 1998.

[200] P. W. Wilson, "Determining optical properties of thin films by modified attenuated total reflection with a charge coupled device," *Journal of Vacuum Science & Technology A: Vacuum, Surfaces, and Films* **6**, p. 2386, July 1988.

[201] K. Orgassa, *Coherent Optical Analysis of the ZnO/CdS/Cu(In,Ga)Se2 Thin Film Solar Cell (Berichte Aus Der Halbleitertechnik)*, Shaker Verlag GmbH, Germany.

[202] W. Pelouch, R. Ellingson, P. Powers, C. Tang, D. Szmyd, and A. Nozik, "Comparison of hot-carrier relaxation in quantum wells and bulk GaAs at high carrier densities," *Physical Review B* **45**, pp. 1450–1453, Jan. 1992.

[203] C. Shank, R. Fork, R. Yen, J. Shah, B. Greene, A. Gossard, and C. Weisbuch, "Picosecond dynamics of hot carrier relaxation in highly excited multiquantum well structures," *Solid State Communications* **47**, pp. 981–983, Sept. 1983.

[204] W. Pötz and P. Kocevar, "Electronic power transfer in pulsed laser excitation of polar semiconductors," *Physical Review B* **28**, pp. 7040–7047, Dec. 1983.

[205] N. Ehrmann and R. Reineke-Koch, "Ellipsometric studies on ZnO:Al thin films: Refinement of dispersion theories," *Thin Solid Films* **519**, pp. 1475–1485, Dec. 2010.

[206] P. D. Paulson, R. W. Birkmire, and W. N. Shafarman, "Optical characterization of CuIn(1-x)Ga(x)Se2 alloy thin films by spectroscopic ellipsometry," *Journal of Applied Physics* **94**(2), p. 879, 2003.

[207] E. Khawaja and S. G. Tomlin, "The optical constants of thin evaporated films of cadmium and zinc sulphides," *Journal of Physics D: Applied Physics* **8**, pp. 581–593, Apr. 1975.

[208] R. Matson, O. Jamjoum, A. Buonaquisti, P. Russell, L. Kazmerski, P. Sheldon, and R. Ahrenkiel, "Metal contacts to CuInSe2," *Solar Cells* **11**, pp. 301–305, Apr. 1984.

[209] A. Campa, J. Krc, J. Malmström, M. Edoff, F. Smole, and M. Topic, "The potential of textured front ZnO and flat TCO/metal back contact to improve optical absorption in thin Cu(In,Ga)Se2 solar cells," *Thin Solid Films* **515**(15), pp. 5968–5972, 2007.

[210] T. Nakada, Y. Hirabayashi, and T. Tokado, "Cu(In1-x, Gax)Se2-Based Thin Film Solar Cells Using Transparent Conducting Back Contacts," *Japanese Journal of Applied Physics* **41**, pp. L1209–L1211, Nov. 2002.

[211] T. Nakada, Y. Hirabayashi, T. Tokado, D. Ohmori, and T. Mise, "Novel device structure for Cu(In,Ga)Se2 thin film solar cells using transparent conducting oxide back and front contacts," *Solar Energy* **77**, pp. 739–747, Dec. 2004.

[212] P. Rostan, J. Mattheis, G. Bilger, U. Rau, and J. Werner, "Formation of transparent and ohmic ZnO:Al/MoSe2 contacts for bifacial Cu(In,Ga)Se2 solar cells and tandem structures," *Thin Solid Films* **480-481**, pp. 67–70, June 2005.

[213] C. Hubert, N. Naghavi, O. Roussel, A. Etcheberry, D. Hariskos, R. Menner, M. Powalla, O. Kerrec, and D. Lincot, "The Zn(S,O,OH)/ZnMgO buffer in thin film Cu(In,Ga)(S,Se) 2 -based solar cells part I: Fast chemical bath deposition of Zn(S,O,OH) buffer layers for industrial application on Co-evaporated Cu(In,Ga)Se 2 and electrodeposited CuIn(S,Se) 2 solar cells," *Progress in Photovoltaics: Research and Applications* **17**, pp. 470–478, Nov. 2009.

[214] D. Hariskos, B. Fuchs, R. Menner, N. Naghavi, C. Hubert, D. Lincot, and M. Powalla, "The Zn(S,O,OH)/ZnMgO buffer in thin-film Cu(In,Ga)(Se,S) 2 -based solar cells part II: Magnetron sputtering of the ZnMgO buffer layer for in-line co-evaporated Cu(In,Ga)Se 2 solar cells," *Progress in Photovoltaics: Research and Applications* **17**, pp. 479–488, Nov. 2009.

[215] J. M. Siqueiros, R. Machorro, and L. E. Regalado, "Determination of the optical constants of MgF_2 and ZnS from spectrophotometric measurements and the classical oscillator method," *Applied Optics* **27**, p. 2549, June 1988.

[216] K. Orgassa, H. Schock, and J. Werner, "Alternative back contact materials for thin film Cu(In,Ga)Se2 solar cells," *Thin Solid Films* **431-432**, pp. 387–391, May 2003.

[217] T. Wada, N. Kohara, S. Nishiwaki, and T. Negami, "Characterization of the Cu(In,Ga)Se2/Mo interface in CIGS solar cells," *Thin Solid Films* **387**, pp. 118–122, May 2001.

[218] T. Wada, N. Kohara, T. Negami, and M. Nishitani, "Chemical and Structural Characterization of Cu(In,Ga)Se2/Mo Interface in Cu(In,Ga)Se2 Solar Cells," *Japanese Journal of Applied Physics* **35**, pp. L1253–L1256, Oct. 1996.

[219] J. Malmström, O. Lundberg, and L. Stolt, "Potential for light trapping in Cu(In,Ga)Se2 solar cells," in *Proceedings 3rd World Conference on Photovoltaic Energy Conversion*, pp. 344–347, 2004.

[220] E. Moons, T. Engelhard, and D. Cahen, "Ohmic contacts to p-CuInSe2 crystals," *Journal of Electronic Materials* **22**, pp. 275–280, Mar. 1993.

[221] T. Anegawa, Y. Oda, T. Minemoto, and H. Takakura, "Comparison of lift-off processes and rear-surface characterization of Cu(In,Ga)Se2 thin films for solar cells," *Journal of Crystal Growth* **311**, pp. 742–745, Jan. 2009.

[222] T. Minemoto, Y. Abe, T. Anegawa, S. Osada, and H. Takakura, "Lift-Off Process for Flexible Cu(In,Ga)Se 2 Solar Cells," *Japanese Journal of Applied Physics* **49**, p. 04DP06, Apr. 2010.

[223] M. Powalla, M. Cemernjak, J. Eberhardt, F. Kessler, R. Kniese, H. Mohring, and B. Dimmler, "Large-area CIGS modules: Pilot line production and new developments," *Solar Energy Materials and Solar Cells* **90**, pp. 3158–3164, Nov. 2006.

[224] Z. Jehl Li-Kao, *Elaboration of ultrathin Copper Indium Gallium Di-Selenide based Solar Cells.* PhD thesis, University Paris XI, 2012.

[225] C. Guillen and J. Herrero, "Effects of Thermal and Chemical Treatments on the Composition and Structure of Electrodeposited CuInSe2 Thin Films," *Journal of The Electrochemical Society* **141**, p. 225, Jan. 1994.

[226] T. Hildebrant, *Etude de couches minces de CIGS: determination de la cinétique d'attaque, caractérisation de la surface et de piles.* PhD thesis, Grenoble-INP PHELMA (University Grenoble 1), 2009.

[227] S. Y. Chou, P. R. Krauss, and P. J. Renstrom, "Imprint of sub-25 nm vias and trenches in polymers," *Applied Physics Letters* **67**(21), p. 3114, 1995.

[228] S. Chou, "Nanoimprint lithography," *Journal of Vacuum Science ...* , pp. 3557–3563, 1996.

[229] J. Haisma, "Mold-assisted nanolithography: A process for reliable pattern replication," *Journal of Vacuum Science & Technology B: Microelectronics and Nanometer Structures* **14**, p. 4124, Nov. 1996.

[230] T. W. Odom, J. C. Love, D. B. Wolfe, K. E. Paul, and G. M. Whitesides, "Improved Pattern Transfer in Soft Lithography Using Composite Stamps," *Langmuir* **18**, pp. 5314–5320, June 2002.

[231] J. Chen, J. Shi, D. Decanini, E. Cambril, Y. Chen, and A.-M. Haghiri-Gosnet, "Gold nanohole arrays for biochemical sensing fabricated by soft UV nanoimprint lithography," *Microelectronic Engineering* **86**, pp. 632–635, Apr. 2009.

[232] C. Luo, X. Ni, L. Liu, S.-i. M. Nomura, and Y. Chen, "Degassing-assisted patterning of cell culture surfaces.," *Biotechnology and bioengineering* **105**, pp. 854–9, Mar. 2010.

[233] G. F. A. Cattoni E. Cambril D. Decanini, A. M. Haghiri-Gosnet, A. Cattoni, E. Cambril, D. Decanini, and G. Faini, "Soft UV-NIL at 20nm scale using flexible bi-layer stamp casted on HSQ master mold," *Microelectronic Engineering* **87**, pp. 1015–1018, May 2010.

[234] A. Cattoni, D. Decanini, E. Cambril, G. Faini, and A. M. Haghiri-Gosnet, "Degassed Assisted Pattering at 15 nm scale," in *MNE*, 2011.

[235] M. Alonso, M. Garriga, C. Durante Rincón, E. Hernández, and M. León, "Optical functions of chalcopyrite CuGa x In 1-x Se 2 alloys," *Applied Physics A: Materials Science & Processing* **74**, pp. 659–664, May 2002.

[236] S. Ninomiya and S. Adachi, "Optical properties of wurtzite CdS," *Journal of Applied Physics* **78**(2), pp. 1183–1190, 1995.